PolKa: a Polarimeter for Submillimeter Bolometer Arrays

Dissertation

zur

Erlangung des Doktorgrades (Dr. rer. nat.)

der

Mathematisch-Naturwissenschaftlichen Fakultät

der

Rheinischen Friedrich-Wilhelms-Universität Bonn

vorgelegt von

Giorgio Siringo

aus

Comiso

Bonn, April 2003

Angefertigt mit Genehmigung der Mathematisch-Naturwissenschaftlichen Fakultät der Rheinischen Friedrich-Wilhelms-Universität Bonn

1. Referent: Prof. Dr. U. Klein
2. Referent: Prof. Dr. K. M. Menten

Tag der Promotion:

Abstract

Starting from measurements of the linear polarization of the radiation emitted by celestial objects it is possible to estimate some physical parameters of the source. For example, magnetic field intensities and directions or, when the magnetic field is already known, the processes producing the polarization.

A new concept of polarimeter has been designed to be used together with the arrays of bolometers developed in the Bolometer Group at the Max-Planck-Institut für Radioastronomie in Bonn. The new polarimeter has the unique characteristic of being tunable over a wide range of wavelengths and of producing a negligible absorption. It has been used at the Heinrich Hertz telescope in Arizona, to measure the linear polarization of some quasars and of some extended sources inside our galaxy.

Some results are presented. We detected polarization on the quasars 3C279 and 1633+382. On 3C279 we also detected polarization variability on a time scale of a week. Three maps of extended sources are presented: the BN/KL complex in Orion OMC-1, a filament cloud in Orion OMC-3 and the massive star forming region IRAS 05358+3543. The first map shows the polarization pattern in OMC-1 over an extended sky area with high signal-to-noise and accurate detection of the position angle. The filament in OMC-3 was observed for a short integration time and is presented here only to show the agreement with published data even under conditions of a weak signal-to-noise. The third map is the first detection of polarization in the high-mass star forming region IRAS 05358+3543.

The polarimeter has low spurious polarization and a good efficiency and the tests at the telescope show that it is well suited to become a permanent facility.

Contents

Abstract **III**

Introduction **1**

I About linear polarization at mm/submm wavelengths and how to detect it **7**

1 Polarimetry with bolometers **9**

1.1 Linear polarization of the continuum emission 9

1.1.1 Polarization in dust clouds 10

1.1.2 Polarization in Active Galactic Nuclei 15

1.2 Basic concepts of bolometric receivers 18

1.2.1 Thermal detectors 19

1.2.2 Composite bolometers 19

1.2.3 Arrays of bolometers 22

1.3 The detectability of linear polarization 24

2 The design of a polarimeter for mm/submm wavelengths **29**

2.1 The standard scheme of a polarimeter 29

2.2 Polarimetry with a half-wave plate 32

2.3 Polarimeter using a reflection-type half-wave plate 36

II Construction of the polarimeter, and observations **43**

3 Production of wire-grid polarizers **45**

3.1 Introduction 45
3.2 General concepts of wire-grid polarizers 46
3.3 The wire-grids of 146 mm diameter 49
3.4 The wire-grid machine and its upgrade 50
3.5 The wire-grids of 246 mm diameter 54

4 The reflection type half-wave plate 59
4.1 The prototype 59
4.2 Design of the 146 mm half-wave plate 63
4.3 Design of the 246 mm half-wave plate 72

5 The polarimeter at the telescope 75
5.1 Introduction 75
5.2 The Heinrich Hertz Telescope 76
5.2.1 Receivers 78
5.2.2 The wobbler 80
5.2.3 Polarization modulation 82
5.3 Observing modes 82
5.3.1 Total power `On-Off` (`TPOO`) 83
5.3.2 Total power `On-the-Fly` (`TPOtF`) 84
5.3.3 Other total power observing modes 85
5.3.4 Polarization `On-Off` (`POO`) 86
5.3.5 Polarization `On-the-Fly` (`POtF`) 87
5.4 The data acquisition 88
5.4.1 The total power backend DRUMBEAT 88
5.4.2 The polarimeter backend PolKABBA 89
5.4.3 Sync and blank 90
5.4.4 Acquisition bit 91
5.5 First telescope run: May 2001 93
5.6 Second telescope run: January 2002 95
5.6.1 Installation 97
5.6.2 Source list and observations 99

III Data reduction and results 101

6 Data reduction 103

6.1 Software development . . . 103

6.1.1 Despiking . . . 104

6.1.2 Total-Power `On-Off` reduction software . . . 104

6.1.3 The software Lock-In . . . 108

6.1.4 Polarization `On-Off` reduction software . . . 111

6.1.5 Polarization `On-the-Fly` maps reduction software . . . 114

6.1.6 The graphical representation of polarization maps . . . 117

6.2 Calibrations . . . 119

6.2.1 DRUMBEAT/PolKABBA conversion factor . . . 119

6.2.2 Counts/Jansky conversion factor . . . 120

6.2.3 Bolometer gain correction . . . 121

6.2.4 Bolometer frequency response . . . 121

6.2.5 Spurious polarization: planets as unpolarized sources . . . 122

6.2.6 Absolute position angle . . . 126

7 Results 127

7.1 Introduction . . . 127

7.2 Polarization of point sources: detections . . . 127

7.2.1 3C279 . . . 127

7.2.2 1633+382 . . . 131

7.3 Polarization of point sources: upper limits . . . 133

7.4 Polarization of extended sources . . . 133

7.4.1 Orion A OMC-1 . . . 133

7.4.2 Orion A MMS3/MMS4 . . . 139

7.4.3 IRAS 05358+3543 . . . 141

Conclusions 148

Appendices 149

A Polarization `On-Off` data 149

B Polarization upper limits **151**

C Polarization maps data **153**

Acknowledgements **164**

Bibliography **164**

List of Figures **174**

Introduction

My Ph.D. project has taken place in the Bolometer Development Group, a section of the Submillimeter Technology Division of the Millimeter and Submillimeter Astronomy Group at the Max-Planck-Institut für Radioastronomie (hereafter MPIfR) in Bonn.

The main interest of our group is the study of interstellar matter, in the Milky Way and in external galaxies. Of special interest is the physics and chemistry of molecular clouds, which make up the denser portions of the interstellar medium.

Our studies aim at a better understanding of the star formation process and they concentrate on molecular clouds because it is in the highest density regions of such clouds that new stars are forming.

The radiation coming from a sky source can be separated mainly into three categories:

- radiation emitted by thermal emission, whose maximum intensity is related to the temperature of the source following Wien's displacement law;
- line emission, produced by transitions between different energy states of molecules and atoms;
- "non-thermal" synchrotron radiation, emitted by ions accelerated in a magnetic field.

Molecular clouds give rise to spectral line emission, produced by atoms and molecules, and continuum emission, mostly coming from dust grains. Synchrotron emission is normally negligible and is instead dominant in the radiation coming from quasars and, in general, active galactic nuclei.

Starting from observations of molecules and dust it is possible to get information on densities, temperatures, kinematics, magnetic fields, and chemical abundances in the emitting regions.

The research done in the last years, thanks to increasing interest in the far-infrared and millimeter and sub-millimeter astronomy and to the improvement of observational techniques in this part of the electromagnetic spectrum, has shown the extent to which dust grains are vital ingredients for the star formation process and for the star evolution which follows.

Dust grains of the interstellar medium are essential participants in the early stages of star formation. They are necessary for the formation of molecules, they can drive a star to the end of its life, they contribute to form planets around stars like the Sun but, despite their importance, their study is a new field in astrophysical research and they are still not well understood.

The study of dust particles in astrophysical environments is one of the most challenging areas of contemporary astrophysics. It involves many areas of physics, to understand how they interact with radiation, how they are heated by the surrounding hot gas, what chemical reactions take place on their surfaces and so on.

In the millimeter and submillimeter wavelength range, we can use two classes of receivers: heterodyne receivers and bolometers. Bolometers are the best receivers to collect photons produced by continuum thermal emission, because of their high sensitivity due to the large bandwidth. Heterodyne receivers are mainly used to study lines and synchrotron emission because they work over a very narrow bandwidth and are then the best receivers to perform spectroscopy. Of course, both types of receivers are able to detect photons produced by any of the mentioned processes.

The dust particles in the interstellar medium at typical grain temperatures emit radiation essentially in the Rayleigh-Jeans tail of the black-body spectral energy distribution, at millimeter wavelengths. It is a continuum thermal emission and therefore bolometers are the best receivers to study the dust thermal emission.

The study of the intensities of the radiation emitted by the grains at different wavelengths can provide good knowledge about their emissivity and about their chemical composition.

The study of the polarization degree of that radiation is a good tool to get information about the grain sizes and their geometrical properties, and about the strength of the magnetic field.

Furthermore, the study of the polarization alignment, along magnetic field's lines, gives information about composition and geometry of the grains but, on the other hand, it is a tracer for the magnetic field itself in the molecular cloud.

Magnetic fields definitely play an important role in the star formation process: the study of polarization of thermal radiation emitted by grains is indeed one of the most powerful tools we have to investigate how magnetic fields interact with particles and gas determining dynamics and evolution of molecular clouds.

The aim of my Ph.D. project has been to provide the Millimeter and Submillimeter Astronomy Group at MPIfR with a polarimeter to study the linear polarization of the radiation emitted by dust particles of the interstellar medium.

The polarimeter, *PolKa* (Polarimeter für Bolometer Kameras) has already been tested at the Heinrich Hertz Telescope in Arizona. The tests were successful and we are now planning to install it as a permanent instrument at the IRAM 30 meter telescope in Spain. A modified version will be installed at the APEX (Atacama Pathfinder Experiment) telescope in Chile, in the near future.

We put some constraints on the properties of our polarimeter. First of all, the polarimeter will mainly be used together with the bolometric receivers produced in the MPIfR Bolometer Development Group: the MAMBO (Max-Planck Millimeter Bolometer Array) and MAMBO-2 arrays of 37 and 117 bolometers, respectively, operating at a central wavelength of 1.2 mm, HUMBA (Hundred Millikelvin Bolometer Array) at 2.0 mm, and the HHT-19-channel array at 0.87 mm. It is clear, then, that we need a polarimeter able to cover a wide range of wavelengths, but not necessarily at the same time. We decided to produce a tunable instrument, able to switch easily from one frequency to another over a wide range. Secondly, the polarization degree of the dust thermal emission is typically very low, in the order of a few percent: this means our polarimeter should produce as little attenuation of the signal as possible. We designed a polarimeter that makes use of only metallic reflections, avoiding any absorption by crystals. Thirdly, using arrays of bolometers and a polarimeter based on metallic reflections, we are forced to go on the focal plane of the telescope, where the beam is fairly large. This means the polarimeter itself must be large enough to cover it.

This work is divided into three parts.

- First of all, an overview of the properties of polarized radiation produced by the astronomical sources is given, to understand what should be the optimal design of a polarimeter to detect it.

  In the first chapter, I'll give a short description of the basic principles of bolometric receivers and of the basic processes producing linear polarization, in dust clouds and in quasars.

  The second chapter gives a description of the typical design of a polarimeter for millimeter waves, and of the special design of our polarimeter.

- The second part is about the most experimental part of my work: the construction of the polarimeter, the installation at the telescope and the observations.

  At the beginning of the third chapter, I will describe the properties of polarizing filters used in our range of wavelengths, the wire-grid polarizers. Given the need of a large reflecting half-wave plate we were forced to produce large wire-grid polarizers in our laboratories. In that chapter I will explain how we produced our own polarizers.

  The fourth chapter is dedicated to the design and the first lab tests of the reflection type half-wave plate.

  The fifth chapter is about the installation of the polarimeter at the telescope and all the related issues, such as the characteristics of the telescope, the data acquisition system, the observing modes that we defined and the sources observed.

- The third part describes the final part of my work: the data reduction, the results we got and a preliminary interpretation of them.

  Given a brand new instrument whose operation principles are new, there was no software ready to be used for the data reduction. I was obliged to write the software myself, and in chapter 6 I will describe some details of the software and, in general, of data reduction and calibration.

  Chapter seven is devoted to the description of our first polarization results, with tables and images. Hints for a possible interpretation are also given.

In the conclusive chapter, I will summarize the results and I will discuss merits and defects of our polarimeter. This is the starting point for an understanding where the system has to be improved and for planning a future permanent installation at the telescopes.

Part I

About linear polarization at mm/submm wavelengths and how to detect it

Chapter 1

Polarimetry with bolometers

1.1 Linear polarization of the continuum emission

Before starting the description of the polarimeter it is necessary to spend some time pointing out the constraints we have to deal with in the design of such an instrument.

First of all, we should have an idea about the expected amount of polarization in the radiation coming from a celestial source. Our main targets are dust clouds, but quasars are also interesting in their own right, and useful for testing the instrument, because polarization at radio wavelengths has already been detected in many of them. Given the different physical environments in these two kinds of source, linear polarization will in general be produced in different ways in the two cases. The next section will give a basic description of the processes leading to polarization in dust clouds and in quasars, together with a rough estimate of the degree of polarization that one could expect to detect.

The next step is to consider the technological limitations. We want to detect linear polarization of the continuum emission in the millimeter and submillimeter wavelength range, and to do that we are going to use bolometers. The second section of this chapter is a brief overview of bolometric receivers. At the end of the chapter, in the third section, I will combine the information we have about the sources that we would like to observe, and about the detectors that we are going to use, with the aim of estimating the detectability of linear polarization.

1.1.1 Polarization in dust clouds

Primeval matter in the universe consists almost entirely of hydrogen ($\sim$ 73%) and helium ($\sim$ 25%) with negligible amounts of heavier elements. Dust grains of the interstellar medium are typically rich in elements like C, O, Si, Fe, Al, Mg. This means that interstellar grains cannot have formed in interstellar space: grains must form in stellar atmospheres and then be injected into the interstellar medium. Then grains evolve and change: they can grow by condensation of common astronomical composites or can be destroyed by collisions with other grains or by sputtering or by other violent processes. Grains can be amorphous or crystalline and their shape is, in general, not spherical. The polarization of starlight passing through dust clouds is a strong evidence of this (Evans, 1994).

Radiation from stars is almost entirely thermal in origin and for this reason it should be not polarized. From the observations, however, it is found that the light of many stars is indeed polarized. The degree of polarization is found to be correlated both with the location relative to the plane of our Galaxy and with the amount of interstellar extinction. This suggests that the observed polarization is not intrinsic to the source but is due to anisotropic extinction by the interstellar medium along the line of sight. Responsible for this anisotropic extinction are the dust grains. Extinction by spherical grains will not preferentially absorb or scatter radiation having any particular state of polarization. On the other hand, non-spherical grains will do so.

In the simplest model, we have a uniform distribution of cylindrical grains, each of radius a and all with their long axes aligned parallel to each other. We consider now the propagation and consequent extinction of an electromagnetic wave through the grain population.

If the wave is polarized in such a way that the electric vector is parallel with the grain axes then the consequent extinction optical depth over a path length D is

$$\tau_{\mathrm{E}} = n_{\mathrm{g}} \pi a^2 Q_{\mathrm{E}} D \tag{1.1}$$

where n_{g} is the grains' density and Q_{E} is the electric extinction efficiency factor; when the wave is polarized with its magnetic vector parallel to the grain axes, the corre-

sponding extinction optical depth is

$$\tau_{\rm H} = n_{\rm g}\pi a^2 Q_{\rm H} D \tag{1.2}$$

where $Q_{\rm H}$ is the magnetic extinction efficiency factor.

In the general case, the incident radiation is unpolarized but we can always represent it as a superposition of two incoherent polarized waves of equal amplitude, and with electric vectors at right angles.

Since $Q_{\rm H} \neq Q_{\rm E}$ we can expect a net polarization even though the original radiation is unpolarized. The degree of polarization will be then

$$p = \frac{Q_{\rm H} - Q_{\rm E}}{Q_{\rm H} + Q_{\rm E}} \tag{1.3}$$

At long wavelengths we can assume the same efficiency factor both for extinction and emission (Hildebrand, 1983). This means that measurements of the polarization of dust thermal emission at millimeter and submillimeter waves are a direct way to study the properties of grains and the alignment efficiency.

The first explanation of the mechanism aligning dust grains to the interstellar magnetic field, based on paramagnetic absorption, was given by Davis & Greenstein (1950).

Consider a non-spherical grain immersed in the interstellar gas: it will acquire rapid spinning motion as a result of the random collisions with gas atoms. In thermal equilibrium one can expect that the energy associated with the grain's spin is comparable with the thermal energy of an atom in the gas,

$$\frac{1}{2} I\omega^2 \approx k_{\rm B} T_{\rm gas} \tag{1.4}$$

where I is the moment of inertia of the grain about its axis of rotation, $k_{\rm B}$ is the Boltzmann constant and $T_{\rm gas}$ is the temperature of the gas.

For a cylindrical grain of mass M and length $2l$, spinning end-over-end, we have

$$I = \frac{1}{3} M l^2 \tag{1.5}$$

and given $l \sim 0.1\mu$m , $M \sim 6 \cdot 10^{-18}$Kg, $T_{\rm gas} \simeq$100 K we get

$$\omega \simeq 3 \cdot 10^5 \ {\rm s}^{-1} \tag{1.6}$$

and so an elongated grain will spin rapidly.

The essence of the Davis-Greenstein mechanism of grain alignment is an interstellar grain, containing paramagnetic impurities, spinning in the interstellar magnetic field. As a result of the rotation, the field internal to the grain becomes misaligned with the external field, resulting in a torque which opposes any component of rotation which has an axis perpendicular to the interstellar magnetic field. Let's consider one grain of interstellar dust, at temperature $T_{\rm g}$ having a magnetic static susceptibility χ_0, relative permeability $\mu_{\rm r}$ (~ 1) in the static magnetic field $\mathbf{B_0}$. In absence of grain spin the magnetization of the grain is

$$\mathbf{M} = \frac{\chi_0}{\mu_0 \mu_{\rm r}} \mathbf{B_0} \tag{1.7}$$

If the temperature of the grains is a few tens of Kelvin, well below the Curie temperature of most plausible grain materials (e.g. for iron 1043 K), the static susceptibility is given by Curie's law

$$\chi_0 = \frac{\mu_0 \mu_{\rm r} \mu_{\rm B}^2 N J(J+1)}{3kT_{\rm g}} \tag{1.8}$$

where $\mu_{\rm B}$ is the Bohr magneton, g is the Landé g-factor, N is the number of magnetic atoms per unit volume and J is the angular momentum quantum number.

We may assume that the dust grains consist mainly of crystals of substances such as methane and ammonia ice, with various heavier atoms present as diffuse impurities. In particular, about one atom in one hundred should be iron or a similar atom having a large magnetic moment. For Fe^{3+} ions, which we can suppose to be the dominant responsible for the magnetic properties of the grains, we have $J = \frac{5}{2}$ and $g = 2$. In this case the static susceptibility is

$$\chi_0 = \frac{7.28n}{T_{\rm g}} \tag{1.9}$$

where n is the number of Fe ions per cubic angstrom.

If the grain is spinning with frequency $\omega \sim 10^5$ s^{-1}, it will experience a magnetic field that varies its magnitude as $B = B_0 \sin \omega t$ and ω is large enough that the field internal to the grain lags the external field. This can be expressed by writing the susceptibility as the complex quantity

$$\chi = \chi' - i\chi'' \tag{1.10}$$

The imaginary part of the magnetic susceptibility characterizes the phase delay between the grain magnetization and the rotating magnetic field. Because of this

delay, a grain rotating in a static magnetic field experiences a decelerating torque and the energy dissipated in the grain comes from rotational kinetic energy.

At low frequencies, $\chi' \approx \chi_0$ and $\chi'' = 0$ that means the grain behaves as in a static field. At higher values of ω, however, the atomic dipoles, in which the paramagnetism of the grain originates, fail to follow the external field, and consequently the internal field has a component perpendicular to the external field and a direction that tends to oppose the rotation of the grain. As a result, grains tend to rotate with angular momenta parallel to the interstellar magnetic field.

For a grain rotating with frequency ω the imaginary part of the susceptibility may be written as

$$\chi'' = \chi_0 \frac{\omega}{\omega_0} \exp\left(-\frac{\omega^2}{2\omega_0^2}\right) \tag{1.11}$$

where ω_0 is defined as

$$\omega_0 = \frac{2}{\hbar}\mu_{\mathrm{B}}^2 N[8S(S+1)\alpha]^{1/2} \tag{1.12}$$

where S is the total spin quantum number ($S = \frac{5}{2}$ for Fe^{3+}) and α is a numerical constant that depends on how the magnetic ions are distributed inside the grain. When we consider just Fe^{3+} ions, we can write ω_0 as

$$\omega_0 = 3.66 \cdot 10^{12} n \tag{1.13}$$

If we consider a reasonable number of ions per cubic angstrom

$$n > 2 \cdot 10^{-7} \quad \text{Å}^{-3} \tag{1.14}$$

then from equation (1.13) and equation (1.6) we find that the ratio ω/ω_0 in equation (1.11) is small enough to consider for the exponential to be taken as unity. Substituting equations (1.9) and (1.13) in (1.11) we have

$$\chi'' = 2.5 \cdot 10^{12} \frac{\omega}{T_{\mathrm{g}}} \tag{1.15}$$

which is essentially independent of the number of Fe ions per cubic angstrom as long as the condition (1.14) is satisfied over a wide range of concentrations.

When a grain rotates with the vector angular velocity $\mathbf{\Omega}$ its magnetization is

$$\mathbf{M} \approx \frac{\chi''}{\mu_0 \mu_{\mathrm{r}}} \left(\frac{\mathbf{\Omega}}{|\mathbf{\Omega}|} \times \mathbf{B}\right) \tag{1.16}$$

and because it is dragged along with the material, it is in general not parallel to the field $\mathbf{B}$.

If V is the volume of the grain, its magnetic moment is $V\mathbf{M}$ and, since $\mathbf{M}$ and $\mathbf{B}$ are not parallel, there is the retarding torque

$$L = V\mathbf{M} \times \mathbf{B} = V\frac{\chi''}{\mu_0\mu_{\mathrm{r}}}(\frac{\mathbf{\Omega}}{|\mathbf{\Omega}|} \times \mathbf{B}) \times \mathbf{B} \tag{1.17}$$

which acts to damp out any rotation about any axis that has a component at right angles to the field.

The net result is that grains, on the average, end up with their long axes perpendicular to the local magnetic field. We should therefore find that the polarization vectors of the dust thermal emission are well organized on the plane of the sky when our line of sight cuts the aligning magnetic field at right angles, whereas the vectors should be chaotically distributed when we view along the field. This is indeed what is found from observations.

From 1950 until now, various mechanisms and their revisions have been proposed, including grains with super-paramagnetic inclusions, mechanical alignment, alignment due to suprathermal rotation, alignment by radiation torques and so on. Nevertheless, the essential idea behind the Davis-Greenstein mechanism remains the best starting point to understand the basics of alignment of dust grains.

Although interstellar extinction, dust thermal emission and polarization have their common origin in interstellar dust grains, their relationships are somehow complicated because polarization depends also on the degree of grain alignment and this is likely to vary from location to location. Furthermore, thermal emission and extinction over a path length accumulate like scalar quantities, while polarization is a vector quantity and therefore polarization produced along one part of the path may be canceled by the polarization produced along another part.

This means that the interpretation of polarization maps is usually not straightforward and that the measured polarization pattern is not necessarily a direct measurement of the magnetic field.

Figure 1.1 shows the degree of polarization versus the total flux of the source, measured in the galactic cloud M17 using the polarimeter HERTZ at 350 μm (Houde et al., 2002). From this plot we see that the degree of polarization shows values of a few

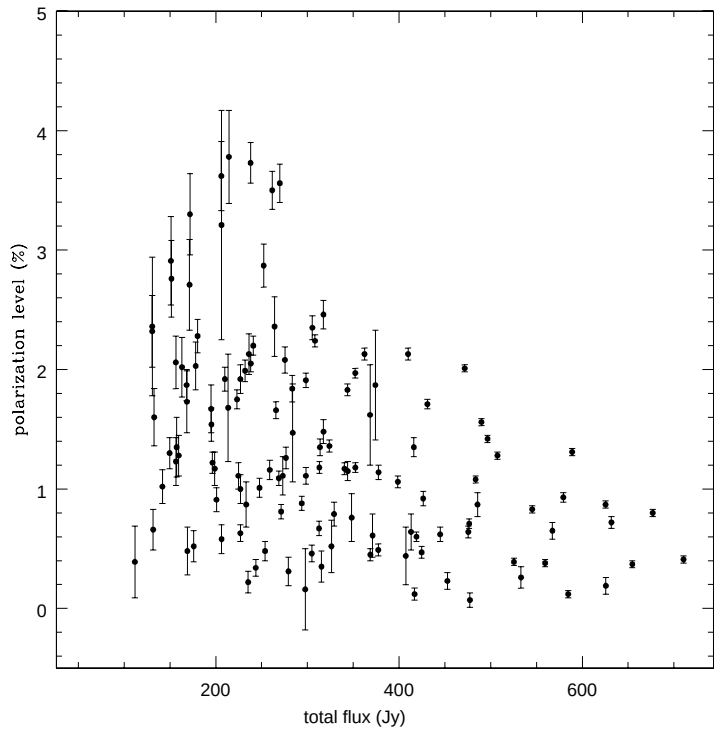

Figure 1.1: Polarization level vs. the total flux taken from a 350 μm polarization map of the galactic cloud M17 (Houde et al., 2002).

percent: this is not only true for M17 but is typical of all the dust sources. The picture shows also a special feature, the so called *depolarization effect*: regions of higher total flux have, in general, a significantly lower level of polarization associated with them.

1.1.2 Polarization in Active Galactic Nuclei

Active Galactic Nuclei (hereafter AGN) are nuclei of galaxies that show energetic phenomena in several bands of the electromagnetic spectrum. Some of the main characteristics used to define a galaxy as an AGN are:

- compact nuclear region, normally brighter than the corresponding region in normal galaxies of the same type.
- non-thermal continuum emission
- strong emission lines
- both continuum and lines emission show variability

- strong radio emission, thought to be powered by a black hole

The definition of an AGN is somewhat vague and the features in the list above are not necessarily all present together in a single AGN.

The following astronomical objects are usually classified as AGNs:

- radiogalaxies
- quasars
- Seyfert galaxies
- BL Lac objects (blazars)
- low ionization nuclear emission-line regions (LINERS), nuclear HII, star burst galaxies, strong IRAS galaxies, optically violent variables (OVV).

In the past decades these objects have been widely studied in the radio, IR, optical and X-ray bands of the electromagnetic spectrum. In comparison, observations at mm/submm wavelengths are relatively recent, and polarization of the continuum emission, in particular, is definitely something new.

With the prospect of being able to perform linear polarization measurements at mm/submm wavelengths with our polarimeter, we were contacted by Thomas Krichbaum and Giuseppe Cimó (VLBI group, MPIfR) and a collaboration was set up to look for linear polarization in quasars and BL Lacs known to be variable on a short time scale (IDV, intraday variable sources, Witzel et al. 1986; Wagner & Witzel 1995). For this reason, we observed just these two classes of AGN.

The non-thermal continuum emission of AGNs is mainly produced by synchrotron emission and the spectral flux density distribution is

$$S(\nu) \propto \nu^{-\alpha} \tag{1.18}$$

Quasars are the most powerful known AGNs, they have strong and broad emission lines and in some 10% of the cases they are strong radiosources. These quasars have a flat spectrum at radio wavelengths, being $-0.5 < \alpha < 0.5$. They are usually variable.

BL Lacs are similar to flat-spectrum quasars but they are lacking emission lines. In most cases, lines are totally absent.

Both flat-spectrum quasars and BL Lacs show strong linear polarization in the radio and optical bands. This is because of the synchrotron emission, emitted by relativistic electrons that follow spiral orbits about the lines of the magnetic field. The emission is strongly directional, being focused inside a cone of angular semi-amplitude $1/\gamma$ where γ is the Lorentz factor $\gamma = (1-(\frac{v}{c})^2)^{-\frac{1}{2}}$. The observer will see the signal from the electron just when the line of sight is in the plane of the orbit. If the line of sight is exactly in the plane of the orbit the observed polarization will be linear; when the line of sight is slightly out from the plane of the orbit, but still inside the emitting cone, the observer will see radiation elliptically polarized. The direction of the electric vector, in case of linear polarization, or the major axis of the polarization ellipse, in case of elliptical polarization, is along the plane of the orbit and so it will always be perpendicular to the magnetic field. Let's consider now an ensemble of relativistic electrons. The observer will see the radiation emitted by those electrons whose instantaneous velocity is at angles smaller than $1/\gamma$ to the line of sight. If we consider now that the velocities are not ordered, then each electron will have a different velocity, the planes of the orbits will be slightly different, the polarization ellipses will have different orientations, and the different contributions of elliptical polarization will average to linear. The polarization of an ensemble of electrons will be again linearly polarized but the degree of polarization will be smaller.

However, the assumption we made, that the flux from a group of relativistic electrons is merely the arithmetical sum of the radiation from the individual electrons, is not always true. When the apparent brightness temperature of the source approaches the equivalent kinetic temperature of the electrons then self-absorption becomes important and part of the radiation is absorbed. The precise form of the radiation spectrum can be calculated from the emission and absorption coefficients of relativistic electrons in a magnetic field (Verschuur & Kellermann, 1974). There are two different expressions giving the polarization degree of the relativistic synchrotron radiation, one for the transparent part and the other for the opaque part of the source. If δ is the power law index of the energy distribution of the electrons, namely

$$N(\varepsilon) = N_0 \varepsilon^{-\delta} \tag{1.19}$$

then we can write the polarization degree as

$$p(\delta) = \frac{3\delta + 3}{3\delta + 7} \tag{1.20}$$

in the transparent part of the source, and the polarization vector is found to be perpendicular to the magnetic field. On the other hand

$$p(\delta) = \frac{3}{16\delta + 13} \tag{1.21}$$

in the opaque part of the source. In this case the polarization vector is parallel to the magnetic field. We can also relate the spectral index α to the electron energy distribution, given the relation

$$\alpha = \frac{\delta - 1}{2} \tag{1.22}$$

For a flat-spectrum source we have $\alpha \sim 0$, $\delta \sim 1$ and from equations (1.20, 1.21) we see that, in the transparent part of the source, the polarization degree can be as high as 60%, but in the opaque part, only $\sim 10\%$.

At mm/submm wavelength we are looking through the transparent part of the source and the radiation we observe is the continuum emission coming from the opaque part. This means that in our selected quasars and BL Lacs we should not expect polarization degrees larger than $\sim 10\%$ percent.

1.2 Basic concepts of bolometric receivers

At millimeter and submillimeter wavelengths we can use mainly only two types of receivers: heterodyne receivers and thermal detectors.

Heterodyne receivers are coherent detectors and for this reason intrinsically sensitive to the state of polarization of the incident radiation. On the other hand, they have a narrow bandwidth which gives them low sensitivity for continuum emission.

Thermal detectors like bolometers, can be used over a wide bandwidth and are the most sensitive receivers for continuum emission. Unfortunately they are *incoherent* detectors in that they only measure the intensity of incoming radiation and do not preserve phase information and this means that they are not able to detect the state of polarization. To perform polarimetry with bolometers we have to find a way to transform the information about the state of polarization to signals that bolometers can reveal.

1.2.1 Thermal detectors

All thermal detectors include an absorbing element with heat capacity C which converts the incident electromagnetic radiation to heat, and which is attached to a heat sink at temperature T_S via a thermal conductance G.

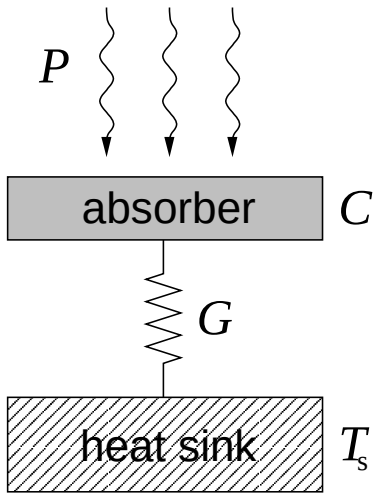

Figure 1.2: Schematic design of a thermal detector

After the incident radiation power P is turned on, the temperature T_B of this absorbing element initially increases with time at a rate $dT_B/dt = P/C$ and approaches the limiting value $T_B = T_S + P/G$ with the thermal time constant $\tau = C/G$. When the radiation is turned off, it relaxes back to T_S with the same τ. Thermal detectors are frequently used to give a periodic response to a signal which is modulated at a frequency $\omega \approx 1/\tau$.

1.2.2 Composite bolometers

The bolometer is a thermal infrared detector which employs an electrical resistance thermometer to measure the temperature of the radiation absorber. Bolometers may differ in their way of reading out the temperature changes in the radiation absorber (Richards, 1994).

The temperature dependence of the resistivity of some materials can be very large and many types of resistance thermometers have been proposed. At long wavelengths, the conflicting requirements of large absorber area and low heat capacity has led to the

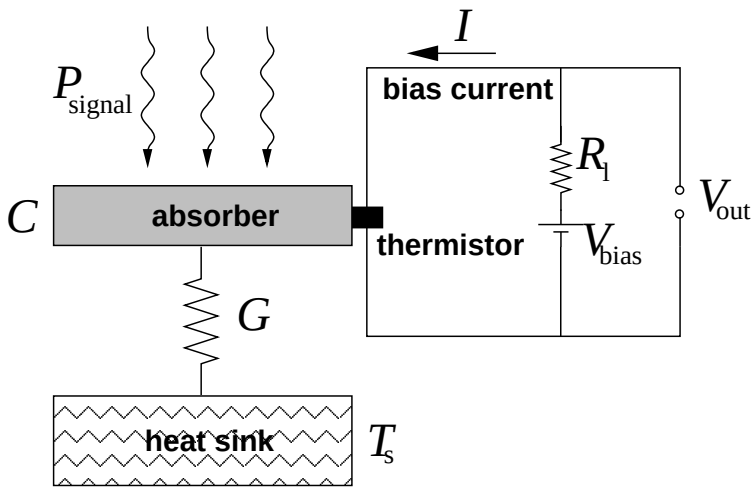

Figure 1.3: Schematic design of a semiconducting composite bolometer

development of composite bolometers.

The radiation absorber has a size appropriate to intercept the signal to be measured, a large absorptivity over the frequency range of interest, and a low heat capacity. The supporting substrate has a low heat capacity and large thermal conductivity, so that it remains isothermal during bolometer operation. The thermometer is thermally attached to the radiation absorber and/or the supporting substrate. It has low heat capacity, low electrical noise, and an adequate temperature dependence of its electrical resistance. The thermal link, which connects the thermally active portions of the bolometer to the heat sink has low heat capacity and an appropriate thermal conductance for the required application. The heat sink has a stable temperature appropriate for the application. The mechanical support for the thermally active portion of the bolometer has low heat capacity, low thermal conductance, and must be stiff enough that the mechanical resonant frequencies are higher than the operating frequency of the bolometer.

Bolometers combine these various elements in various ways. In some bolometers, a single element is used for several functions. In composite bolometers, these functions are accomplished by separate elements so that thermal conductivity, heat capacity and absorptivity can be optimized independently.

If the thermometer has a negative temperature coefficient, as is the case for semiconductors, a constant current bias has to be applied for negative thermal feedback,

which is a condition for stable operation. In this case, the thermometer is connected to a bias circuit with a voltage source $V_{\rm bias}$ and a load resistor $R_{\rm l}$. A constant current I flows through the thermistor. The signal radiation, $P_{\rm signal}$, will cause the bolometer temperature to increase according to:

$$T = T_0 + (P_{\rm signal} + P_{\rm bias})/G \tag{1.23}$$

where $P_{\rm bias} = V_{\rm bias} I$. This temperature rise causes a change in the electric resistance of the thermistor and consequently in the voltage across it. This output voltage is amplified and measured. The thermistor is therefore made of a material that produces a large change is resistivity for a small change in temperature. The two most important parameters to characterize a bolometer are the time constant τ and the *Noise Equivalent Power* (NEP) that is the power absorbed that produces a signal-to-noise ratio of unity at the output (Holland et al., 2002). The NEP can be split in two components as

$$NEP^2 = NEP^2_{\rm detector} + NEP^2_{\rm background} \tag{1.24}$$

In the best case the performance of the bolometer is *background limited*; that means the contribution to the NEP from the detector noise is negligible compared to the contribution from the thermal background noise from the optics and the sky.

The bolometer is a direct detector and the noise can only be evaluated after post-detection averaging. For this reason, the adopted units of the NEP are usually W Hz$^{-1/2}$. The main contributions to the detector noise are Johnson noise and phonon noise. The first one is the noise due to the random motion of electrons in the thermistor and can be written as

$$NEP^2_{\rm Johnson} = \frac{4 k_{\rm B} T R}{S^2} \tag{1.25}$$

where $k_{\rm B}$ is the Boltzmann constant and S is called responsivity of the bolometer and gives the output voltage per input power, in units of V W^{-1}. The phonon noise is due to the quantization of the lattice vibrations in terms of phonons that transport thermal energy between the absorber and the heat sink along the thermal conductance G and can be written as

$$NEP^2_{\rm phonon} = 4 k_{\rm B} T^2 G \tag{1.26}$$

The background contribution to the NEP, due to the sky, telescope and optics emission, also called photon noise, arises from the random fluctuations in the rate of absorption of photons. In the Rayleigh-Jeans approximation ($h\nu < k_{\mathrm{B}}T$) and with the assumption that the passband is limited to a frequency interval $\Delta\nu$ around a central frequency ν_0, then the photon noise can be written as

$$NEP^2_{\mathrm{photon}} = 2(h\nu_0 + \eta\epsilon k_{\mathrm{B}}T)P_{\mathrm{signal}} \tag{1.27}$$

where η is the overall transmission of the system, ϵ is the average emissivity and T is the temperature of the background. The absorbed incident power, P_{signal}, is then given by

$$P_{\mathrm{signal}} = A\Omega B(\nu_0, T)\eta\epsilon \tag{1.28}$$

where $A\Omega$ is the throughput of the telescope and $B(\nu_0, T)$ is the Planck function.

Each of the NEP terms is an uncorrelated noise source and so these can be added together in quadrature. The overall NEP for an ideal bolometer can be therefore written as

$$NEP^2 = \frac{4k_{\mathrm{B}}TR}{S^2} + 4k_{\mathrm{B}}T^2G + 2(h\nu_0 + \eta\epsilon k_{\mathrm{B}}T)P_{\mathrm{signal}} \tag{1.29}$$

To optimize the system we have to increase the signal-to-noise which means minimizing the NEP. From the above expression we see that we need to minimize T, G, R and P_{signal} and maximize S. It is evident that the operating temperature of the bolometers is an important parameter. Lowering the temperature dramatically decreases the noise. For this reason bolometers for astronomical purposes are operated at cryogenic temperatures, usually well below 1 Kelvin. The time constant $\tau = C/G$ is a measure of the response time to the incoming radiation of thermal receivers. The larger the value of G, the faster the bolometer response time will be, but, on the other hand, the larger will be the phonon noise. Hence, there is a trade-off between NEP and τ in terms of selection of G. Often the product $NEP\tau^{1/2}$ is used as performance criterion.

1.2.3 Arrays of bolometers

The bolometers developed at the MPIfR are composite bolometers and they all have the same basic architecture even if their parameters are then optimized to work at different wavelengths.

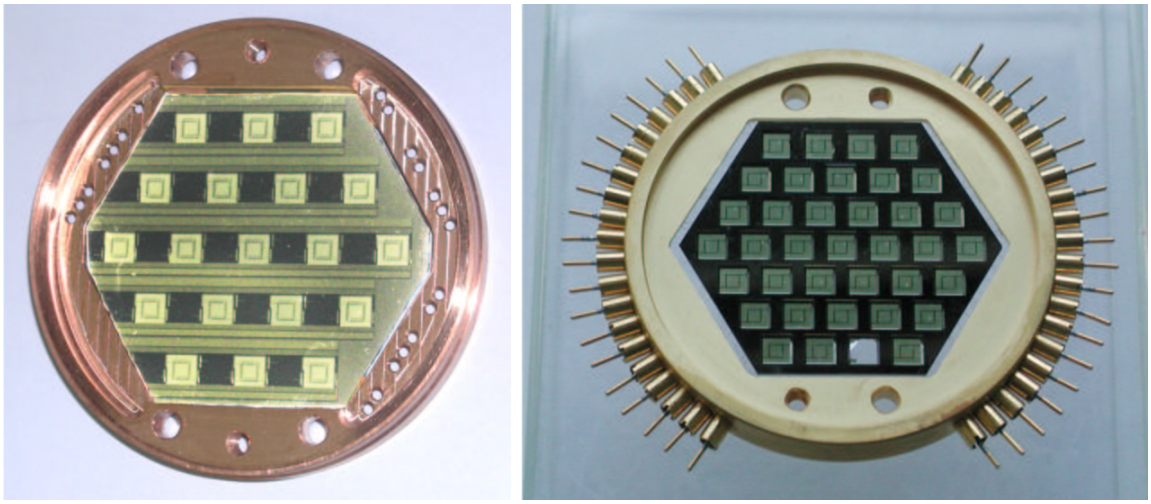

Figure 1.4: *Left:* HUMBA array of 19 bolometers optimized to work at 2.0 mm wavelength. *Right:* MAMBO-1 array of 37 bolometers optimized to work at 1.2 mm. One membrane is broken.

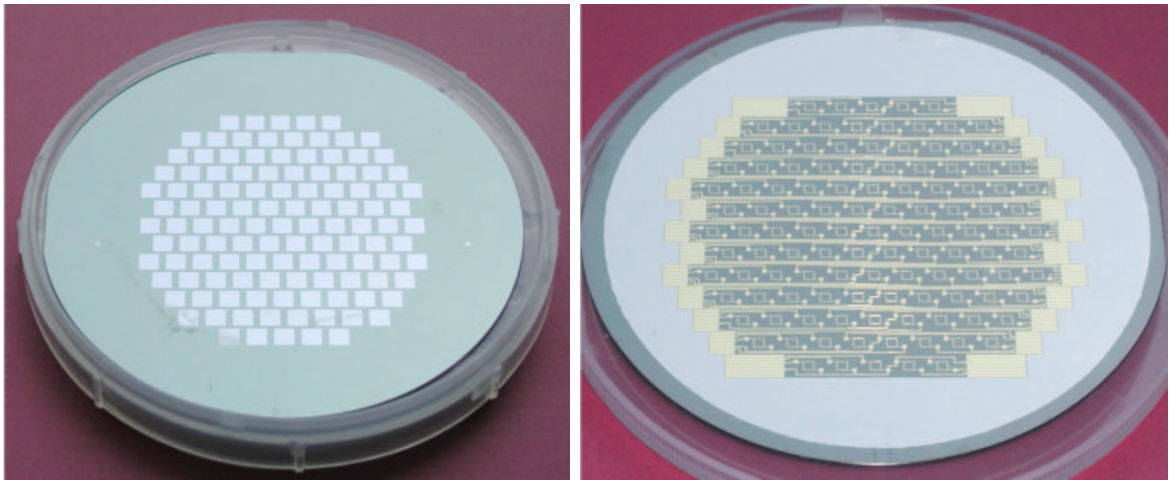

Figure 1.5: MAMBO-2 array of 117 bolometers. *Left:* membrane side. *Right:* wiring side.

The thermal, electrical and mechanical structure of the bolometer array is produced microlithographically with high precision on a silicon wafer. With this technique it is easy to produce large arrays of identical bolometers, closely packed, on the same silicon wafer. Free-standing membranes of silicon nitride provide low thermal conductivity for the bolometers by virtue of their amorphous structure.

The membranes have a thickness of about 1 micron and an area of a few square millimeters, and are relatively strong. An absorbing thin layer of Titanium is sputtered on the back side of the wafer. Being on the opposite side of the wafer, separated by

the nitride film, the absorber has no electrical connection to the wiring layer. An evaporated square ring of gold, visible in figures 1.4 and 1.5, will collect the phonons that were created within its inner area.

Thermistors are made from ultrapure Ge crystals by neutron transmutation doping (NTD Haller et al., 1982), manually attached to the gold rings. Electrical connections to the gold rings with negligible thermal conductivity across the membrane are provided by 80 nm thick sputtered niobium wires (Kreysa et al., 2002).

The radiation coming from the telescope is coupled to the bolometers through an array of conical horns, and in front of the horn array are filters at different temperatures for defining the bandpass and for rejecting high-frequency thermal background. The optical coupling is done with a room temperature optical system of lenses and mirrors and therefore a small cryostat is sufficient to accommodate even fairly large arrays.

1.3 The detectability of linear polarization

A frequently used parameter to express the sensitivity of the whole system, made up of the receiver and the telescope, is the *Noise Equivalent Flux Density* ($NEFD$). That is the flux density that produces a signal-to-noise of unity in a second of integration, given by

$$NEFD = NEP/(\Delta\nu\ \eta_{\rm c}\eta_{\rm t}\ A_{\rm e}\ e^{-\tau_{\rm z}A}) \tag{1.30}$$

where $\Delta\nu$ is the filters bandpass, $\eta_{\rm c}$ is the modulation efficiency factor, $\eta_{\rm t}$ is the overall optical efficiency, $A_{\rm e}$ is the effective area of the telescope, $\tau_{\rm z}$ is the zenithal optical depth and A is the source airmass (see section 5.2).

The $NEFD$ is very much dependent on the weather conditions. In the mm/submm bands the dominant cause of sky noise is the water vapor that is present along the line of sight because it can produce fluctuations of the sky transmission. The water vapor content decreases rapidly with altitude and this is the main reason why submillimeter telescopes are positioned on high mountains.

Sky emission has two components: an offset, mainly due to the mean atmospheric emission; and local spatial and temporal variations of the emissivity of the atmosphere above the telescope. The standard photometric techniques of sky chopping and telescope nodding, i.e. switching periodically from the source to a blank sky position not

too far from it, remove the offset efficiently. However, since the chopped beams travel through slightly different atmospheric paths, the effects of the variability of the emission are not completely removed by this procedure. The residual noise is called *sky-noise* and can degrade the $NEFD$ by more than one order of magnitude in unstable weather conditions.

Observing with arrays of bolometers, rather than with a single pixel detector, can dramatically improve the quality of the measurements.

Above a good submillimeter site (altitude ≥ 3 Km) the atmospheric layer producing sky fluctuations reaches to 2 km of altitude and, in combination with typical wind speeds and the observed frequencies of the fluctuations, this means that these will have a scale size of order of 1000 arcsec or more, under typical observing weather conditions. Hence, sky noise is caused by features larger than the portion of sky seen by the array, typically $\sim$100 arcsec. The sky noise signal will be the same in all the bolometers and it can be successfully removed, during the data reduction, by subtracting from the signals the part that is correlated over the array. This can reduce the $NEFD$ close to its theoretical value.

In the case of polarization measurements, a fast modulation of the signal is produced by means of an optical device able to modulate the polarized component only of the radiation, rejecting as much as possible the unpolarized component (see section 2.1). It is a very efficient way to extract the polarized signal from the sky noise.

The main difference between the two modulation systems is that in a typical photometric observation the signal generated by the wobbler is integrated during the whole duration of the scan, whereas in a typical polarimetric observation we have to nod the telescope alternatively on and off the source, and this reduces the integration time by a factor of 2.

In terms of $NEFD$, this translates in a factor $\sqrt{2}$. In the end, we can assume that

$$NEFD_{\rm pol} = \sqrt{2}\ NEFD_{\rm tp} \tag{1.31}$$

so that the polarization $NEFD$ is a factor $\sqrt{2}$ worse than the total power one.

We can now calculate what is the signal-to-noise that we should expect when making polarization measurements using bolometers.

The PolKa polarimeter has been used at the HHT telescope, where the MPIfR array of 19 bolometers, operating at the central wavelength of 345 GHz, has been operating since the beginning of year 2000 (see section 5.2).

There are two possible observing strategies (see section 5.3), leading to different values of the photometric $NEFD$ for that system:

- `On-Off` (`OO`):

  this is the standard procedure for flux measurements or detection experiments of point sources. In this case, at the HHT the $NEFD$ is estimated to be

  $$NEFD_{\mathrm{tp}}^{\mathtt{OO}} \simeq 600\ mJy/\sqrt{t} \tag{1.32}$$

  where t is the integration time of a normal photometry session, that means including the time spent by the wobbler on the `Off` position.

- `On-the-Fly` (`OtF`):

  this is the procedure for mapping extended sources. In this case, with a scanning velocity of 8 arcsec/second and after co-adding the 19 channels, the $NEFD$ is expected to be

  $$NEFD_{\mathrm{tp}}^{\mathtt{OtF}} \simeq 150\ mJy/beam \ \text{ per coverage} \tag{1.33}$$

These values already include the elimination of correlated atmospheric noise during data reduction.

To calculate the corresponding $NEFD$ for polarization measurements, we have to multiply by a factor $\sqrt{2}$. We get:

$$NEFD_{\mathrm{pol}}^{\mathtt{OO}} \simeq 850\ mJy/\sqrt{t} \tag{1.34}$$

$$NEFD_{\mathrm{pol}}^{\mathtt{OtF}} \simeq 220\ mJy/beam \ \text{ per coverage} \tag{1.35}$$

Now we can write a useful formula to calculate the integration time that we need to achieve signal-to-noise of R given the flux per beam F of the source and its degree of polarization p:

$$t = \left(R\ \frac{NEFD}{\eta\ p\ F}\ 100 \right)^2\ sec \tag{1.36}$$

where η is the polarization efficiency of the system ($0 < \eta < 1$).

For example, doing polarization `On-Off` measurements on a point source whose flux is 10 $Jy/beam$ and that we suppose to be about 5% polarized, and assuming an efficiency of 90%, we should be able to get a 3 σ detection in just over 30 seconds and a polarization `On-Off` of just 8 subscans, 10 seconds each, should be enough. In a similar way, we can estimate an upper limit to the polarization for a non detection:

$$p \leq \frac{NEFD}{\eta F \sqrt{t}} \; 100 \; \% \tag{1.37}$$

For example, we observe a source whose flux is $500 mJy/beam$ doing an `On-Off` of 32 subscan, 20 seconds per subscan, and the signal-to-noise is less than unity. The integration time in this case is 640 seconds, because in the `On-Off` procedure we spend half of the time on the blank sky. We can say that the source has a degree of polarization less than 10 % and nothing more. This is quite a high value to be an upper limit and this example shows how much difficult it is to detect polarization. Polarimetry requires much more integration time than normal photometry.

Let's now move our attention to extended sources. The best observing strategy, in this case, is to perform `On-the-Fly` maps. We don't use the wobbler and so the time spent on doing a scan is pure integration time; we can add the signals from the bolometers of the array and we can efficiently remove the correlated noise. If we consider, then, that many extended dust clouds have a strong flux, it seems reasonable to think that polarization detection on extended sources could be easier than on point sources.

For example, Orion OMC-1, in the area of the BN/KL sources, has a flux that can be as high as 170 Jy/beam, observed at 345 GHz with the HHT telescope. Using formula (1.36) and the value (1.35) for the $NEFD$, to get a 5 σ detection on an area that is just 2% polarized, assuming a mean flux of 100 Jy/beam, we need just roughly 1 hour, that means just two coverages are enough. This example gives an idea about how powerful `On-the-Fly` mapping can be, doing polarization measurements using an array of bolometers.

Chapter 2

The design of a polarimeter for mm/submm wavelengths

2.1 The standard scheme of a polarimeter

For a better explanation of the choices we made in the design of PolKa, I have to spend some words describing the standard technique for polarization measurements in the millimeter and submillimeter wavelength range. In order to extract the polarized signal from the unpolarized foreground it is common to use the modulation/demodulation technique. It is actually the same principle as used for performing the usual total power measurements. In that case, a wobbling secondary mirror is used to chop between two positions in the sky, so as to generate a modulated signal that is then demodulated by the backend computer (these concepts will be discussed in more detail in section 5.2.2 and following).

This computer takes the difference of the signal in the two wobbler positions and the result is proportional to the flux of the source. In this way the atmospheric foreground is almost completely removed, except for the atmospheric fluctuations at frequencies close to the chopping frequency. The latter must be known with high precision and a reference signal, carrying the information about the wobbler position, is fed into the backend.

Making use of a special device, that we will call *polarization modulator*, the polarized component of the incoming radiation is modulated at a precise frequency, chosen according to some criteria that I will describe later. If the modulation acts only on the Q and U Stokes parameters of the radiation, its intensity will be unchanged, at least

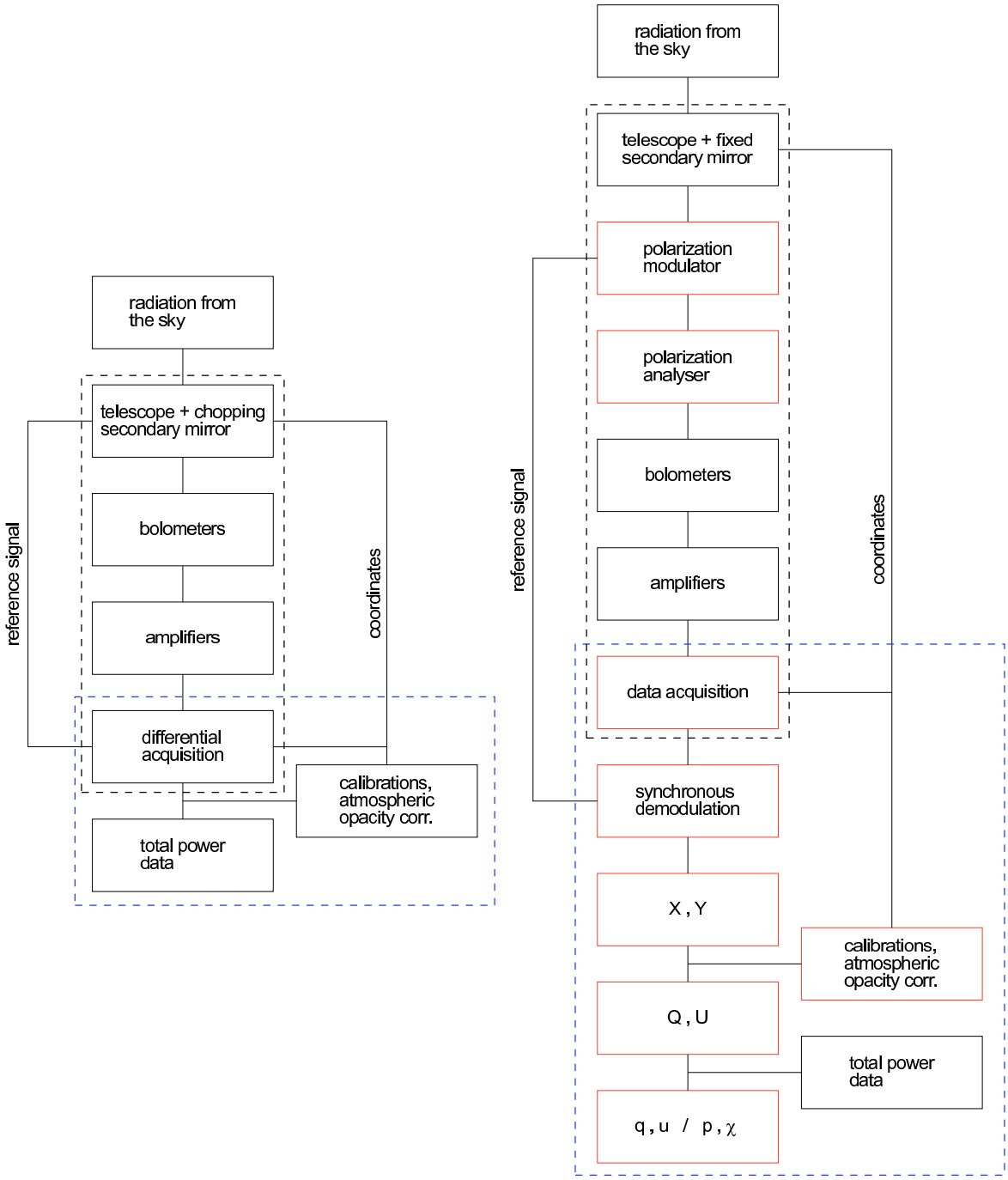

Figure 2.1: The diagram shows, on the left, the scheme of total power measurements and, on the right, the scheme of polarization measurements. Red boxes show the component added to the total power system to transform it in a polarimeter. The dashed black line encloses the hardware. The dashed blue line encloses the software.

in the ideal case. Since bolometers are incoherent detectors, they are not sensitive to the phase of the wave but only to its intensity. We need to insert, along the optical path, a linear polarizer: this will translate the modulation of the Stokes parameters in a modulation of the intensity of the wave transmitted but, unfortunately, half of the signal will be lost.

If we compare the typical scheme of the system used for total power measurements to that of polarization measurements (see figure 2.1) we can see the changes that have to be done to that system in order to transform it into a polarimeter. One of the necessary constraints in the design of PolKa has been to minimize the modifications to the total power system, in order to be able to switch from polarization to total power measurements with ease, saving telescope time.

The simplest way to modulate the Q and U Stokes parameters is to put a linear polarizer along the beam path and rotate it. In this case, however, the total intensity of the radiation will be modulated simultaneously, together with the Stokes parameters, and there is no need to use an analyzer. Given the Müller matrix for a rotating linear polarizer

$$\mathbf{P}(\omega t) = \frac{1}{2}\begin{pmatrix} 1 & \cos 2\omega t & \sin 2\omega t & 0 \\ \cos 2\omega t & \cos^2 2\omega t & \sin 2\omega t \cos 2\omega t & 0 \\ \sin 2\omega t & \sin 2\omega t \cos 2\omega t & \sin^2 2\omega t & 0 \\ 0 & 0 & 0 & 0 \end{pmatrix} \tag{2.1}$$

where ω is the mechanical rotation frequency, and assuming the polarizer horizontal at $t = 0$, we can calculate the Stokes vector of the radiation going to the bolometers. In the most general case, the incoming radiation has Stokes parameters I, Q, U, V, and the bolometers will see

$$\mathbf{P}(\omega t)\begin{pmatrix} I \\ Q \\ U \\ V \end{pmatrix} = \frac{1}{2}\begin{pmatrix} I + Q\cos 2\omega t + U \sin 2\omega t \\ I\cos 2\omega t + Q\cos^2 2\omega t + U \sin 2\omega t \cos 2\omega t \\ I \sin 2\omega t + Q \sin 2\omega t \cos 2\omega t + U \sin^2 2\omega t \\ 0 \end{pmatrix} \tag{2.2}$$

Bolometers will detect just the first component of that Stokes vector and the output signal will be

$$V_{\text{out}} = \frac{1}{2}\left(I + Q\cos 2\omega t + U \sin 2\omega t\right) \tag{2.3}$$

We see that the total intensity is reduced to 50% and the Stokes parameters are modulated at frequency 2ω, the double of the mechanical one. This kind of modulation, however, is not so useful when dealing with very low signal-to-noise ratios, because

linear polarization has a periodicity of π and every spurious effect produced by the rotating polarizer (emission, multiple reflections, effects due to misalignments) will have the same frequency and will be added to the measured signal. These effects may be negligible when doing lab measurements, but in astronomical applications can become orders of magnitude larger than the signal we want to detect.

2.2 Polarimetry with a half-wave plate

The way to improve the system is to use an *half-wave plate*, instead of a linear polarizer, to produce the modulation. An half-wave plate (hereafter HWP) is an optical device producing a phase shift equal to π (or half a wave) between the two orthogonal components of the linear polarization. It is part of the more extended group of optical devices generally called *retarders* or *phase shifters*.

If we put a rotating HWP along the beam path we will produce a modulation of the Stokes parameters but the total intensity will remain unchanged. To quantify this assertion, let's consider the Müller matrix for a rotating HWP

$$\mathbf{H}(\omega t) = \begin{pmatrix} 1 & 0 & 0 & 0 \\ 0 & \cos 4\omega t & \sin 4\omega t & 0 \\ 0 & \sin 4\omega t & -\cos 4\omega t & 0 \\ 0 & 0 & 0 & -1 \end{pmatrix} \tag{2.4}$$

From the mathematical point of view, if we compare this matrix with the rotation matrix

$$\mathbf{R}(\vartheta) = \begin{pmatrix} 1 & 0 & 0 & 0 \\ 0 & \cos 2\vartheta & \sin 2\vartheta & 0 \\ 0 & -\sin 2\vartheta & \cos 2\vartheta & 0 \\ 0 & 0 & 0 & 1 \end{pmatrix} \tag{2.5}$$

we see that it produces a rotation of the polarization vector in the opposite direction, which makes the HWP a *pseudo-rotator*. Nevertheless, we see that the rotation frequency is doubled and this is the biggest benefit that we gain using an HWP instead of a linear polarizer. Most of the spurious effects, in fact, will have a frequency equal to the mechanical one, ω, while the polarization signal will be modulated at 4ω resulting in an improved extraction of the signal from foregrounds and systematics. As already

stated before, the total intensity I of the Stokes vector modulated by the HWP

$$\mathbf{H}(\omega t)\begin{pmatrix} I \\ Q \\ U \\ V \end{pmatrix} = \begin{pmatrix} I \\ Q\cos 4\omega t + U\sin 4\omega t \\ Q\sin 4\omega t - U\cos 4\omega t \\ -V \end{pmatrix} \tag{2.6}$$

is not modified because the polarization vector is rotated without any change in its magnitude, at least in the ideal case. At this point we have to introduce a fixed linear polarizer into the beam to produce an intensity modulation detectable by the bolometers. If we use a horizontal linear polarizer we have

$$\frac{1}{2}\begin{pmatrix} 1 & 1 & 0 & 0 \\ 1 & 1 & 0 & 0 \\ 0 & 0 & 0 & 0 \\ 0 & 0 & 0 & 0 \end{pmatrix}\begin{pmatrix} I \\ Q\cos 4\omega t + U\sin 4\omega t \\ Q\sin 4\omega t - U\cos 4\omega t \\ -V \end{pmatrix} = \frac{1}{2}\begin{pmatrix} I + Q\cos 4\omega t + U\sin 4\omega t \\ I + Q\cos 4\omega t + U\sin 4\omega t \\ 0 \\ 0 \end{pmatrix} \tag{2.7}$$

and the bolometer output will be

$$V_{\text{out}}^{\text{H}} = \frac{1}{2}\left(I + Q\cos 4\omega t + U\sin 4\omega t\right) \tag{2.8}$$

that is similar to equation (2.3) but doubled in frequency. If we use a vertical linear polarizer we have

$$\frac{1}{2}\begin{pmatrix} 1 & -1 & 0 & 0 \\ -1 & 1 & 0 & 0 \\ 0 & 0 & 0 & 0 \\ 0 & 0 & 0 & 0 \end{pmatrix}\begin{pmatrix} I \\ Q\cos 4\omega t + U\sin 4\omega t \\ Q\sin 4\omega t - U\cos 4\omega t \\ -V \end{pmatrix} = \frac{1}{2}\begin{pmatrix} I - Q\cos 4\omega t - U\sin 4\omega t \\ -I + Q\cos 4\omega t + U\sin 4\omega t \\ 0 \\ 0 \end{pmatrix} \tag{2.9}$$

and the bolometer output in this case is

$$V_{\text{out}}^{\text{V}} = \frac{1}{2}\left(I - Q\cos 4\omega t - U\sin 4\omega t\right) \tag{2.10}$$

To minimize the impact on the total power system, we are going to use the polarimeter at the telescope with the receiver already installed, as shown in figure 2.1. This means that we will use the same receivers and the same amplifiers. The total power system is optimized to work at the wobbler frequency of 2 Hz. For this reason, the amplifiers have filters cutting off signals below 1 Hz. This will suppress the 1/f noise and the very slow fluctuations of the offset present in the signals. In other words, the bolometers readout is AC coupled and constant offsets are eliminated. If we apply such a filter to equations (2.8) and (2.10) we see that the information about the total

intensity I of the signal is lost because it is not modulated. The signals going to the data acquisition are then

$$V_{\rm out}^{\rm H} = \frac{1}{2}\left(Q\cos 4\omega t + U\sin 4\omega t\right) \tag{2.11}$$

$$V_{\rm out}^{\rm V} = -\frac{1}{2}\left(Q\cos 4\omega t + U\sin 4\omega t\right) = -V_{\rm out}^{\rm H} \tag{2.12}$$

However, this result is correct only in the ideal case. The acquired signals $V_{\rm out}^{\rm H}$ and $V_{\rm out}^{\rm V}$, in the real case, are a bit different because we didn't take into account the efficiency factors of the polarizers and of the HWP and the gain factor due to the amplifier. If $\eta_p^{\rm H}$ and $\eta_p^{\rm V}$ are the transmission efficiencies for the two linear polarizers and $\eta_{\rm HWP}$ is the transmission efficiency of the HWP, and if g is the gain factor due to the amplifier, in a more realistic description, the signals are

$$V_{\rm out}^{\rm H} = \frac{1}{2}\,\eta_p^{\rm H}\,\eta_{\rm HWP}\,g\,\left(Q\cos 4\omega t + U\sin 4\omega t\right) \tag{2.13}$$

$$V_{\rm out}^{\rm V} = -\frac{1}{2}\,\eta_p^{\rm V}\,\eta_{\rm HWP}\,g\,\left(Q\cos 4\omega t + U\sin 4\omega t\right) \tag{2.14}$$

and one will be the opposite of the other when $\eta_p^{\rm H} = \eta_p^{\rm V}$.

The choice of the modulation frequency is mainly based on two considerations.

- The total power system is optimized to work at 2 Hz because of the mechanical frequency limit of the wobbling secondary mirror. Atmospheric emission fluctuations can have frequencies even higher than 2 Hz, and increasing the modulation frequency would then improve the stability of the signal. In principle, doing polarimetry without the wobbler, we are free to go to much higher frequencies. Nevertheless we should avoid pushing the polarization modulation frequency to values too far beyond 2 Hz, because the bolometer time constant is optimized for that value and the responsivity will drop down rapidly.

- The polarization will be modulated at four times the mechanical frequency: we can easily reach high frequencies in polarization without the need of a fast rotation. On the other hand, the error of the position angle of the polarization vector will be four times larger than the mechanical error on the position of the HWP. An accurate determination of the instantaneous position of the HWP is essential.

A *retarder* is a polarizing optical device able to change the phase of the radiation passing through it. The correct name should be *phase shifter*. However, for historical

reasons, the alternative names *retarder*, *wave plate* or *compensator* are more common. Retarders introduce a phase shift of φ between the orthogonal components of the incident radiation. If we consider, in a local reference system, the two polarization directions to be horizontal and vertical, then we can say that a retarder introduces a phase shift of $+\varphi/2$ along the horizontal axis and $-\varphi/2$ along the vertical axis. In optics, the two axis are referred to as the *fast* and *slow* axes, respectively.

The simplest way to produce a retarder is to use crystals. The study of retarders is also important from an historical point of view because it is closely connected to the discovery of polarization. The polarization of light was first discovered by Bartholinus, while investigating the transmission of unpolarized light through a crystal of calcite, also known as *Iceland spar*. From Collett (1993):

> *Many types of crystals have been known since time immemorial, e.g., diamonds, sapphires, topaz, emeralds, etc. Not surprisingly, therefore, they have been the subject of much study and investigation for centuries.*
>
> *One type of crystal, calcite, was probably known for a very long time before Bartholinus discovered in the late seventeenth century that it was birefringent. Bartholinus apparently obtained the calcite crystals from Iceland (Iceland spar); the specimens he obtained were extremely free of striations and defects. His discovery of double refraction (birefringence) and its properties was a source of wonder to him. According to his own accounts, it gave him endless hours of pleasure - as a crystal he far preferred it to diamond! It was Huygens, however, nearly 30 years later, who explained the phenomenon of double refraction.*

Up to date many polarimeters have been developed for various telescopes (see, for example, Emerson et al. (1979), Troland & Heiles (1982), Crutcher & Kazes (1983), Inoue et al. (1984), Hildebrand et al. (1984), Morsi & Reich (1986), Barvainis et al. (1988), Fiebig & Guesten (1989), Novak et al. (1990), Flett & Murray (1991), Platt et al. (1991), Crutcher et al. (1993), Tsuboi et al. (1995), Akeson et al. (1996), Crutcher et al. (1996), Glenn et al. (1996), Schleuning et al. (1997), Rao et al. (1998), Shinnaga et al. (1999), Matthews & Wilson (2000b)).

In all the cases, with just few exceptions, the polarization modulation is produced

using a retarder made of a crystal, namely quartz or sapphire. However, there are some good reasons to look for a different solution when designing a polarimeter for astronomical research. Crystal retarders produce some undesired effects that are intrinsically connected to the nature of the retarder itself. In optical media, the velocity of the light transmitted depends on the refractive indices of the axes which are transverse to the direction of propagation. Birefringent crystals have two principal axes of transmission characterized by two different refractive indices. This is the reason why the axes are called fast and slow: the radiation propagates at different velocities along the two. Cutting the crystal in a proper way, and choosing the thickness according to the wavelength of the radiation, it is possible to produce the desired phase shift between the two transmitted orthogonal polarizations. In particular, the crystal will be an HWP when the phase shift will be equal to 180 degrees. Unfortunately, the complex part of the refractive index is responsible of the absorption of the radiation by the crystal and this clearly means that the two transmitted beams will have different intensities. This effect is unavoidable and, once the crystal is used as a modulator in a polarimeter, it can produce a spurious polarization as high as $\sim$ 15%. This combines with the attenuation of the intensity of the signal due to the insertion loss produced by the absorption by the crystal. For example, Schleuning et al. (1997) report a modulation efficiency of 75% using a 6mm quartz HWP cooled down to 1.5K; Novak et al. (1989) report a polarization efficiency of 81%.

Hildebrand et al. (1984) proposed to rotate the polarization plane with an Abbe/König *K-mirror* (Naumann, 1967) emphasizing the increased polarization signal, as compared to the alternative of a crystal HWP. The K-mirror, however, has the disadvantage of rotating the image, as well as the plane of polarization and this introduces systematic effects that are hard to control.

2.3 Polarimeter using a reflection-type half-wave plate

There are other solutions for making a retarder. One possibility is a dielectric plate, usually made of Teflon or high-density polyethylene, with grooves in its surface. In this case, however, there is still some insertion loss (much smaller than in crystals) and the efficiency is very low. Another alternative is the *reflection-type* half-wave plate

(hereafter RHWP). This kind of retarder seems to have been used for astronomical polarimetry only twice: at the NRAO 12 m telescope by Glenn et al. (1997) and at the Nobeyama 45 m telescope by Shinnaga et al. (1999). In the first case, the authors report an overall polarization efficiency too close to 100% to be measured and of too small an insertion loss to need correction. In the second case, the authors report an efficiency of 98% and an insertion loss less than half of what it was with their previous modulator, a transmission-type HWP made of grooved Teflon.

Given these promising results, we decided to design the PolKa polarimeter around a reflection-type half-wave plate. It is made of two parts: a wire-grid polarizer and a

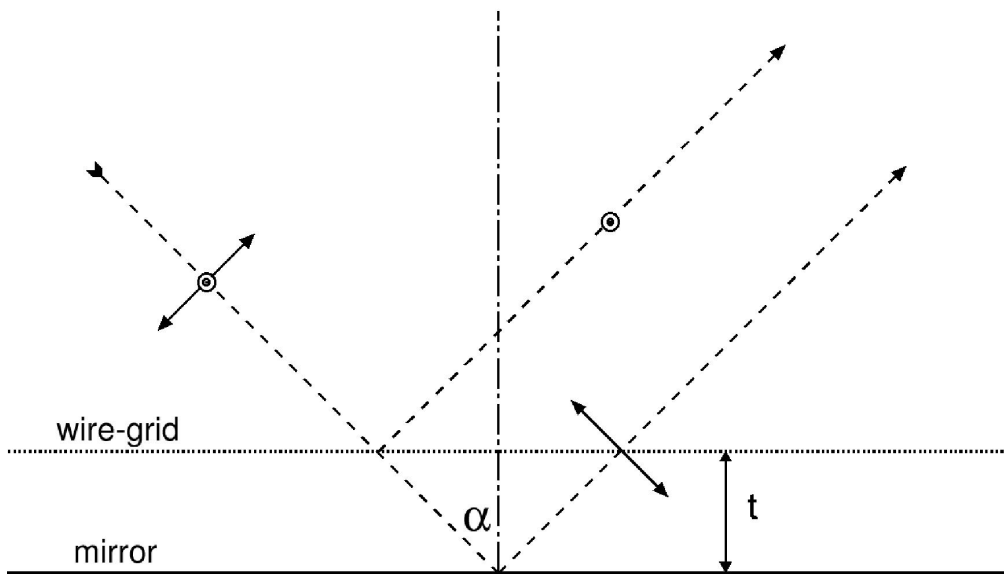

Figure 2.2: Scheme of a reflection-type half-wave plate. The incident radiation is divided in two beams with orthogonal polarization states. The two emerging rays will have a phase shift proportional to t.

mirror. Tuning the distance between the two parts (see figure 2.2), according to the working wavelength, it is possible to produce a 180 degrees phase shift between the two components of polarization, because one is reflected by the wires, the other one by the mirror, taking a longer path. The phase shift is given by the simple relation

$$\varphi(\lambda) = 2\pi \frac{t}{\lambda \cos \alpha} \tag{2.15}$$

where t is the distance between the polarizer and the mirror, α is the angle of incidence of the incoming radiation and λ is the operating wavelength. To have an HWP we assign $\varphi = k\pi$ where k is a positive integer representing the order of the solution ($k = 1, 2, ...$).

The possible values of t for a central operating wavelength λ_0 are then given by

$$t = \frac{1}{2} k \lambda_0 \cos\alpha \tag{2.16}$$

The first derivative of equation (2.15) is

$$\frac{\partial\varphi}{\partial\lambda} = -2\pi \frac{t}{\lambda^2 \cos\alpha} = -\pi k \frac{\lambda_0}{\lambda^2} \tag{2.17}$$

and we see that the phase shift has a slope proportional to t and k. To minimize the distribution of the phase shift over our bolometer bandwidth, the better choice is the first order, $k = 1$. Figure 2.3 shows the behavior of the phase shift as a function of the wavelength, for a RHWP tuned at $\lambda_0 = 1$ mm, for the first three orders.

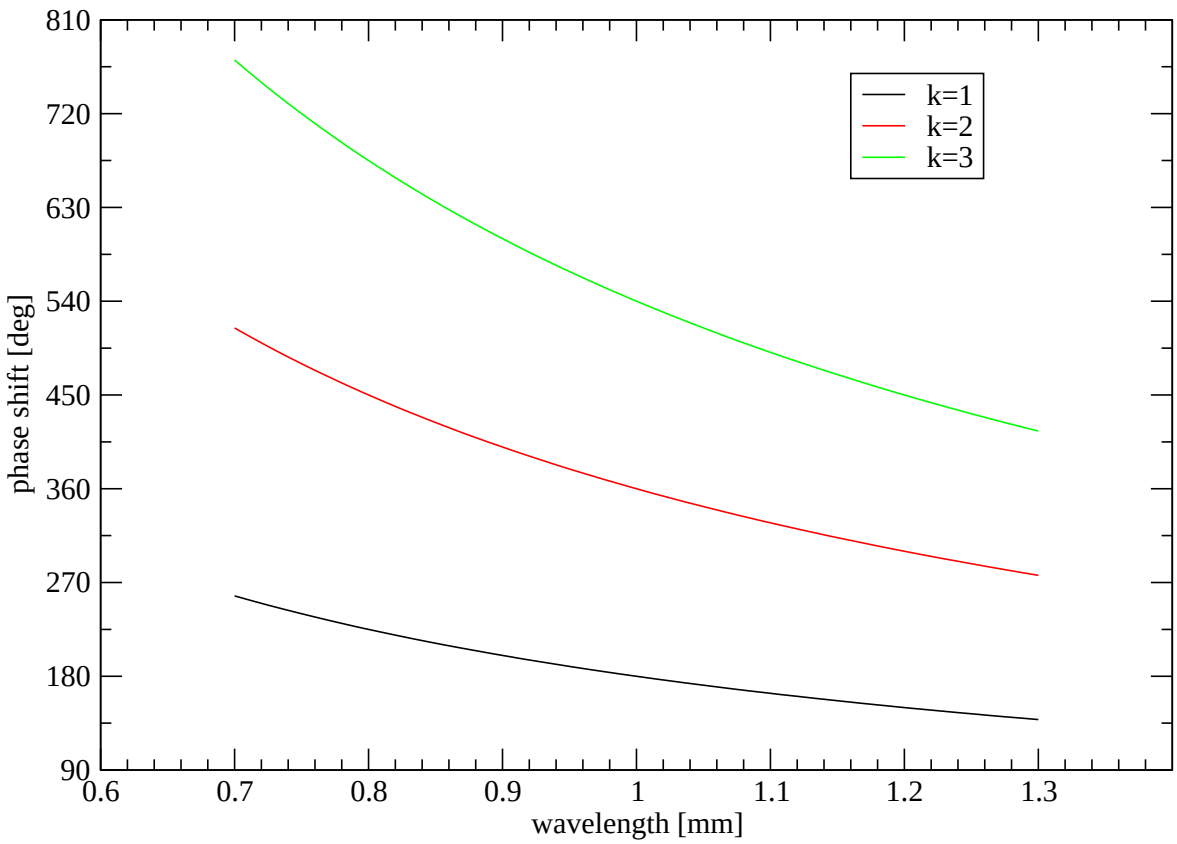

Figure 2.3: Phase shift vs. wavelength for different values of the RHWP order, k. The RHWP is tuned at $\lambda_0 = 1.0$ mm.

Table 2.1 shows some values of t calculated at the operating wavelengths of the MPIfR bolometers arrays for different incidence angles.

Once the RHWP is tuned to operate at λ_0 according to formula (2.16), its efficiency will also be a function of the incidence angle. Assuming a Gaussian beam, the rays will

be distributed inside the beam and they will have slightly different incidence angles. The phase shift, then, will again be distributed about the central value of 180 degrees.

λ [mm]	15°	30°	45°	60°	75°
2.0	0.9659	0.8660	0.7071	0.5000	0.2588
1.2	0.5795	0.5196	0.4242	0.3000	0.1552
0.87	0.4201	0.3767	0.3076	0.2175	0.1125

Table 2.1: Values of t at different incidence angles calculated for the central wavelengths of the MPIfR bolometer arrays using $k = 1$.Values are in millimeters.

Figure 2.4 shows the behavior of the phase shift as a function of the incidence angle. In this case the RHWP is tuned for the central wavelength $\lambda_0 = 0.87$ mm and for three different setups: 15°, 30° and 45°. The plot shows that phase shift functions have a slope that is steeper going to larger setup angles. To minimize the distribution of the phase shift we have to minimize the incidence angle, avoiding configuration at angles larger than 45 degrees. We will later find one more reason to do that (see section 4.2). We can now consider the real transmission through the RHWP in two cases: the HHT 19 channel array at $\lambda_0 = 0.87$ mm and MAMBO-2 at $\lambda_0 = 1.2$ mm, installed at the IRAM 30 m telescope since the end of the year 2001. Assuming the radiation incident at $\alpha = 45°$ and described by the Stokes parameters I, Q, U, V, we can calculate the intensity transmitted to the bolometers, as a function of the rotation angle ϑ, integrated over the bandwidth $\Delta\lambda$ of the receiver:

$$\begin{aligned} I_{\rm bol}(\vartheta) = \frac{1}{2}\int_{\Delta\lambda} f(\lambda)[I + Q(\cos^2 2\vartheta + \cos\varphi(\lambda)\sin^2 2\vartheta) + \\ U(1-\cos\varphi(\lambda))\sin 2\vartheta\cos 2\vartheta + \\ V\sin\varphi(\lambda)\sin 2\vartheta]\left(\frac{\partial\varphi}{\partial\lambda}\right) d\lambda \end{aligned} \tag{2.18}$$

where $\varphi(\lambda)$ and $\partial\varphi/\partial\lambda$ are given by equations (2.15) and (2.17) and $f(\lambda)$ is the transmission function of the receiver filters. Figure 2.5 shows the transmission over the bandwidth of the HHT 19 channel bolometer array for different values of the rotation angle ϑ, calculated assuming radiation 100% linearly horizontally polarized ($Q = I, U = V = 0$) using the function in the integral (2.18). In this case we see that when the RHWP is at 45° the transmission is almost zero and the polarization modulation efficiency is then $\sim 100\%$. Figure 2.6 shows the transmission over the bandwidth of the MAMBO-2

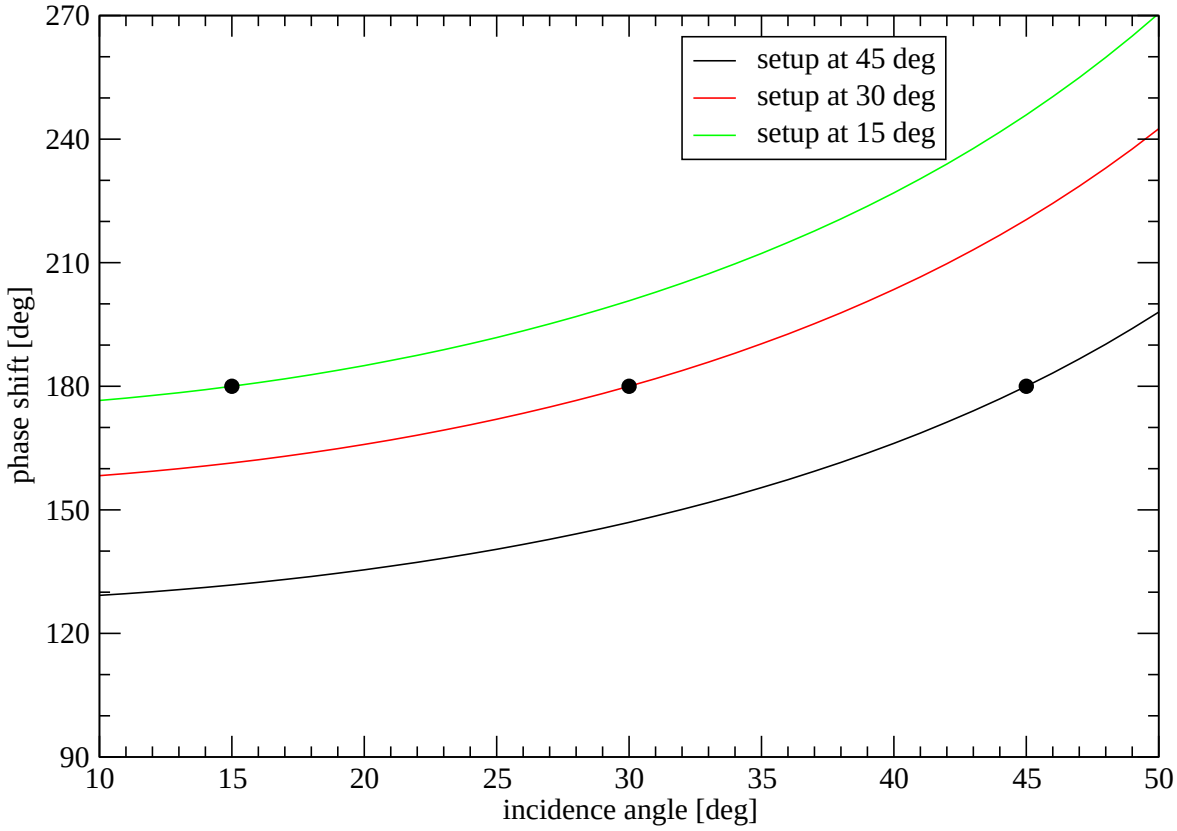

Figure 2.4: Phase shift vs. incidence angle for $\lambda_0 = 0.87$ mm, $\alpha = 15°, 30°, 45°$. For different setups, the phase shift has a slope that is steeper for larger setup angles.

bolometer array for different values of the rotation angle ϑ, again calculated assuming radiation 100% linearly horizontally polarized. In this case the bandwidth is too large and we see that transmission never reaches zero. In particular, this effect is more relevant going to wavelengths shorter than λ_0. In both the cases, the function $f(\lambda)$ has been replaced with the measured spectral response of the receivers, measured in the lab using a Martin-Puplett interferometer (Martin & Puplett, 1969).

It is very important to note that a RHWP uses only metallic reflections and absorption is therefore negligible.

This device also has disadvantages. The reflection implies that the RHWP must stay at a certain angle α to the beam coming from the telescope. To instal it at the telescope we will have to modify the optical setup. The receiver will see the RHWP projected on the focal plane and it will appear shrunk by a factor $\cos\alpha$. This creates an undesired effect: the radiation will see the RHWP at an angle that is the projection

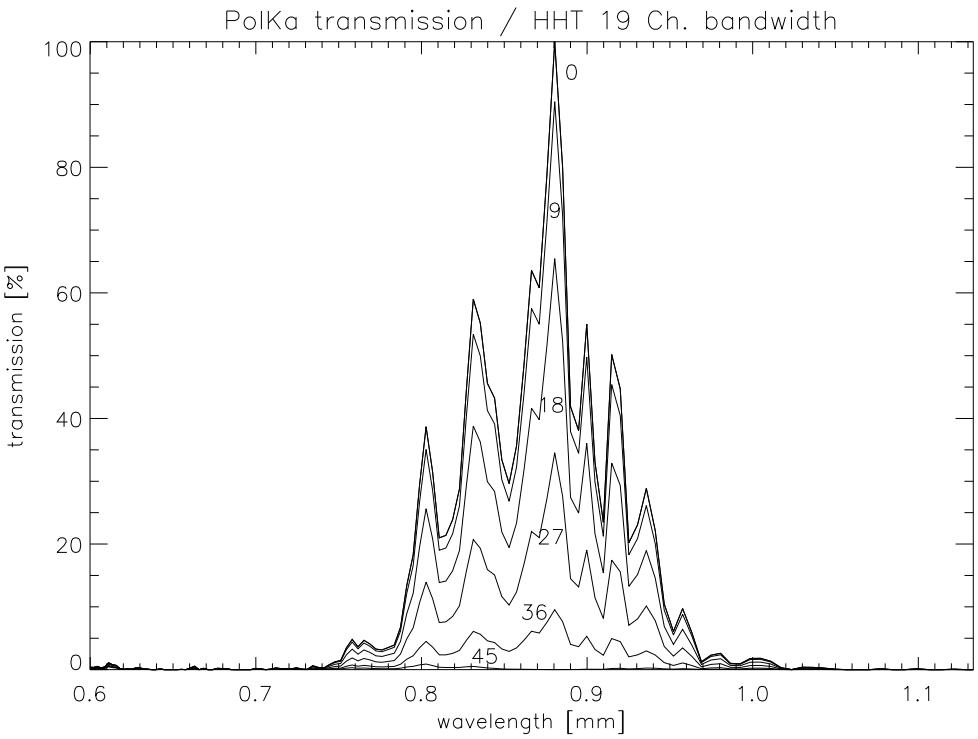

Figure 2.5: Transmission vs. wavelength for different values of the rotation angle ϑ when the PolKa polarimeter is used with the HHT 19 channel array.

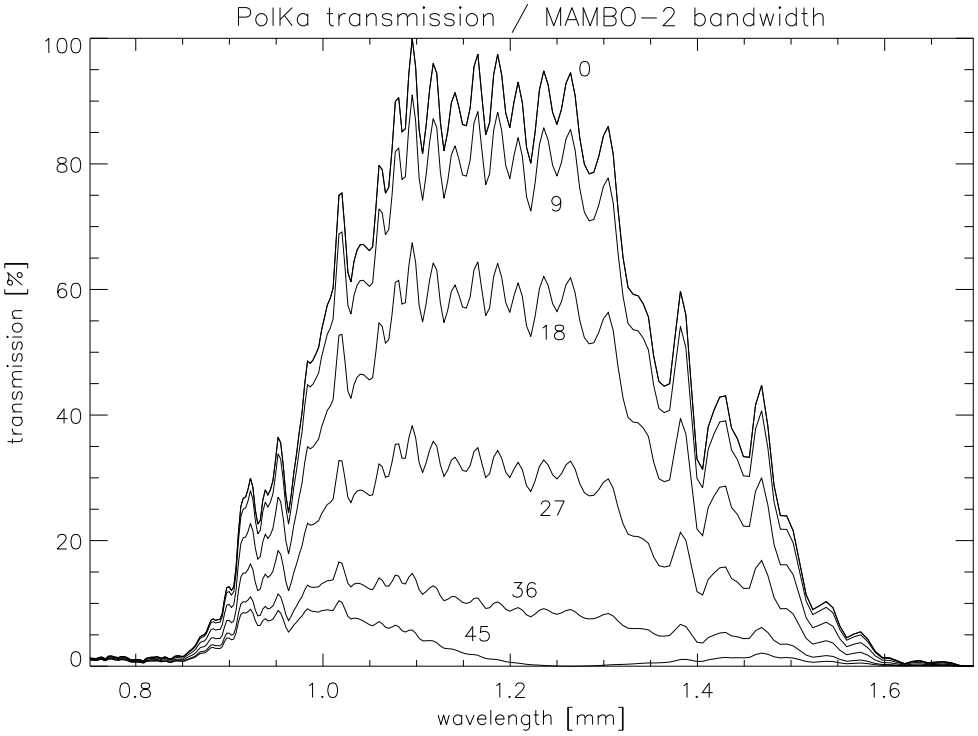

Figure 2.6: Transmission vs. wavelength for different values of the rotation angle ϑ when the PolKa polarimeter is used with the MAMBO-2 array.

of the true rotation angle, and the relation between the two,

$$\vartheta' = \tan^{-1}(\tan\vartheta\cos\alpha) \tag{2.19}$$

is not linear. We will see later (chapter 4) that this effect has some important consequences.

Given the large beam of the telescope at the focal plane, the HWP must be fairly large to fill the whole array To produce a big RHWP for our polarimeter we were forced to produce large polarizers for mm/submm wavelengths.

Part II

Construction of the polarimeter, and observations

Chapter 3

Production of wire-grid polarizers

3.1 Introduction

In the (sub)millimeter wavelength range, a linear polarizer is usually made of a set of thin, parallel and conducting wires whose thickness and spacing must be chosen according to the wavelength. Polarizers of this type are called *wire-grid polarizers* and the wires can be free-standing or embedded in a dielectric substrate. See Houde et al. (2001) for a detailed study of wire-grid polarizers.

In the design of the polarimeter we had to take into account its intended use with arrays of bolometers at large (sub)millimeter telescopes. In this case, a reflective half-wave plate (hereafter RHWP) has to be fairly large to fill the large combined optical beam, especially when the incidence angle is more than a few degrees. For the manufacture of a large RHWP the limiting factor is the size of the wire-grid polarizer. The other parts of it can be easily machined in any workshop but a large wire-grid is not easy to obtain. At the beginning we thought it was possible to buy them, but we found that the delivery time of a couple of large wire-grids is more than one year and that only one company is able to produce them with the required accuracy. Another problem is the price, easily more than 5000 dollars for a wire-grid having the required quality and a diameter of 15 cm. For these reasons we decided to build our own polarizers. In the past, the Submillimeter Technology Division of the MPIfR had already been involved in the production of wire-grid polarizers for ground based receivers and for the ISOPHOT instrument on board the ISO satellite (Infrared Space Observatory). Unfortunately, the machine used to produce those polarizers is limited to diameters of just over 10 cm and we had to modify it to produce larger wire-grids.

3.2 General concepts of wire-grid polarizers

Consider a planar grid of thin, parallel and conducting free-standing wires. If the wavelength of the incident radiation is large enough compared to the grid constant d, the wave transmitted will be linearly polarized, because the component of the electric field parallel to the wires will see the grid as a plane metallic mirror and will be reflected. The reflected wave will be then linearly polarized in the direction of the wires. The transmitted wave will be linearly polarized in the orthogonal direction, if the wires are thin enough compared to the wavelength, because the component of the electric field orthogonal to the wires will see the grid as a dielectric and will pass through it (see figure 3.1). This simple picture suggests the following characteristics of a wire-grid polarizer: the thickness of the wires $2a$, the grid constant d and the operating wavelength λ. The equations describing the interaction of an electromagnetic wave

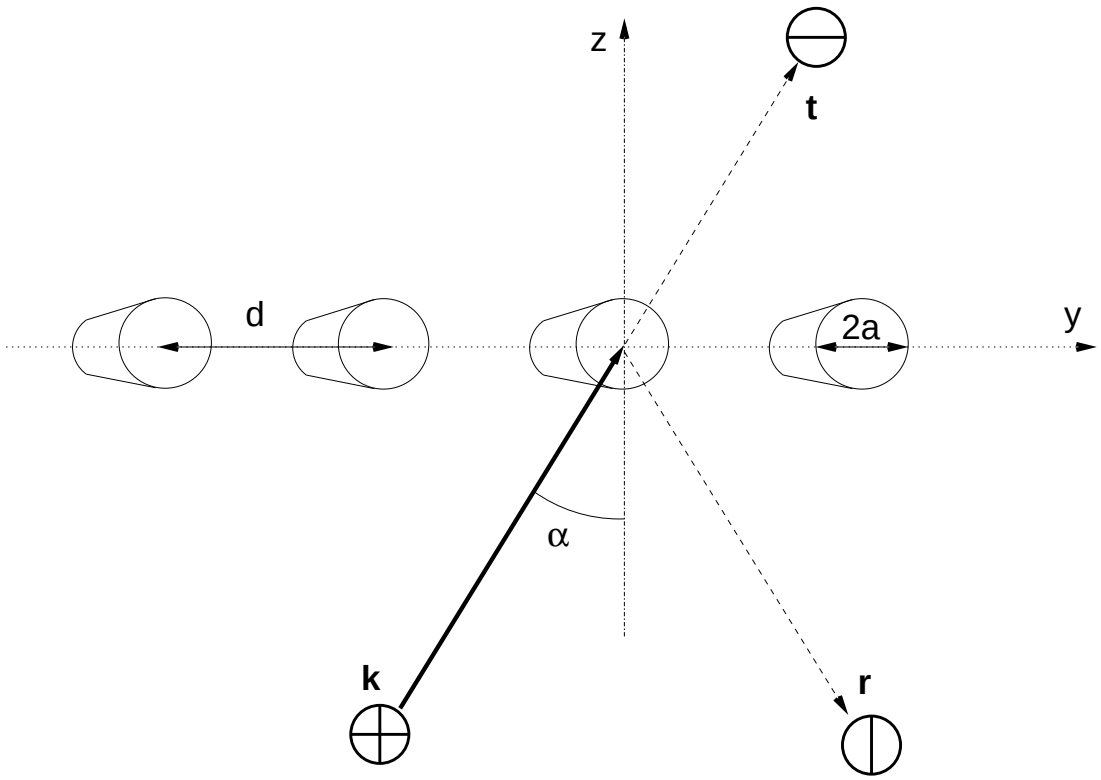

Figure 3.1: Schematic drawing of a wire-grid polarizer. The wires have radius a and the grid has spacing d. The wave vector $\mathbf{k}$ has incidence angle α. The reflected wave, $\mathbf{r}$, is totally linearly polarized along the direction of the wires; the transmitted one, $\mathbf{t}$, along the orthogonal direction. The circles represent the polarization state. The reference system has its x axis along the wires.

with a wire-grid polarizer are, in general, complicated. However, we can use some approximate formulas under the assumption that $\lambda > 40a$ and $d > 4a$, where a is the radius of the wires. This is not a severe restriction because typical grids used at millimeter wavelengths easily satisfy those conditions.

According to Houde et al. (2001, pag.631, eq.(64)(65)) the optimum values for the wire radius and the spacing are given by the following approximate equations:

$$a \simeq \left[\frac{\lambda^5}{(1-k_x^2)^4\pi^7\sigma Z_0}\right]^{\frac{1}{6}} \tag{3.1}$$

$$d \simeq 2\pi a \tag{3.2}$$

where k_x^2 is the component of the wave vector $\mathbf{k}$ along the wires, σ is the wire conductivity and Z_0 is the impedance of free space. If we consider a central wavelength $\lambda = 0.87\mu$m, $k_x^2 = 0$ and Tungsten wires ($\sigma = 1.77 \cdot 10^7 \Omega^{-1} m^{-1}$ at 27°C) the above equations give $a \simeq 17\mu$m and therefore $d \simeq 107\mu$m. In the case of radiation with an incidence angle of 45° on the plane orthogonal to the wires, these values are larger, going up to $a \simeq 27\mu$m, $d \simeq 170\mu$m.

Another set of approximations (Huard, 1997) gives the transmission of a wire-grid polarizer in the two cases of incident radiation polarized parallel and perpendicular to the wires:

$$T_{\text{parallel}} \simeq \frac{4nA^2}{1+(1+n)^2A^2} \tag{3.3}$$

$$T_{\text{perpendicular}} \simeq \frac{4nB^2}{1+(1+n)^2B^2} \tag{3.4}$$

where n is the refractive index of the dielectric substrate ($n = 1$ in the case of free-standing wires) and A and B are the two numbers

$$A = \left(\frac{d}{\lambda}\right)\left[0.347 + \frac{Q}{4+Q} + 4\cdot 10^{-3}\left(\frac{d}{\lambda}\right)^2\right]$$

$$B = \frac{1}{4A}$$

and Q is the quantity

$$Q = \left[1 - \left(\frac{d}{\lambda}\right)^2\right]^{-\frac{1}{2}}$$

Figure 3.2 shows the transmission curves for a wire-grid polarizer having $a = 10\mu$m and $d = 2\pi a$.

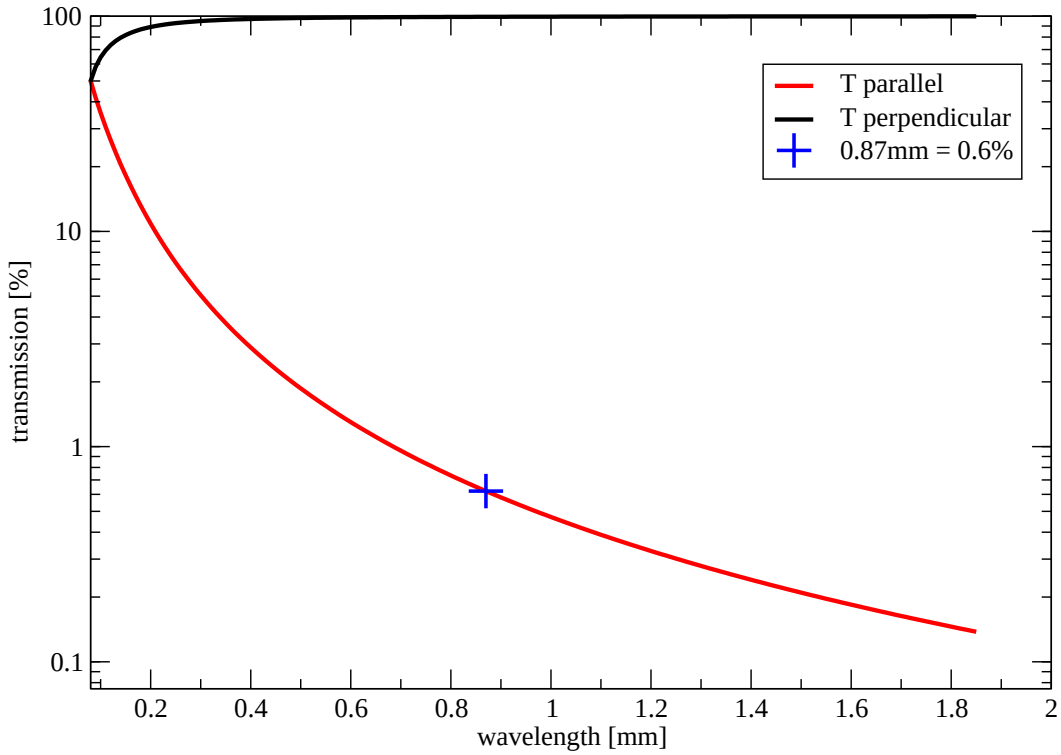

Figure 3.2: Transmission curves of a wire-grid polarizer calculated using equations (3.3),(3.4) for a wire-grid having $a = 10\mu$m, $d = 2\pi a$.

So far we did not consider the imperfections that are likely to be introduced during the fabrication of a wire-grid. They are mainly of two types: random errors in wire spacing and random errors in the wire diameter. Even commercially available grids show these defects when observed under a microscope. Visually, the most obvious is the irregular spacing between wires. Perturbations caused by the errors in the size of the wires are generally much smaller than those caused by the errors in the spacing and can be neglected. The quality of a wire-grid therefore can be characterized by the distribution of the spacing of the wires about the nominal value. Shapiro & Bloemhof (1990) have published measurements of the unwanted cross-polarized transmittance through grids on which they had purposely introduced random errors in the wire positioning. They used wires of 12.5μm and introduced random variation in the distance with amplitudes of 52%, 23%, 7% of the mean spacing 114μm, 109μm and 103μm respectively. At a wavelength of 0.87 mm they report a cross-polarization of $\sim$ 2% in the first case, reduced to 1% and 0.7% in the other two cases respectively.

3.3 The wire-grids of 146 mm diameter

At the beginning of year 2001 we designed a reflection-type half-wave plate that uses a large wire-grid having a clear aperture of 146 mm. Two wire-grids of that size were manufactured by us in our labs but the sets of wires were a gift from Manfred Tonutti (Rheinisch-Westfälische Technische Hochschule, RWTH, Aachen, Germany). The two sets were made of gold coated Tungsten wires with a diameter of 25μm glued at the extremities on two thin Aluminum bars at a step of 100μm. Figure 3.3 shows one of the two sets of wires as it was when we received it. The left picture shows the entire

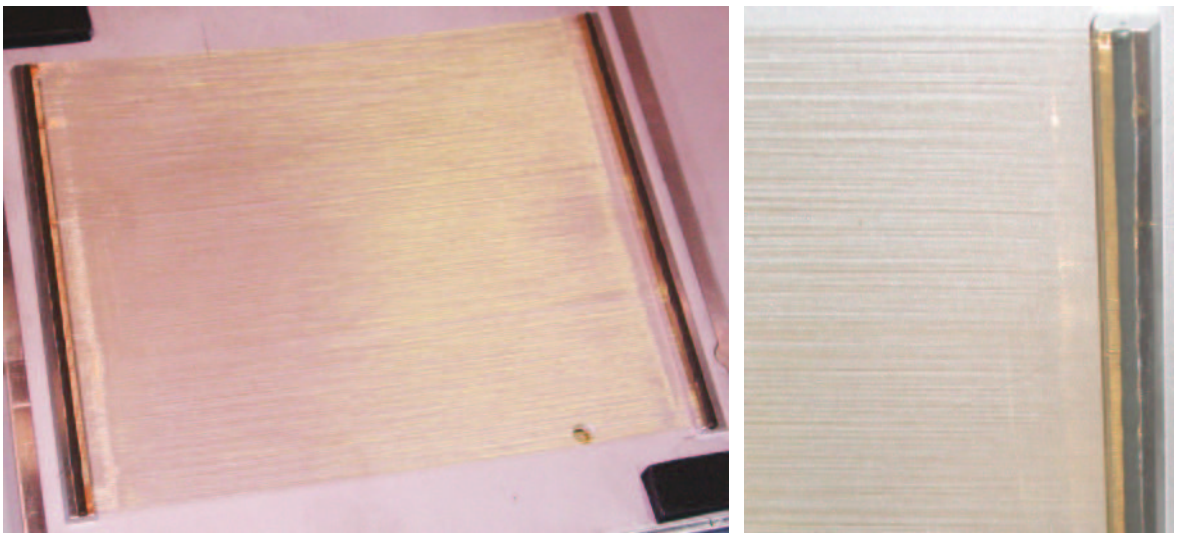

Figure 3.3: One of the two sets of golden Tungsten wires as it was when we received it from Dr.Tonutti. The extremities of the wires are glued on two thin Aluminum bars.

set, roughly 170 mm x 148 mm in size. On the right side is a detail showing how the wires are glued on the metal bars. The grey strip along the bar is the glue, in this case a Ciba/Geigy two component Araldite K138, that after preparation has a pot-life long enough to machine a set of wires of that size ($\sim$ 1.5 hours at room temperature). In the next section I will describe how the two sets were machined at the RWTH.

We designed the tools needed to perform the steps following the preparation of the set of wires: stretching and cleaning of the wires, gluing them on a circular frame, cutting of the excess wires along the outer edge of the frame. This frame is a ring of brass with a 10 mm square section, grooved on the surface to increase the shear strength of the glue interface. We used a Epo-Tek 301 two component epoxy to glue the wires to the ring, cured for 1 hour at 60°C. The picture on the left side of figure 3.4

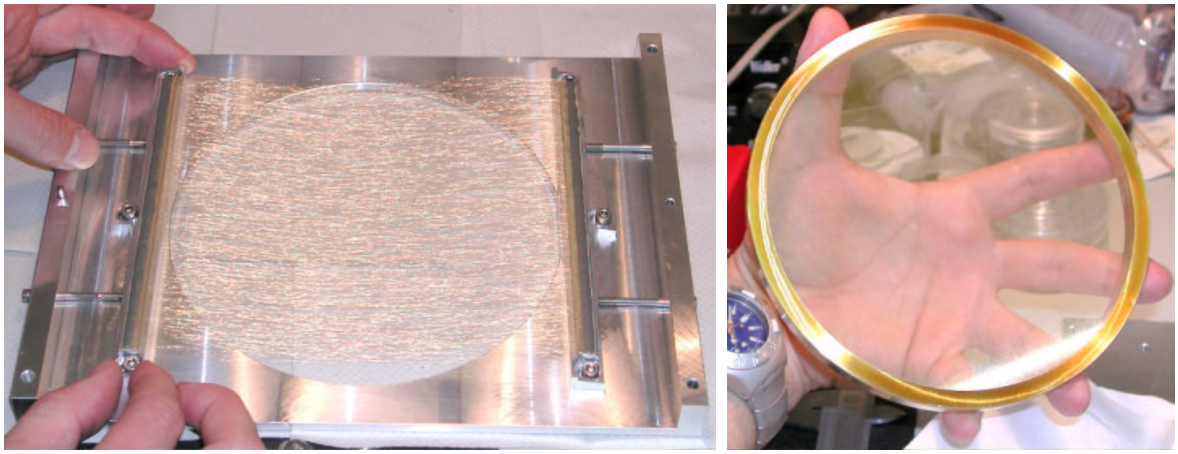

Figure 3.4: *Left*: The set of wires going to be stretched and cleaned. *Right*: The final product ready to be used.

shows the set of wires going to be stretched and cleaned, before being glued onto the circular frame. The final product is visible on the right side of the same figure, ready to be used. We produced two twin wire-grid polarizers of 146 mm clear aperture, which we used in the first prototype of RHWP tested at the HHT telescope in May 2001. As predicted, we found that just the inner 7 channels of the bolometer array were able to point at the sky, because the size of the RHWP was too small for all the beams. We found, however, that the RHWP was working nicely, producing low insertion losses and high efficiency in polarization modulation. The first tests convinced us that was worthwhile to put some more effort in producing larger polarizers (see sections 4.2 and 5.5).

3.4 The wire-grid machine and its upgrade

The machine used to produce the free-standing wire-grids at MPIfR was originally built for winding coils and has been slightly modified for wire-grids. It has two moving parts: a wire collector, rotating about a horizontal axis (see figure 3.5, left) and a wire dispenser, sliding parallel to it. Controlled by an electronic counter, the wire dispenser moves in steps, synchronized to the rotation of the collector. The step size can be fixed between 35 μm and 999 μm with a resolution of 2 μm. The rotor rotates continuously with adjustable speed. The rotor holds a rectangular frame that accumulates the wire during operation. At the end of this process, the frame will be wrapped by a spiral of wire that constitutes two sets of wires (one per side, see figure 3.6), ready to be

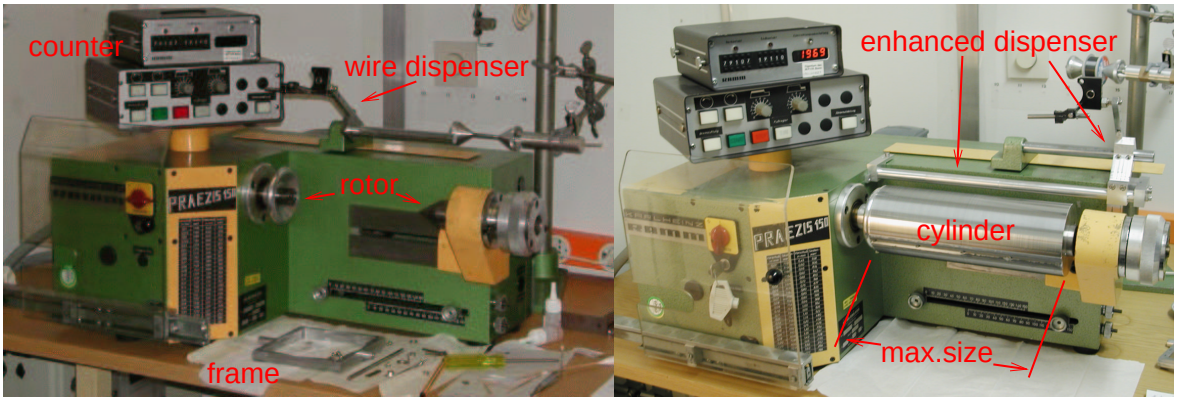

Figure 3.5: *Left*: The wire-grid machine as it was before the modifications. On the table the frame used to collect the wire is visible (see also figure 3.6, left). *Right*: The machine after the modifications. The wire dispenser now can use the full length of the machine. The frame is replaced by a cylinder (see also figure 3.6, right).

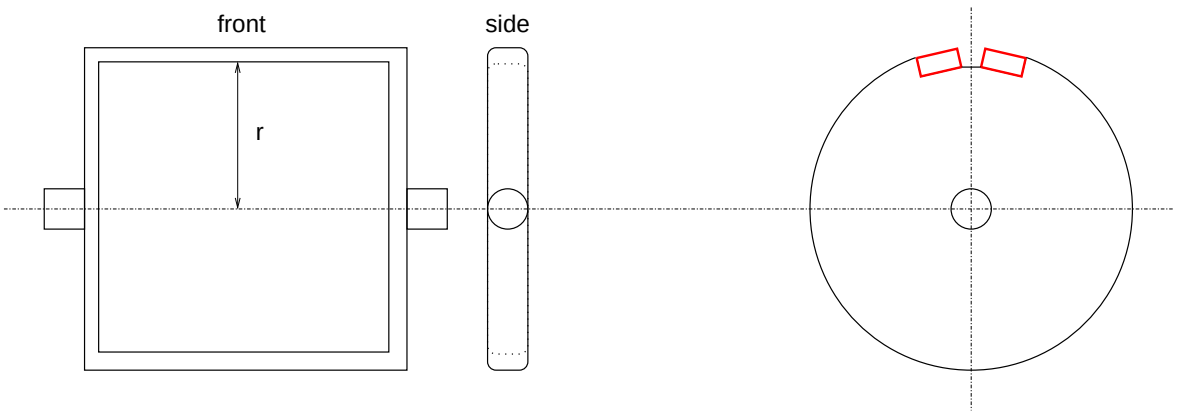

Figure 3.6: *Left*: Scheme of the frame used to collect the wire before the upgrade. This frame is mounted in the rotor axis (see the left picture of figure 3.5). At the end of the winding process, two sets of wires are collected, one per side. These can be used to produce two wire-grids whose size will be a bit smaller than $\sim 2r$, the size of the frame. *Right*: Section of the cylinder that replaced the rectangular frame. The wires are glued onto the two bars (cross-section drawn in red) fixed into the cylinder (see also figure 3.8). At the end of the winding process the wires are cut along the gap between the two bars. We get just one set of wires but the size is now $\sim 2\pi r$.

glued on the polarizer frames. The main limitation of this system is that the size of the frame cannot be larger than twice the distance from the axis of the rotor to the machine body. The size of the frame is limited to less than 15 cm and the maximum diameter for a wire-grid is then about 12 cm.

The contribution by Dr.Tonutti and his group to our project was not just limited to the two sets of wires they donated to us: they also suggested the way to upgrade our wire-grid machine to larger grid sizes.

In order to produce large sets of wires, they use a standard lathe in the mechanical workshop of RWTH. Using a spool of wire on the carriage of an automatic lathe, and operating it in the mode normally used to make threads, they can dispense wire over a long path, of the order of one meter or more. The size of the set of wires is limited by the maximum diameter that the machine can handle, which can be quite large. Their idea to increase the size of the set of wires, is to collect the wire on a cylinder rather than on a rectangular frame (see figure 3.6, right). The set of wires will be larger because it is wound around the surface of the cylinder and at the end of the process it will be $2\pi r$ long, if r is the cylinder radius. Even though this technique can give good results, there are some points that can be improved. For example, the lathe's rotor has poor speed control, and, especially at the start, could produce an excess of tension along the wire. There is a high risk of breaking it and this risk increases if one goes to thinner wires. Then we have to consider manufacturing our grids in an environment cleaner than a machine shop, where dust and small metallic particles are unavoidable.

Therefore we transferred their basic idea to our wire-grid machine and the modified version is visible in the right picture of figure 3.5. In our case, the cylinder diameter could be as large as the size of the rectangular frame, ($d \sim 15$ cm) so that sets of wires up to $\sim$ 45 cm long are possible.

Unfortunately, we found another limitation: the longest possible path for the wire dispenser is about 15 cm. To overcome this problem we decided to use the machine in two steps. During the first step, we collect the wire on the cylinder, moving the dispenser from the beginning to the end of its path, as usual. Then we need to freeze the position of the wire and move the dispenser back to the starting point without moving the wire.

We then start a second process but this time the wire will be collected starting from the point where it was at the end of the first half. (See figure 3.7 for a more extensive explanation). At the end of this double process, the total path of the wire will be double the usual one, meaning that we could get up to $\sim$ 30 cm. To do this we had to modify the machine, adding some parts. In particular, a device to hold the wire in position was designed and added to the machine body.

After these modifications, we still have the limitation that the length of the cylinder cannot be longer than 25 cm. This is the main reason why we produced wire-grid

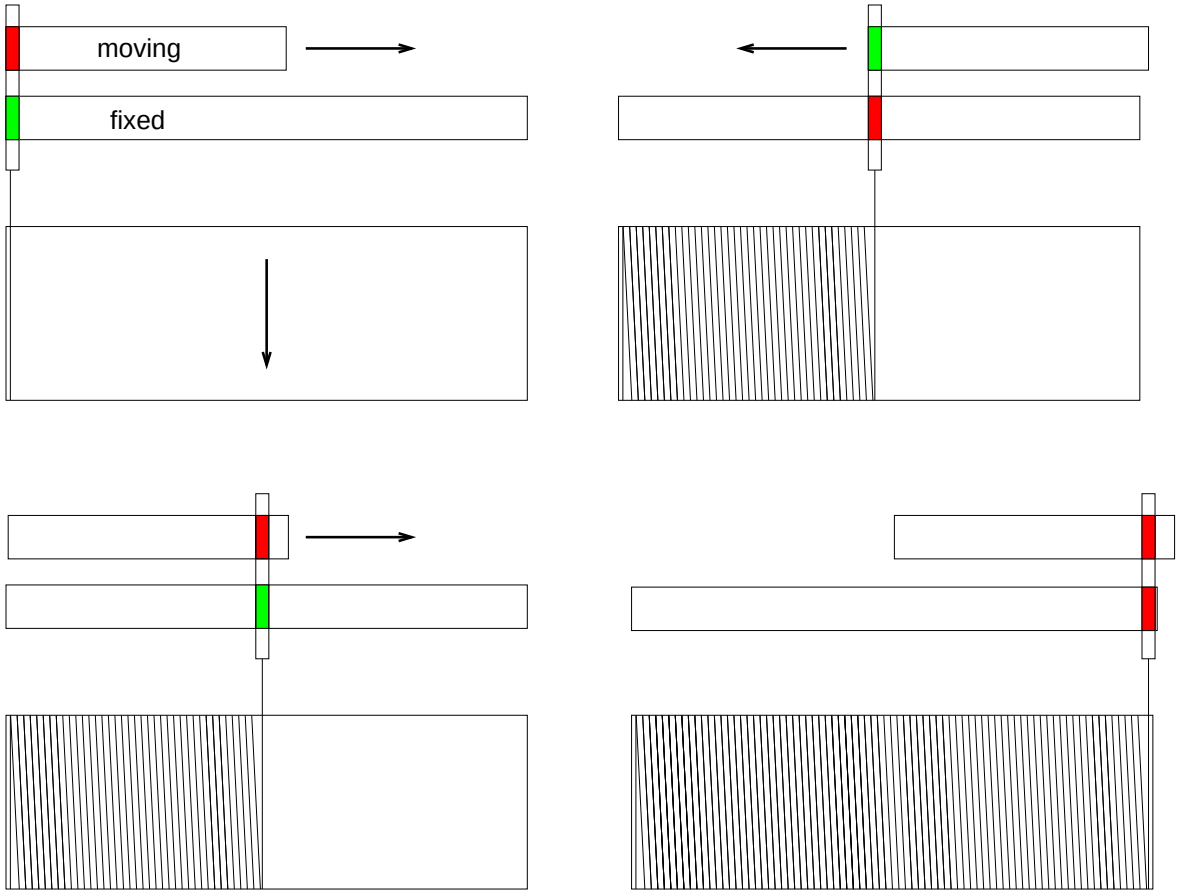

Figure 3.7: Four steps of the winding process. The biggest rectangle represents the cylinder. The other two rectangles are two parts of the machine: the short one is a bar moving horizontally, holding the wire dispenser, the longer bar was attached by us to the machine body. The wire dispenser, shown here by a thin vertical rectangle, can slide on the two bars or can be fixed to one of the two or to both. The red and green colors mean that the wire dispenser is fixed or free to move, respectively, on that bar. *Top, left*: At the beginning of the process the wire dispenser is fixed on the moving bar. This moves to the right while the cylinder rotates collecting the wire. *Top, right*: Once one half of the cylinder is wound with wire, the cylinder is halted, the dispenser is fixed to the other bar and released from the moving one, the latter being moved back to the initial position. *Bottom, left*: When the moving bar is back to the initial position, the dispenser is fixed on it and released from the fixed one. The cylinder starts rotating and the winding process goes on. *Bottom, right*: When the cylinder is completely wound it is halted and the dispenser fixed on the fixed bar. The winding process is done. The picture on the right side of figure 3.5 shows this situation.

polarizers of 246 mm of clear aperture, with a cylinder of 46 mm of radius. In the future, it should be possible to make an extension of the machine body, in order to use a larger cylinder. Doing three or four steps, the same machine could then produce wire-grids with diameters up to $\sim$ 45 cm.

3.5 The wire-grids of 246 mm diameter

To produce one of these large wire-grids we have to go through several steps and it is a long process that takes many days. Collecting one single set of wires takes between 5 and 6 hours. Using a 20 μm wire in steps of 63 μm the cylinder makes $\sim$ 4000 turns, collecting roughly 1.2 km of wire at a speed of $\sim$ 16 turns/minute. The weight of such a set is just about $\sim$ 30 grams.

The cylinder has two thin Aluminum bars screwed onto it (see figure 3.6, right, and figure 3.8). Before we start the winding process we put a line of glue onto them such that during the winding the wires are glued on the bars at the same time. One consideration about the glue is that its viscosity should be low in order to avoid shifting of the wires when they sink into it. On the other hand, the pot-life must be quite long because collecting the wires takes hours. From this point of view, we benefit from our

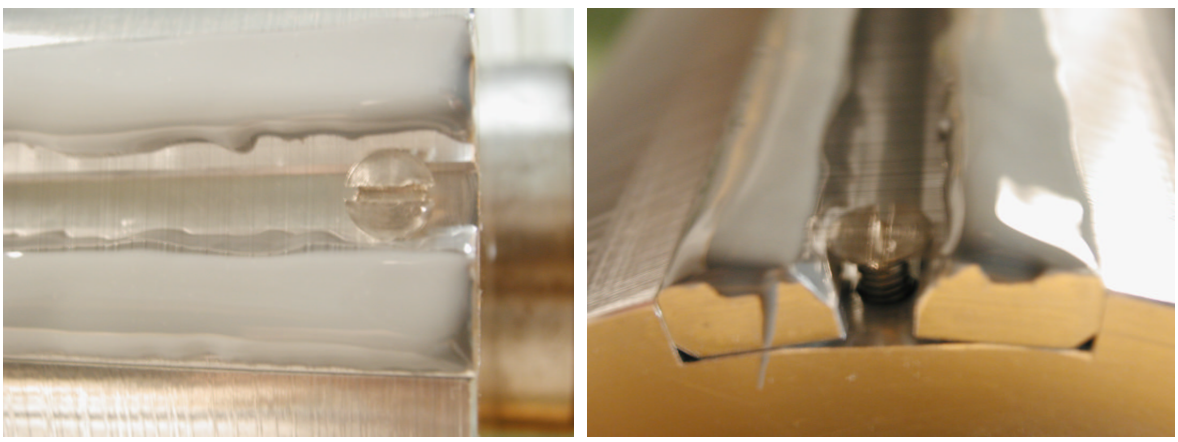

Figure 3.8: *Left*: A detail of the gap between the two bars. The grey part is the glue. *Right*: Side view at the edge of cylinder and bars (see figure 3.6, right). The wires are barely visible.

two-steps process because, after the first half is done, we can prepare some new glue for the second half. The pot-life should then be at least 2 hours. We used the Hardman Epoweld 13230 2 component epoxy, that develops a good combination of shear strength and peel strength with only a room temperature cure. The manufacturer declares a pot-life of 3/4 hours, enough for our purposes, viscosity of 50000 cps at 25°C and a shear strength of 2940 psi after a cure schedule of 18 hours at 25°C plus 2 hours at 100°C.

At the end of the winding process, we give about 12 hours of cure time at room temperature. Then we cut the wires along the gap between the two bars (figure 3.8)

and in this way it is possible to remove the set of wires from the machine (see figure 3.9). The following step is to put the set of wires in an oven, for roughly two hours at 100°C. This high-temperature hardening process is necessary to avoid the possibility

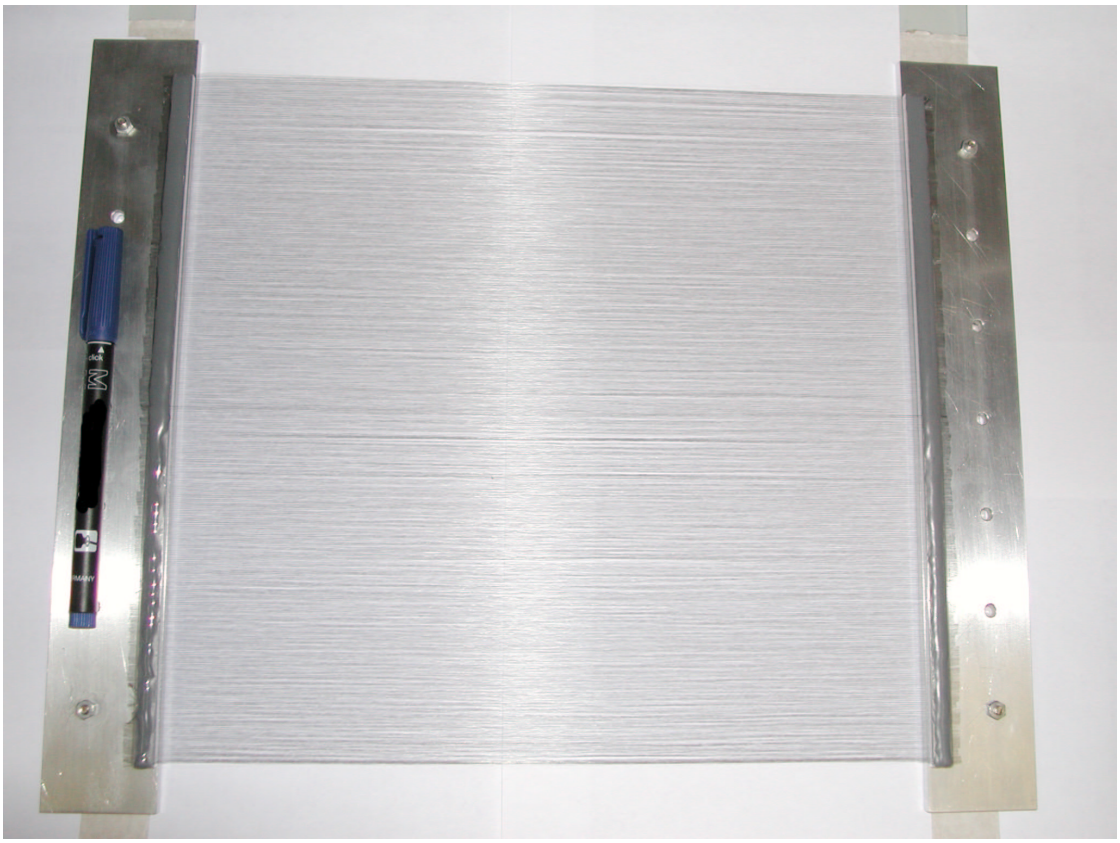

Figure 3.9: A set of wires removed from the machine. The size is rectangular, 250 x 289 mm. A pen is shown for comparison.

that the wires could slip out from the glue during the following stretching process. During stretching, the wires are subject to a strong longitudinal tension in order to make them as parallel as possible.

It is very important to remove as many dust particles as possible, that were collected by the wires during the previous steps. This is one of the most important and delicate steps of the process. We saw that these particles are responsible for most of the imperfections in the ultimate wire-grid: they tend to misplace the wires and to gather some wires into groups. Making use of a microscope, a thin brush, tweezers and compressed air, it is possible to clean the wires but it is very difficult, wires can break and it is time consuming. Obviously, in the future, the winding process should be performed in a clean room environment, especially when going to thinner wires for

shorter wavelengths. When the set looks satisfactory, we put a ring underneath and in a precision device designed for the purpose, we slowly lower the wires until they are just a few microns above the surface of the ring. At this point we drop some glue on the

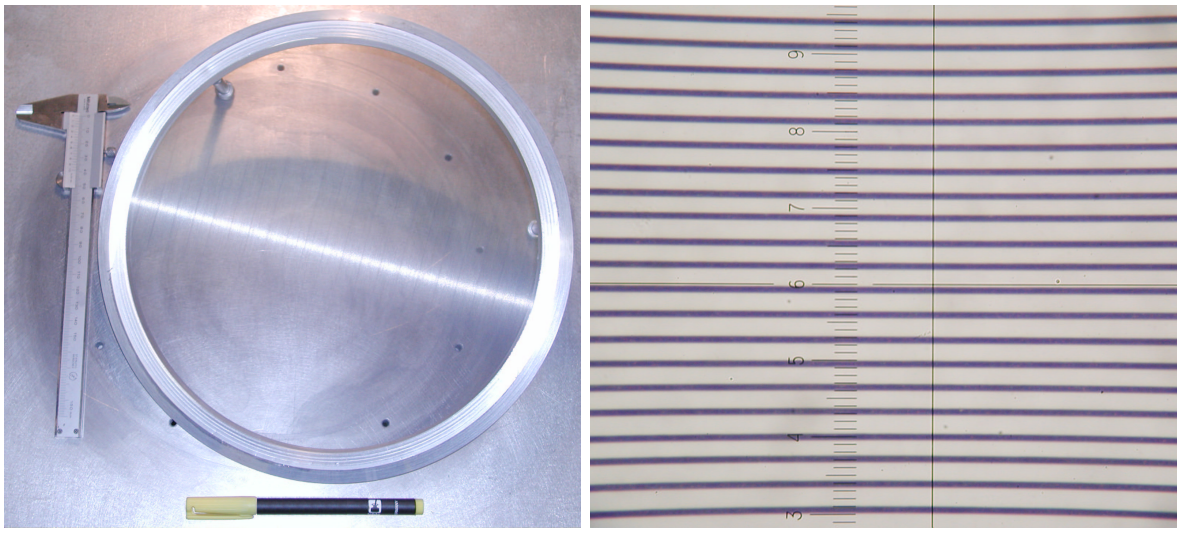

Figure 3.10: *Left*: The ultimate wire-grid. A caliper and a pen are shown to give an idea of the size. The wires are too thin to be seen but it is possible to see the light reflected by them. *Right*: A detailed microscopic view of the wires. The picture represent an area of one square millimeter. The minor ticks in the scale are 20 μm.

wires and via capillary action it will distribute in the grooves on the surface of the ring. We used the Epo-Tek 301 two component epoxy, the same used for the smaller wire-grids of 146 mm diameter, but in this case we don't cure it at high temperature. We do the opposite: we put the system in a refrigerator. Our rings are made of Aluminum and the expansion coefficient for this material is larger than the one for Tungsten. Cooling down the system, the ring will shrink more than the wires. After roughly 24 hours at zero degrees Celsius the glue will be hardened and when we transfer the system to room temperature the ring will expand more than the wires, producing a very strong tension along them. This is very important because at the telescope the wire-grid will operate at the Nasmyth focus, where the temperature is usually just few degrees above zero, and the hardening of the glue at low temperature ensures that the wires are well stretched even in that condition.

The last step is to cut the wires along the outer edge of the ring. This must be done very carefully, because the wires are under a strong tension and if any increased stress is applied to the glue, it will detach from the ring, wasting all the work done prior to

this very last step. Figure 3.10 shows the ultimate product, ready to be mounted on the reflection-type half-wave plate. The outer diameter is 286 mm. The picture on the right shows the wires seen under a microscope. They are well parallel and the spacing is very regular. This is important to get high efficiency. The measured mean error in the wire spacing is 18 μm r.m.s. .

A final comparison can be carried out between the efficiency of these wire-grids and the 146 mm ones. The smaller ones had 25μm wires and 100μm spacing, therefore not well optimized, the spacing being a bit larger than $2\pi a$ (see equations (3.1), (3.2)). The size of the wires is now smaller, 20 μm, and the spacing is optimized, so that we expect to increase the transmission by 0.4% and to lower the cross-polarization from 0.6% to 0.3%, at 0.87 mm.

Chapter 4

The reflection type half-wave plate

4.1 The prototype

The prototype that we used in the lab, in order to test the feasibility of a reflection-type half-wave plate was a small device, made of an Aluminum mirror and a wire-grid polarizer, with a diameter of 65 mm. The wire-grid is fixed in front of the mirror which can be moved by means of three micrometers (see figure 4.1). The experimental

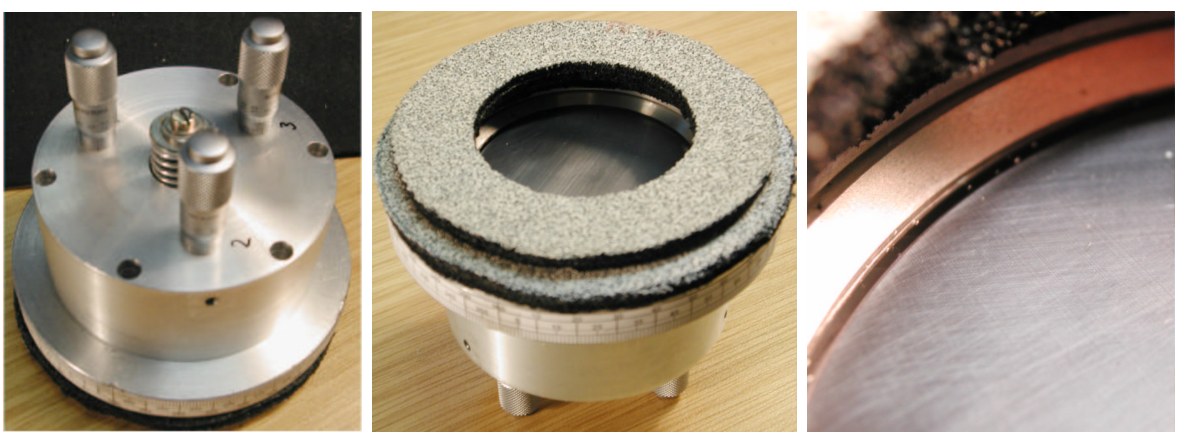

Figure 4.1: The RHWP prototype. *Left*: Bottom view. The three micrometers are visible. *Center*: Front view. *Right*: Detail of the gap between wire-grid and mirror.

setup for this first test is shown in figure 4.2. The receiver is a bolometric two-channel polarimeter operating at the central wavelength of 1.2 mm. Inside a ^{3}He/^{4}He cryostat, at a temperature of 300 mK, there are two bolometers and a wire-grid polarizer used as a polarization beam-splitter. The receiver looks downwards, where a plane mirror at 45° reflects the radiation coming from a lab source. Inside the cryostat, the optical beam is divided, into two orthogonal beams by the cold wire-grid polarizer positioned at 45° to

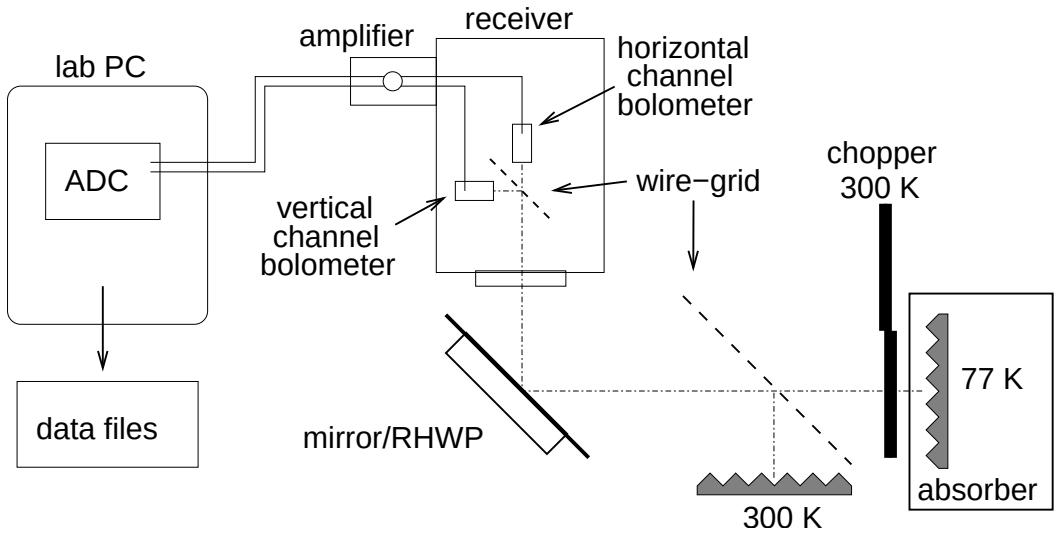

Figure 4.2: Experimental setup for the lab tests done in December 2000. Radiation is switched between 77K and 300K by the chopper wheel, linearly polarized by a wire-grid and reflected by the RHWP into the receiver. Here it is split in the two orthogonal components by a second wire-grid and detected by the bolometers.

the optical path, such that the horizontal polarization goes straight to one bolometer while the vertical polarization is reflected to the other one. The mirror can be replaced by the RHWP and this can be rotated about its optical axis to any angle. The lab source is made of an absorber (Eccosorb AN72) at liquid nitrogen temperature chopped by a rotating sector-wheel whose sectors are covered by absorber at room temperature. In front of the source is a linear polarizer that can be rotated about the optical axis to produce radiation with a well known state of polarization. The micrometer heads used in this RHWP have a resolution of 10 μm and accuracy of 2 μm. To perform these measurements the position of the mirror relative to the polarizer was tuned with high accuracy, according to equation (2.16), repeating the positioning several times to ensure its reproducibility. Several measurements were made in December 2000 for different position angles of the RHWP and for different polarization angles of the lab source in the lab reference system. Data were acquired in our lab PC using a National Instruments PCI 6033E ADC board, at a sample rate of 500 samples/second. The signals that we expected have the form given by equations (2.13) and (2.14) and must have 4 periods over 360°. Figure 4.3 shows the measured *polarization modulation efficiency* (hereafter PME) when the source is horizontally polarized. Data were taken in steps of 5 degrees of the RHWP. The total intensity was measured for each data

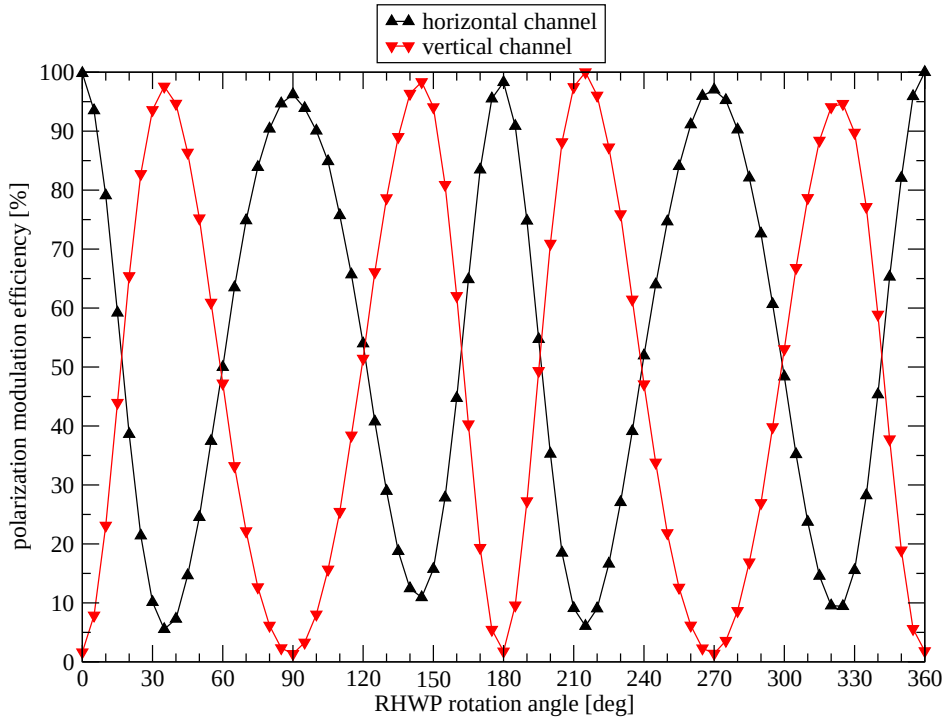

Figure 4.3: Results of the lab tests of the RHWP prototype. The PME is shown for different rotation angles of the RHWP. In this case the source was 100% linearly polarized along the horizontal axis. Errors on PME are in the order of 5% for the horizontal channel and 2% for the vertical. The error of the rotation angle is $\sim 1°$.

point by replacing the RHWP with a plane mirror. The two channels show different efficiencies because the horizontal channel has a lower responsivity, as shown by the load curves (see figure 4.4). Therefore the actual efficiency of the RHWP is better represented by the vertical channel because the other one has a low signal-to-noise ratio, especially when the signal is close to zero. The data show the value of the maxima never lower than 95% and all the minima are below 3%.

These lab tests were made just to check the feasibility of designing a polarimeter for bolometer arrays making use of a RHWP. Nevertheless, these results clearly show that a RHWP has a high PME and is a good alternative to crystalline HWP.

In figure 4.3 we can see a side effect of the reflection type HWP: the modulation is not a pure sine wave. This effect is due to the projection of the rotation angle that we measure on the plane of the HWP, upon the plane orthogonal to the direction of the incident radiation, in our case at 45°. In other words, the bolometers see the projection of the RHWP upon the plane of the wave front (see figure 4.5, left). We will have to compensate for this effect during the data reduction, taking into account the relation

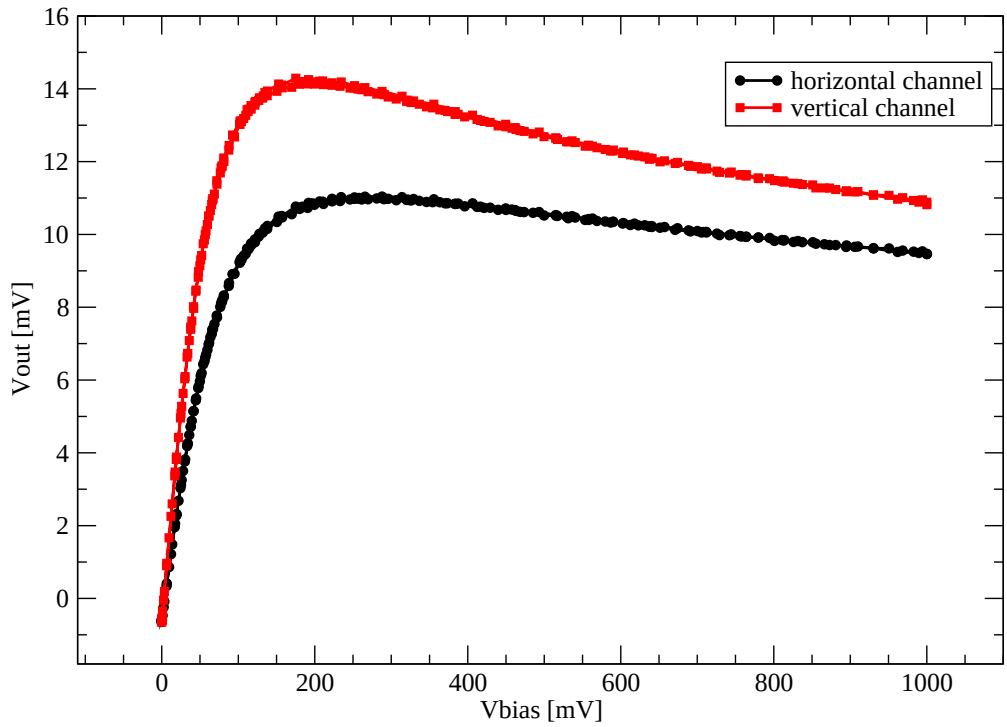

Figure 4.4: Load curves of the two bolometers of the two-channel polarimeter. The horizontal channel has a lower responsivity than the vertical one.

between the two angles

$$\gamma' = \arctan\left[\tan\gamma / \cos\alpha\right] \tag{4.1}$$

This relation is explained geometrically in figure 4.5. For example, in figure 4.3 the

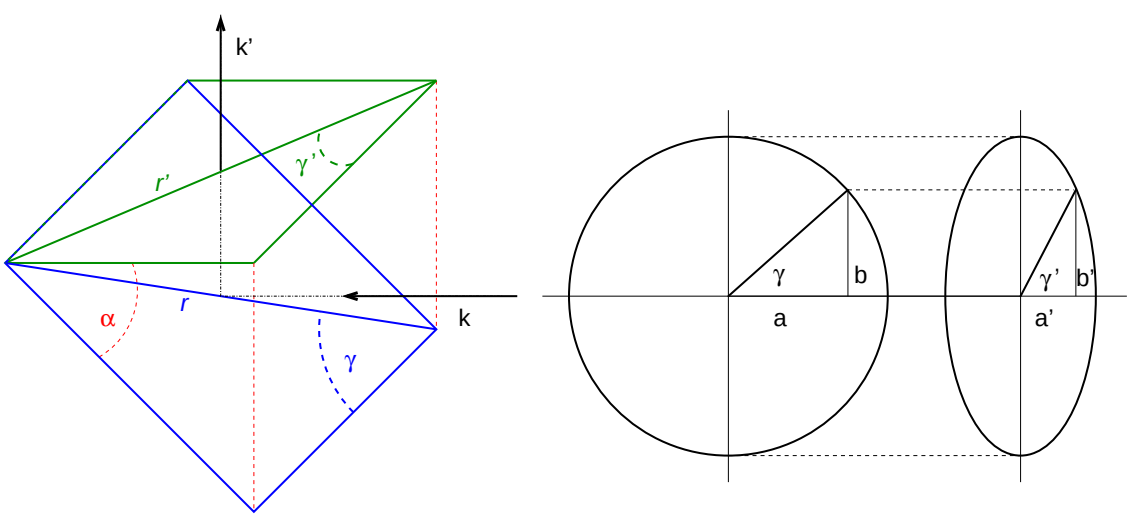

Figure 4.5: *Left*: Radiation with incidence angle α (wave vector $\mathbf{k}$) is reflected by the RHWP (blue plane) when its retardation axis r has position angle γ. The bolometers will see its projection r' (green plane) at angle γ'. *Right*: Geometrical relation between γ, γ' and α ($a' = a\cos\alpha, b' \equiv b$).

first maximum of the vertical channel is when the bolometers see the RHWP at the projected angle $\gamma' = 45°$. This happens when the true rotation angle γ is

$$\gamma = \arctan\left[\tan\gamma' \cos\alpha\right] = 35°15'52''$$

being $\alpha = 45°$. The plot in figure 4.3 confirms this result.

4.2 Design of the 146 mm half-wave plate

Given the positive results of the tests with our prototype, we decided to manufacture a larger RHWP. At the beginning of year 2001 we designed a RHWP making use of the wire-grid described in section 3.3. The size of 146 mm is already large enough to be used at the HHT telescope with the inner 7 channels of the 19 channel bolometer array.

Our system works with reflections and we want it to rotate fast. This could be a complication because even a small oscillation of the rotation axis can produce a large oscillation of the beam and this increases the noise in the measurements. On the other hand, the RHWP has the advantage that radiation does not pass through it and therefore can be supported from the back. For these reasons we decided to

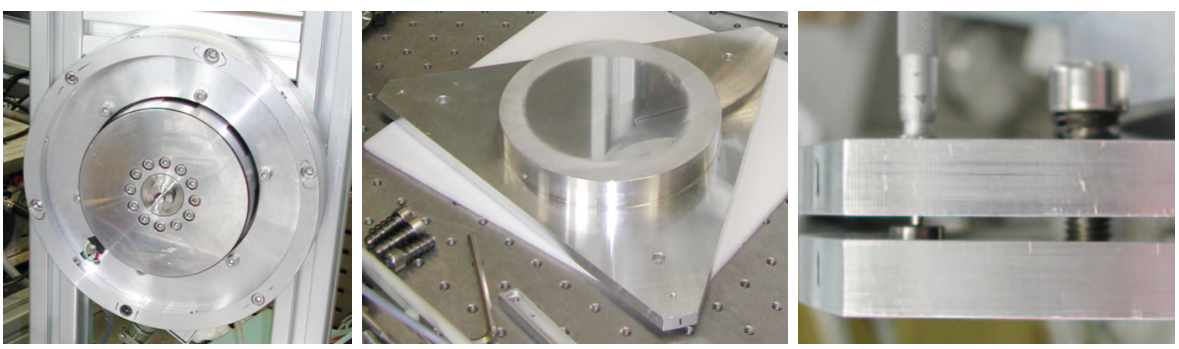

Figure 4.6: The 146 mm RHWP. *Left*: The air bearing. *Center*: The mirror plate. *Right*: A detail of the two plates and one of the three screws used to adjust the distance.

mount it on a motorized air bearing (model IT103M by INTOP division of Kollmorgen Corp., see figure 4.6, left). This device has an on-axis electric motor embedded in it and, according to the manufacturer, it is able to maintain the rotation plane within an error less than 1 μm (Langenbeck, 1980). In order to minimize the errors when positioning the wire-grid parallel to the mirror, we minimized the number of surfaces to be machined. Our design has just three parts: one plane-parallel plate screwed

onto the air bearing on one side and polished to be a mirror on the other side (figure 4.6, center); a second plate, with a 146 mm hole in the center to hold the wire-grid, whose distance from the mirror can be adjusted by three micrometer heads (figure 4.6, right); one of the two wire-grids of 146 mm diameter (see section 3.3). The pictures

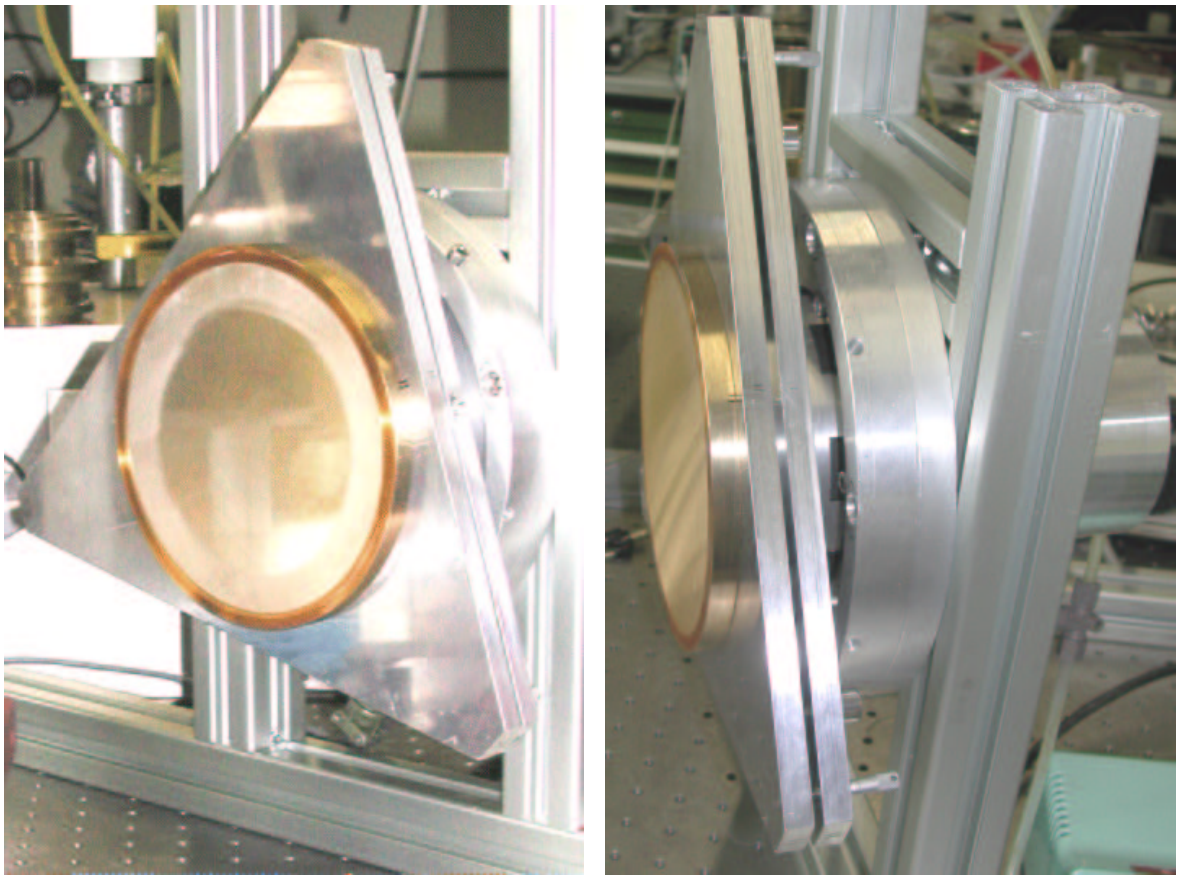

Figure 4.7: The 146 mm RHWP mounted on the air bearing in the lab. *Left*: Front view. *Right*: Side view. Two of the three micrometric screws are visible.

in figure 4.7 show the system mounted in the lab. The mirror plate is mounted on the air bearing and the gold-coated wire-grid is fixed on the second plate. The RHWP can be tuned to the operating wavelength, according to equation (2.16), by means of three Mitutoyo 148-216 micrometer heads , having a resolution of 10 μm and accuracy of 5 μm, These screws are just 21x9 mm in size and were chosen to minimize the part of the screws that juts out from the back side of the mirror plate.

The air bearing is driven by an AC three phase motor and therefore there is no direct control over the position of the rotor. We thought of monitoring the rotation angle by a position reference system made of an optoelectric sensor: an emitting infrared

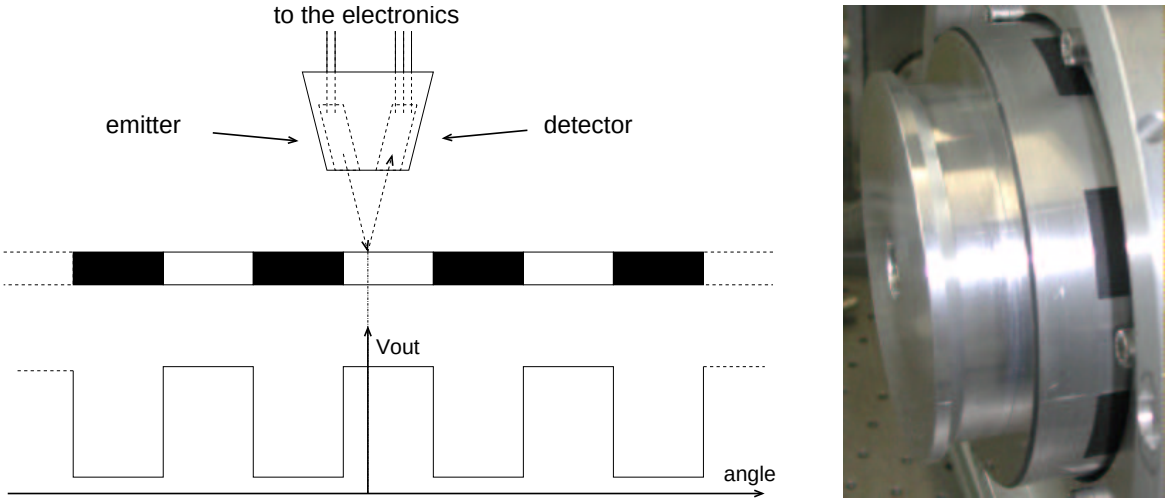

Figure 4.8: *Left*: Scheme of the position angle reference system. The optoelectric sensor is made of two parts: an emitting diode and a photo-transistor detector. During operation, marks on the bearing produce an alternate signal synchronous with the position angle. *Right*: A detail of the rotating part of the bearing: three reference marks are visible.

diode illuminates the surface in front of it and a photo-transistor collects the reflected radiation (see figure 4.8). On the surface of the rotating part of the bearing we put a set of marks. When one mark moves in front of the sensor it reduces the intensity of the radiation reflected into the photo-transistor. This signal is then shaped by an electronic circuit, resulting in an alternating electric signal, similar to a square wave. During normal operation, the RHWP rotates fast, with constant angular velocity, and the output voltage of the reference system is a TTL-compatible digital signal synchronous with the position angle of the RHWP (see figure 4.9). The reference set is made of 8 marks and produces one complete period every 45°, with 22°.5 being the duration of one TTL logical level. One of the marks has a hole in the center and produces a signal that differs from the others, providing additional information about the absolute position of the RHWP.

We tested the 146 mm RHWP in our lab in April 2001. The experimental setup is almost the same as used to test the small prototype (figure 4.2), the same receiver and the same source, but this time radiation is subject to one more reflection (see figure 4.10). During operation the RHWP rotates at the mechanical frequency of 5.5 Hz that produces polarization modulation at 22 Hz (see equations (2.13) and (2.14)). The acquisition during these lab tests was pushed up to 2000 S/s (samples/second), that means 363 samples per turn, an angular resolution of $\sim 1°$ per sample and ~ 91 samples per polarization cycle. The signals from the two channels of the receiver and from the

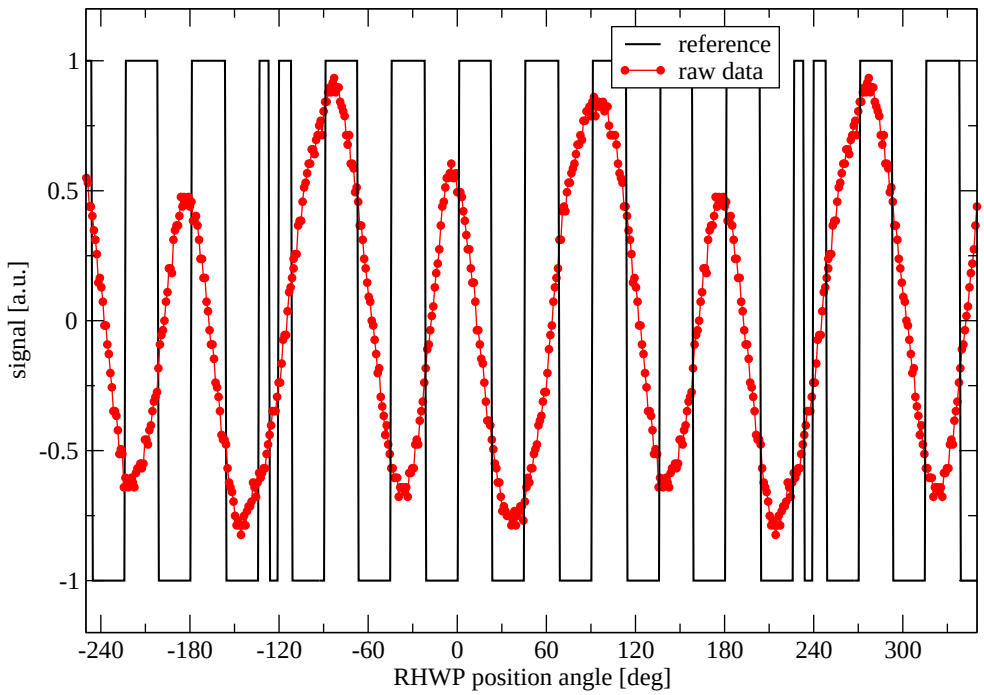

Figure 4.9: A signal modulated by the RHWP (red) is plotted together with the signal from the reference system (black) used to restore the information about the position angle of the RHWP. One turn produces 8 pulses. One of them has a different shape and gives information about the absolute position.

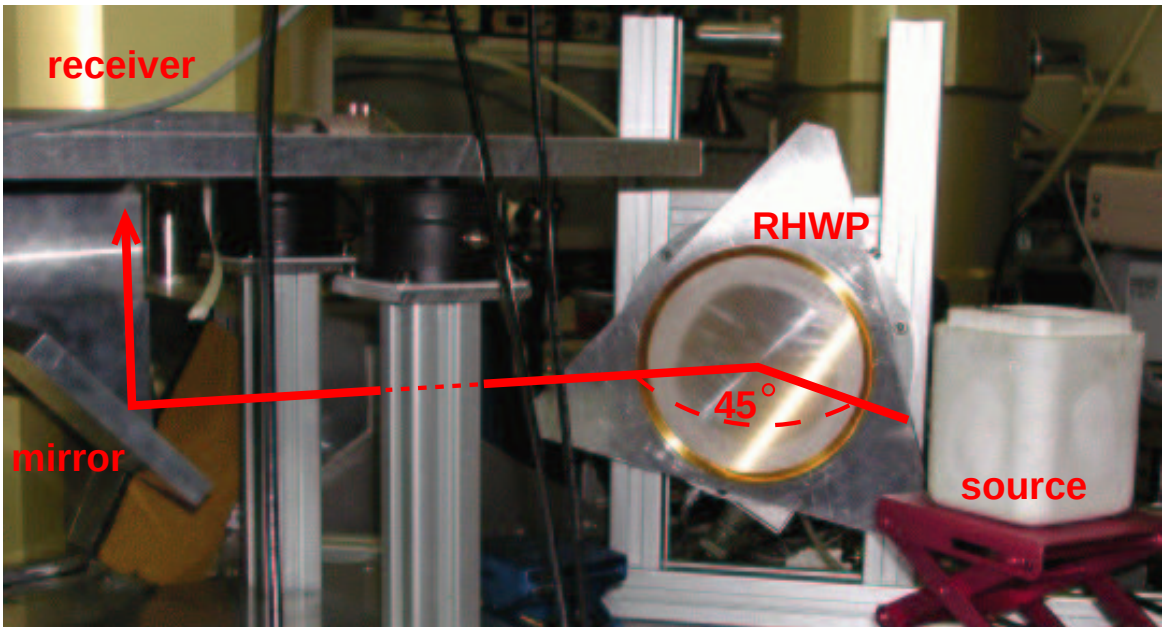

Figure 4.10: Setup used in the lab to test the 146 mm RHWP. The chopper and the source polarizer were added after the picture was taken. See also figure 4.2.

position reference are acquired simultaneously. Data are taken for different polarization states of the source. For each polarization state a time series of data is acquired. One acquisition file is typically 11 seconds long, that means 22000 data points, ~ 60 turns of the RHWP and ~ 242 polarization cycles. In the data reduction process, data are then converted, via software, from a time series to a function of the rotation angle, using the reference information. The 242 cycles are averaged in groups of 4 polarization cycles within one turn of the RHWP. Figure 4.11 shows the modulation produced by the RHWP when the source is 100% linearly polarized horizontal (top) and vertical (bottom).

We now see a new effect that was not present in the measurements with the small 65 mm RHWP. The PME is not constant but it is a function of the rotation angle. In particular, we see that it has a periodicity that is twice the mechanical rotation frequency. It was not easy to understand the nature of this effect. In the end, we discovered that its cause is not in the RHWP itself but rather the combination of the bolometer frequency response with the fast spinning technique. It was not present in the previous lab measurements because in that case the RHWP was turned in steps and the signal was modulated by a chopper wheel. In the case of fast rotation of the RHWP, the modulation is produced directly and the bolometer frequency response comes into play because the modulation is not a perfect sine wave. The explanation of this effect is based on the relation between the mechanical rotation angle and the projected one, given by equation (4.1). Consider the RHWP rotating with constant angular velocity $\omega = \partial\gamma/\partial t$. We can calculate the angular velocity of the projected RHWP seen by the bolometers:

$$\omega' = \frac{\partial\gamma'}{\partial t} = \frac{c\,\omega}{\cos^2\gamma + c^2\sin^2\gamma} \tag{4.2}$$

where $c = 1/\cos\alpha$. Figure 4.12 shows some values of ω' calculated for some typical incidence angles. It has peak values at 0° and 180°: when the RHWP is close to these positions it produces variations in the intensity of the radiation that are faster than in other positions and the bolometer response will be a bit smaller. The result is that the amplitude of the acquired signal is not constant but modulated by ω' such that it will be smaller at 0° and 180° and will have the regular value at 90° and 270°. The plot at the bottom shows the maximum variations of the frequency as a function of

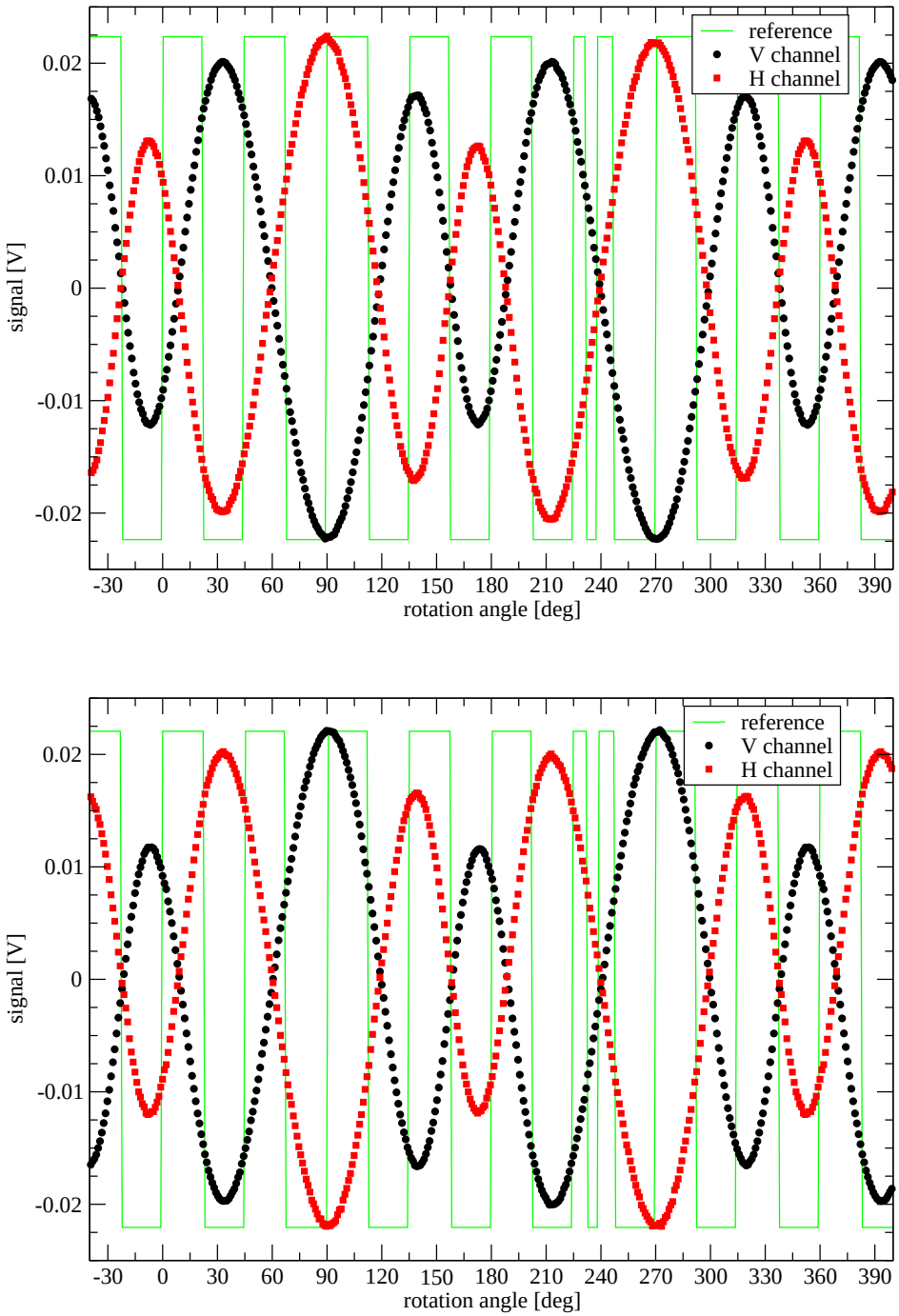

Figure 4.11: Polarization modulation produced by the 146 mm RHWP. Signals detected by the two bolometers in the receiver (vertical channel is black, horizontal channel is red) are plotted together with the signal coming from the position reference (green). Errors are too small to be plotted. *Top*: In this case the source is horizontally 100% linearly polarized. *Bottom*: When the source is vertical the signal changes to the opposite.

the base frequency, and suggests that high frequencies should be avoided, and that the incidence angle should be minimized as much as possible.

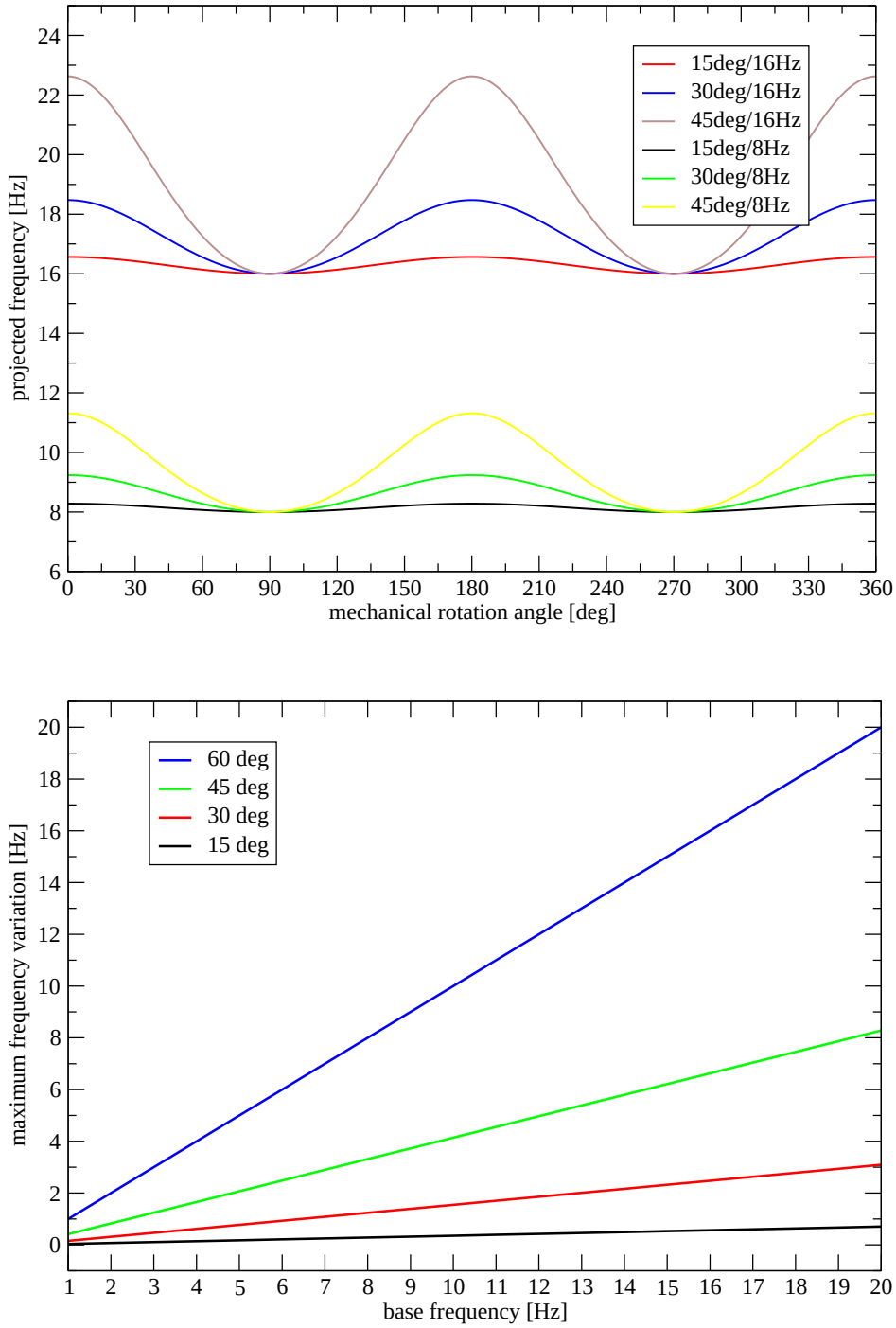

Figure 4.12: Projected angular velocity of the RHWP. *Top*: Values calculated using equation 4.2 at 3 different incidence angles,$15°, 30°, 45°$ for the mechanical frequencies of 8 and 16 Hz. *Bottom*: Maximum variation of the frequency for different values of the incidence angle.

The efficiency of the RHWP is usually determined by comparing the transmission of the system at the minima and at the maxima with the transmission measured by replacing the RHWP with a mirror, using a chopper to modulate the signal at the

same frequency. In our case, given the modulation of the amplitude seen above, we can just compare the values measured at positions where the projected frequency has the minima, namely at 90° and 270°.

As we acquire the two polarization components simultaneously, we can use this double information to calculate the efficiency of the RHWP. Let's assume the source is 100% horizontally linearly polarized. It can be described by the four Stokes parameters $I = Q = I_0,\ U = V = 0$. When we replace the RHWP with a plane mirror and we use the chopper to modulate the intensity of the radiation, the bolometer signals (after relative gain and efficiency correction) will be

$$H_{\mathrm{C}} = I_0 \cos \omega_{\mathrm{C}} t \tag{4.3}$$

$$V_{\mathrm{C}} \simeq 0 \tag{4.4}$$

where H, V represent the horizontal and the vertical channel respectively and ω_{C} is the chopper frequency. When we use the actual RHWP to modulate the radiation instead, the output signals will follow equations (2.13) and (2.14), where in our case $Q = I_0$ and $U = 0$. After relative gain and efficiency correction, we have

$$H_{\mathrm{R}} = \frac{1}{2} I_0 \cos 4\omega_{\mathrm{R}} t \tag{4.5}$$

$$V_{\mathrm{R}} = -\frac{1}{2} I_0 \cos 4\omega_{\mathrm{R}} t \tag{4.6}$$

where ω_{R} is the RHWP mechanical angular frequency. We now consider the difference and the sum of the two:

$$(H_{\mathrm{R}} - V_{\mathrm{R}}) = I_0 \cos 4\omega_{\mathrm{R}} t \tag{4.7}$$

$$(H_{\mathrm{R}} + V_{\mathrm{R}}) \simeq 0 \tag{4.8}$$

When the chopper frequency is $\omega_{\mathrm{C}} = 4\omega_{\mathrm{R}}$ then we can calculate the efficiency of the RHWP by a direct comparison of the two pairs of signals. The maximum transmission will be given by $(H_{\mathrm{R}} - V_{\mathrm{R}})/H_{\mathrm{C}}$ while the minimum transmission will be $(H_{\mathrm{R}} + V_{\mathrm{R}})/H_{\mathrm{C}}$ because equation (4.8) is an estimation of the maximum attenuation of the signal. The plot on the top of figure 4.13 shows these signals as acquired in the lab. We see that $(H_{\mathrm{R}} + V_{\mathrm{R}})$ is always of the same order of V_{C}. In the positions where the polarization is modulated by the RHWP exactly at $4\omega_{\mathrm{R}}$, $(H_{\mathrm{R}} - V_{\mathrm{R}})$ is very close to H_{C}, being just

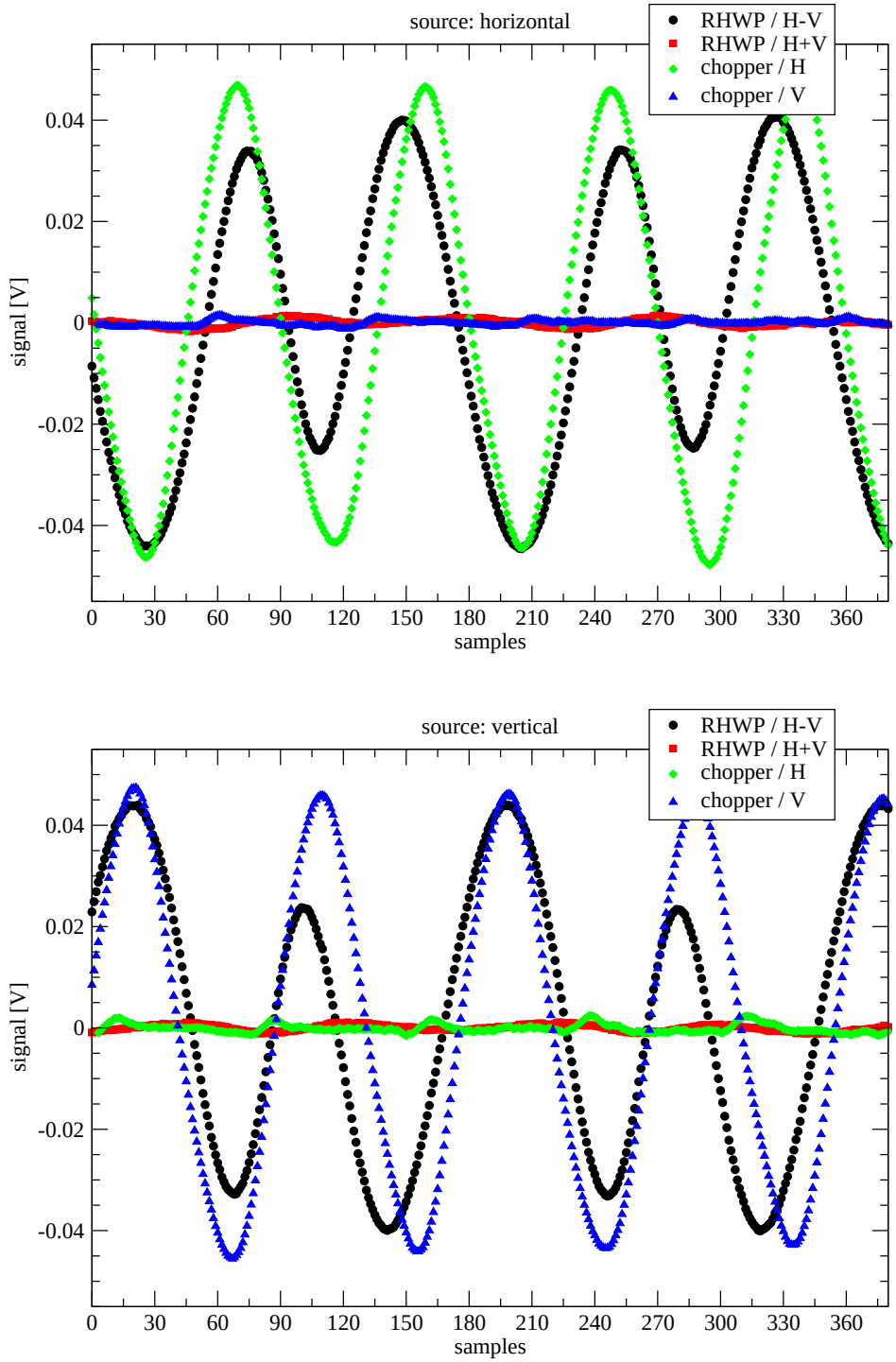

Figure 4.13: Signals produced by the spinning RHWP (see equations (4.7) and (4.8)) are plotted together with the signal produced by a chopper spinning at the polarization modulation frequency. *Top*: In this case the source is 100% horizontally polarized. *Bottom*: The source is vertically polarized.

a bit smaller. On the bottom of the same figure the data acquired when the source is vertically polarized are shown. These result are summarized in tables 4.1 and 4.2.

source pol.	H_C[mV]	V_C[mV]	$(H_R - V_R)$[mV]	$(H_R + V_R)$[mV]
H	45.22	0.51	44.35	0.74
V	0.81	45.87	44.10	0.63

Table 4.1: Measured signals (r.m.s.) in the two configurations of the source when the radiation is modulated by the chopper and by the 146 mm RHWP.

source pol.	$(H_R - V_R)/V_C$[%]	$(H_R + V_R)/V_C$[%]
H	98.1	1.6
V	96.1	1.4

Table 4.2: Maximum and minimum transmission of the 146 mm RHWP in the two configurations of the source.

4.3 Design of the 246 mm half-wave plate

The test of the 146 mm RHWP at the HHT telescope in May 2001 was so satisfactory that we decided to make a new, much larger, RHWP that would fit the whole bolometer array. During the second half of the year 2001 we designed a new RHWP incorporating the new 246 mm wire-grids that were in preparation (see section 3.5). Redesigning the RHWP and the wire-grids at the same time gave us the chance to optimize the various parts. For example, it was possible to design the rings of the wire-grids so as to be mounted directly on the mirror plate. This way we reduced to only two the number of surfaces to be machined with high accuracy: the mirror plate and the upper side of the ring. The experience gained at the telescope with the 146 mm RHWP had given us some ideas about how to improve the system. One problem that we found was produced by the micrometric screws. Due to the friction with the air during fast spinning, the screws slowly loosened their positioning, detuning the half-wave plate slightly. We decided to solve this problem by using bigger and more reliable micrometer heads, in the new design. We chose three Mitutoyo 148-803 screws: these have a spherical face and a spindle lock, a resolution of of 10 μm and an accuracy of 2 μm. The part of the screws that juts out from the backside of the mirror plate is now 2 cm longer and we had to compensate for this in the new mirror design.

During reduction of data acquired with the 146 mm RHWP we found it inconvenient

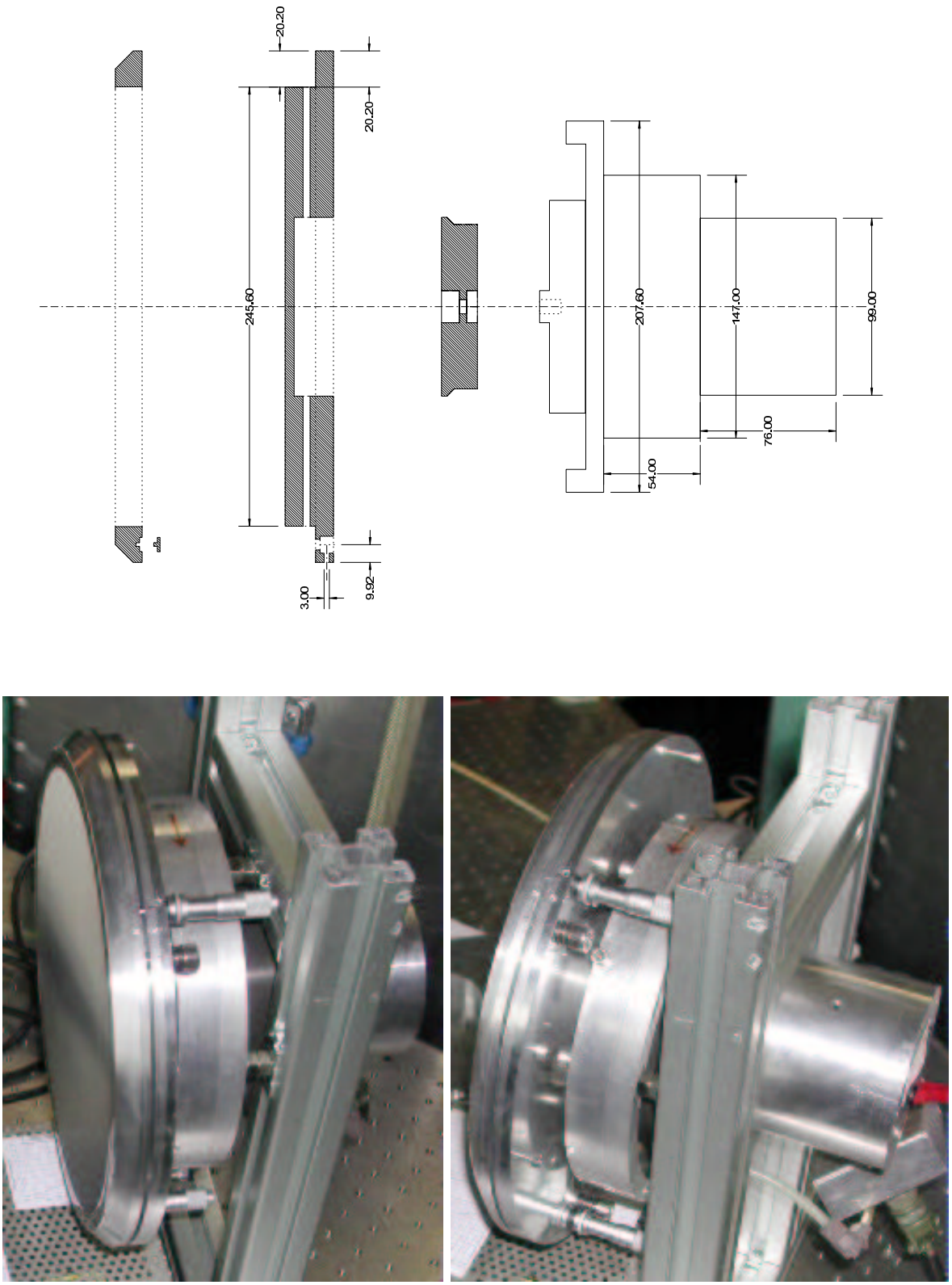

Figure 4.14: The 246 mm RHWP. *Top*: Drawing of a section of the system. From left to right: the ring of the wire-grid; the mirror plate; an interface to fix the mirror plate to the bearing; the air bearing. *Bottom*: Two pictures of the system mounted in the lab.

to have only one set of reference marks for both relative and absolute angular position. Therefore we added a second set of marks. This is actually made of one single mark, producing one period per turn of the RHWP, with the duration of the logical level being 180°. This way we also have a double set of information about the position angle of the plate and this can improve the accuracy.

Chapter 5

The polarimeter at the telescope

5.1 Introduction

The lab tests done in April 2001 were promising, and it was time to check the performance of the polarimeter at the telescope. The choice of the telescope was not difficult. Our bolometer development group at MPIfR has relatively good access to two big radiotelescopes, for technical tests: the IRAM 30 meter Millimeter Radio Telescope (MRT) on Pico Veleta, in Spain, and the Heinrich-Hertz 10 meter Submillimeter Telescope (HHT) on Mount Graham, in Arizona. The polarimeter can in principle be tuned over a wide range of wavelengths, but high efficiency is, of course, harder to achieve as the wavelength gets shorter. It is clear then, that tests are more significant at the telescope that can work with the shortest possible wavelength. The choice was the HHT, were the MPIfR 19 channel bolometer array at 0.87 mm of wavelength (345 GHz) is in operation.

First light for the polarimeter at the telescope was in May 2001. Unfortunately, the weather conditions were quite bad during that period. Nevertheless, it was a good test of all the components of the polarimeter and we made some first calibrations. We went to the HHT a second time when the new 25 cm RHWP was ready. This was in January 2002 and the weather was much better and we had a couple of nights of excellent atmospheric transmission.

5.2 The Heinrich Hertz Telescope

The Mount Graham International Observatory (MGIO) is located on Emerald Peak of Mt.Graham, approximately 120 km north-east of Tucson, Arizona (USA).

The Heinrich Hertz Submillimeter Telescope, operated as a joint facility for the University of Arizona's Steward Observatory and the MPIfR of Bonn, is part of the MGIO, together with the Vatican Advanced Technology Telescope (VATT) and the Large Binocular Telescope (LBT), still under construction.

The geographical coordinates are:

- Longitude: 109° 53′ 28″.48 W
- Latitude: 32° 42′ 05″.8 N
- Altitude: 3185.963 m

The telescope has the following geometry:

- Main reflector: paraboloid D=10 m F/D=0.35
- Subreflector: hyperboloid d=0.69 m Fe/D=13.8
- Focus: two Nasmyth foci (one outside each elevation bearing)

The main reflector is supported by a spaceframe made of *carbon fiber reinforced plastic* (CFRP) tubes with Invar steel joints (3040 kg total weight). The reflector is composed of 60 panels arranged in three rings. The center ring has 12 panels and the outer two rings have 24 each. Surface accuracy has been measured by holography observations. The dish has an r.m.s. deviation of 15 microns over the entire surface, as determined by holography measurements. The panels have CFRP skins on a Aluminum honeycomb core (110 Kg weight). Aluminum foil is bonded to the skin on the reflective side of the panel. The subreflector is supported by CFRP tube quadrupod (110 kg weight) and it is a single mirror made of CFRP.

Some data about the telescope mount:

- Altitude/Azimuth - steel with thermal insulation
- Absolute pointing accuracy: 1 arcsecond r.m.s.

Figure 5.1: The Heinrich Hertz Telescope

- Tracking precision: 0.2 arcsecond r.m.s.
- Azimuth range: $\pm$ 270 degrees
- Elevation range: -2 degrees to 91 degrees
- Slew speed: 60 degrees/min

The telescope is scheduled for around-the-clock observing for 10 months of the year, with the remaining time, during summer, used for long term maintenance.

5.2.1 Receivers

The HHT is sheltered by a co-rotating dome, which also houses two receiver laboratories, one around each Nasmyth flange, and the telescope control room. In the left laboratory are the heterodyne receivers while the right one is devoted to bolometers. The receivers are mounted on flanges that are not connected to the building but rather to the telescope assembly, thus they move with the telescope. Between the two receiver laboratories, located in the Cassegrain room, is the tertiary mirror that can send the beam to either the right or left flange. It is necessary to change its orientation when changing from spectrometers (heterodyne receivers) to bolometers. Experiments made with the tertiary mirror show that it has an extremely high degree of repeatability in mirror location and changing the mirror does not affect pointing for any of the receivers.

During our observations there were two receivers mounted on the right flange: the Hot-Electron Bolometer (HEB) receiver and the MPIfR 19-channel bolometer array (see figure 5.2). Despite its name, the HEB is not a bolometric continuum system but rather a sophisticated heterodyne receiver for THz frequencies.

The HEB shares the right Nasmyth focus with the MPIfR 19-channel 345 GHz (870 μm) bolometer array installed in March 2000 by the Bolometer group of the MPIfR. The array operates at a temperature of 300 mK, inside a commercial ^{4}He Infrared Lab cryostat[1] model HDL-8, equipped with a very compact ^{3}He sorption cooler developed in France (Torre & Chanin, 1985).

The system is optically coupled to the telescope by means of two lenses, made out of high-density Polyethylene (HDPE), in Gaussian confocal configuration. The

[1]Infrared Laboratories, Inc., 1808 East 17th Street, Tucson, Arizona 85719, USA

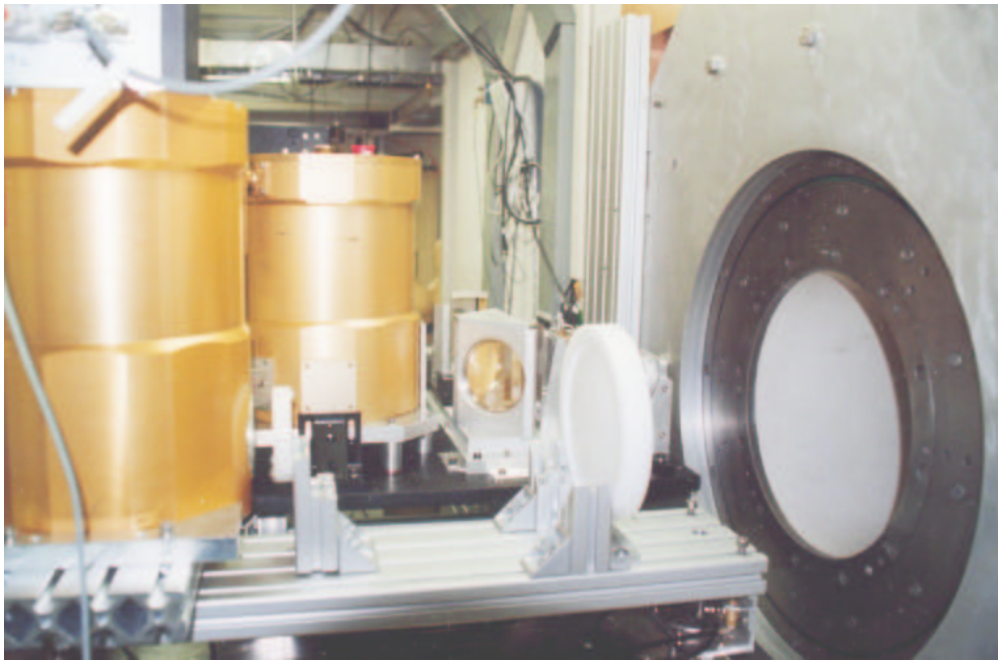

Figure 5.2: The 19 channel receiver is the golden cryostat on the left of the picture, aiming straight into the Nasmyth tube through two HDPE lenses. In the background, the HEB cryostat is visible .

bolometers are DC biased and AC coupled to a special low noise 20 channel FET-amplifier. The central channel (also called channel 1) is, at the same time, AC and DC coupled, allowing measurements of absolute total power, for example to measure the atmospheric emission. Figure 5.3 shows the position of the bolometers in the array

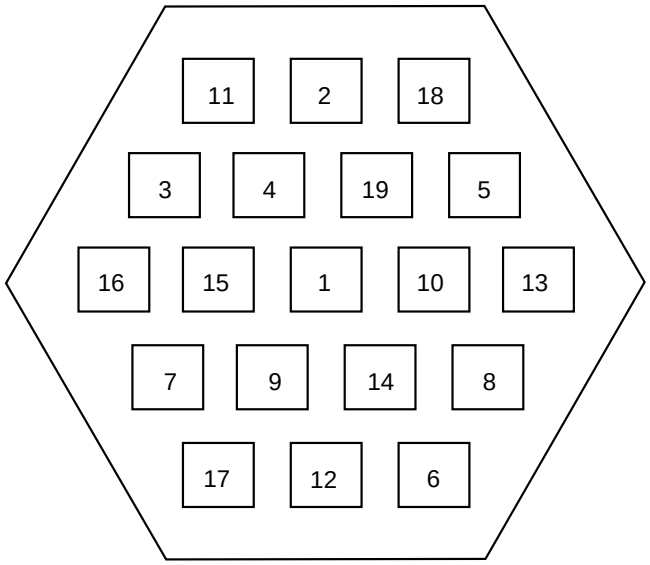

Figure 5.3: Layout of the HHT 19 channel bolometer array. The numbers refer to the data acquisition channels. See also figure 1.4.

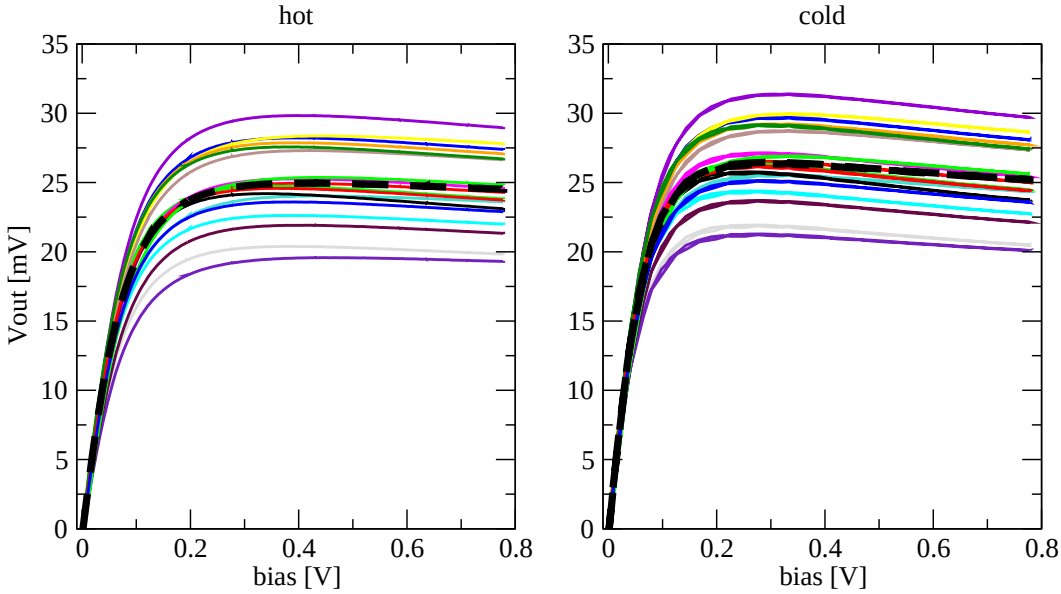

Figure 5.4: Load curves of the 19 bolometers of the array, taken at the telescope on May 4th 2001, with hot (left) and cold (right) load. The thick dashed line represents channel 1. See also figure 4.4.

and the corresponding channel number. The responsivity changes a little from one bolometer to the other and figure 5.4 shows the load curves for all the bolometers on the array in the two cases of hot (300 K) and cold (77 K) load. We see that most of the bolometers behave in the same way and only a few of them have much higher or lower responsivity. We will compensate for these differences using appropriate gain correction factors (see section 6.2.3). Another important parameter is the spectral response of the bolometer. We will have to take it into account during the data reduction. I will discuss it later, in section 6.2.4.

5.2.2 The wobbler

Astronomical observations from ground based telescopes in the millimeter and submillimeter range of wavelengths are strongly compromised by fluctuations of the atmospheric emission. This is especially true for broadband measurements with sensitive detectors like bolometers (see also section 1.3). In order to subtract the atmospheric contribution from the measurements, dual beam techniques are commonly used. One option is to use a chopping secondary mirror, the so-called *wobbler*, which alternatively points the beam to two adjacent positions on the sky (see figure 5.5). Instead of directly measuring a signal, one measures the difference between the two positions on the sky

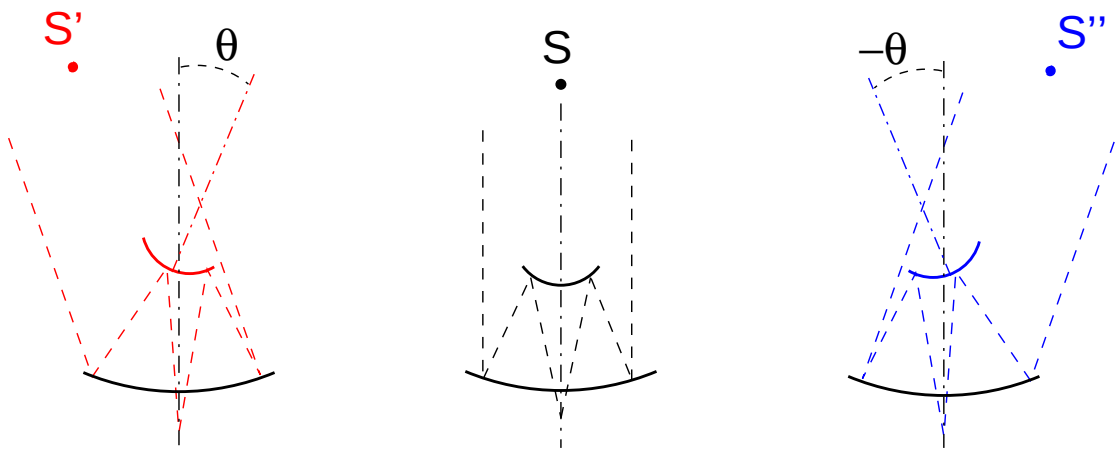

Figure 5.5: *Center*: Standard configuration of a Cassegrain telescope. The beam points to the source S on the sky. *Left*: Rotating the secondary mirror by an angle θ the beam will point to the source S', without any need to move the telescope. *Right*: Wobbling the secondary mirror between $-\theta$ and θ, the beam will switch between the two sources S' and S''. The angular distance of the two sources is one *beamthrow*, 2θ.

by quickly changing the direction of observation by tilting the secondary mirror. After phase sensitive detection, spatial and temporal emission fluctuations should cancel, at least to first order.

Since the introduction of the EKH algorithm (Emerson et al., 1979) this mapping technique has been applied even to extended sources which are many times larger in angular extent than the separation of the beams. Invented originally for single pixel detectors, this method is used today even with large arrays of detectors.

Despite the great success of this technique, a wobbling secondary mirror has some major disadvantages. A fast, precisely moving mirror is quite a technical challenge, particularly for large telescopes. Therefore, in practice only low modulation frequencies are possible. The mechanics of a wobbling mirror usually allows only a certain direction of movement, which restricts the coordinate system of the observing modes. It is also a source of vibrations that can lead to microphonics in the signals of highly sensitive bolometers. Small asymmetries in the wobbling can lead to large offsets, due to the different optical paths of each beam.

The HHT has a wobbling secondary mirror that, despite its 69 cm diameter, can wobble up to 25 Hz when the beamthrow is 25 arcseconds. During normal observations with bolometers, however, the beamthrow must be much larger, to avoid overlap of the bolometer beams in the two adjacent positions. The movement is restricted to the

azimuthal direction. The largest possible beamthrow, due to mechanical limitations, is 240 arcseconds and the typical wobbling frequency for such a large throw is 2 Hz.

5.2.3 Polarization modulation

As already stated, one of the features that makes the PolKa polarimeter different from others is the fast spinning technique: the modulation of the incoming radiation is produced by the fast spinning RHWP. This technique has the following characteristics:

- Given the factor of four between the frequencies of the mechanical rotation and the polarization modulation, the latter can easily be pushed to frequencies much higher than typical wobbler ones.
- There are no restrictions on the scanning direction.
- A wobbling secondary mirror is always off-axis and this produces a relevant amount of spurious polarization; in our case the mirror is always on-axis.
- Small asymmetries in the wobbling can produce artifacts and spurious polarization; we don't have these problems.
- We separate the polarized component from the unpolarized background and at the same time we produce the modulated signal necessary for AC coupled bolometers and phase-sensitive detection.

5.3 Observing modes

The 19-channel bolometer array is used at the HHT to perform flux measurements of the continuum emission at 0.87 μm. There are essentially just two observing modes: `On-Off` (`OO`) and `On-the-Fly` mapping (`OtF`) (see also section 1.3). As already mentioned, in the design of PolKa we tried to minimize the modifications to the total power system. On the other hand, all the telescope's facilities are designed to perform standard flux measurements and the implementation of a polarimeter is not straightforward. We had to find the way to do polarization measurements using the telescope's procedures. By writing a set of macros to force the standard total power software

to satisfy our requirements, we transposed the observing modes in the polarization version.

5.3.1 Total power `On-Off` (`TPOO`)

This is the preferred observing mode for point-like sources i.e. sources whose angular size is smaller than the beam of a single channel ($\sim$ 20 arcsecond). In this case, the signal coming from the source is concentrated in one single channel and the other 18 channels will monitor the sky around the source. During the data reduction it is then possible to remove sky noise fluctuations by subtracting the correlated part of the signal detected in the outer 18 channels from the signal of the channel aiming at the source. One can, of course, observe extended sources in this way but then it will not be possible to eliminate the sky noise correlated across the array. This observing mode can give good sensitivity even when then the weather is not too stable, and detections of sources with fluxes of the order of a few tens of mJy are possible in a relatively short integration time. A typical `TPOO` scan is made with an even number of subscans of equal duration. During the observation, the telescope is moved subscan by subscan, switching alternatively between two positions on the sky with an angular separation equal to the wobbler beamthrow (see figure 5.6). For example, if even subscans have

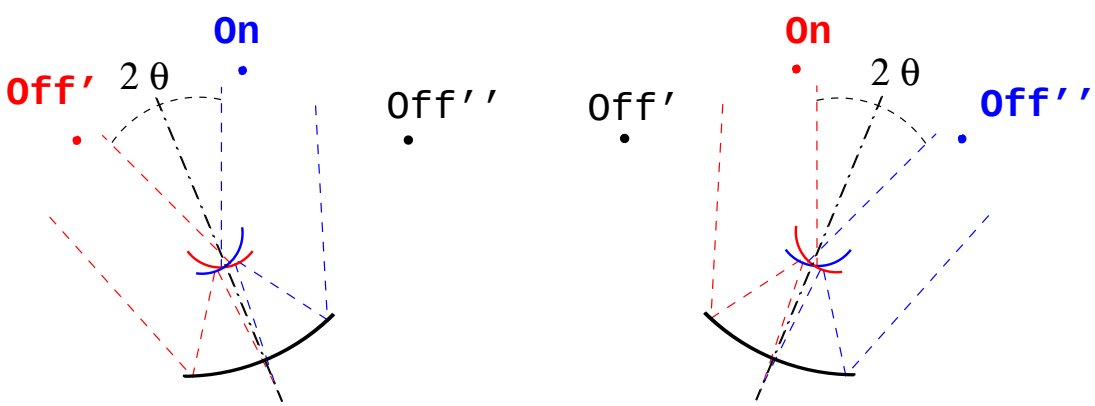

Figure 5.6: Total power `On-Off` observing mode. *Left*: During the first subscan the wobbler alternates the signal coming from the source, `On` position, to the signal coming from the blank sky position `Off'`, at the angular distance of one beamthrow. *Right*: After completion of the first subscan, the telescope moves of one beamthrow in azimuth. During the following subscan, the wobbler alternates the signal coming from the source to the signal coming from a different blank sky position `Off''`, still at angular distance of 1 beamthrow but on the opposite side. See also figure 5.5.

the source in the left wobbler beam, odd subscans will have the source in the right beam, while the other beam will always be on the blank sky. In the end, the resulting signal will be the weighted mean of the differences between signals acquired at the two positions of the telescope. Thanks to the symmetry of this procedure, eventual asymmetries in the wobbling will be averaged to zero during the data reduction. A `TPOO` is usually made of 8 or 16 pairs of subscans, each subscan can last 10 or 20 seconds and the total duration of a complete scan is usually less than 15 minutes, including the time used to move the telescope. Notice that during `TPOO` scans the source is always off-axis.

5.3.2 Total power `On-the-Fly` (`TPOtF`)

In the `On-the-Fly` observing mode, the telescope is continuously moved in azimuth and in steps in elevation so as to scan a large area of the sky. This is useful to map extended sources (see figure 5.7). During the scan, the wobbler produces a modulated signal but only the difference of the signals detected in the two wobbler positions is acquired by the total power acquisition computer. Scan size and duration depends on the size of the source to map and on the chosen beamthrow, the latter being large enough to beam overlap. The scanning velocity must be carefully calculated so as to avoid undersampling of the source. For example, given a wobbler frequency of 2 Hz and a beam size of about $20''$, the scanning velocity should never exceed $20''$ per second, as that produces one data point every half beam. Considering that the scanning is usually in the same direction as the wobbling, a smaller velocity is recommended to avoid smearing of the map in azimuth direction. A typical value for the scan velocity is then $8''$ per second. This value is the same as that recommended for the separation in elevation between subscans. The scan in figure 5.7 shows how the use of the wobbler increases the size of the sky area to be scanned by the telescope and consequently the time needed to complete a `TPOtF`. This is because the telescope points all the time in the position centered between the two wobbler beams and therefore, to completely scan the selected area, the telescope has to move half a beamthrow further along the azimuth direction on both sides. The result is that the azimuth size of the area to be scanned is increased by a beamthrow. The scan in figure 5.7 is made of 45 subscans, each one $560''$ along the azimuth direction, and it requires more than 55 minutes to be

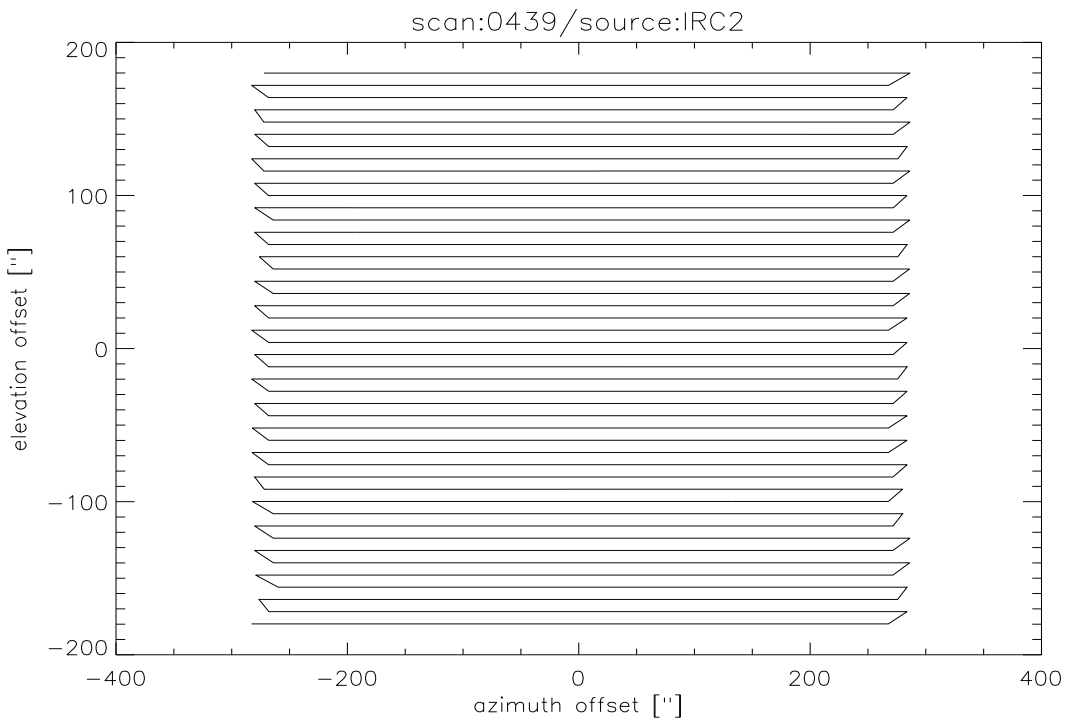

Figure 5.7: Positions of the telescope on the sky during a total power `On-the-Fly`. In this example the size of the resulting map is $360'' \times 360''$. Given a wobbler throw of $200''$, the telescope has to scan $560''$ in azimuth. The area scanned by the telescope is a rectangle $560'' \times 360''$.

completed at $8''$ per second. Notice, once again, that during `TPOtF` scans the beam is always off-axis, although symmetric to the optical axis in the two wobbler phases.

5.3.3 Other total power observing modes

Apart from the `TPOO` and `TPOtF`, there are three other total power observing modes that are not very important from a scientific point of view but absolutely essential for any observing session.

- `Pointing`: At the beginning of any observing session it is important to check the pointing accuracy. The `pointing` procedure consists of one or more scans in azimuth and elevation across a bright point-like source, such as Mars or a strong quasar. Right after the scan an automated task performs a fit of the data suggesting the best values to correct the pointing in the two directions.

- `Focus`: After a `pointing` it is advisable to check the focus of the telescope. This can change because of deformations in the telescope's structure at different

telescope positions due to gravity and due to temperature variations. During the `focus` procedure, the secondary mirror is moved up and down along the optical axis at six different positions while pointing on a bright source in the sky. At the end of the scan, an automated task performs a fit and suggests the correction. After a `focus` it is recommended to check the pointing again, thus the `focus` is usually done between two `pointings`.

- `Skydip`: In the submillimeter range of wavelengths, the Earth's atmosphere has significant opacity, which may change rapidly in time. It is very important to check the atmospheric opacity on a regular basis, at least once every 2 hours. The `skydip` procedure consists of pointing the telescope at seven different angles of elevation while acquiring the signal in the channel that is DC coupled. This gives an absolute measure of the atmospheric emission at different air-masses. From this set of data it is possible to calculate the zenithal atmospheric opacity that will be used to calibrate the data.

5.3.4 Polarization `On-Off` (`POO`)

This is the polarization observing mode used to perform measurements of polarized flux or detection experiments on point sources. The observing strategy is quite different from the corresponding total power mode. We are not using the wobbler and consequently we cannot apply the standard `OO` telescope control procedure. One major difference is that during `POO` the telescope has to point directly at the source or to the `Off` reference position, while in the `TPOO` mode the telescope points in between the two wobbler beams. One `POO` scan is made of an even number of subscans, one half of them acquired while pointing on the source, the other half on a reference blank sky position. During the observation, the RHWP spins, producing the modulated polarization signals which are recorded by the purpose built polarization acquisition system. In parallel, the telescope's data acquisition computer is logging the coordinates and other telescope information. The data will be reduced by extracting the polarized signal from each subscan and subtracting the signals of the `Off` subscans from the signals of the `On` subscans. The final value of the measurement is the weighted mean of the differences. After the reduction of the data, a `POO` scan gives the two measured Q and U Stokes

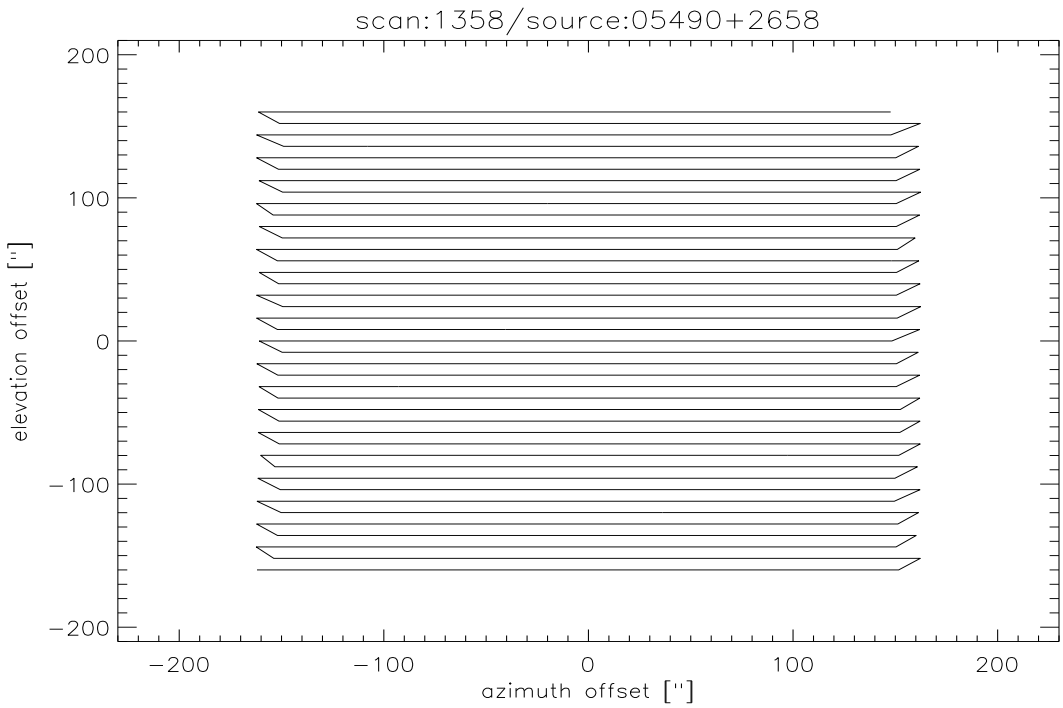

Figure 5.8: Positions of the telescope on the sky during a polarization `On-the-Fly` map. In this example the size of the resulting map is $320'' \times 320''$. The area scanned by the telescope is a square $320'' \times 320''$. For comparison, see figure 5.7.

parameters for each channel of the array.

5.3.5 Polarization `On-the-Fly` (`POtF`)

This observing mode follows the same strategy of the equivalent `TPOtF`, but with some important differences. As in total power mapping, the telescope scans the sky in subscans along the azimuth, changing the elevation in steps (see figure 5.8). During the scan, the RHWP produces a modulated signal, sampled at very high frequency by the polarization data acquisition system. In parallel, the standard total power acquisition computer is used to acquire the information about the coordinates, simulating a normal total power observation. In this way we avoid the problems related to the use of the wobbler and the scan size will be the true size of the resulting map. The duration of the scan depends just on the size of the map and on the chosen scanning velocity. Even though the polarization data can be acquired up to 2000 samples per second, the telescope data are sampled at the mechanical frequency of the RHWP which is never more than 4 Hz. The limitation is mainly due to the telescope's acquisition computer that is optimized to acquire data at the wobbler frequency, 2 Hz, and cannot sample

faster than 4 Hz. The scanning velocity must then be calculated bearing in mind this limitation: again, a good value is 8″ per second and 8″ for the separation in elevation between subscans. The scan in figure 5.7 is made of 40 subscans, 320″ each along the azimuth direction, and it takes about half an hour at 8″ per second. Notice that in principle, during a `POtF` one could scan along any direction other than the azimuth and that the beam is always on-axis. After the reduction of the data, a `POtF` scan produces two sets of values, the two Q and U Stokes parameters maps.

5.4 The data acquisition

PolKa produces a polarization modulation acting on the Q and U Stokes parameters. The information about the first Stokes parameter, the total intensity of the source, is lost during polarization measurements. Thus, to calculate the normalized Stokes parameter and the degree of polarization, we need some independent measurement of the total intensity of the source. We take advantage of the ease at which it is possible to switch between polarization modes and total power modes, to perform a total power measurement before or right after each of the polarization observations.

For this reason, we need to alternate between the total power data acquisition and our polarization data acquisition.

5.4.1 The total power backend DRUMBEAT

The telescope's backend, called *DRUMBEAT* (Digital Recording Using Multichannel BackEnd with AT), is a 64 channel backend derived from the Effelsberg 80 channel backend. The signals coming from the bolometers are digitized by voltage-to-frequency converters (VFC) that produce a pulse train whose frequency is proportional to the input voltage.DRUMBEAT integrates these pulses, transforming them into blocks of data that are transferred and stored into the data reduction computer. During total power modes, the wobbler moves at 2 Hz and it stays in one position for about 210 ms, with the time to move from one position to the other being about 40 ms.

For one single data point and for each bolometer of the array, DRUMBEAT integrates the signals during each of two consecutive wobbler phases and calculates their difference. The calculated value is labelled with a timestamp, which is derived from

the time signals of the station clock. The data are sent via Ethernet to the reduction computer where they will be merged with the information coming from the telescope's control software (coordinates, offsets, sidereal time and so on) and stored in a file. The synchronization of the data acquisition with the wobbler is controlled by two reference signals that are fed from the wobbler into the computer (see section 5.4.3). The total power backend is also used for all the other three observing modes, `pointing`, `focus` and `skydip`.

5.4.2 The polarimeter backend PolKABBA

Polarization signals are modulated at a much higher frequency than the total power signals. Furthermore, in order to fully sample one polarization cycle, the Nyquist theorem demands a sampling frequency at least four times as high. For example, if the RHWP rotates at 4 Hz, the polarization will be modulated at 16 Hz and the data acquisition must sample at least 64 values per second. It is evident, at this point, that there is no way to do polarization observations using DRUMBEAT.

Over almost the same period of time that PolKa was designed, the MPIfR Bolometer group also designed and installed the new backend ABBA (Adc Backend for Bolometer Arrays) at the 30 meter MRT in Spain. ABBA is a commercial off-the-shelf PC with two National Instruments PCI6033E A/D converters plugged into its PCI bus, each with 64 multiplexed input channels. The first test of ABBA was in October 2000 and it became fully operative for the winter observing session of 2001.

The two main reasons for developing a new backend were:

- The installation of the new MAMBO-2 array of 117 bolometers required a number of acquisition channels larger than what was available with the old VFC-based backend.

- A new observing technique, called *fastscanning*, was in development at that time, requiring a fast data acquisition (Reichertz et al., 2001). This technique is now extensively used at the SEST observatory (Swedish-ESO Submillimetre Telescope) in Chile, to map large areas without wobbling the secondary mirror, using the MPIfR 37 channel bolometer array SIMBA (Sest IMaging Bolometer Array).The backend is a VFC-based system and this puts limitations on the number

of bolometers in the array (37 is the maximum) and on the scanning velocity.

Furthermore, ABBA has some other positive points: it is a very compact system, it can be easily upgraded to more channels, it is made of commercial products, requiring very little in-house development and it is less expensive than a VFC-based system with equivalent performance.

The new backend design was fitting our purpose very well and we decided to use an ABBA-clone, called *PolKABBA*, to acquire the polarization data.

The polarization backend acquires 23 signals at a time: they are the 19 AC channels, 1 DC channel plus three reference signals. Each data point is labelled with an absolute timestamp synchronized by the IRIG-B signal of the telescope's GPS receiver. Data are stored in a local hard-disk in 2-byte-integer format. The sample rate used is 512 S/s. When the RHWP rotates at 4 Hz, one polarization cycle has a period of 62.5 ms. We acquire 32 points per cycle. The resulting angular resolution is $2^{\circ}.8$ per point. The time resolution in the data files is $\sim$2 ms. The data acquisition software is written in National Instrument's language, LabVIEW.

5.4.3 Sync and blank

The data acquisition needs to be synchronized to the device that produces the modulation of the signals, in total power as well as in polarization modes.

During standard total power observations, signals coming from the encoders that monitor the position of the wobbler are used to generate a square wave signal, called *sync*, whose upper and lower levels correspond to the two wobbler phases. This signal is fed into the acquisition computer DRUMBEAT and into an electronic delay-box that produces a TTL pulse 40 ms after the rising edge of the sync, called *blank*. The acquisition is triggered by these signals: it will start when the blank pulse is received and will stop when the falling edge of the sync is detected. The synchronization ensures that data are acquired just when the wobbler is stationary in one of the two beams, and avoids acquiring data when it moves.

During a polarization observation, the modulation is produced by the RHWP and the signals generated by the angular reference system can be used to trigger the acquisition (see also section 4.2). Unfortunately, during both telescope tests, the external

triggering was not implemented in the data acquisition software. Instead, PolKABBA, acquires the two reference signals at the resolution given by the sample rate and writes the values in the data files together with the bolometer signals (see figure 5.10). The data acquisition is started manually a few seconds before starting the telescope scan and stopped manually right after completion of the scan. During the scan the acquisition is controlled by the internal clock of the ADC boards. We found this clock reliable with an accuracy better than 100 ns. The reconstruction of the position of the RHWP will then later be performed via software during the data reduction. See figure 5.9 for an example. The sync signal also goes into DRUMBEAT for synchronization of the acquisition of the telescope information. During the data reduction, it will then be possible to merge the data by matching the timestamps of the two data streams.

5.4.4 Acquisition bit

Apart from the bolometer signals, the sync and the blank, PolKABBA also acquires one more TTL signal, the so-called *acquisition bit*. This logical signal stays in its higher level as long as the telescope is moving. When the telescope starts tracking on the source, the acquisition bit falls down to the lower logical level. This information is acquired by the computer and will be restored during the data reduction to divide the scans into subscans. This acquisition strategy gives us full control about the behavior of the various parts of the system involved in the observations. We have full information, with a time resolution of 2 ms, of the conditions of the RHWP and of the telescope for each data point. Thanks to the completeness of our information, we detected some imperfections in the telescope control. For example, figure 5.9 already shows that the length of one subscan is more than 20 s although the command given to the telescope control software was to integrate 20 s per subscan. Moreover, we found, that the amount of time added to the subscans is not regular, changing from one subscan to the other. In some cases, we found that the telescope was not moving at all between two consecutive subscans, changing the order of the `On` and `Off` phases. All this information may be redundant when doing photometry. But in polarimetry we try to detect a signal that, in the best case, is one order of magnitude smaller than the total flux of the source and even a small deviation of the real system from the ideal can affect the results in a significant way.

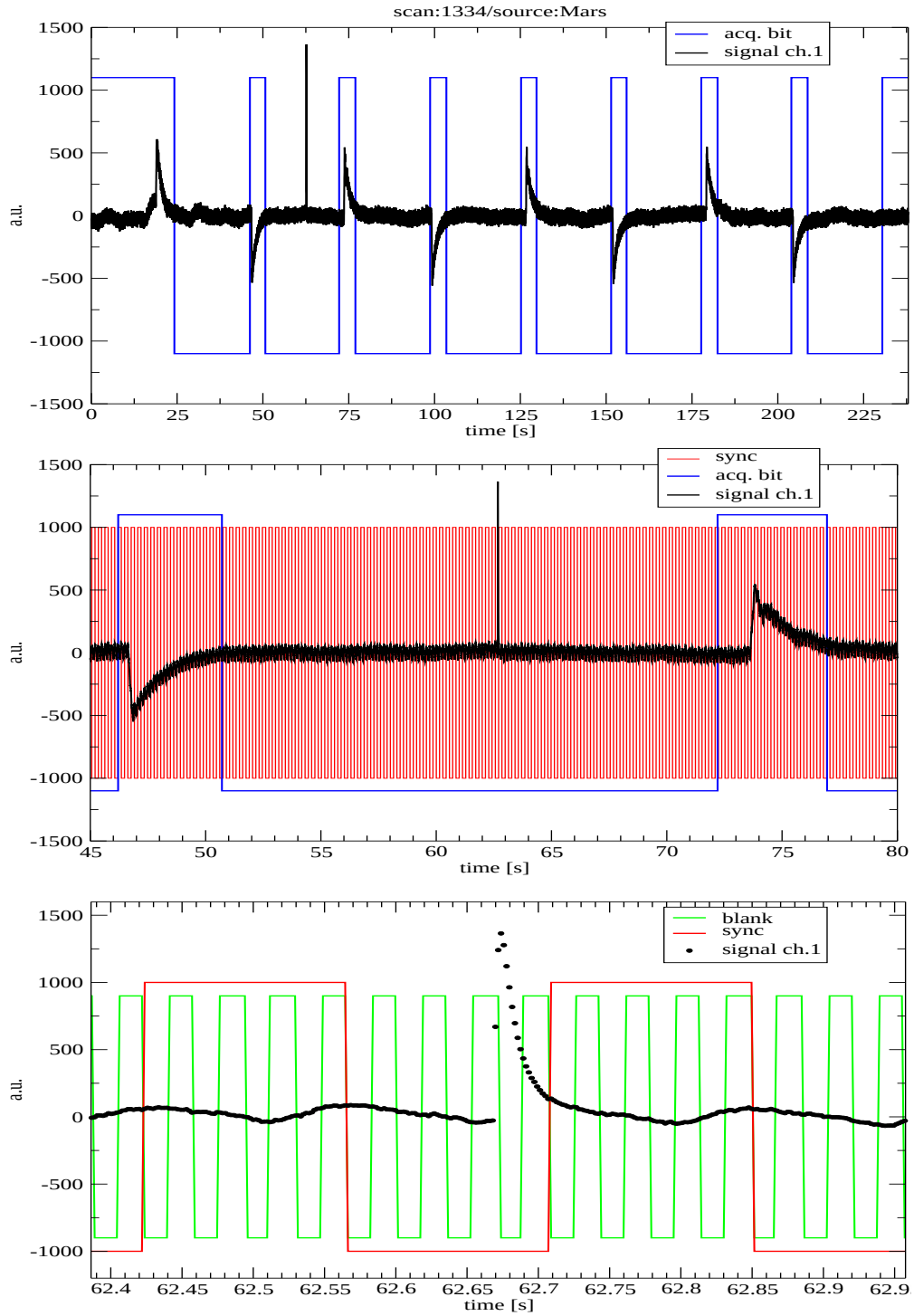

Figure 5.9: Data acquisition example: a POO scan on Mars. The RHWP rotates at 3.5 Hz. *Top*: The central channel raw signal (in black) is plotted together with the acquisition bit (blue). This scan is made of 8 subscans and 122000 data points acquired in 238 s. Notice how the signal jumps up and down when the telescope moves on and off Mars. *Center*: The second subscan. The sync (red) produces one pulse per turn of the RHWP. The plot is 35 s long, 17920 data points, 122.5 RHWP turns. *Bottom*: Two RHWP periods around a spike, just 0.57 s, 292 data points. The bolometer signal shows a spurious feature at twice the frequency of the RHWP, due to systematic effects, that will be filtered out during the data reduction.

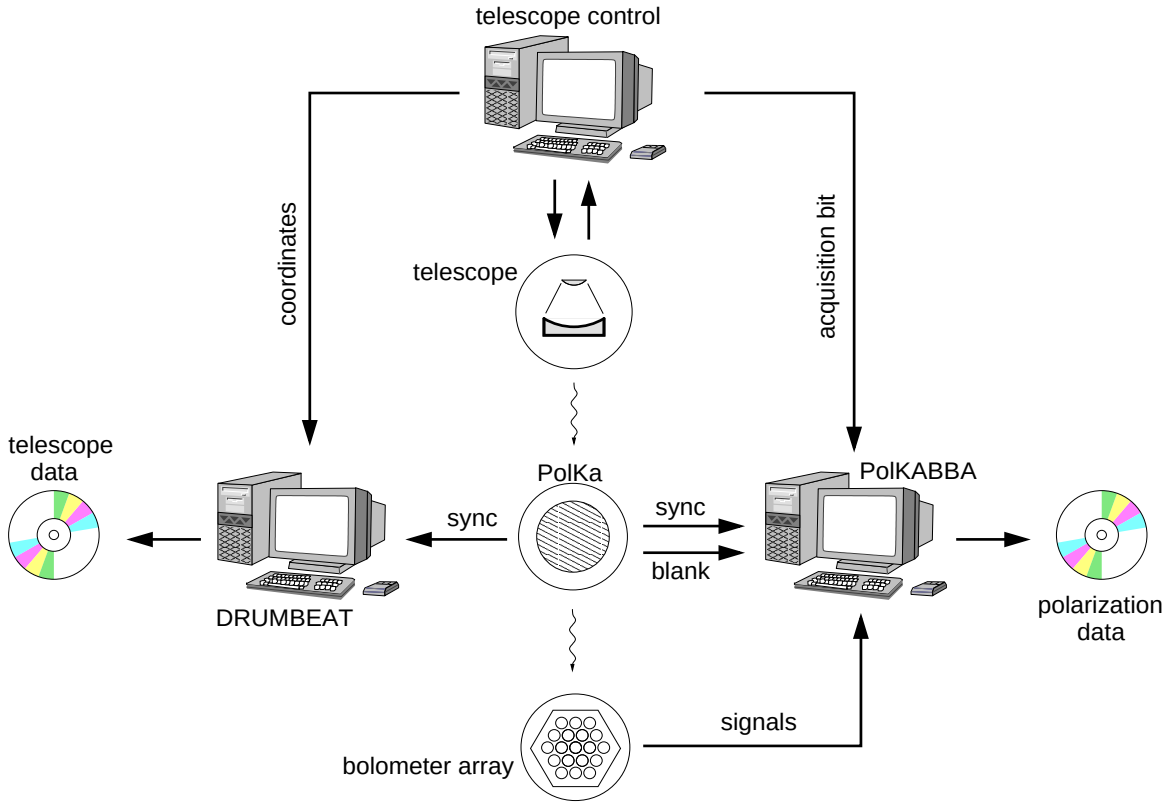

Figure 5.10: Schematic drawing of the data acquisition during polarization observations.

5.5 First telescope run: May 2001

The PolKa polarimeter had its first light at the Heinrich Hertz Telescope in May 2001, with the 146 mm version of the HWP. This was our first experience with the polarimeter at the telescope and we had to start from scratch defining the observing modes and doing the first calibrations. The first week at the telescope was devoted to the installation of the polarimeter and to the consequent alignment of the optical system. During that time the weather was not too bad. But unfortunately, in Arizona, May can mark the beginning of the monsoons. When the polarimeter was ready to observe, the weather changed rapidly and it was raining almost every day. Figure 5.11 shows the atmospheric opacity measured at the observatory during our stay at the telescope. The plot shows the values of the opacity at 225 GHz. For typical conditions, at 345 GHz the opacity is about a factor of five higher (see, for example, figure 5.15). After the first few days of the month there was a change in the general weather conditions, and only very bright sources were observable. Given the bad

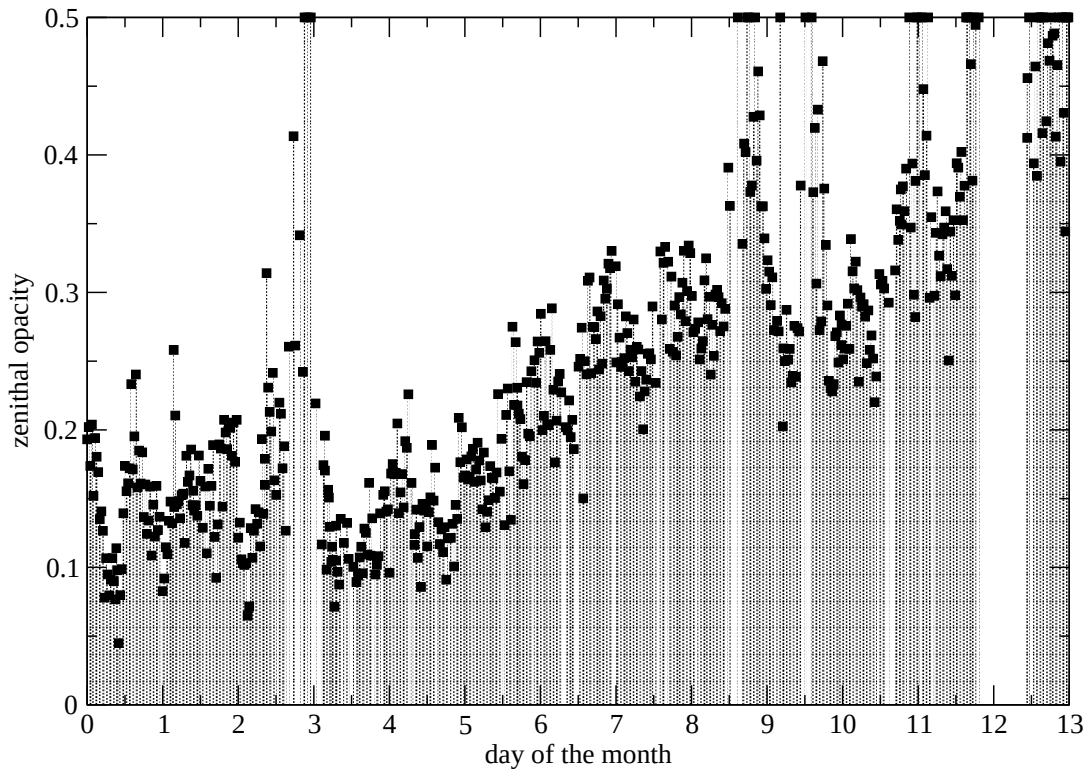

Figure 5.11: Atmospheric opacity at the HHT during our stay at the telescope on May 2001. The polarimeter was ready from the second. Where data are missing the telescope was shut down because of bad weather.

weather, we had time to work in the receiver cabin, to test the instrument and perform calibrations using lab sources. Thus, this telescope session was very useful to check the compatibility of our instrument with the telescope facilities, to test the insertion loss and to perform the first calibrations. The most important result was the calibration of the polarization position angle as a function of the elevation.

Figure 5.12 shows the PME measured at the telescope using a lab source (a Gunn oscillator) in front of the secondary mirror. The plot shows the signal from the central channel of the bolometer array. In this case the RHWP is spinning at the mechanical frequency of 4 Hz. The source is linearly polarized with position angle at 5° from the horizon. This is just one example taken from a set of measurements we made to calibrate the measured Stokes parameters. The telescope was moved in elevation in steps of 5°, starting from 5° and going up to 85°. One more point at 89° was also taken. Data have been demodulated and for each scan a value of the Stokes parameters and of the position angle have been calculated. Figure 5.13 shows the results for the

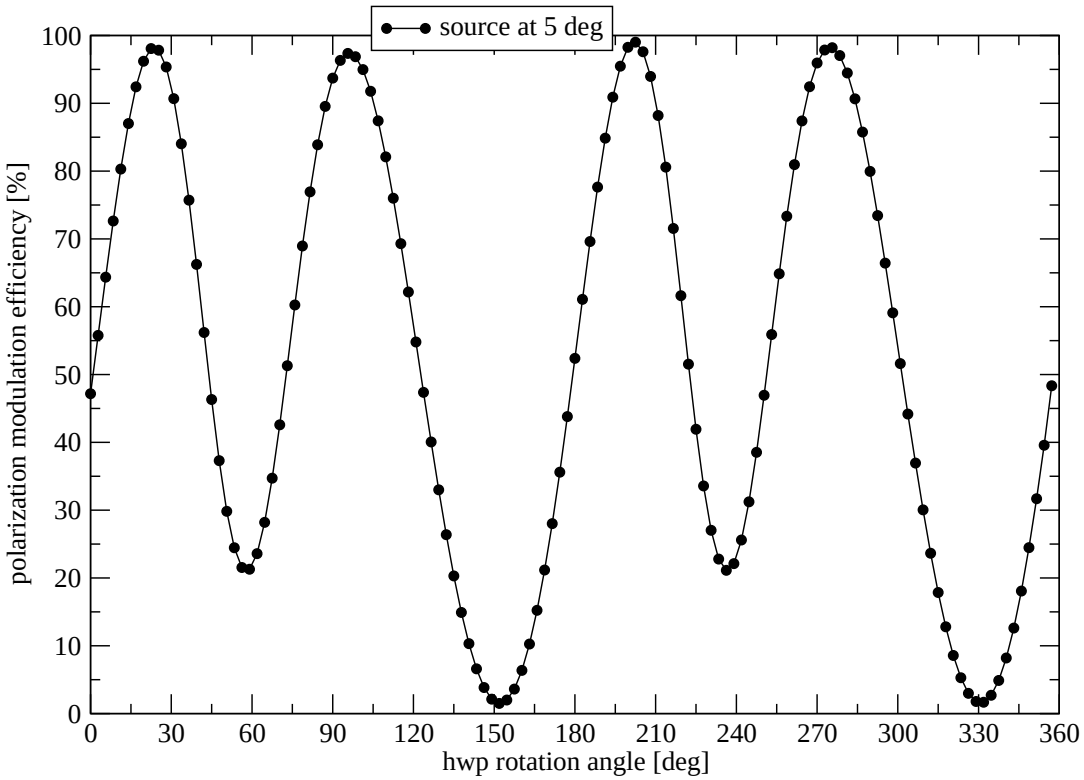

Figure 5.12: PME measured at the telescope using a lab source. Only the signal from the central channel of the array is plotted. Errors are less then 2%.

19 channels. These measurements provide us accurate calibrations of the measured position angle for most of the channels. For example, figure 5.14 shows the calibration of the central channel.

5.6 Second telescope run: January 2002

We were at the HHT for a second time during January 2002 with the new PolKa featuring the 246 mm RHWP. We spent the first days on the installation of the polarimeter and the subsequent alignment of the optical system. This time, in general, we had much better atmospheric conditions than during the first run. Figure 5.15 shows the atmospheric opacity measured at the observatory during our stay at the telescope. Values of the opacity at 225 GHz, measured by the telescope's radiometer, are plotted together with the values measured using the bolometers via the `skydip` procedure.

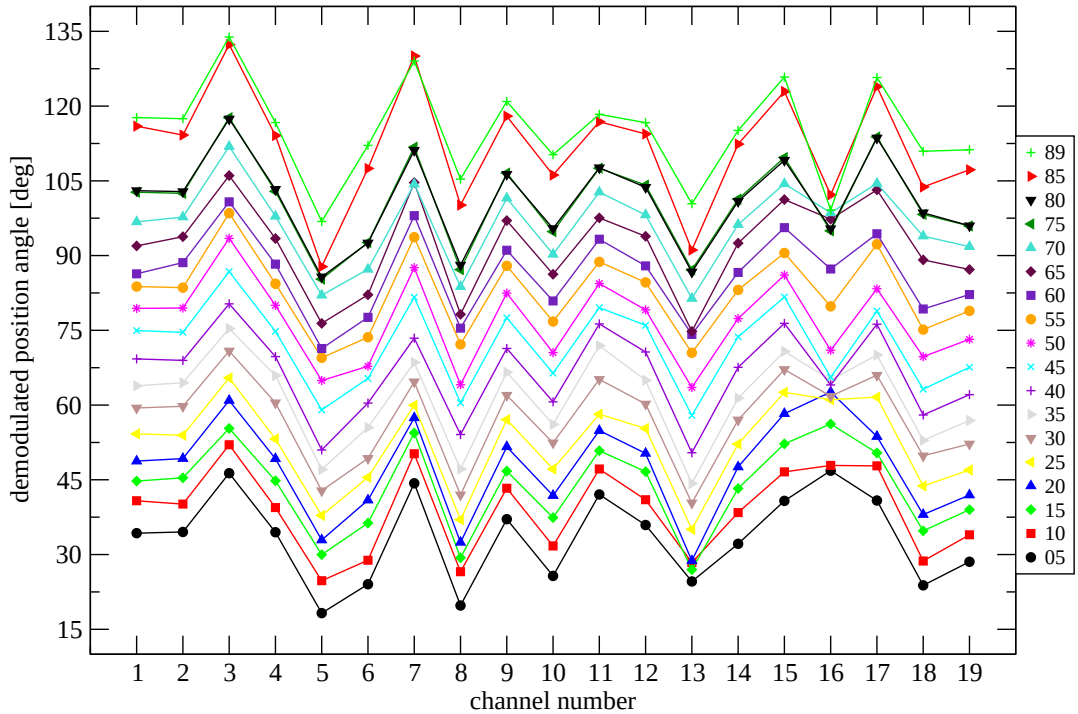

Figure 5.13: Uncalibrated position angle measured for different position angles of the source, for the 19 channels. Channels 3, 5, 7, 8, 13, 16 are not well illuminated by the source because the RHWP is too small and they give less consistent results.

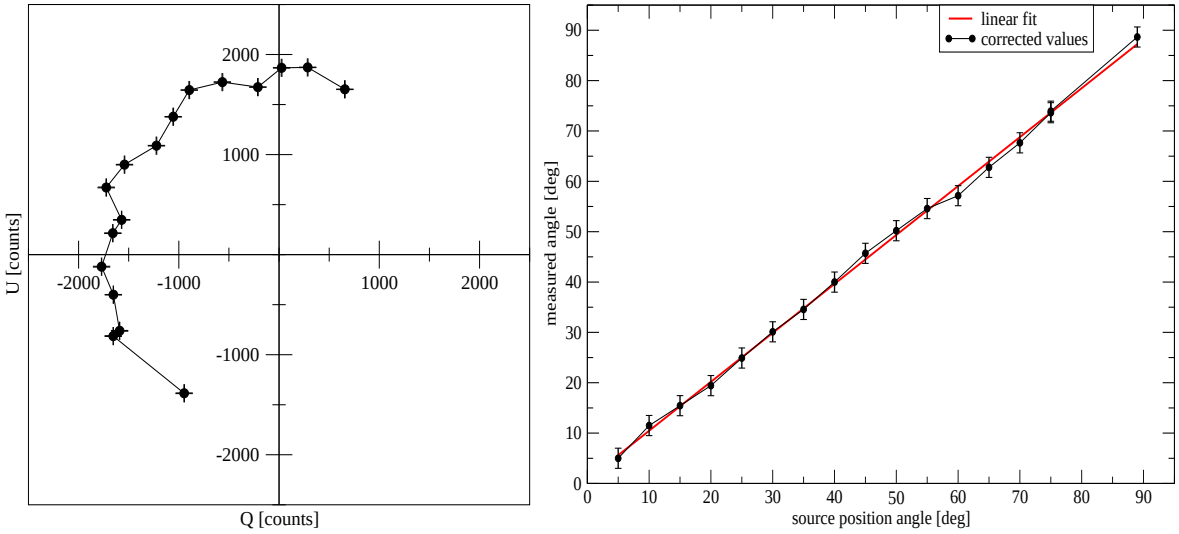

Figure 5.14: *Left*: The measured Stokes parameters, uncalibrated. Notice that when the source rotates by 90° the measured Stokes vector rotates by 180°. *Right*: Measured position angle as a function of the source position angle, after the calibrations. Both illustrations refer to the central channel of the array

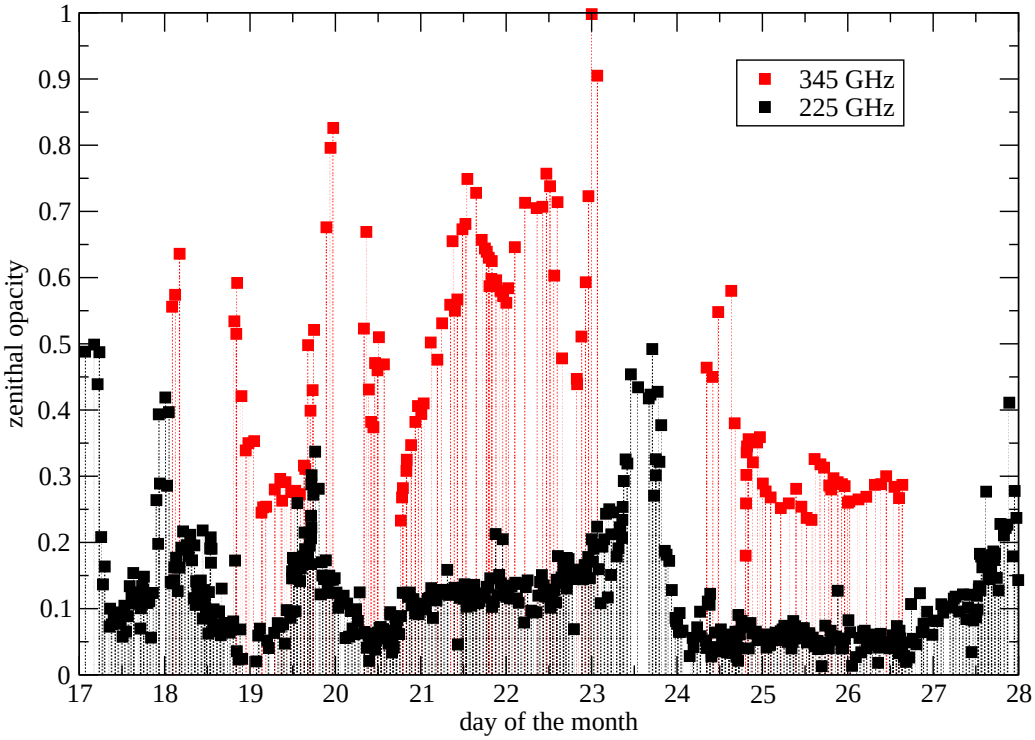

Figure 5.15: Atmospheric opacity at the HHT during our stay at the telescope in January 2002. Red points are the result of the measurements at 345 GHz (`skydip`). See also figure 5.11.

5.6.1 Installation

The polarimeter was installed at the Nasmyth focus of the right receiver cabin. We had to remove the HEB receiver from the focal plane and to rotate the optical bench of the 19 channel bolometric receiver by 90° . Figure 5.16 shows the polarimeter installed at the telescope. We used two analyzers, mounted in a frame in front of the cryostat window, to easily switch between three different operating modes:

1. horizontal analyzer
2. vertical analyzer
3. no analyzer (empty slot) to be used for normal total power measurements.

The analyzers are two twin 65 mm wire-grid polarizers, wires of 20 μm and spacing of 50 μm. A detail is visible in the picture on the right of figure 5.17. Before starting an observation, we had to select the appropriate analyzer - or none for total power, by sliding the frame manually in front of the cryostat window.

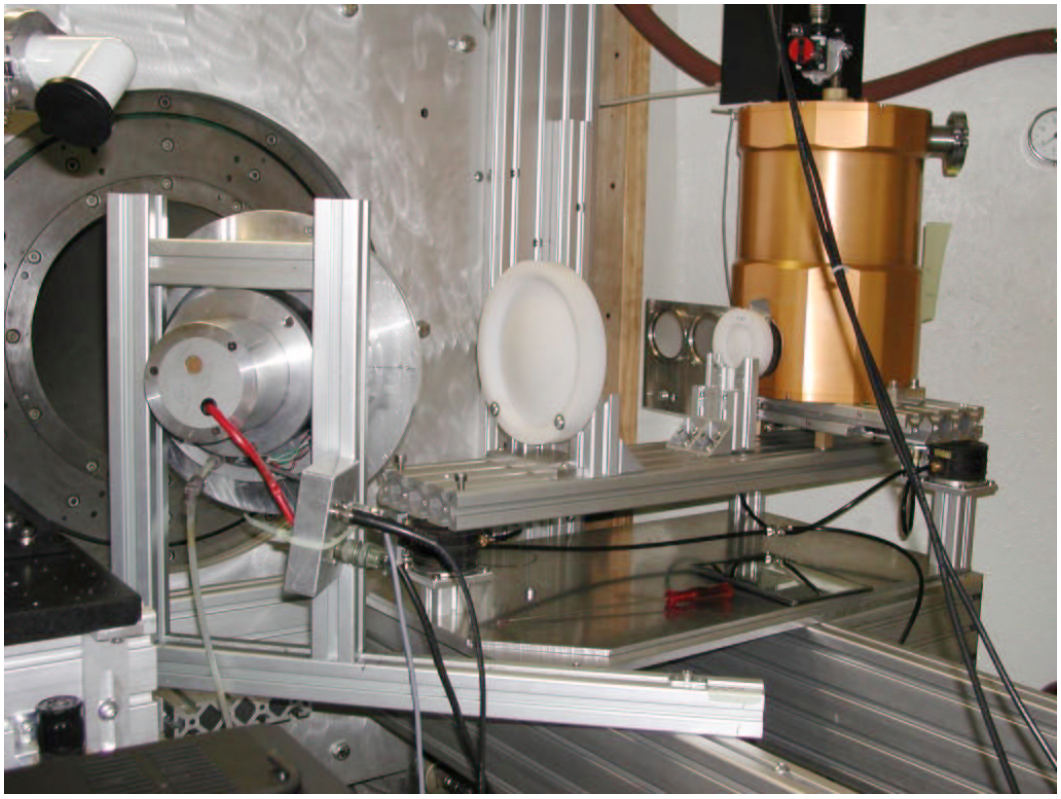

Figure 5.16: PolKa at the HHT on January 2002. The 246 mm RHWP is seen from the back, on its left is the Nasmyth tube, on the right are the lenses and the receiver. See also figure 5.2

Figure 5.17: *Left*: PolKa as seen from the receiver. In the background is the HEB receiver. *Right*: A detail of the frame holding the two analyzers.

Before the start of the observations, the RHWP was accurately tuned, using the three micrometric screws. It is very important to get the right distance between the wire-grid and the mirror to maximize the PME.

5.6.2 Source list and observations

Our observing time was shared with Dr.Giuseppe Cimò, from the VLBI group (Very Long Baseline Interferometry) of the MPIfR, who was planning to observe a number of intraday variable sources (IDV) (Cimò et al., 2002). In a collaborative effort, it was planned to detect their polarization using our polarimeter. We hoped to find from among them, a source with a high degree of polarization, which we could then use to check the rotation of the polarization angle. IDVs are AGNs that show variations of their total flux with time-scales that range from few hours to few days. Part of our observing time was then devoted to total power measurements of IDVs.

It is important to stress that our polarimeter is designed to detect linear polarization and does not allow direct measurements of the total flux of the source. When observing with the polarimeter, the information about the first and the fourth Stokes parameters is lost. This implies that an independent measurement of the total flux of the source is needed to retrieve full information about its linear polarization.

A typical observation session consisted of several steps. First of all, we had to perform the usual routine scans: a pointing on a strong point-like source, a focus, a second pointing and a skydip.

Then, to retrieve the first three Stokes parameters, we needed to perform a total power scan to detect the flux of the source (Stokes parameter I, either a `TPOO` or a `TPOtF`, according to the size of the source) and then a polarization scan (Stokes parameters Q and U). To reduce the systematic effects and to have a better removal of the spurious polarization, each polarization scan was repeated twice, one time using the horizontal analyzer and the second time using the vertical one. At the end of this sequence, we performed another skydip.

Table 5.1 shows the list of sources for this telescope campaign. Planets Mars, Jupiter and Saturn have also been observed and were used as unpolarized calibrators. The other planets were too close to the Sun to be observable. For safety reasons the telescope control software prevents the telescope to pointcloser than 30° from the Sun. This is because the surface of the primary mirror is a good concentrator for visible light too. As a consequence, it often happens that planets are too close to the Sun to be observable.

SOURCE LIST

AGN				
source	other name	type	α	δ
0716+714		Blazar	07 16 13.0	+71 26 15
0736+017		QSO	07 36 42.5	+01 44 00
0851+202	OJ287	Blazar	08 51 57.3	+20 17 58
0923+392	4C39.25	Seyfert 1	09 23 55.3	+39 15 24
1055+018		QSO	10 55 55.3	+01 50 04
1156+295	4C29.45	QSO	11 56 57.8	+29 31 26
1226+023	3C273	Blazar	12 26 33.3	+02 19 43
1253-055	3C279	Blazar	12 53 35.8	-05 31 08
1334-127		Blazar	13 34 59.8	-12 42 10
1633+382	4C38.41	QSO	16 33 30.6	+38 14 10
1641+399	3C345	QSO	16 41 17.6	+39 54 11
1726+455		Seyfert 1	17 26 01.2	+45 33 05
1749+096	4C09.57	Blazar	17 49 10.4	+09 39 43
2200+420	BL Lacertae	Blazar	22 00 39.4	+42 02 09
Peculiar Galaxies				
source	other name	type	α	δ
M82	3C231/NGC3034		09 51 42.0	+69 54 57
M87	3C274/Virgo A		12 28 17.6	+12 40 02
IRAS Sources				
source	other name	type	α	δ
05358+3543		YSO/MC	05 35 48.8	+35 43 41
05490+2658		YSO	05 49 05.2	+26 58 52
05553+1631		H II	05 55 20.3	+16 31 46
23139+5939		MC	23 13 57.9	+59 39 00
23151+5912		H II	23 15 08.7	+59 12 25
Other Clouds				
source	other name	type	α	δ
Ori A/OMC-1	M42/IRc2	H II/MC	05 32 47.0	-05 24 24
Ori A/OMC-3	MMS3/MMS4	H II/MC	05 32 51.4	+05 02 47
SH 2-100	K3-50A	H II	19 59 50.1	+33 24 19
SH 2-106		H II	20 25 33.5	+37 12 50
DR21		H II/MC	20 37 14.8	+42 08 56
W3(OH)		MC	02 23 16.5	+61 38 57
Tau A	M1	SNR	05 34 32.0	+22 00 52
CW Leo		H II/MC	09 45 14.8	+13 30 41

Table 5.1: List of the sources observed in the second telescope run. Coordinate epoch is 1950.0 (FK4 catalog).

Part III

Data reduction and results

Chapter 6

Data reduction

6.1 Software development

When a telescope session is over, a large amount of data is stored in several files where all the signals acquired during the observations are recorded. These data are almost meaningless until they are transposed from their original raw form to a more meaningful form that can be interpreted by the astronomers. This transformation process, that usually involves heavy numerical calculations, is known as *data reduction*.

The HHT is a telescope designed to measure the total flux of astronomical objects in the millimetric and submillimetric regime and the data acquisition DRUMBEAT is designed to acquire the bolometer signals. To reduce total flux measurements done with the 19-channel bolometer array there are two software packages ready to use. One is *NIC* [1] originally written at MPIfR and IRAM/Grenoble (Broguiére et al., 1995), based on the *NOD2* package by Haslam (1974). The other package is *MOPSI* (Zylka, 1998), written by Robert Zylka (MPIfR) for his private data reduction purposes. Both the packages make use of the EKH algorithm (Emerson et al., 1979). In general, MOPSI gives more possibilities to access and manipulate the data than NIC, but is less well documented. Both these packages can read the files produced by DRUMBEAT and completely reduce the data up to publication-quality plots.

Polarization data are acquired using a different backend and are produced with a different modulation strategy: there is no way to reduce polarization data using these two packages and we were obliged to write the polarization reduction software, starting from scratch. Furthermore, the two backends, DRUMBEAT and PolKABBA,

[1] The acronym stands for New Imaging Concept and follows a suggestion of G.Haslam of MPIfR.

have different characteristics (dynamical range, gain factors and so on) and in order to combine total power and polarization measurements we need a conversion factor to convert between data acquired by the two systems. To do that, we used PolKABBA to acquire a certain number of total power scans of planets to compare with the results from DRUMBEAT. Of course, for the reduction of these data, it is not possible to use any of the standard software; we also had to write the software to reduce total power scans acquired by PolKABBA.

For the quick-look of the data at the telescope, Lothar Reichertz (MPIfR) wrote some part of the demodulation routines using the National Instrument's LabVIEW graphical programming environment. Most of the final data reduction software was written by me in the IDL (Interactive Data Language, Research Systems Inc.) programming language.

6.1.1 Despiking

Both total power and polarization scans are equally affected by spikes, which are occasional disturbances of the signal on a very short time scale (see figure 5.9 for an example), generated by cosmic rays or other interferences. Especially at low levels, it is not obvious how to distinguish between a spike and a signal, and a despiking algorithm can follow different strategies. Thanks to our fast acquisition, we can resolve the spikes, as shown in the bottom panel of figure 5.9, and this helps to remove them. Our choice was a differential despiking algorithm.

6.1.2 Total-Power `On-Off` reduction software

When DRUMBEAT acquires the data of a total power scan it actually doesn't acquire the raw signals modulated by the wobbler but it dumps out just one data point per wobbler cycle, already demodulated. This is because, for DRUMBEAT, one data point is the difference of the mean of the signals acquired during the two wobbler phases (see section 5.4.1). Therefore all the frequencies present in the bolometer signal that are higher than the wobbler frequency are filtered out, and the information about the signal, at time-scales shorter than one single wobbler phase, is lost.

During total power measurements performed using PolKABBA the acquisition is much faster than with DRUMBEAT, typically 512 samples per second. Along with

the bolometer signals (19AC+1DC), we acquire a TTL logical reference signal which traces the position of the wobbler. This way we have full information about the signals and about the wobbler status, up to frequencies of the order of 250 Hz. Figure 6.1 shows an example of total power acquisition made by PolKABBA. The plot at the

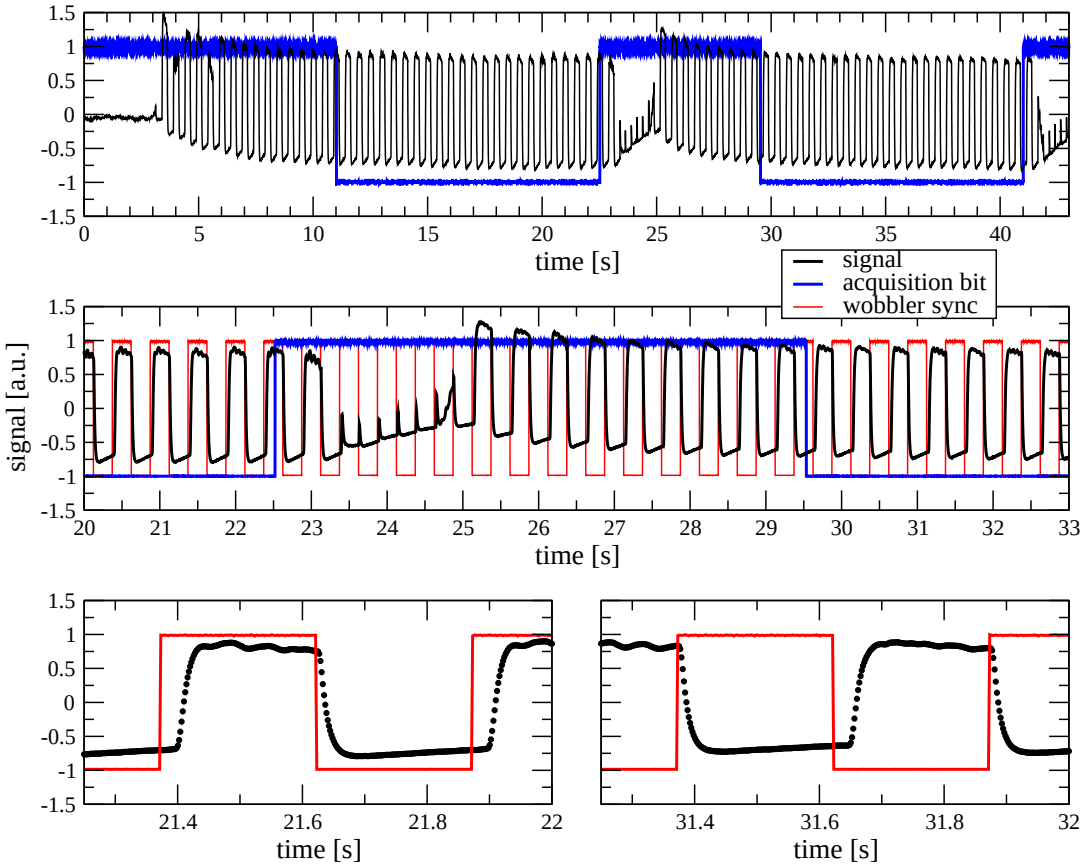

Figure 6.1: Raw data acquired by PolKABBA during a `TPOO` scan. *Top*: The plot shows the signal of the central channel (black) during the first two subscans, identified by the lower level of the acquisition bit (blue). *Center*: A detail of the signals between the two subscans. *Bottom, left*: One wobbler phase in the `On` subscan: it is in phase with the sync (red). *Bottom, right*: One wobbler phase in the `Off` subscan: it has the opposite phase to that of the sync. The wobbler throw is 200″. See also figure 5.9.

top of the figure shows the beginning of a scan on Saturn. Just the first two subscans are visible (the whole scan is made of eight) and they can be identified by the lower level of the acquisition bit (blue). The acquisition starts when the telescope is still moving and the source is not yet in the `On` beam. After ∼3 s we see the first chopped signal (black). When the telescope's control software reaches a satisfactory pointing the acquisition bit falls to the lower level and the acquisition of the coordinates (with

DRUMBEAT) starts. This happens after ∼11 s. The plot in the central panel shows a detail of the signals between the two subscans. When the acquisition bit goes to the upper level the subscan ends and the telescope starts moving to the `Off` position. We see that the chopped signal decreases when the source goes out from the `On` beam and then increases again when the sources goes inside the `Off` beam, but the phase is now shifted by 180°. The bottom panel shows a single wobbler phase for each subscan. In the left plot we see how, during the `On` subscan, the signal is in phase with the sync (in red). In the right plot, in the `Off` subscan the bolometer signal and the sync are in opposition. The scan in figure 6.1 is made of height subscans, about 10 s of integration time each (scan 0570 on Saturn done on the 20th of January 2002). PolKABBA, in ∼ 3 minutes, acquired 96000 samples for a total of ∼ 4.5 MByte.

The first part of the data reduction software goes through the following steps:

- Despike of the 19 signals.
- Split the scan in $2S$ subscans, S `On` the source and S `Off`.
- Compute the number W_s of wobbler phases inside the s-th subscan ($s = 1, 2, ..., 2S$).
- Split each phase, made of $2P$ samples per channel, into two sets: the P samples acquired when the wobbler is `On` the source and the P samples acquired when it is `Off`.
- Compute the differences of the mean signal of each set:

$$d_{ws}(k) = \frac{1}{P}\left[\sum_{i=1}^{P} v_{iws}(k) - \sum_{i=P+1}^{2P} v_{iws}(k)\right] \tag{6.1}$$

  where $v_{iws}(k)$ is the value of the i-th sample of the w-th wobbler phase ($w = 1, 2, ..., W_s$) of the s-th subscan and k is the number of the channel.

At this point, the numbers $d_{ws}(k)$ are equivalent to the data points acquired by DRUMBEAT during a standard `TPOO` scan. The results of this procedure, for the scan of figure 6.1, are shown in figure 6.2. The central channel shows a strong signal (planets are the brightest sources) that inverts the sign from one subscan to the other. The outer channels of the array do not detect any signal because the apparent angular size of Saturn, on that date, was less than 20 arcsecond (major axis = 19″.64; minor axis =

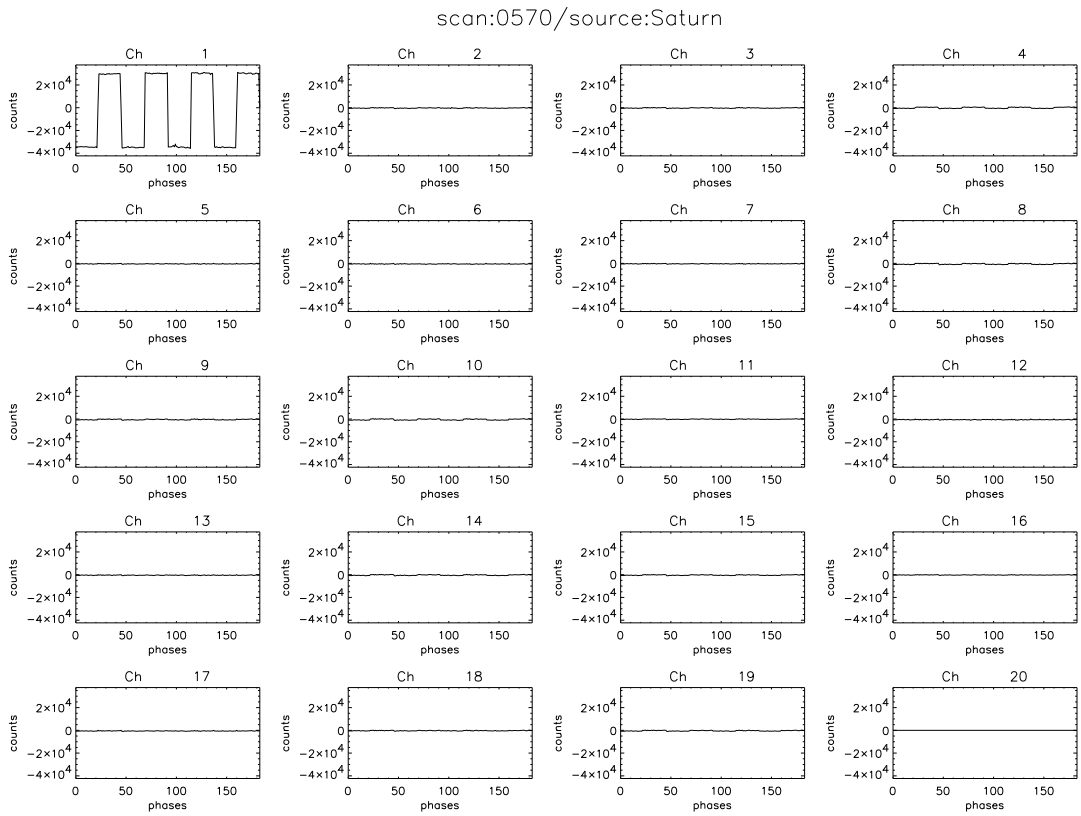

Figure 6.2: Typical signals of a `TPOO` scan for the 19 channel after the first part of the data reduction.

17″.53) and therefore, being smaller than the beam, it is a point-like source. Actually, some channels adjacent to channel 1 (4, 9, 10, see figure 5.3) show a weak signal that can be due to sidelobes. Starting from this point the data reduction follows the same procedure used by NIC or MOPSI to reduce the usual DRUMBEAT `TPOO` scans.

In what follows, I will consider only pairs of consecutive subscans, the first pair being composed by the first subscan `On` the source, that has index $s = 1$, and the first subscan `Off`, that has index $s = 2$, and so on. The index for the pairs will be $p = 1, 2, ..., S$. The subscans in the p-th pair have indexes $s_{\texttt{On}} = (2p-1)$ and $s_{\texttt{Off}} = 2p$, and I will use the labels `On` and `Off` to identify them. For each channel k of the array, the software goes through the following steps:

- remove the baseline from the data by least-square fitting to a straight line
- compute the mean signal and its variance for all the $2S$ subscans

$$< V_s(k) >= \frac{1}{W_s} \sum_{w=1}^{W_s} d_{ws}(k)$$

$$\sigma_s^2(k) = \frac{1}{W_s} \sum_{w=1}^{W_s} [d_{ws}(k) - < V_s(k) >]^2$$

- compute the weights of each pair of subscans (`On`, `Off`)

$$m_p(k) = \frac{1}{\sigma_{\texttt{On}}^2(k) + \sigma_{\texttt{Off}}^2(k)}$$

- compute the weighted mean of the differences between the `On` and `Off` signals of each pair

$$V_{\texttt{OO}}(k) = \frac{\sum_{p=1}^{S} m_p(k)[< V_{\texttt{On}}(k) > - < V_{\texttt{Off}}(k) >]}{\sum_{p=1}^{S} m_p(k)}$$

- compute the standard error on $V_{\texttt{OO}}(k)$

$$\sigma_{\texttt{OO}}(k) = \frac{1}{S} \sqrt{\sum_{p=1}^{S} \frac{1}{m_p(k)}}$$

The results for the 19 channel are then written in an output file, together with the beam offsets and the equatorial coordinates.

6.1.3 The software Lock-In

The data acquired by PolKABBA contain the information about the Q and U Stokes parameters of the source modulated by the polarimeter. This information has to be recovered by demodulation of the data. It is, in principle, the same process that DRUMBEAT performs: the wobbler produces a modulated signal, DRUMBEAT acquires the signal and simultaneously averages the differences at the same frequency. This is a demodulation process and its output is proportional to the flux of the source.

This is, in general, the principle of the synchronous demodulation, a powerful technique to detect weak signals affected by strong noise. It is very common to use *lock-in amplifiers* for this type of measurement in the laboratory (Meade, 1983). These special amplifiers can recover weak signals hidden in noise if the signal is modulated at a precise frequency, and if an accurate reference signal corresponding to the modulation is supplied.

In our special case we take advantage of the fast acquisition made by PolKABBA to demodulate the data via software, following an algorithm called *software lock-in*.

Let's assume we perform a polarization scan using the horizontal analyzer.

- The RHWP rotates at frequency ω (e.g. 3.5 Hz) and the modulated signal is given by equation 2.13. After gain and efficiency corrections, it can be written as

$$V(\theta) = \frac{1}{2}(Q\cos 4\theta + U\sin 4\theta) \tag{6.2}$$

$$\theta = \omega t + \theta_0 \tag{6.3}$$

  where θ is the position angle of the RHWP. For the sake of simplicity, in the following calculations we assume $\theta_0 = 0$ but a value of θ_0 must be derived by the calibrations of the position angle (see, for example, figure 5.14).

- PolKABBA acquires the data at a sample rate of S sample/second. In one turn of the RHWP we acquire a set $\{V_i\}$ made of N ($\sim S/\omega$) samples (e.g. $S = 512$ sample/s, $\omega = 3.5$ Hz, $N = 146$ sample/turn). At this point, we can assume that we know the modulation of the signal. We know that one turn of the RHWP produces four cycles in the polarization signal. If we know exactly how many acquisition points correspond to each turn of the RHWP then we can restore the relative phase between the modulator and the modulated signal and therefore we can demodulate the signal. It is in this step that the software emulates the lock-in amplifier. The sync signal (see section 5.4.3) is used as a reference in order to retrieve the number of samples in each turn, and thus to lock the phase of the polarization signal.

- The value of one single sample is

$$V_i = V(t_i) = \frac{1}{2}(Q\cos 4\theta_i + U\sin 4\theta_i) \tag{6.4}$$

$$\theta_i = \omega t_i \tag{6.5}$$

- We define the two $2N$ quantities $S_i = 4\sin 4\theta_i$, $C_i = 4\cos 4\theta_i$.

- We compute the 2 numbers

$$X = \frac{1}{N}\sum_{i=1}^{N} C_i\, V_i = \frac{2}{N}\left[Q\sum_{i=1}^{N}\cos^2 4\theta_i + U\sum_{i=1}^{N}\cos 4\theta_i \sin 4\theta_i\right]$$
$$Y = \frac{1}{N}\sum_{i=1}^{N} S_i\, V_i = \frac{2}{N}\left[Q\sum_{i=1}^{N}\cos 4\theta_i \sin 4\theta_i + U\sum_{i=1}^{N}\sin^2 4\theta_i\right]$$

When $N \gg 1$ we have

$$\frac{1}{N}\sum_{i=1}^{N} \cos^2 4\theta_i = \frac{1}{N}\sum_{i=1}^{N}\sin^2 4\theta_i \simeq \frac{1}{2} \tag{6.6}$$
$$\frac{1}{N}\sum_{i=1}^{N} \cos 4\theta_i \sin 4\theta_i \simeq 0 \tag{6.7}$$

and we get the demodulated Stokes parameters

$$X \equiv Q \tag{6.8}$$
$$Y \equiv U \tag{6.9}$$

When we perform a polarization scan using the vertical analyzer, the two numbers have the opposite values:

$$X \equiv -Q \tag{6.10}$$
$$Y \equiv -U \tag{6.11}$$

The two demodulated numbers, however, are not yet the Stokes parameters of the radiation coming from the source. We still have to:

- Remove the instrumental spurious polarization.
- Rotate the polarization vector to compensate for the rotation of the source with elevation due to the Nasmyth optical system.
- Rotate the polarization vector to compensate for the parallactic angle of the source.
- Use the calibrations made with a reference source to remove the offset angle θ_0 (see section 6.2.6).

All the polarization scans need to be demodulated using this procedure. The results are always the two measured Stokes parameters of the source.

6.1.4 Polarization `On-Off` reduction software

A typical `POO` scan is made of $2S$ subscans (index $s = 1, 2, ..., 2S$) and one subscan is made of W_s phases or RHWP turns (index $w = 1, 2, ..., W_s$). The reduction of the `POO` follows these steps:

- Despike of the 19 signals.
- Split the scan in its $2S$ subscans, S `On` the source and S `Off`.
- Compute the number W_s of RHWP phases inside the s-th subscan.
- Apply the software lock-in to each phase. The output are the demodulated Stokes parameters of that phase, $X_{sw}(k), Y_{sw}(k)$, where k is the channel number.
- Compute the mean values of X_{sw}, Y_{sw} and their variance in each subscan:

$$< X_s(k) >= \frac{1}{W_s}\sum_{w=1}^{W_s} X_{ws}(k) \quad , \quad \sigma^2_{<X_s>}(k) = \frac{1}{W_s}\sum_{w=1}^{W_s} [X_{sw}(k) - < X_s(k) >]^2$$

$$< Y_s(k) >= \frac{1}{W_s}\sum_{w=1}^{W_s} Y_{ws}(k) \quad , \quad \sigma^2_{<Y_s>}(k) = \frac{1}{W_s}\sum_{w=1}^{W_s} [Y_{sw}(k) - < Y_s(k) >]^2$$

- Divide the subscan in S pairs. I will use the index $p = 1, 2, ..., S$ for the pairs and labels `On` $= (2p-1)$ and `Off` $= 2p$ for the subscan in the p-th phase, as done in section 6.1.2.
- Compute the weights of each pair of subscans

$$m_{p,X}(k) = \frac{1}{\sigma^2_{<X_{\mathtt{On}}>}(k) + \sigma^2_{<X_{\mathtt{Off}}>}(k)} \quad , \quad m_{p,Y}(k) = \frac{1}{\sigma^2_{<Y_{\mathtt{On}}>}(k) + \sigma^2_{<Y_{\mathtt{Off}}>}(k)}$$

- Compute the `On-Off` signal for each pair:

$$< X_{p,\mathtt{OO}}(k) > \; = \; < X_{\mathtt{On}}(k) > - < X_{\mathtt{Off}}(k) > \tag{6.12}$$

$$< Y_{p,\mathtt{OO}}(k) > \; = \; < Y_{\mathtt{On}}(k) > - < Y_{\mathtt{Off}}(k) > \tag{6.13}$$

- Derotate each vector $(< X_{p,\mathtt{OO}}(k) >, < Y_{p,\mathtt{OO}}(k) >)$ to compensate for the Nasmyth and the parallactic angle rotation.

- Check for the analyzer: if it is vertical then transform

$$\begin{aligned} X &\longrightarrow -X \\ Y &\longrightarrow -Y \end{aligned}$$

- Apply the correction for the sky opacity calculated from tabulated values of the zenithal opacity measured with the `skydip` procedure (see figures 5.11 and 5.15).

- Remove the spurious polarization according to the analyzer that was used (see section 6.2.5).

- Compute the weighted mean of the measured Stokes parameters:

$$Q(k) = \frac{\sum_{p=1}^{S} < X_{p,\mathtt{OO}}(k) > \; m_{p,X}(k)}{\sum_{p=1}^{S} m_{p,X}(k)} \tag{6.14}$$

$$U(k) = \frac{\sum_{p=1}^{S} < Y_{p,\mathtt{OO}}(k) > \; m_{p,Y}(k)}{\sum_{p=1}^{S} m_{p,Y}(k)} \tag{6.15}$$

- Compute the standard error on the measured Stokes parameters:

$$\sigma_Q(k) = \frac{1}{S}\sqrt{\sum_{p=1}^{S} \frac{1}{m_{p,X}(k)}} \tag{6.16}$$

$$\sigma_U(k) = \frac{1}{S}\sqrt{\sum_{p=1}^{S} \frac{1}{m_{p,Y}(k)}} \tag{6.17}$$

Besides the two Stokes parameters, polarization intensity, polarization degree and position angle are also calculated. In order to calculate the polarization degree, the software uses tabulated values of the total flux of the sources, that have been previously calculated using NIC to reduce the `TPOO` observations we made at the telescope.

- Polarization intensity P:

$$P(k) = \sqrt{Q^2(k) + U^2(k) - f z^2(k)} \tag{6.18}$$

where

$$z(k) = \sqrt{\sigma_Q^2(k) + \sigma_U^2(k)}$$

and f is a debiasing factor that must be determined empirically ($f \sim 1$) to shift to zero the positive bias added by the uncertainties on Q and U(Mack et al., 1997). Given the definition (6.18) of P, in fact, even when Q and U are affected by Gaussian errors, P will follow a Rice-distribution and will be a biased estimator of the true polarization intensity (Wardle & Kronberg, 1974; Simmons & Stewart, 1985).

The error on P is given by:

$$\sigma_P(k) = \frac{1}{P(k)} \sqrt{Q^2(k)\sigma_Q^2(k) + U^2(k)\sigma_U^2(k)}$$

- Polarization degree p: given the total intensity of the source I and its error σ_I we have

$$p(k) = 100\ \frac{P(k)}{I} \quad [\%] \tag{6.19}$$

and its error is

$$\sigma_p(k) = 100\ \sqrt{\left(\frac{\sigma_P(k)}{I}\right)^2 + \left(P\ \frac{\sigma_I}{I^2}\right)^2} \quad [\%]$$

- Position angle:

$$\chi(k) = \frac{1}{2}\ \arctan\left[\frac{U(k)}{Q(k)}\right] \quad [\text{rad}] \tag{6.20}$$

$$\sigma_\chi = \sqrt{\left(\chi_0\ \frac{\sigma_p}{p}\right)^2 + (\Delta_\chi)^2} \tag{6.21}$$

where χ_0, in our case, is 0.5 radians (Platt et al., 1991) and Δ_χ is the angular resolution of the RHWP reference system.

The calculated values are written in tables in the output files. The POO reduction software has also a graphical output (see figure 6.3) to display the polarization vectors for each beam of the array.

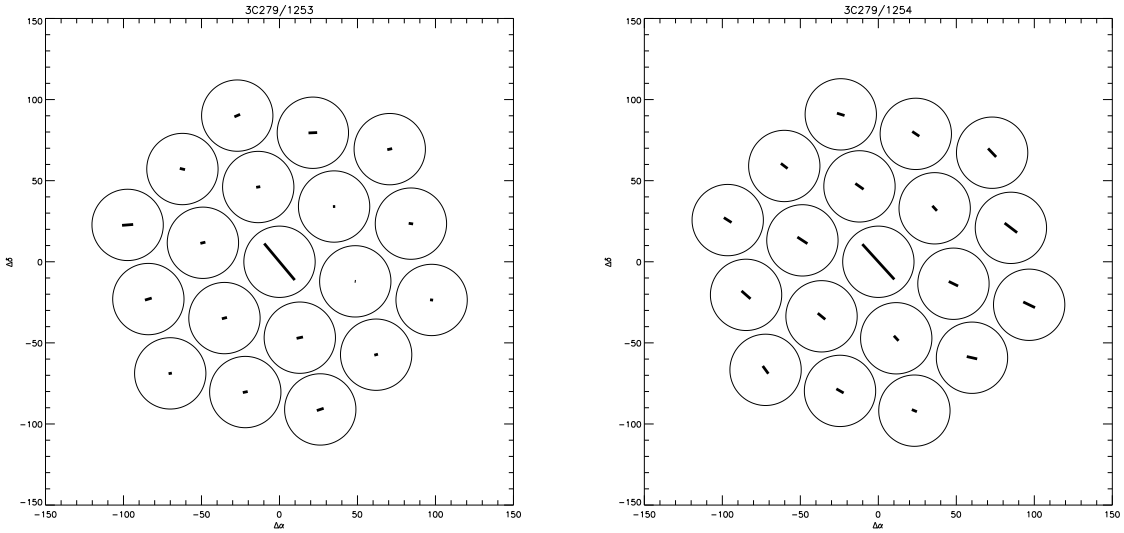

Figure 6.3: Example of graphical output of the `POO` procedure: the configuration of the beams on the sky is shown, together with the measured polarization vectors of each channel. *Left*: Scan 1253 on the blazar 3C279. In this case with the horizontal analyzer. *Right*: Scan 1254, performed few minutes later with the vertical analyzer. Offsets are in arcseconds. The absolute coordinates are given in table 5.1. See also figures 7.1 and 7.2.

6.1.5 Polarization `On-the-Fly` maps reduction software

The reduction of `POtF` scans is more difficult than the reduction of `POO`. The main complication arises from the fact that the data are acquired by two computers, one to acquire the telescope data, and the other for the signals (see figure 5.10). The data acquired by DRUMBEAT, for each data point, are the local apparent sidereal time (LAST), the absolute azimuth and elevation and the offsets in azimuth and elevation from the center of the map. The acquisition is triggered by the rotating RHWP such that the data are sampled at its mechanical rotation frequency.

The data acquired by PolKABBA, at the sample frequency of 512 Hz, are the universal time (UT), the 19 signals from the AC coupled bolometers, the signal from the DC coupled bolometer and the three reference signals: acquisition bit, sync and blank.

A typical `POtF` scan is made of S subscans (index $s = 1, 2, ..., S$) (see figure 5.8). For example, a map of $360'' \times 360''$ scanned in elevation in steps of $8''$ is made of $S = 4$ subscans. If the azimuthal scanning velocity is $15''$/s each subscan requires 24 seconds to be scanned. If the RHWP rotates at 3.5 Hz then DRUMBEAT acquires 84 data

points while PolKABBA acquires 12288 data points, per subscan. The resolution in the coordinates will be of $\sim 4''$ per point. Four polarization cycles sampled in 146 points (36 points per cycle) correspond to each one of the 84 coordinate points. The whole map is made of 3780 of these sets of four polarization cycles that will be demodulated via software lock-in.

The reduction of the `POtF` follows these steps:

- Despike of the 19 signals.
- Calculate the LAST for all the data points acquired by PolKABBA.
- Split the scan in the S subscans according to the timestamps of the data points acquired by DRUMBEAT. The time resolution in PolKABBA is $\sim$ 2ms while the time resolution in DRUMBEAT is $\sim$ 286ms. A subscan is well defined, then, simply matching the first and the last DRUMBEAT timestamp.
- Compute the number W_s of RHWP phases inside the s-th subscan.
- Apply the software lock-in to each phase. The output consists of the demodulated Stokes parameters of that phase, $X_{sw}(k), Y_{sw}(k)$, where k is the channel number.
- Merge the data acquired with the two backends by associating to each data point, the coordinates $A_{sw}(k), E_{sw}(k)$, taken from the DRUMBEAT file, to the demodulated values $X_{sw}(k), Y_{sw}(k)$, to form the set of values $[A_{sw}(k), E_{sw}(k), X_{sw}(k), Y_{sw}(k)]$ where i is an index running over the whole scan.
- Apply the corrections to get Q and U from X and Y:
  - Compensation for the analyzer type
  - Nasmyth derotation
  - Parallactic angle derotation
  - Spurious polarization removal
- Shift each channel in azimuth and elevation to remove the offsets relative to the center of the array.

- Define the size of the map in pixels by setting the resolution ρ in arcsecond per pixel. For example, if the scan is $360'' \times 360''$ and we set a resolution of $\rho = 10''$ per pixel, the resulting map will have $36 \times 36 = 1296$ pixels.

- For each channel, construct a Delaunay triangulation of the irregularly gridded coordinates $[A_{sw}(k), E_{sw}(k)]$ to get $[A_i, E_j]$ where (i, j) are the indexes of the pixels in the map.

- For each channel, compute a regular grid of interpolated values of the measured Stokes parameters, $[Q_{ij}(k), U_{ij}(k)]$, based on the previous triangulation of the coordinates.

- Add the values of all the channels:

$$Q_{ij} = \sum_{k=1}^{19} Q_{ij}(k) \quad , \quad U_{ij} = \sum_{k=1}^{19} U_{ij}(k)$$

  to get the two sets of values

$$[A_i, E_j, Q_{ij}] \quad , \quad [A_i, E_j, U_{ij}]$$

  that are the two Stokes parameters maps in local coordinates.

- Convert the map to equatorial coordinates:

$$[A_i, E_j] \longrightarrow [\alpha_i, \delta_j]$$

  Therefore

$$[\alpha_i, \delta_j, Q_{ij}] \quad , \quad [\alpha_i, \delta_j, U_{ij}]$$

  are the two Stokes parameters maps in equatorial coordinates.

- Write in an output file the Stokes parameters tabulated together with the coordinates.

- Plot the map.

There are several ways to plot a polarization map. One way is to draw, over a total power map $[\alpha_i, \delta_j, I_{ij}]$ of the same source, vectors whose components (x_{ij}, y_{ij}) are given

by

$$x_{ij} = P_{ij} \cos \chi_{ij}$$
$$y_{ij} = P_{ij} \sin \chi_{ij}$$

where P is the polarization intensity defined by

$$P_{ij} = \sqrt{Q_{ij}^2 + U_{ij}^2 - f\sigma_{QU}^2} \tag{6.22}$$

where σ_{QU} is the mean value of the noise in the Q and U maps and f is a debiasing factor to be determined empirically ($f \sim 1$) to shift to zero the peak of the positive noise distribution function (Wardle & Kronberg, 1974; Simmons & Stewart, 1985; Mack et al., 1997), and

$$\chi_{ij} = \frac{1}{2} \arctan\left(\frac{U_{ij}}{Q_{ij}}\right) \tag{6.23}$$

In this case we have a *polarization intensity map.* The most common way, however, is to divide, pixel by pixel, the polarization intensity map by the flux of the source in the corresponding pixel of the total power map. This way we get a *polarization degree map.*

6.1.6 The graphical representation of polarization maps

In order to give a graphical representation to the demodulated values, we wrote some routines in the IDL language. As an example of their graphical output, see figure 7.9. We assume that a number N of polarization scans is available and the demodulated values are in the form $[\alpha_i, \delta_j, Q_{ij}(k)]$, $[\alpha_i, \delta_j, U_{ij}(k)]$ where k is the index of the scan.

These are the main steps to arrive at a polarization degree map:

- The software starts with the reduction of a total power map of the source. The result must be resampled on the size of the polarization map, the latter being in general a wobbler throw smaller in azimuth. In the end, we get $[\alpha_i, \delta_j, I_{ij}]$.

- Define the number of vectors in the map by setting the resolution ϕ of the field in arcsecond per vector. One vector will cover a square area (a bin) whose side is made of ϕ/ρ pixels (ρ is the number of arcsecond per pixel, defined in the previous section).

- Rebin the data according to the resolution of the field. The indexes i, j refer now to the bins.

- Compute the normalized Stokes parameters:

$$\begin{aligned} q_{ij}(k) &= 100\ \frac{a\ Q_{ij}(k)}{f\ I_{ij}} \\ u_{ij}(k) &= 100\ \frac{a\ U_{ij}(k)}{f\ I_{ij}} \end{aligned}$$

  where a is the PolKABBA-to-DRUMBEAT conversion factor and f is the frequency conversion factor (see next section).

- Compute the mean values and the standard error of the normalized parameters for each bin:

$$\begin{aligned} < q_{ij} > &= \frac{1}{N}\sum_{k=1}^{N} q_{ij}(k)\ , \qquad \sigma_{q_{ij}} = \frac{1}{N}\sqrt{\sum_{k=1}^{N}(q_{ij}(k) - < q_{ij} >)^2} \\ < u_{ij} > &= \frac{1}{N}\sum_{k=1}^{N} u_{ij}(k)\ , \qquad \sigma_{u_{ij}} = \frac{1}{N}\sqrt{\sum_{k=1}^{N}(u_{ij}(k) - < u_{ij} >)^2} \end{aligned}$$

- Compute the polarization degree map $[\alpha_i, \delta_j, p_{ij}]$ where

$$p_{ij} = \sqrt{q_{ij}^2 + u_{ij}^2}$$

- Compute the standard error map $[\alpha_i, \delta_j, \sigma_{p_{ij}}]$

$$\sigma_{p_{ij}} = \frac{1}{p_{ij}}\sqrt{\sigma_{q_{ij}}^2\ q_{ij}^2\ +\ \sigma_{u_{ij}}^2\ u_{ij}^2}$$

- Debias of the polarization degree:

$$p_{ij_{\mathrm{deb}}} = \sqrt{p_{ij}^2 - \sigma_{p_{ij}}^2}$$

- Compute the position angle map $[\alpha_i, \delta_j, \chi_{ij}]$ where

$$\chi_{ij} = \frac{1}{2}\ \arctan\left(\frac{u_{ij}}{q_{ij}}\right)$$

- Define a minimum threshold t for the total power that will be used to avoid plotting vectors where there is no significant signal. If m is the mean value of I_{ij} over the map then $t =< \{I_{ij} <\ m\} >$

- Define the length n in pixels of the maximum vector to plot. A good choice is the diagonal of one bin.
- Plot the total power map at the resolution of ρ arcsecond per pixel.
- For all the bins that satisfy the conditions

$$\begin{aligned} I_{ij} &> t \\ p_{ij_{\mathrm{deb}}} &> \sigma_{p_{ij}} \end{aligned}$$

  proceed as follows:

  - Calculate the maximum degree of polarization L
  - Calculate the length in pixels of each vector: $l_{ij} = n\ p_{ij_{\mathrm{deb}}}/L$
  - Draw the vector of components

$$v_\alpha = l_{ij}\ \cos(\pi\ -\ \chi_{ij})$$

$$v_\delta = l_{ij}\ \sin(\chi_{ij})$$

    in the center of the bin (i, j) over the total power map.

6.2 Calibrations

Polarization observations are considerably more complicated than standard total power observations, and several parameters are involved in the reduction of the data. It is very important, then, to calibrate these quantities to minimize the uncertainties of the results.

6.2.1 DRUMBEAT/PolKABBA conversion factor

The two backend acquiring the data have different characteristics (dynamical range, gain factors and so on) and therefore the analog-to-digital conversion of the bolometer signals will lead to different counts in the two systems even when the input signals are the same.

In order to compensate for this effect, we need a conversion factor to convert between the counts acquired by the two systems. During the second telescope campaign,

scan	source	PolKABBA counts	DRUMBEAT counts	ratio D/P
0398	Mars	2956 ± 32	461880	156.3 ± 3.4
0399	Mars	2852 ± 26	461863	161.9 ± 3.0
0570	Saturn	12944 ± 84	2848379	220.1 ± 2.9
0694	Saturn	17068 ± 28	2843659	166.6 ± 0.6

Table 6.1: Summary of the results of the `TPOO` observations made with the two backends to calculate the counts conversion factor.

we acquired four total power `On-Off` observations performed on planets with PolKABBA. Two of them are on Mars and the other two are on Saturn. The data were reduced with the algorithm described in section 6.1.2. For these two planets many other `TPOO` observations were made acquiring with DRUMBEAT, following the standard total power procedure. The results are shown in figure 6.4. These results have been used to interpolate the counts corresponding to the data acquired with PolKABBA. All

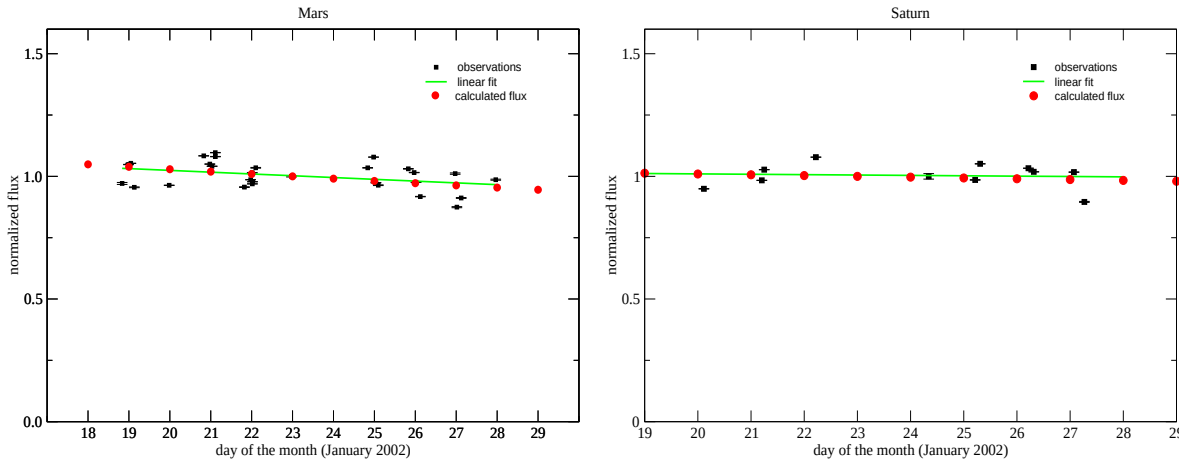

Figure 6.4: Results of the `TPOO` scans on the planets, acquired with DRUMBEAT and reduced with NIC. The green line is the fit of the observations. The red dots are values of the flux calculated with the program ASTRO (GILDAS package). The data refer to the second telescope campaign.

the data have been corrected for the atmospheric opacity. Table 6.1 shows the results of the data reduction. The deduced value of the conversion factor is 176.2 ± 5.4 DRUMBEAT/PolKABBA counts.

6.2.2 Counts/Jansky conversion factor

Another important conversion factor is the ratio between the counts measured during the observations and the flux in Jansky of the sources. This number can be estimated from the observations of bright sources of known flux. Starting from observations of

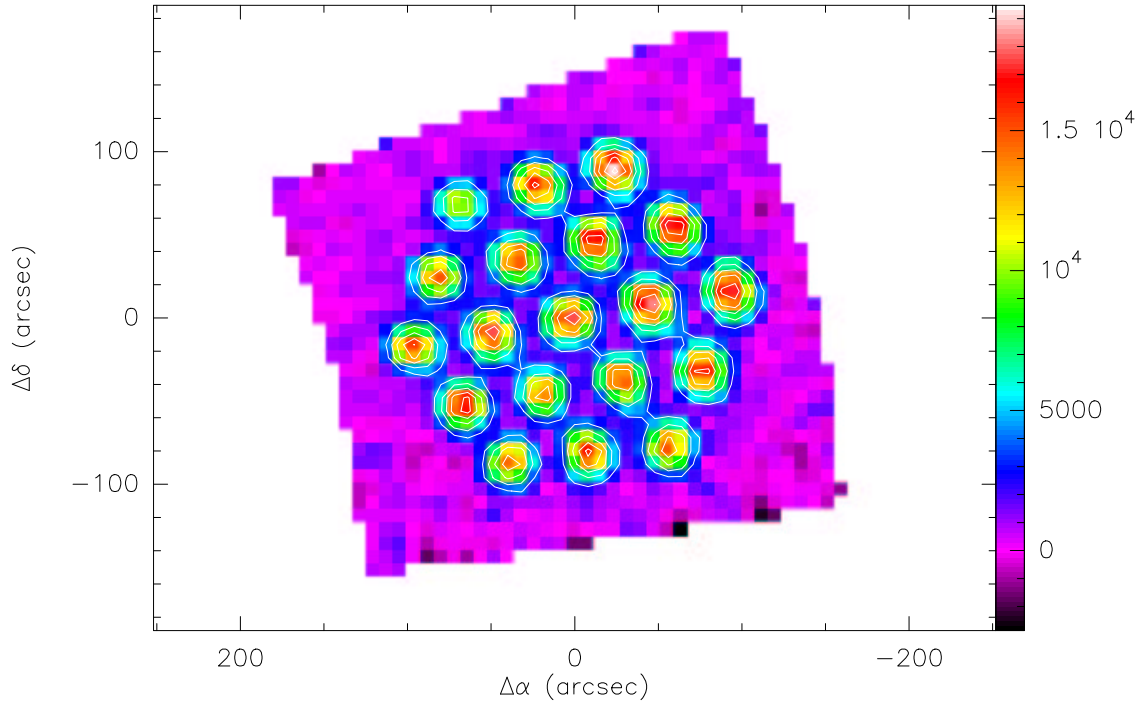

Figure 6.5: Bolometer beam map from a total power `On-the-Fly` map of Mars. Values are in DRUMBEAT counts.

Saturn, Mars, Orion IRc2, DR21, W3(OH), K3-50A it has been possible to calculate the value of 1147 ± 123 DRUMBEAT counts/Jy. Notice that the error on this factor is ∼10%, that is the typical uncertainty on flux measurements at the HHT.

6.2.3 Bolometer gain correction

The load curves in figure 5.4 show that each of the 19 bolometers in the array has a slightly different responsivity. In order to compensate for this effect we need to calculate the gain factors for all the 19 bolometers. Figure 6.5 shows the beam map produced by NIC reducing a `TPOtF` of Mars following a special procedure. The program calculates the signal in each channel of the array, and then divides it by the signal of the central channel. These numbers, shown in table 6.2 are the gain factors of the 19 channels. They are used during the data reduction to balance the responsivities.

6.2.4 Bolometer frequency response

It has already been shown in section 4.2 how the combination of the bolometer frequency response with the fast spinning technique produces a modulation of the PME.

ch	g	ch	g	ch	g	ch	g
01	1.00	06	0.89	11	1.06	16	1.11
02	0.95	07	0.96	12	0.70	17	0.98
03	0.98	08	0.89	13	0.71	18	0.82
04	1.08	09	0.85	14	0.89	19	0.93
05	0.88	10	0.79	15	0.97	-	-

Table 6.2: Gain factors of the 19 channels of the array.

The bolometer frequency response must also be taken into account when comparing results of observations carried out at different modulation frequencies. The degree of polarization, for example, is the ratio between the polarization intensity and the total flux of the source. In standard total power observations, the modulation produced by the wobbler is always at 2 Hz, whereas in polarization observations, the polarization modulation produced by the RHWP in the first and in the second telescope campaigns was 16 Hz and 14 Hz respectively. It is therefore necessary to compensate for the different bolometer response before dividing counts acquired at different frequencies. In order to measure the bolometer frequency response over a wide range of frequencies, we used the RHWP to modulate 100% polarized radiation coming from a lab source. Given the factor of four between the mechanical rotation frequency and the polarization modulation, it was possible to go up to 100 Hz. Thanks to the high sampling rate of PolKABBA and to the RHWP position reference system, it was possible to monitor the rotation frequency with high accuracy up to frequencies of ~ 80 Hz. Figure 6.6 shows the results of these measurements. The values for the frequencies of interest in our experiment are also summarized in table 6.3.

6.2.5 Spurious polarization: planets as unpolarized sources

In order to evaluate the instrumental spurious polarization (hereafter ISP) of the whole system consisting of the telescope, the polarimeter and the receiver optics, we performed a certain number of `POO` on the planets Mars and Saturn. These two planets, during our observations, had an apparent size smaller than our beam and therefore they were the two strongest point-like sources available. Jupiter was also observable but with an apparent size of $\sim 45''$ which was more than twice our beam.

The thermal radiation emitted by the planets, in the millimetric and submillimetric regime, is supposed to be linearly polarized in the radial direction. This means that

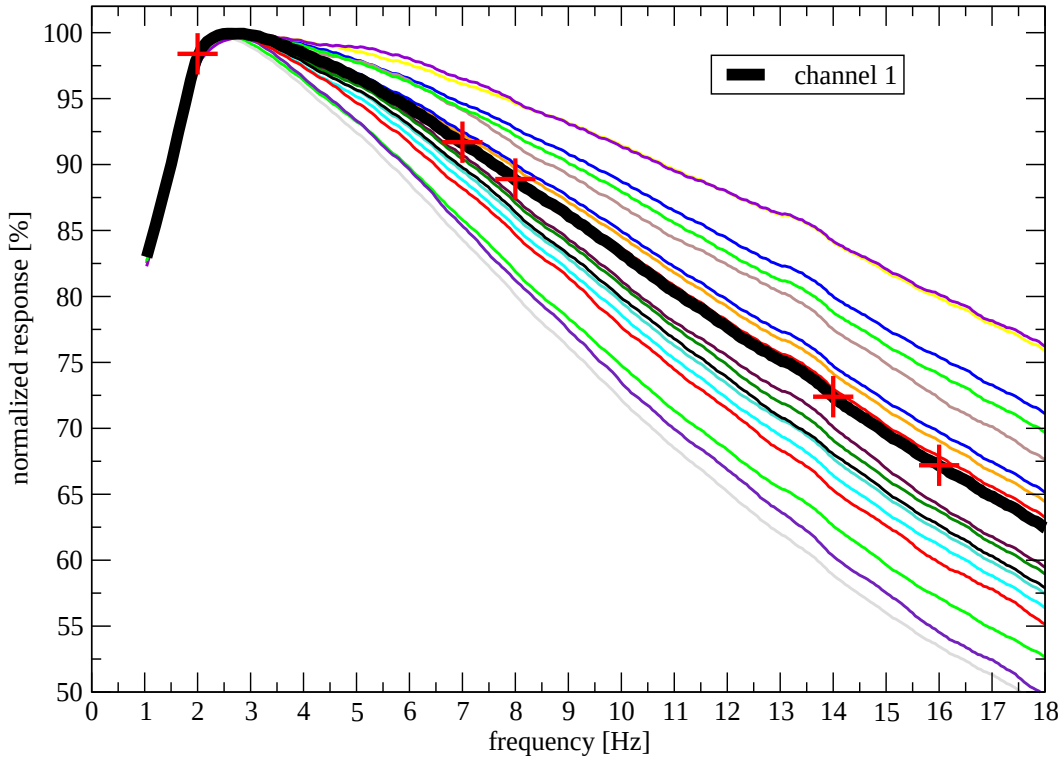

Figure 6.6: Normalized bolometer response for the 19 channel of the HHT array. The thick black line is the central channel. The crosses indicate the frequencies of interest in our experiment (see also table 6.3).

in our case the net linear polarization is averaged to zero, because we collect the radiation emitted by the whole planetary disks. Saturn, given its asymmetrical shape, could give rise to a small amount of linear polarization but well below the sensitivity of our detection. In this frame, we can consider the two planets as two strong point-like unpolarized sources in the sky. Figures 6.7 and 6.8 show the results of these measurements.

Our instrument was installed at the Nasmyth focus of the telescope. The tertiary mirror, rotating about the elevation axis, might produce a spurious polarization signal function of the elevation. The bending of the quadrupod that supports the subreflector, an effect of its weight, is another cause that might produce a spurious polarization signal function of the elevation. It is important, then, to have many observations at different elevation angles to evaluate this effect. Unfortunately, our time at the telescope was too short to perform a larger number of observations on planets, whereas a better sample of elevation angles would be required. Nevertheless, we see that the ISP is always below 1%, even at very low elevation angles, where one does not usually observe.

channel	2 Hz	7 Hz	8 Hz	14 Hz	16 Hz	max. at
01	98.4	91.7	89.0	73.2	67.9	2.6
03	99.2	85.8	81.7	62.8	57.2	2.5
04	98.4	94.7	92.8	80.2	75.5	2.9
05	98.1	96.2	94.7	84.3	80.0	3.2
06	98.4	94.2	91.5	77.7	72.4	2.9
07	99.3	84.3	80.1	59.0	53.5	2.4
08	98.1	96.5	94.8	84.4	80.2	3.2
09	99.1	88.8	85.3	66.6	61.2	2.5
10	98.8	91.7	88.9	72.7	67.4	2.9
11	98.9	92.3	89.7	74.3	69.1	2.9
12	99.1	85.3	81.3	60.5	54.6	2.5
13	98.8	90.7	87.5	70.3	64.3	2.9
14	99.1	89.5	86.1	67.9	62.3	2.5
15	99.1	90.4	87.1	69.3	63.8	2.5
16	99.1	89.8	86.4	68.2	62.7	2.5
17	99.2	88.2	84.7	65.5	59.9	2.5
18	98.4	94.3	92.2	79.0	74.2	2.9
19	98.8	92.5	90.0	74.9	69.8	2.9

Table 6.3: Percentage of the normalized bolometer response for the 19 channel of the HHT array at the frequencies of interest in our experiment. The last column gives the frequency of the response maxima. See also figure 6.6.

Furthermore, from the data, we see that there is a constant offset in the position angles of the two spurious signals produced with different analyzers. There is no

analyzer	p_{ISP}[%]	χ_{ISP} [°]
H	0.36 ± 0.12	49.8 ± 3.2
V	0.26 ± 0.15	33.8 ± 6.2

Table 6.4: Mean values of the ISP for the two configurations of the polarimeter.

evidence of a relation between the ISP and the elevation angle and therefore only the mean values will be removed from the data. The mean values are shown in table 6.4. Even though it is a small effect, the ISP is taken into account in the data reduction. The two Stokes parameters of the ISP corresponding to a given source whose total intensity is I_0 are

$$Q_{\mathrm{ISP}} = \frac{I_0\, p_{\mathrm{ISP}}}{\sqrt{2}} \cos 2\, \chi_{\mathrm{ISP}}$$

$$U_{\mathrm{ISP}} = \frac{I_0\, p_{\mathrm{ISP}}}{\sqrt{2}} \sin 2\, \chi_{\mathrm{ISP}}$$

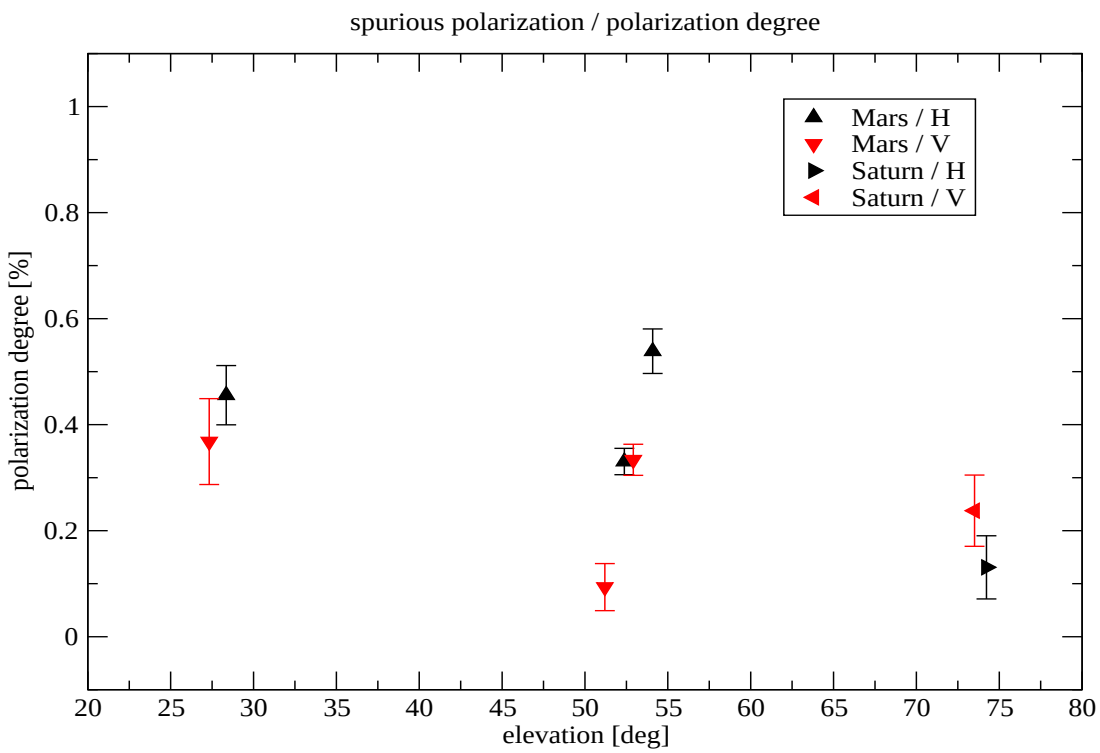

Figure 6.7: Observed ISP on Mars and Saturn. Polarization degree.

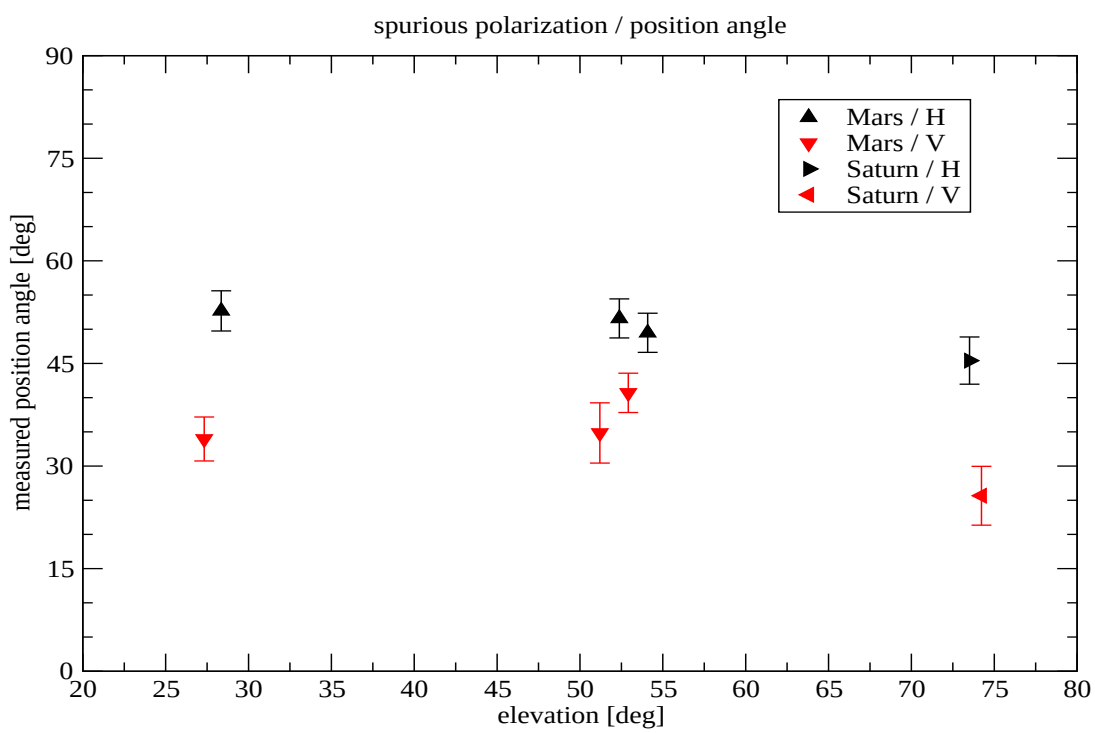

Figure 6.8: Observed ISP on Mars and Saturn. Polarization position angle.

6.2.6 Absolute position angle

We made some measurements in the receiver cabin using a lab source similar to the one described in sections 4.1 and 4.2. The aim of these measurements was to determine the angular offset between the measured polarization vector and the original position angle of the source. Due to us having made these measurements, which were essential to calibrate the demodulated position angle, the polarimeter was able to give absolute results on astronomical objects without the need of a calibration source in the sky. The results are shown in figure 6.9. The measurements were repeated several times, for

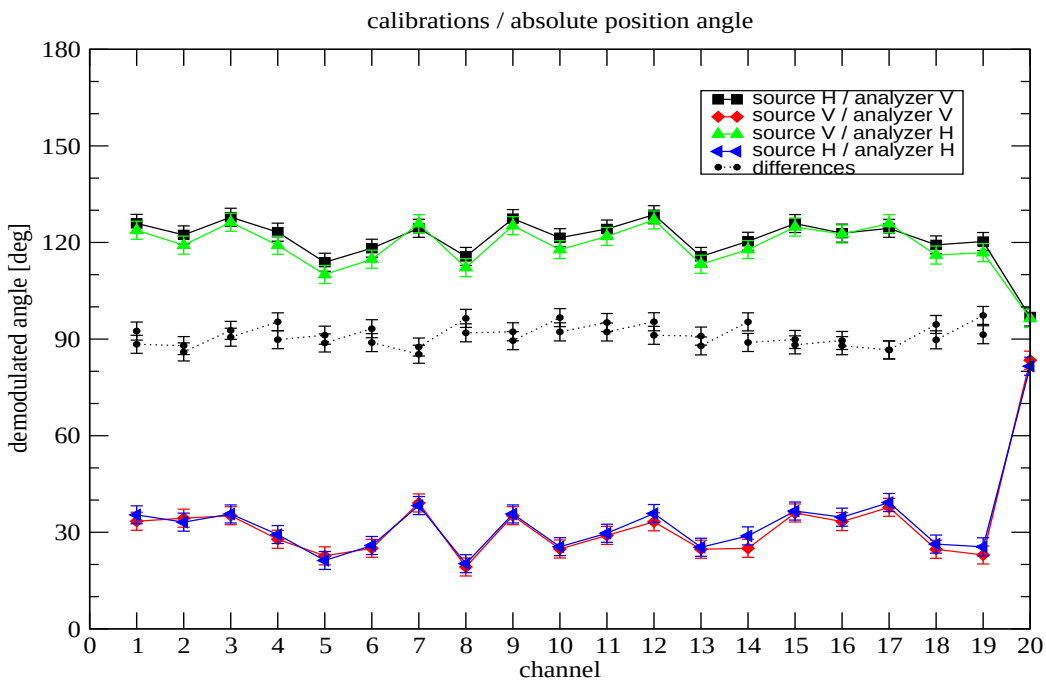

Figure 6.9: Measured values of the absolute position angle for the 19 channels and for different configurations. "H" stays for horizontal, "V" stays for vertical.

horizontal and vertical position angles of the source and for the two different analyzers. There are two sets of values: the values measured when the source is parallel to the analyzer and the values measured when the source is cross-polarized. The mean value of the differences between the two sets of value is $91° \pm 3°$. The measured offsets are used in the data reduction to calibrate the measured position angle for each channel of the array.

Chapter 7

Results

7.1 Introduction

The following sections summarize the results of the observations. For an immediate understanding, the data are showed in terms of polarization degree and position angle, even though all the calculations have been carried out on the Stokes parameters and converted to p and χ just at the end of the reduction process. The position angles are referred to the equator, with zero angle at east and growing counterclockwise (following the rotation of the sky). Polarization has a periodicity of 180° and therefore only angles between 0° and 180° are considered.

7.2 Polarization of point sources: detections

Linear polarization has been detected on two AGNs: 3C279 and 1633+382. On the other point sources we did not detect any polarization at a signal-to-noise better than three sigmas. Nevertheless, we can estimate an upper limit, depending on the integration time and on the flux density of the source. The following sections summarize these results.

7.2.1 3C279

The blazar 3C279 (1253-055) is one of the brightest AGNs in the sky. For this reason it is well known as a pointing source but it is not a good flux calibrator because its flux density is variable. This source is also known to be linearly polarized over a wide range of wavelengths; polarization degree and position angle also are known to be variable

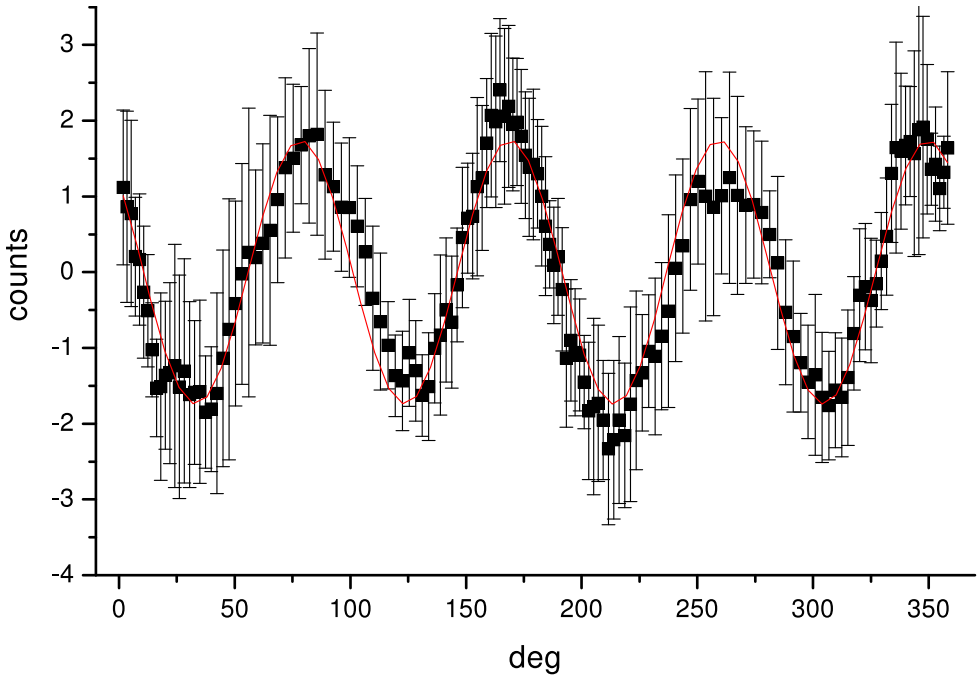

Figure 7.1: Modulation of the polarized signal vs. the RHWP rotation angle, POO scan 1253 on 3C279. The polarization signal is strong enough to fit a sine wave on it. This is the result of a preliminary data reduction. The data are corrected for the RHWP projected angle but not demodulated. See also figure 6.3. Data taken on 2002 January 26, 13:17 U.T..

(for example, see Stevens et al. (1996), Taylor (2000) or Attridge et al. (2000)). During our second telescope run, we performed several observations in total power, either for pointing corrections or in order to check for flux variations. We measured a flux density of about 14 Jy, stable within the errors during our week of observations (see table A.2). We also performed 14 POO scans, 7 per analyzer configuration. Figure 7.1 shows that the polarized signal from this source was so strong that it is possible to fit the data with a sine function. The scan is the number 1253, acquired on the 26th of January 2002, 13:17 U.T., and the plot on the left of figure 6.3 shows the configuration of the array during the observations. Figure 7.2 shows the configuration of the beams on the sky and the measured polarization vectors of each channel for the scans 0451 and 0452. The detection of the signal in the central channel is evident. These are the first two scans that we made on this source, performed on January 19 2002, starting from 9:27 U.T.. The absolute coordinates are given in table 5.1. For comparison, see also figure 6.3 where the last two scans that we made in the 2002 campaign are shown .

Figure 7.3 shows the value of the polarization degree averaged over the 14 scans. The central channel is shown together with the outer channels of the array to compare

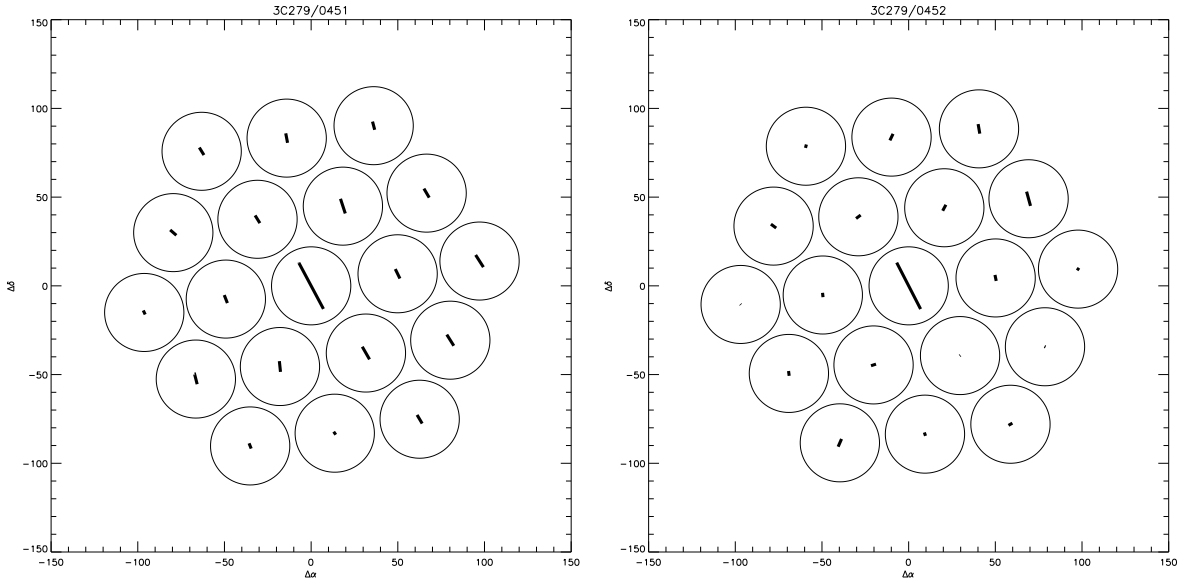

Figure 7.2: Configuration of the beams on the sky and the measured polarization vectors of each channel. *Left*: Scan 0451, performed on January 19 2002, 9:27 U.T., using the horizontal analyzer. *Right*: Scan 0452, performed few minutes later (9:36 U.T.) using the vertical analyzer. Offsets are in arcseconds. The absolute coordinates are given in table 5.1. See also figure 6.3

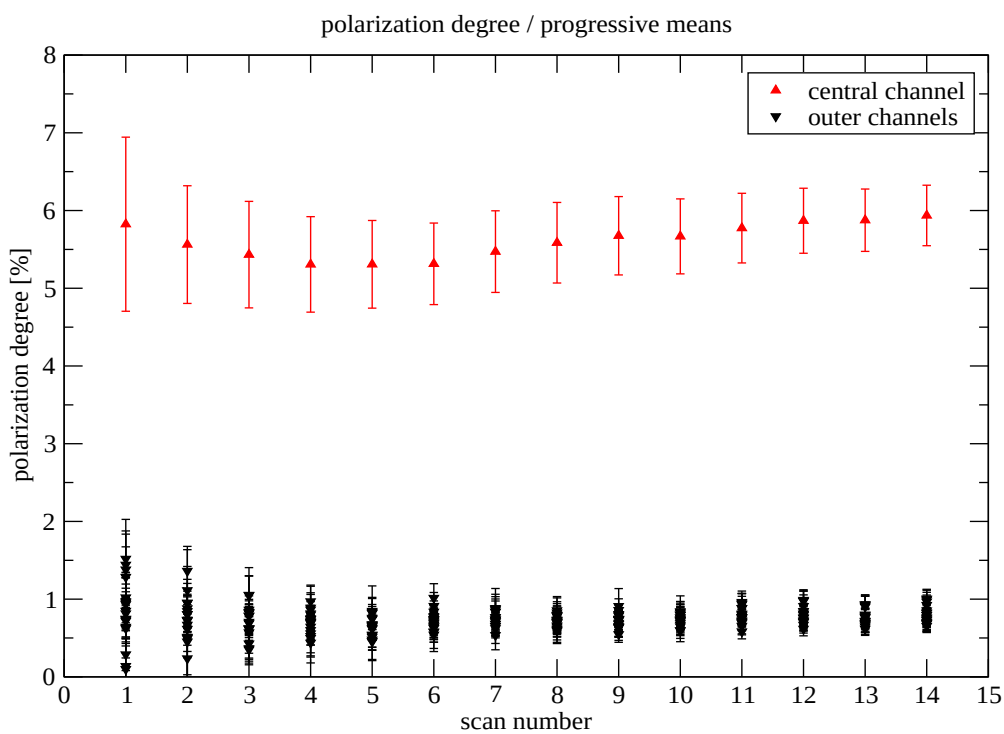

Figure 7.3: Progressive averages of the signals detected in the 14 scans.

the signal from the source with the signal from the empty sky. We can see how the central channel stabilizes its value at about 6% while the outer channels collect only

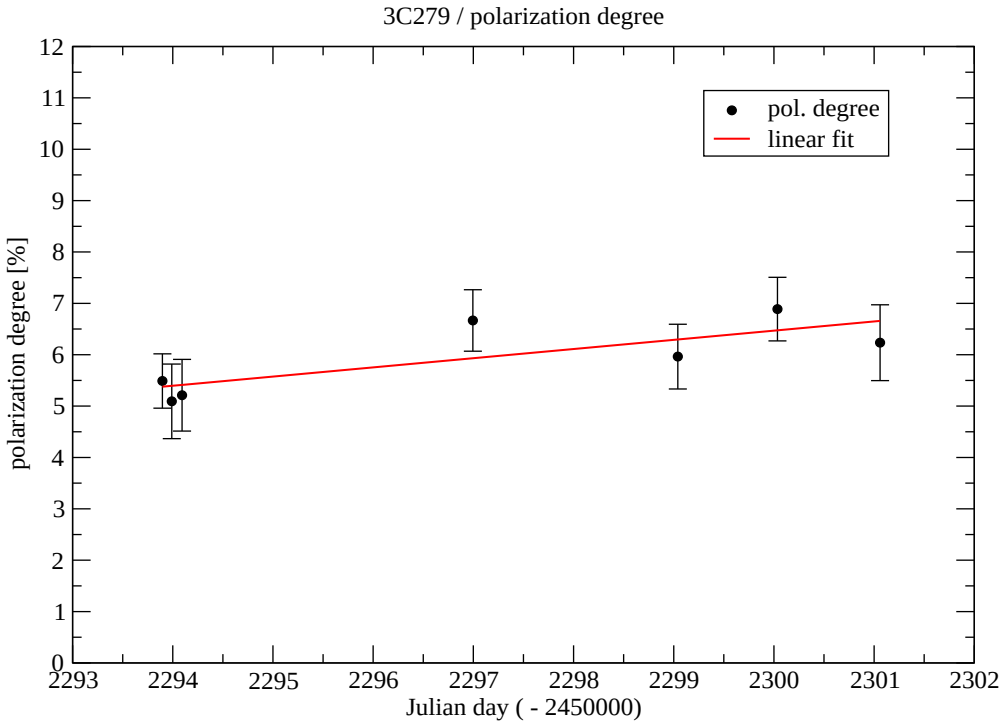

Figure 7.4: Polarization degree vs. Julian day.

noise up to a level that is smaller than 1%. This value could be reduced by removing noise that is correlated on the outer 18 channels of the array, during the data reduction, but this algorithm is not yet implemented in the software. The mean value of the polarization degree, observed during that week, is $p = 5.9 \pm 0.3$ %. Figure 7.4 shows the observed polarization degree during the second run at the telescope. There is no evidence, within the errors, of any indication of a change in the degree of polarization. Each observation is always repeated twice, for the other analyzer configuration and the time interval between the two is only ~ 10 minutes. Therefore, in this plot observations performed in the two configurations have been averaged to one point. The linear fit gives a correlation coefficient of 0.78.

However, we found the most interesting feature in the position angle rather than in the polarization degree. Already by comparing the two plots in figure 7.2 with the two plots in figure 6.3 it is possible to see that the position angle has different values at the beginning and at the end of our observations. Figure 7.5 shows the position angle of 3C279 during the 7 days of operation of PolKa. The angle shows a variation of about 14°. The plot shows also a linear fit of the data. The correlation coefficient of the fit is 0.97. It is well known that the position angle of the polarized radiation emitted by

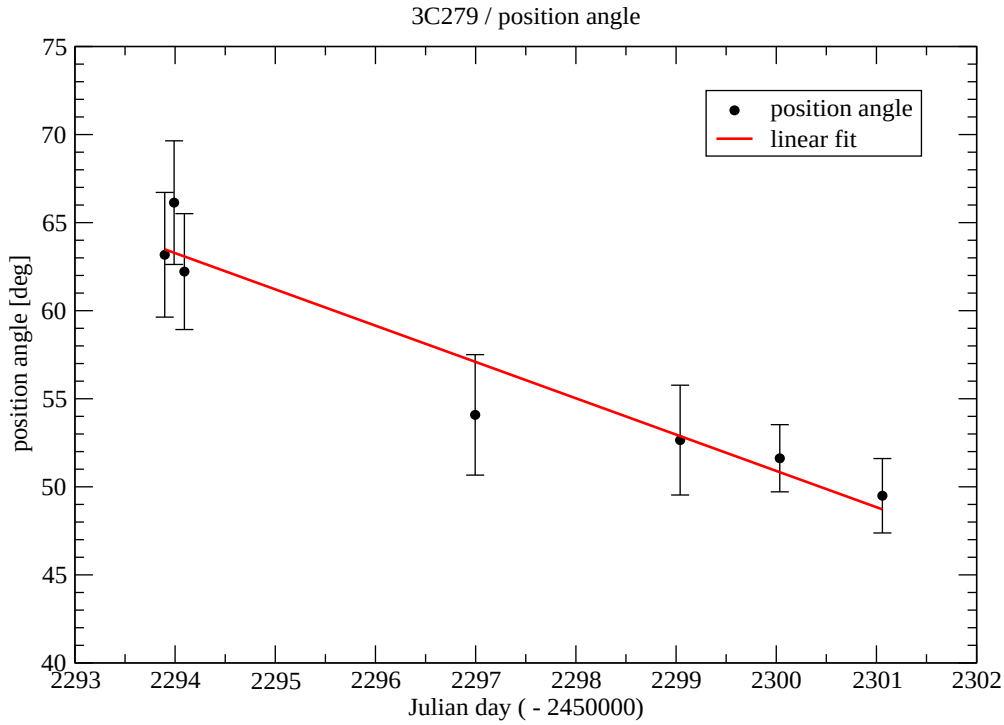

Figure 7.5: Position angle of 3C279 in the 7 days of observations. The variation is about 14°. The linear fit gives a correlation coefficient of 0.97.

the core of 3C279 varies with time. From VLBI (Very Long Baseline Interferometry) observations, Homan et al. (2002) show that in epoch 1996.41 at 15 GHz the position angle of the core polarization of 3C279 was about zero. Taylor (1998) shows that, six month later, in epoch 1997.07, at the same frequency the core has a polarization angle of about 50° and Taylor (2000) shows that in epoch 1998.59, about one year later, at the same frequency, the position angle is different again, about 70°. The three observations seem to be ordered and one could conclude that the variation of about 70° has occurred in just over than two years. On the other hand, these are the only three observations available and we do not know if variations at smaller time scales have occurred too. The data relative to the observations on 3C279 are summarized in table A.2.

7.2.2 1633+382

The second detection of linear polarization is in the quasar 1633+382. This source is not as bright as 3C279 but its flux of about 4 Jy was enough to detect a small percentage of polarization. Figure 7.6 shows the progressive averages of the polarization degree.

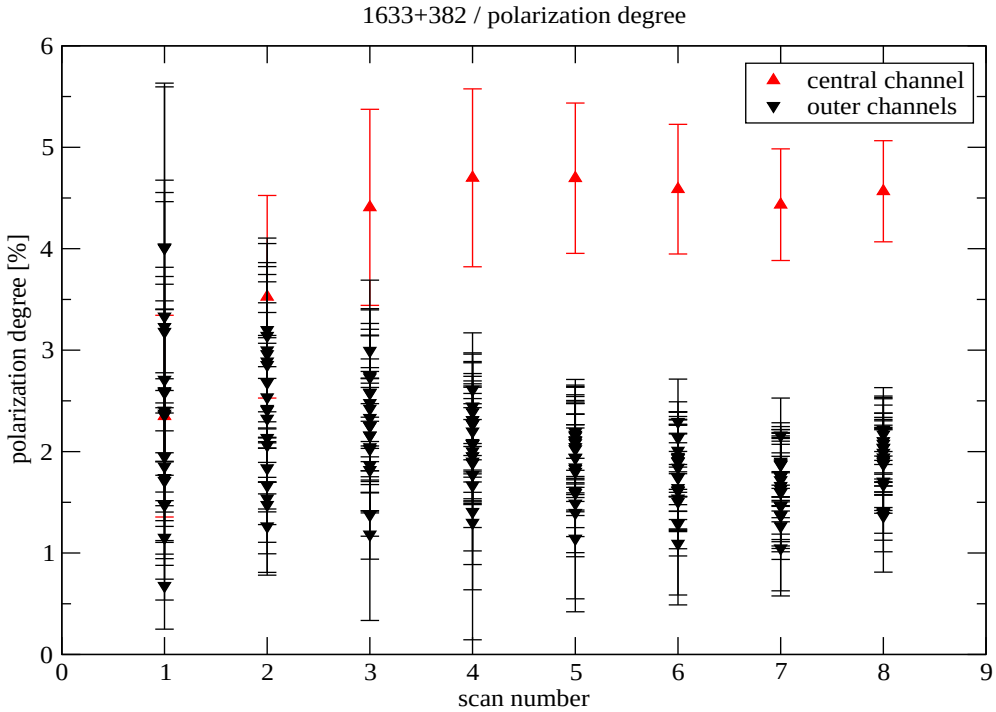

Figure 7.6: Progressive averages of the signals detected in the 8 scans on 1633+382.

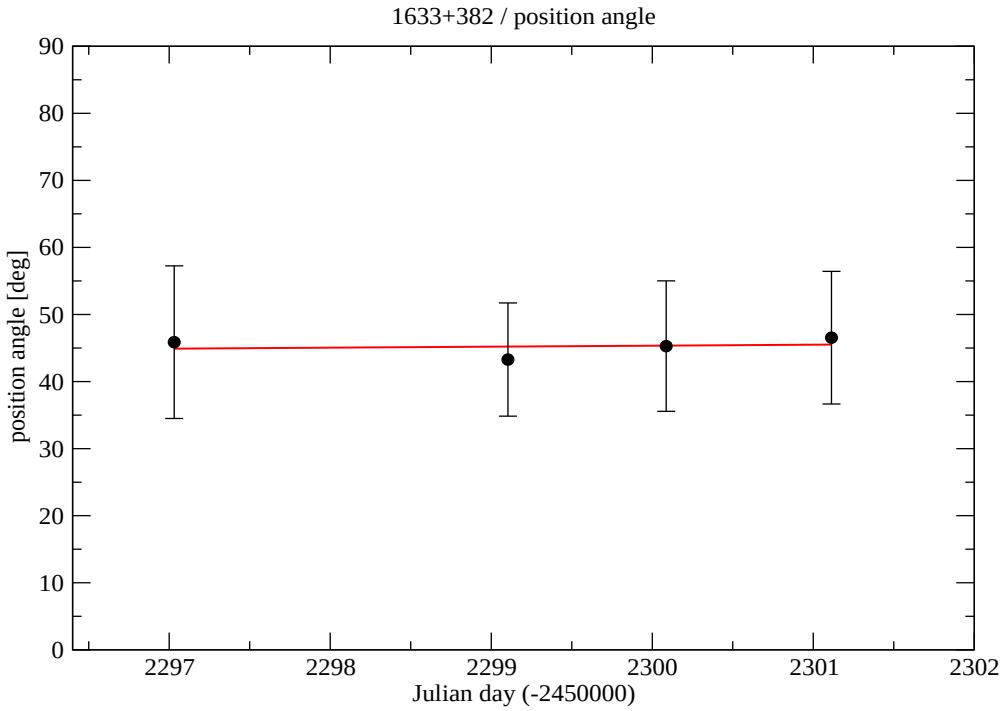

Figure 7.7: Position angle of 1633+382 in the 7 days of observations. There is no evidence of variability.

These observations are more buried in the noise, compared to the observations on 3C279. The observed value, averaged on the 8 scans, is $p = 4.6 \pm 0.5$ %. Figure 7.7

shows the position angle of this source. We see that in this case there is no appreciable variation of the position angle. The observed value is $\chi = 45°.2 \pm 9°.8$, and is in good agreement with the VLBI measurements at 5 GHz, published by Cawthorne et al. (1993). The data relative to the observations on 1633+382 are summarized in table A.1.

7.3 Polarization of point sources: upper limits

The relation 1.37, at the end of the first chapter, gives a criterion to estimate an upper limit to the linear polarization of a source. We observed 14 point sources with the polarimeter but on only two of them we detected a polarization signal. This means that the other sources, at 870 μm, have a polarized flux below the limit of our experiment for that integration time and for the given total flux of the source. Table B.1 gives the values calculated with equation (1.37) for a 3 σ detection, for the sources that we observed.

7.4 Polarization of extended sources

7.4.1 Orion A OMC-1

The large complex called Orion Giant Molecular Cloud is divided in two large areas, Orion A and Orion B, where dark clouds, H II regions, supernova remnants and both high mass and low mass star forming regions coexist. It lies in the Cygnus Arm of our galaxy, only 500 pc from our solar system, it is the closest site of star formation, and is also the most studied. The Orion Molecular Cloud 1 (OMC-1) is a part of the Orion A complex and extends in the area of the sword of the Orion constellation. In front of it, in our direction, is the famous M42 nebula, a compact H II region (diameter of $\sim$ 0.5 pc) that is excited by the young stars of class OB forming the Trapezium Cluster. Figure 7.8 shows the position of Orion OMC-1 in the sky. For comparison, our polarization map is drawn in the same figure.

Within OMC-1, but presumably not too far from its surface, lie four mass concentrations distributed along a ridge (Mundy et al., 1988). One of them is the complex that surrounds the Becklin-Neugebauer object (BN) thought to be about 0.5 pc beneath

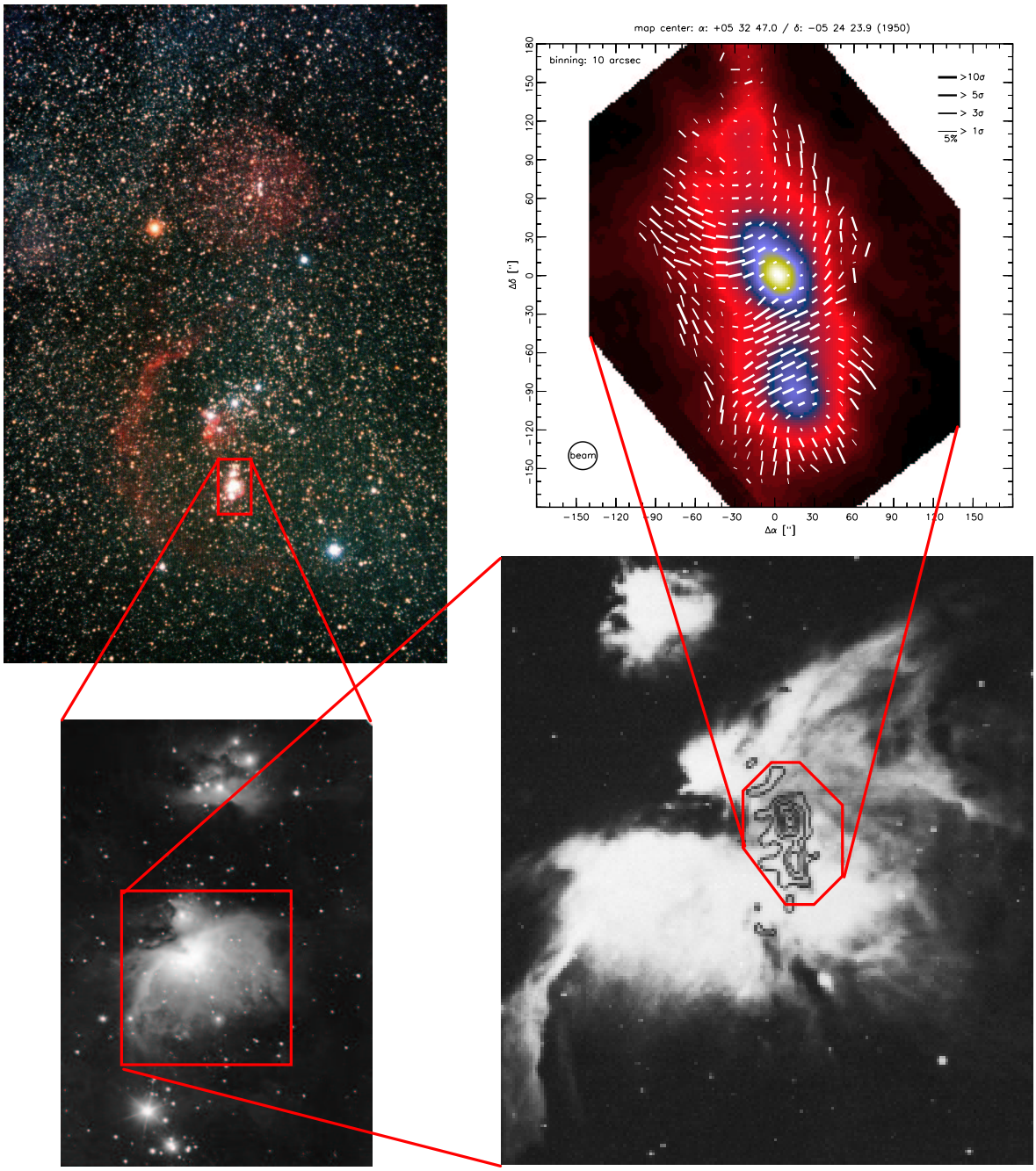

Figure 7.8: On the left side of the figure, the Orion constellation (top) and the M42 nebula (bottom) located in the Orion sword. On the right side, the position of OMC-1 inside the nebula (bottom).

the surface of the Orion Nebula. BN is accompanied by the infrared Kleinmann-Low (KL) nebula. The entire infrared nebula is often referred to as BN/KL. It contains two massive young stellar objects (YSO), one is the BN object and the other is the IRc-2 infrared star, which exhibits a powerful bipolar outflow. This area of OMC-1 is one

of the most powerful submillimeter sources. Another submillimeter peak is found 90″ south of BN/KL, along the Orion ridge and is called KHW after the discoverers Keene, Hildebrand and Whitcomb (Keene et al., 1982). The KHW source is supposed to have the same mass as BN/KL but lower dust temperature.

Magnetic fields are basic to the process of star formation. They influence the macroscopic formation of molecular clouds (Parker, 1966); the magnetic pressure may regulate the star formation rate (Mouschovias, 1976); and once cloud cores have formed they may transfer angular momentum from the core to the outer envelopes, enabling further collapse to form protostars (Mouschovias & Paleologou, 1980). Magnetic fields are also invoked to stop the accretion process: the observed molecular outflows from YSOs could be magnetically driven and their force could halt further accretion (Pudritz & Norman, 1983).

OMC-1 is the molecular cloud that offers the best conditions to study the relation between magnetic fields and star formation. It is close to our solar system and therefore offers more details than other objects. It has a high flux that gives the opportunity to perform observations with high signal-to-noise ratio; it covers a large region of sky and shows extended feature better than any other source; and there is evidence for magnetically regulated star formation in it (Schleuning, 1998).

For all these reasons OMC-1 has been a favorite target for all the polarization experiments, (for example Burton et al., 1991; Chrysostomou et al., 1994; Davidson et al., 1995; Platt et al., 1995; Schleuning et al., 1997; Matthews & Wilson, 2000a; Greaves et al., 2003).

OMC-1 has been our obvious first target to perform `POtF` maps with PolKa. In particular, the strong flux and the possibility of comparing our results with observations made by other groups were the main reasons for this choice.

The map presented here is the result of 12 scans performed during our 2002 telescope campaign. Each scan covers $360'' \times 360''$ and required a bit more than 30 minutes. We can estimate the total integration time to be 6 hours. The graphical output of the data reduction software is shown in figures 7.9 and 7.10. At the end of section 6.1.5 it has been shown that it is possible to display demodulated data in two different ways: polarization degree and polarization intensity. The map in figure 7.9 is a polarization intensity map. It shows the polarized flux, represented by the colors, and the polariza-

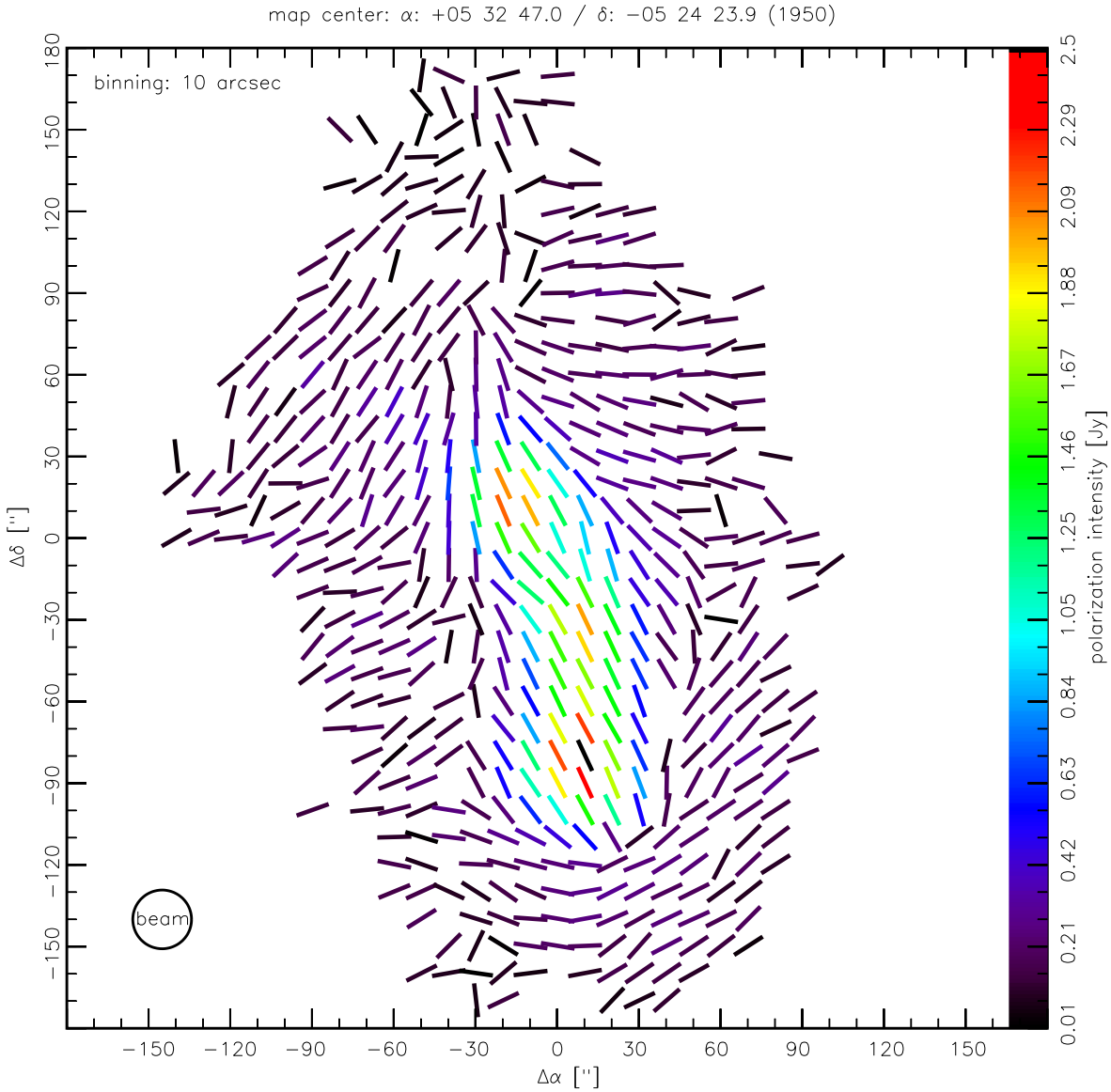

Figure 7.9: Polarization intensity map of Orion OMC-1. The map is centered on IRc-2. The angular resolution is 10″ per polarization vector. All vectors are drawn to the same length. The colors are proportional to the polarized flux. All detections are better than 1 σ. See also figure 7.10.

tion position angle, represented by the direction of the vectors. All the detections are better than 1 σ and vectors are plotted only where the total power flux is more than 2 Jy. In figure 7.10, the same data are displayed in the form of polarization degree map, although the polarization signal is in the Q and U Stokes parameters, and dividing them by the total flux introduces errors. On the other hand, this is the common way to represent polarization data: interpreting the Stokes parameter measured in one point of the cloud as the polarized component of the flux measured at that point.

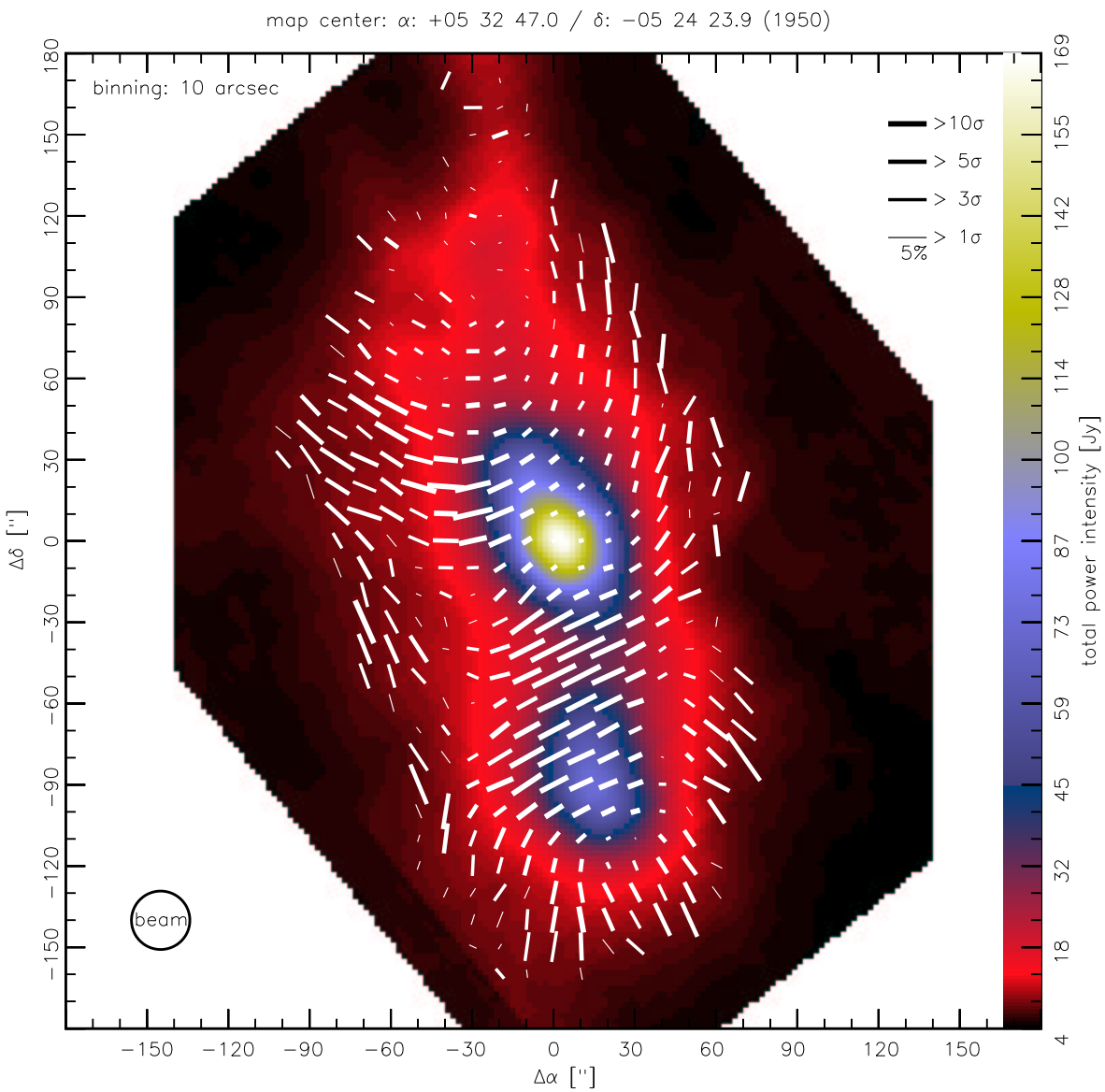

Figure 7.10: Polarization degree map of Orion OMC-1 centered on IRc-2. Polarization vectors are rotated by 90° to show the inferred direction of the magnetic field. The length of the vector is proportional to the polarization degree.

The measured linear polarization indicates the direction of the electric field. In order to show the inferred magnetic field it is common to rotate the polarization vectors by 90°. Figure 7.10 shows the same data as in figure 7.9 but in this case the deduced magnetic field is drawn.

The information shown in the map is manifold. In the background we have a total power map of OMC-1, that gives the information about the spatial distribution of the radiation emitted by the source. On top of it, polarization vectors are drawn with a resolution of 10″ per vector, that is one half of our beam. They carry three different

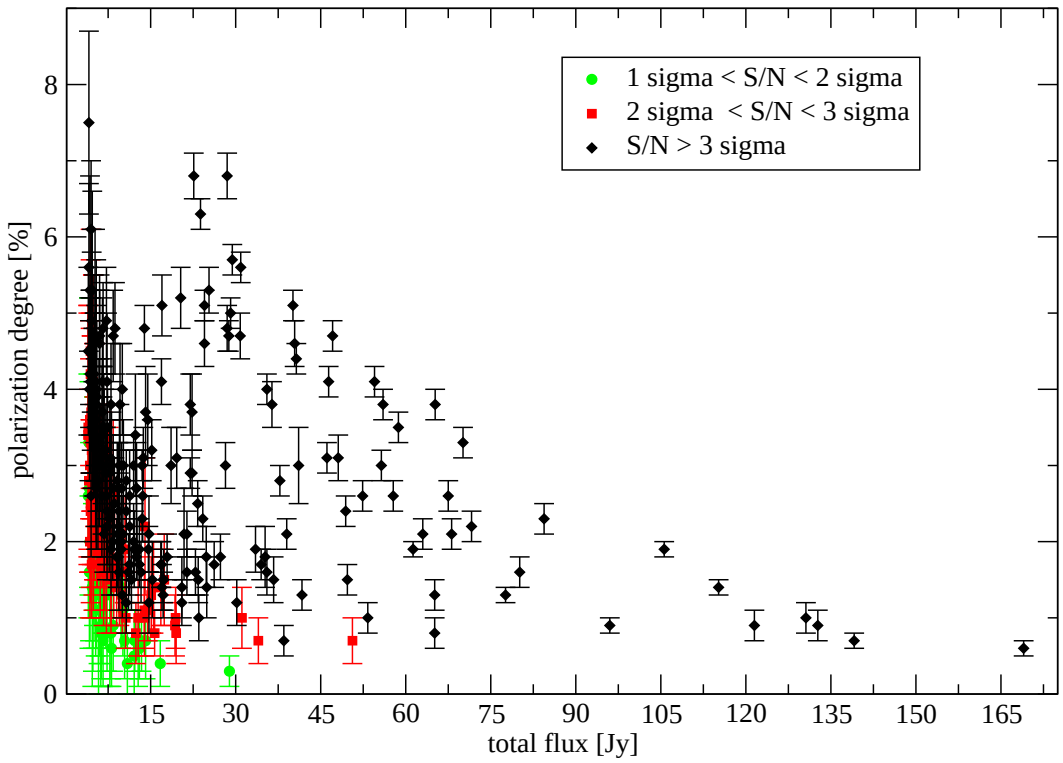

Figure 7.11: Depolarization effect measured by PolKa in OMC-1. Detection better than 3 σ are drawn in black.

pieces of information: the polarization degree, the polarization position angle and the quality of the detection. The polarization degree is proportional to the length of the vectors. In the top right corner is shown the size of a 5% vector, for reference. The position angle is obviously indicated by the direction of the vectors, and it is referred to the equator and increases going from east to west. The quality of the detection is represented by the thickness of the vectors. See the top right corner for the scale of the thickness. The map shows only detections that are better than 1 σ. The total power threshold in this map is fixed to 4 Jy, 2.4% of the peak. Where the total flux is above this threshold, and no vector is drawn, no meaningful polarization signal was detected. The polarization data are also listed in table C.1.

According to equation (1.35) in 12 coverages the NEFD of our system is about 64 mJy. At this level, 1% of polarization is detected at 3 σ where the total flux of the source is about 19 Jy. The maximum flux in the map is in the BN/KL area where the total power has a peak of 169 Jy/beam. In the surroundings of the peak, then, 1% of polarization produces a signal of about 1 Jy and a detection at 15 σ should be possible. We see, however, that the degree of polarization decreases going towards areas of the

map where the total flux is higher. This is a well known depolarization effect, already observed in other dust clouds (Matthews et al., 2001; Houde et al., 2002). Figure 7.11 shows the observed depolarization effect in OMC-1. See also the plot in figure 1.1.

7.4.2 Orion A MMS3/MMS4

Apart from OMC-1, in the Orion A giant molecular cloud there are other two large areas of interest, OMC-2 and OMC-3, that are the consecution of OMC-1 going northwards along the I .e northern

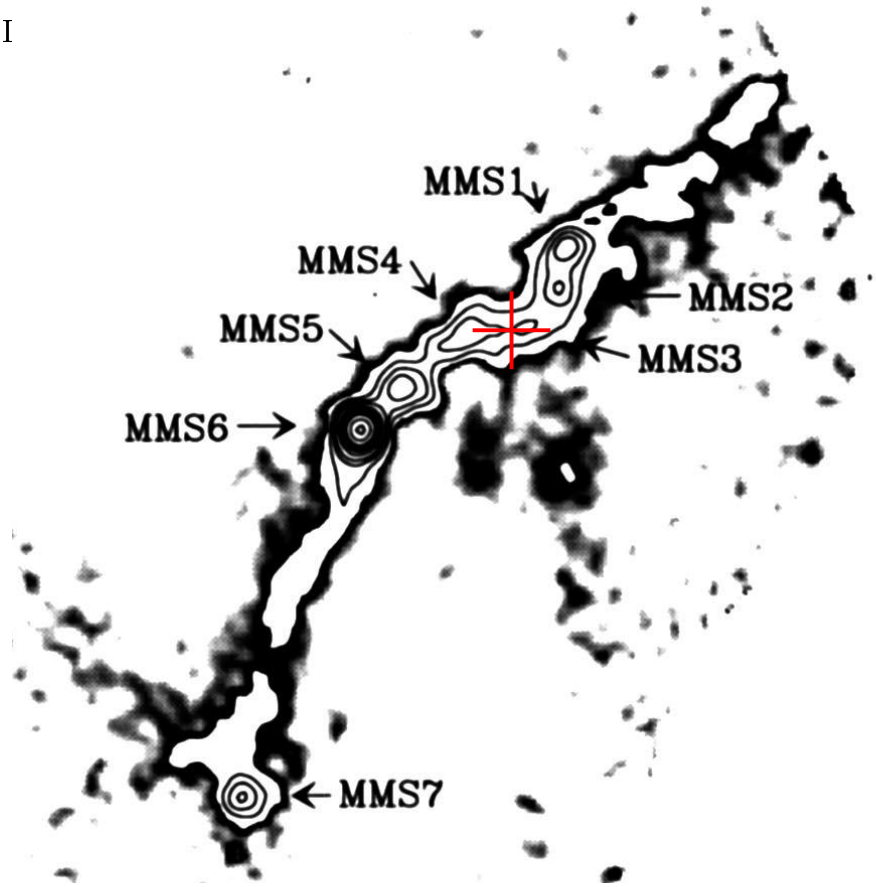

Figure 7.12: Total power map of the Orion OMC-3 region at 1.3 mm by Chini et al. (1997). The red cross indicates the center of our polarization map.

part of OMC-3 where 7 embedded cores have been identified by Chini et al. (1997), named from MMS1 to MMS7. Given the results of Matthews et al. (2001) we decided to scan this area, to test the polarimeter on a dust source of known polarization but weaker than OMC-1. The red cross in figure 7.12 indicates the center of our polarization map, which is shown in figure 7.13. Only three scans were performed, and the total integration time is only 1.5 hours, resulting in a too poor signal-to-noise. The map

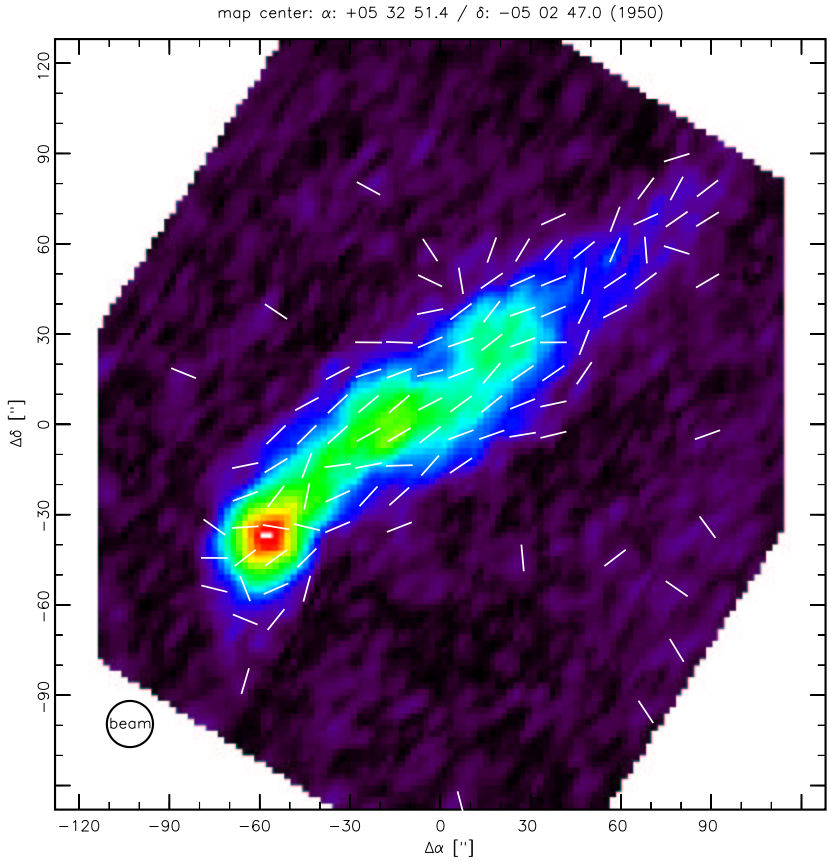

Figure 7.13: Polarization map of Orion OMC-3. The map is centered between the two clumps MMS3 and MMS4. The brightest clump (bottom left) is MMS6 (see also figure 7.12). The vectors have the same length, and show only the position angle of the measured linear polarization.

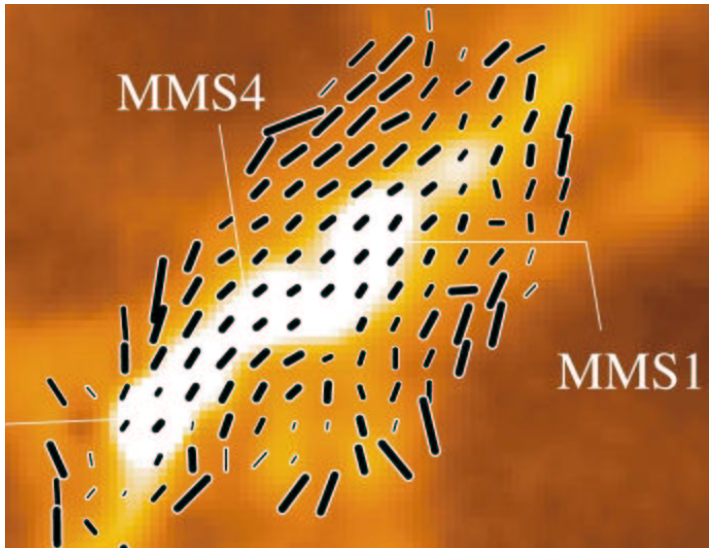

Figure 7.14: Polarization map of the MMS3/MMS4 filament in Orion OMC-3 by Matthews et al. (2001).

has a size of $256'' \times 256''$. The best detection in the map is at 4 σ, but most of the vectors have signal-to-noise between 1 and 3 σ. This map is presented here only to show that, even if the integration time was not enough, the polarization vectors show good accuracy in the detected position angle. Our map shows, in fact, a good agreement with the results published by Matthews et al. (2001), shown in figure 7.14.

7.4.3 IRAS 05358+3543

In recent years massive outflows have been investigated in detail because they can provide information about the innermost parts of star forming regions. The source IRAS 05358+3543 (figure 7.15) is an extremely young and deeply embedded high-mass protostellar object. This source is part of a recent statistical work on massive outflows by Beuther et al. (2002b). They found that low-mass correlations of outflow

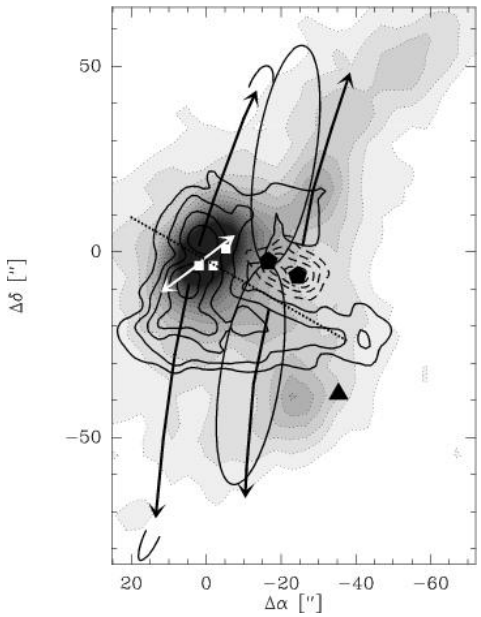

Figure 7.15: The integrated CO 6-5 emission in contours is overlayed on the grey-scale 1.2 mm bolometer map. The overlayed arrows and markers outline the different outflows and sub-sources (from Beuther et al. (2002a)).

and core parameters continue up to the high-mass regime, suggesting that similar star formation processes are responsible for forming stars of all masses. However, massive star formation sites are on average more distant than well known low-mass sources, and thus their angular sizes are smaller in spite of their larger linear sizes. This indicates that high angular resolution is needed to disentangle real source and outflow structures.

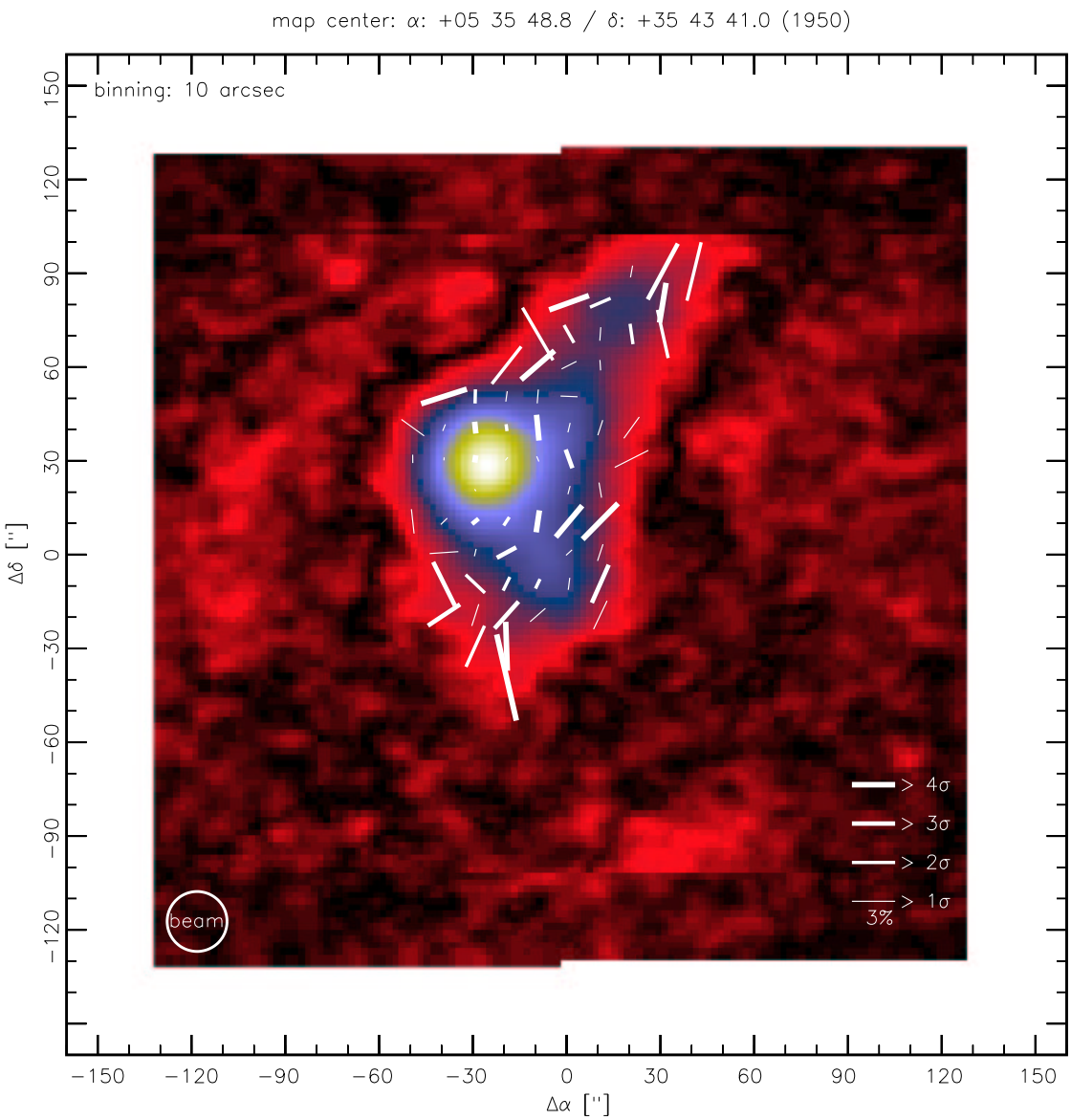

Figure 7.16: Polarization vectors are rotated by 90° to show the inferred magnetic field.

One solution is to study these sources with interferometric techniques at millimeter and submillimeter waves. Ambipolar diffusion is one of the processes regulating the star formation. A by-product of the diffusion is the collisional alignment of dust grains in the molecular cloud. Greaves & Holland (1999) suggest that if the source core is magnetically regulated, then the observed polarization pattern could provide direct information about the dynamics of the grains in the cloud. In this frame, polarization maps can be a powerful way to get information about the order of the structures in the source, and could be a valid complement to interferometric observations. Figure 7.16 shows the first detection of polarization on the source IRAS 05358+3543. We

performed 8 scans on this source, collecting 4 hours of integration time. The size of the map is $320'' \times 320''$. At the HHT the 345 GHz flux peak of the source was 8.4 ± 1.2 Jy/beam, at $\Delta\alpha = -28'', \Delta\delta = 33''$ from the absolute IRAS positions given by Sridharan et al. (2002), where our map is centered. The map shows the polarization vectors rotated by 90° to show the deduced magnetic field directions. All polarimetric detections in the map are better than 1 σ.

From a direct comparison between our polarization map and figure 7.15 (figure 4 in Beuther et al. (2002a)) we can see a correlation between the deduced magnetic field and the direction of the outflows in the source. The polarization signal is subject to the depolarization effect, going toward the most intense areas of the source, behaving in the same way as we found it behaves in low-mass star forming regions. In the north and south edges of the cloud, however, we can see that the strongest polarization signals (detected there at more than 4 σ) are aligned along the direction deduced by Beuther et al. (2002a) for the larger molecular outflows of the source. This is an interesting result that is worthy of further investigation with our polarimeter, at different angular scales and at different wavelengths.

Conclusions

About ten years ago, the first steps were taken toward submillimeter polarimetry, using single-pixel bolometric receivers. Linear polarization of submillimeter continuum radiation can be produced by optically thin synchrotron emission or by the partial magnetic alignment of elongated dust grains. The first type of polarized radiation is dominant in extragalactic objects like radiogalaxies and active galactic nuclei while the second type is common in galactic clouds like molecular outflows, star forming regions and protostellar envelopes. In both cases, magnetic morphology can be deduced from the directions of polarization vectors, and polarimetry at millimeter and submillimeter wavelengths can be more precise than in the optical and radio regimes, where scattering and Faraday rotation dominate the polarized signal. The goal of submillimeter polarimetry is therefore to map the polarization pattern of these sources with the highest possible angular resolution. At submillimeter wavelengths, the instabilities of the atmospheric transmission can be large, and ground based polarimetric observations, requiring high accuracy over periods of minutes to hours, are particularly challenging. In the last few years, great steps have been taken in bolometer development and technology, and today we can make use of large arrays of detectors.

The aim of my Ph.D. project was to provide the Millimeter and Submillimeter Astronomy Group at MPIfR with a polarimeter suitable for the arrays of bolometers developed in the group's Technological Division. The work was started from scratch and grew up following the idea of a versatile instrument, a polarimeter capable of giving good results with any of the MPIfR bolometer arrays, and flexible enough to be installed at any of the telescopes accessible to the group where bolometer arrays are in operation. Bounded by these constraints, in designing PolKa we were motivated

to find unusual solutions, such as the reflection type half-wave plate or the continuous spinning technique. In the end, these choices gave our polarimeter special merits and a touch of uniqueness.

We had to work through the design and the production of many of the elements of which the polarimeter is made: from the production of high-quality large wire-grid polarizers to the design of the reflection type half-wave plates, from the definition of the best strategies for calibrations and observations to the writing of the software for data acquisition, data reduction and for the graphical presentation of the polarization results. PolKa has many characteristics in common with other polarimeters for millimeter and submillimeter wavelengths. In some aspects, however it is unique.

Our polarimeter does not use any crystal or other refractive optical element that could produce selective absorption of the incoming radiation. It uses only metallic reflections and this gives it very low insertion loss and high efficiency.

PolKa is tunable: simply by adjusting three screws is enough to switch from one operating wavelength to another, from one receiver to another. Besides this, PolKa's tunability can be used to transform the half-wave plate to a quarter-wave plate with ease, and the same instrument can be used to perform also circular polarization observations.

The radiation is modulated directly by PolKa, without the need for a chopping secondary mirror. The modulation frequency can be much higher than when using a wobbler, and the polarimeter can be used even in telescopes with a fixed secondary mirror. Furthermore, the polarization signals are restored by digital phase-sensitive detection and not by fitting a sine wave to a noise-dominated signal, as is commonly done in other polarization experiments.

The tests at the telescope showed that PolKa can give high quality polarization data. In particular, it can produce large polarization maps with high signal-to-noise in a relatively short time. Apart from the calibrations and the technical tests, we made observations of several different sources. On the blazar 3C279 we detected linear polarization at a level of 5.6 ± 0.3 %. Furthermore, we observed a variation of the polarization position angle of about 14° in seven days. One more point-like source, the quasar 1633+382, showed a degree of polarization detected by PolKa at the value of 4.6 ± 0.5 %. Other 12 AGNs were observed but no polarization was detected and

we give here only upper limits. However, the best results are given by the large polarization map of Orion OMC-1. For this map, we collected 6 hours of integration time and the polarization detections are very accurate. A depolarization effect is also observed. Other two polarization maps are presented here. One is the first detection of polarization in the IRAS source 05358+3543, a massive protostellar object. The other is presented here only to show how PolKa gives consistent results even in low signal-to-noise condition and it is a map of a filamentary cloud in OMC-3.

However, during the telescope tests we also discovered PolKa's weak points, pinpointing areas where PolKa could be improved. The modulation produced by the reflection type half-wave plate is not a perfect sine wave and this effect can introduce systematic signals reducing the efficiency of the demodulation. To minimize this effect it is important to minimize the incidence angle of the radiation on the half-wave plate. The polarization results presented here, however, were produced with the polarimeter installed at 45°. Another weak point is the angular resolution. Given the fast spinning and the factor of four between mechanical rotation frequency and polarization modulation frequency, it is important to keep minimising the uncertainty on the position angle of the half-wave plate. This is important not only to improve the determination of the polarization position angle but also to improve the intensity of the demodulated signal. The efficiency of the phase-sensitive detection could, in fact, be improved if the phase of the reference signal were known with higher accuracy. In the future, the data acquisition will be triggered by the rotating half-wave plate and this will improve both the demodulation and the angular accuracy.The new version of PolKa will be equipped with quick-look software, for preliminary reduction of the data at the telescope. The data reduction software will be improved and the EKH algorithm will be implemented. The output files will be in the standard FITS format, to be compatible with other software packages.

We are looking forward to installing an improved version of PolKa in other telescopes. The IRAM 30 meter MRT, where MAMBO-2 is operating at 1.2 mm, is one possibility. By using the 117 channel bolometer array and 30 m of collecting area, PolKa could provide unique polarization information of infrared dark cloud and other objects whose thermal radiation is dominated by cold dust.

In few months the new submillimeter telescope APEX on the Atacama desert, in

Chile, will start its operation. This is another possibility where PolKa could work with the new array LABOCA, made of 300 bolometers operating at 870 μm. The combination of PolKa, APEX and LABOCA by virtue of their unique characteristics, will be the most powerful system to observe the polarization of submillimeter continuum radiation.

Appendix A

Polarization `On-Off` data

1633+382

JD	I [Jy]	Q [Jy]	U [Jy]	p [%]	χ [°]
2297.03	5.05 ± 0.66	-0.041 ± 0.080	0.086 ± 0.089	1.78 ± 0.75	57.9 ± 12.4
		0.121 ± 0.078	0.212 ± 0.084	4.15 ± 0.92	30.0 ± 6.9
2299.11	3.78 ± 0.49	0.045 ± 0.087	0.238 ± 0.098	5.15 ± 0.60	39.6 ± 4.3
		-0.002 ± 0.086	0.206 ± 0.094	3.98 ± 0.22	45.3 ± 3.2
2300.09	4.34 ± 0.56	0.003 ± 0.094	0.199 ± 0.081	3.34 ± 0.13	44.4 ± 3.0
		0.002 ± 0.104	0.184 ± 0.072	2.77 ± 0.10	44.8 ± 2.9
2301.12	4.15 ± 0.54	-0.012 ± 0.089	0.141 ± 0.075	1.45 ± 0.44	47.5 ± 9.2
		0.011 ± 0.101	0.235 ± 0.072	4.63 ± 0.19	43.5 ± 3.0

Table A.1: Data relative to the observations carried out on 1633+382 in January 2002. At each epoch were performed one total flux measurement and two polarization measurements (one per analyzer configuration).

3C279

JD	I [Jy]	Q [Jy]	U [Jy]	p [%]	χ [°]
2293.90	15.14 ± 1.66	-0.545 ± 0.109	0.694 ± 0.135	5.70 ± 0.46	64.1 ± 3.6
		-0.456 ± 0.117	0.689 ± 0.144	5.30 ± 0.44	61.7 ± 3.7
2293.99	15.85 ± 1.74	-0.488 ± 0.126	0.684 ± 0.138	5.15 ± 0.48	62.8 ± 3.8
		-0.585 ± 0.143	0.527 ± 0.138	4.78 ± 0.70	69.0 ± 5.0
2294.09	15.73 ± 1.73	-0.452 ± 0.122	0.734 ± 0.134	5.34 ± 0.43	60.8 ± 3.6
		-0.499 ± 0.117	0.676 ± 0.132	5.20 ± 0.46	63.2 ± 3.8
2296.99	15.79 ± 1.74	-0.123 ± 0.109	1.103 ± 0.088	6.96 ± 0.14	48.2 ± 2.9
		-0.496 ± 0.086	0.860 ± 0.083	6.24 ± 0.30	60.0 ± 3.1
2299.04	14.87 ± 1.64	-0.241 ± 0.087	0.985 ± 0.095	6.75 ± 0.18	51.9 ± 2.9
		-0.233 ± 0.094	0.771 ± 0.081	5.34 ± 0.21	53.4 ± 3.0
2300.04	13.62 ± 1.49	-0.200 ± 0.083	0.949 ± 0.106	7.05 ± 0.14	50.9 ± 2.9
		-0.227 ± 0.083	0.897 ± 0.092	6.73 ± 0.16	52.1 ± 2.9
2301.06	13.23 ± 1.45	-0.147 ± 0.072	0.817 ± 0.101	6.20 ± 0.14	50.2 ± 2.9
		-0.106 ± 0.068	0.860 ± 0.086	6.49 ± 0.13	48.5 ± 2.9

Table A.2: Data relative to the observations carried out on 3C279 in January 2002. At each epoch were performed one total flux measurement and two polarization measurements (one per analyzer configuration).

Appendix B

Polarization upper limits

Upper Limits

source	I[Jy]	$p_{3\sigma} \leq$ [%]
0716+714	0.93 ± 0.13	29.7
0736+017	3.48 ± 0.57	6.3
OJ287	1.43 ± 0.30	24.6
0923+392	0.83 ± 0.23	27.0
1055+018	2.06 ± 0.19	12.6
1156+295	1.19 ± 0.18	19.5
3C273	3.46 ± 0.74	7.2
1334-127	2.61 ± 0.15	12.6
3C345	2.11 ± 0.29	17.7
1726+455	1.07 ± 0.11	25.2
1749+096	1.81 ± 0.35	13.8
BL Lac	2.16 ± 0.16	12.6

Table B.1: Upper limits of the linear polarization for the observed AGNs where no polarization was detected. The values are calculated for a 3 σ detection.

Appendix C

Polarization maps data

Orion OMC-1

α	δ	I [Jy]	p [%]	χ [°]
05 32 53.70	-05 24 53.9	4.1	2.8 ± 1.2	140.1 ± 11.8
05 32 53.70	-05 25 03.9	4	2.6 ± 1.6	128.5 ± 18
05 32 53.03	-05 24 33.9	4	3.4 ± 1.6	130.4 ± 13.1
05 32 53.03	-05 24 43.9	4.1	3.3 ± 1.9	162.4 ± 16.4
05 32 53.03	-05 24 53.9	4.4	4.5 ± 1.6	145 ± 10.4
05 32 53.03	-05 25 03.9	4.6	4.5 ± 1.3	132 ± 8.4
05 32 53.03	-05 25 13.9	4.7	3.5 ± 0.8	136.9 ± 6.6
05 32 52.36	-05 24 13.9	4.2	2.7 ± 1.4	158.1 ± 14.9
05 32 52.36	-05 24 23.9	4.9	2.3 ± 1	149.7 ± 11.8
05 32 52.36	-05 24 33.9	5.3	4.1 ± 1.2	132.9 ± 8.2
05 32 52.36	-05 24 43.9	5.1	3.7 ± 0.9	122.4 ± 7.1
05 32 52.36	-05 24 53.9	4.7	5.3 ± 1.3	122.9 ± 7
05 32 52.36	-05 25 03.9	5.3	2.9 ± 1.1	120.9 ± 10.8
05 32 52.36	-05 25 13.9	5.1	2.8 ± 1	118.8 ± 10.5
05 32 52.36	-05 25 23.9	5.1	2.5 ± 1	114.6 ± 11.8
05 32 52.36	-05 25 33.9	4.8	2.4 ± 1.8	130.6 ± 21.2
05 32 52.36	-05 25 43.9	4.5	3.7 ± 1.3	127 ± 9.8
05 32 51.70	-05 23 33.9	4	3.5 ± 1.6	160 ± 13.4
05 32 51.70	-05 23 43.9	4.3	4.2 ± 0.7	158.4 ± 4.4
05 32 51.70	-05 23 53.9	4.5	6.1 ± 0.9	156.2 ± 4.2
05 32 51.70	-05 24 03.9	4.4	3.3 ± 1.5	165.4 ± 13.3
05 32 51.70	-05 24 13.9	4.9	3.4 ± 0.7	150.8 ± 5.6
05 32 51.70	-05 24 23.9	5.7	3.3 ± 0.6	137.9 ± 5.5
05 32 51.70	-05 24 33.9	6	4.7 ± 0.8	107.9 ± 4.9
05 32 51.70	-05 24 43.9	5.9	3.3 ± 1.1	112.3 ± 9.7
05 32 51.70	-05 24 53.9	5.4	4 ± 1.1	114.1 ± 8
05 32 51.70	-05 25 03.9	5.8	2.6 ± 1.1	129.6 ± 12.5

Table C.1: Polarization data of the Orion OMC-1 map. The error on the total intensity is about 5%.

α	δ	I [Jy]	p [%]	χ [°]
05 32 51.70	-05 25 13.9	6.6	4.8 ± 0.6	122.9 ± 3.4
05 32 51.70	-05 25 23.9	7.1	2.9 ± 0.6	123.7 ± 6.2
05 32 51.70	-05 25 33.9	7.3	2.4 ± 0.7	142.8 ± 8.5
05 32 51.70	-05 25 43.9	6.1	1.9 ± 0.9	130.3 ± 12.7
05 32 51.70	-05 25 53.9	5.1	2.8 ± 1.1	117.7 ± 10.9
05 32 51.70	-05 26 13.9	4.5	2.6 ± 0.8	135 ± 8.9
05 32 51.03	-05 23 23.9	4.4	2.4 ± 1.2	164.7 ± 14.5
05 32 51.03	-05 23 33.9	5.3	3.2 ± 1	164.4 ± 9.3
05 32 51.03	-05 23 43.9	5.3	4 ± 1	156.1 ± 6.8
05 32 51.03	-05 23 53.9	5.2	3.4 ± 1.2	151.6 ± 9.9
05 32 51.03	-05 24 03.9	5.4	3 ± 1	137.8 ± 9.7
05 32 51.03	-05 24 13.9	6	2.4 ± 0.9	169.5 ± 11.1
05 32 51.03	-05 24 23.9	6.4	2 ± 1.1	140.9 ± 15.7
05 32 51.03	-05 24 33.9	6.7	3.5 ± 0.7	120.6 ± 6
05 32 51.03	-05 24 43.9	6.7	3.5 ± 0.7	126.9 ± 6.1
05 32 51.03	-05 24 53.9	6.5	3.5 ± 0.8	122.9 ± 6.8
05 32 51.03	-05 25 03.9	7.2	4.9 ± 0.7	120.3 ± 3.9
05 32 51.03	-05 25 13.9	8.4	4.7 ± 0.6	117.8 ± 3.5
05 32 51.03	-05 25 23.9	9.8	2 ± 0.6	117.1 ± 8.6
05 32 51.03	-05 25 33.9	9.5	1.6 ± 0.7	122.4 ± 12.8
05 32 51.03	-05 25 43.9	8.1	0.6 ± 0.5	132.7 ± 22.7
05 32 51.03	-05 26 13.9	6.8	2.1 ± 0.5	126 ± 7
05 32 51.03	-05 26 23.9	5.3	1.6 ± 1.1	141.6 ± 19
05 32 50.36	-05 22 43.9	4.3	2 ± 1.3	156.7 ± 18.8
05 32 50.36	-05 22 53.9	4.1	5.6 ± 1.1	157.4 ± 5.8
05 32 50.36	-05 23 03.9	4.4	4.2 ± 1.5	146.3 ± 10.1
05 32 50.36	-05 23 33.9	6.2	2.6 ± 1.2	137.4 ± 13.3
05 32 50.36	-05 23 43.9	6.5	4.1 ± 1.1	147.2 ± 7.4
05 32 50.36	-05 23 53.9	6	1.5 ± 1	147.2 ± 18.5
05 32 50.36	-05 24 03.9	6.2	0.8 ± 0.7	113.2 ± 27.2
05 32 50.36	-05 24 23.9	7.8	2.9 ± 0.9	113.1 ± 8.9
05 32 50.36	-05 24 33.9	8.4	2.6 ± 1	117.3 ± 11.4
05 32 50.36	-05 24 43.9	8.7	4.8 ± 0.6	106.5 ± 3.8
05 32 50.36	-05 24 53.9	9.6	3.8 ± 0.8	104.5 ± 5.9
05 32 50.36	-05 25 03.9	10	4 ± 0.6	113.4 ± 4.4
05 32 50.36	-05 25 13.9	11.3	2.2 ± 0.5	108.1 ± 6.4
05 32 50.36	-05 25 23.9	12.2	0.7 ± 0.4	121.8 ± 18.1
05 32 50.36	-05 25 33.9	10	1.3 ± 0.5	123.2 ± 11.2
05 32 50.36	-05 25 43.9	8	1.9 ± 0.6	117.4 ± 9.1
05 32 50.36	-05 25 53.9	8	1.4 ± 0.8	130.1 ± 15.7
05 32 50.36	-05 26 23.9	5.8	1.1 ± 1.1	155.7 ± 27.2
05 32 49.70	-05 22 13.9	4.8	1.4 ± 1.1	24.8 ± 22

Table C.1: Polarization data of the Orion OMC-1 map (continued).

α	δ	I [Jy]	p [%]	χ [°]
05 32 49.70	-05 22 33.9	5.5	3.9 ± 1	7.3 ± 7.5
05 32 49.70	-05 22 43.9	5.4	4.7 ± 1	9.1 ± 5.8
05 32 49.70	-05 23 03.9	6.4	1.9 ± 1.1	143.6 ± 16.4
05 32 49.70	-05 23 13.9	6.7	1.6 ± 0.7	143.6 ± 12.8
05 32 49.70	-05 23 23.9	7.2	1.6 ± 0.8	153.5 ± 14.8
05 32 49.70	-05 23 53.9	7.3	1.3 ± 1	165.9 ± 22.4
05 32 49.70	-05 24 03.9	8.5	1.7 ± 0.7	115.2 ± 11.2
05 32 49.70	-05 24 13.9	10.5	1.9 ± 0.7	90.8 ± 10.6
05 32 49.70	-05 24 23.9	12.3	3.4 ± 0.8	91.6 ± 6.7
05 32 49.70	-05 24 33.9	13.7	3.1 ± 0.4	91.9 ± 3.8
05 32 49.70	-05 24 43.9	13.9	4.8 ± 0.3	94.3 ± 2
05 32 49.70	-05 24 53.9	15.2	3.2 ± 0.4	95.6 ± 3.6
05 32 49.70	-05 25 03.9	14.7	2.1 ± 0.5	106.2 ± 6.3
05 32 49.70	-05 25 13.9	13.9	1 ± 0.5	96.3 ± 14.3
05 32 49.70	-05 25 23.9	12.8	0.6 ± 0.5	76.8 ± 20.7
05 32 49.70	-05 25 33.9	10.7	1.2 ± 0.4	126 ± 9.9
05 32 49.70	-05 25 43.9	9	1.4 ± 0.5	129.7 ± 9.7
05 32 49.70	-05 25 53.9	9.8	1.9 ± 0.6	130.3 ± 8.6
05 32 49.70	-05 26 13.9	10.4	0.7 ± 0.5	139.3 ± 21.2
05 32 49.70	-05 26 23.9	8	0.8 ± 0.6	174.9 ± 20.7
05 32 49.70	-05 27 13.9	4.4	2.5 ± 1.1	24.5 ± 12.1
05 32 49.03	-05 22 03.9	4.7	1.4 ± 1.3	17.4 ± 25.7
05 32 49.03	-05 22 13.9	5.4	1.3 ± 0.7	32.5 ± 14.7
05 32 49.03	-05 22 23.9	6.2	2.8 ± 1	2.8 ± 10.6
05 32 49.03	-05 22 33.9	7.3	2.2 ± 0.7	20.2 ± 9.3
05 32 49.03	-05 22 43.9	8.3	2 ± 0.5	32.3 ± 7.3
05 32 49.03	-05 22 53.9	9	1.8 ± 0.5	62.8 ± 7.7
05 32 49.03	-05 23 03.9	9.7	1.6 ± 0.6	57.8 ± 10.1
05 32 49.03	-05 23 33.9	9.4	1.6 ± 0.5	113.3 ± 8.8
05 32 49.03	-05 23 43.9	9.4	1.6 ± 0.6	98.2 ± 10.7
05 32 49.03	-05 24 13.9	17.4	1.5 ± 0.6	87.6 ± 12
05 32 49.03	-05 24 23.9	22.3	3.7 ± 0.5	77.4 ± 3.9
05 32 49.03	-05 24 33.9	25.3	5.3 ± 0.3	77 ± 1.8
05 32 49.03	-05 24 43.9	28.5	4.8 ± 0.3	76.9 ± 1.8
05 32 49.03	-05 24 53.9	28.2	3 ± 0.3	79.5 ± 3
05 32 49.03	-05 25 03.9	23.4	1.5 ± 0.3	89.4 ± 6.3
05 32 49.03	-05 25 13.9	17.9	1.8 ± 0.3	84.7 ± 4
05 32 49.03	-05 25 23.9	14.6	1.9 ± 0.3	88.9 ± 4.3
05 32 49.03	-05 25 33.9	13	1.7 ± 0.3	89.2 ± 5.8
05 32 49.03	-05 25 43.9	12.8	1 ± 0.5	62.6 ± 13.2
05 32 49.03	-05 25 53.9	13	0.6 ± 0.4	136.2 ± 18.5
05 32 49.03	-05 26 13.9	13.4	0.7 ± 0.4	126.6 ± 17.4

Table C.1: Polarization data of the Orion OMC-1 map (continued).

α	δ	I [Jy]	p [%]	χ [°]
05 32 49.03	-05 26 23.9	10.6	1 ± 0.4	105.2 ± 10.9
05 32 49.03	-05 26 33.9	7.8	0.8 ± 0.7	120.7 ± 25
05 32 49.03	-05 27 03.9	5.5	2.4 ± 0.9	89.6 ± 10.1
05 32 48.36	-05 21 43.9	4.6	1.7 ± 0.7	139.5 ± 12.7
05 32 48.36	-05 22 03.9	5.4	2.2 ± 1.2	21.3 ± 16.1
05 32 48.36	-05 22 13.9	5.5	2.6 ± 1.2	35.2 ± 12.6
05 32 48.36	-05 22 23.9	7.2	2.2 ± 0.8	15.1 ± 9.9
05 32 48.36	-05 22 33.9	9.5	3 ± 0.8	23 ± 7.3
05 32 48.36	-05 22 43.9	12	2 ± 0.5	51.9 ± 7.3
05 32 48.36	-05 22 53.9	14.1	3.7 ± 0.6	66.7 ± 4.2
05 32 48.36	-05 23 03.9	14.5	3.6 ± 0.6	58.7 ± 4.8
05 32 48.36	-05 23 13.9	13.5	3 ± 0.2	50.9 ± 2.3
05 32 48.36	-05 23 23.9	12.6	1.9 ± 0.4	57.1 ± 5.2
05 32 48.36	-05 23 33.9	12.5	2.7 ± 0.6	75.9 ± 6.3
05 32 48.36	-05 23 43.9	12.5	2.7 ± 0.5	71.7 ± 5.7
05 32 48.36	-05 23 53.9	14	2.2 ± 0.9	62.9 ± 11.4
05 32 48.36	-05 24 03.9	20.9	2.1 ± 0.6	45 ± 8.2
05 32 48.36	-05 24 13.9	35.2	1.8 ± 0.4	56.6 ± 6.9
05 32 48.36	-05 24 23.9	48.1	3.1 ± 0.3	66.1 ± 2.4
05 32 48.36	-05 24 33.9	56	3.8 ± 0.2	67.3 ± 1.2
05 32 48.36	-05 24 43.9	58.7	3.5 ± 0.2	65.1 ± 1.7
05 32 48.36	-05 24 53.9	52.4	2.6 ± 0.2	66 ± 2.5
05 32 48.36	-05 25 03.9	34.5	1.7 ± 0.2	69.6 ± 3.6
05 32 48.36	-05 25 13.9	21.4	1.6 ± 0.3	76.8 ± 5.7
05 32 48.36	-05 25 23.9	16.8	1.7 ± 0.3	72.3 ± 5.3
05 32 48.36	-05 25 33.9	15.3	1.5 ± 0.5	59.1 ± 8.6
05 32 48.36	-05 25 43.9	14.7	1.2 ± 0.4	48.5 ± 10.1
05 32 48.36	-05 26 03.9	14.1	0.7 ± 0.5	95.7 ± 19.1
05 32 48.36	-05 26 23.9	12.1	0.5 ± 0.5	85.5 ± 24.8
05 32 48.36	-05 26 53.9	7.4	2.2 ± 0.5	69.6 ± 6.4
05 32 48.36	-05 27 03.9	6.3	0.9 ± 0.7	63.4 ± 23.1
05 32 48.36	-05 27 13.9	6.6	0.7 ± 0.6	165.9 ± 23.8
05 32 47.70	-05 21 53.9	5.1	3.8 ± 1.2	8.2 ± 9.4
05 32 47.70	-05 22 03.9	5.7	2.7 ± 1	4.2 ± 10.4
05 32 47.70	-05 22 13.9	6.8	1.7 ± 0.9	24.2 ± 14.8
05 32 47.70	-05 22 23.9	8.4	2.7 ± 0.7	14.6 ± 7.6
05 32 47.70	-05 22 33.9	13.6	2.6 ± 0.6	27.4 ± 6.4
05 32 47.70	-05 22 43.9	19.6	3.1 ± 0.4	52.9 ± 3.2
05 32 47.70	-05 22 53.9	24.5	4.6 ± 0.3	56.1 ± 2
05 32 47.70	-05 23 03.9	24.5	5.1 ± 0.2	60.7 ± 1.4
05 32 47.70	-05 23 13.9	22	3.8 ± 0.4	61 ± 2.7
05 32 47.70	-05 23 23.9	18.6	3 ± 0.5	61.3 ± 4.8

Table C.1: Polarization data of the Orion OMC-1 map (continued).

α	δ	I [Jy]	p [%]	χ [°]
05 32 47.70	-05 23 33.9	16.9	4.1 ± 0.3	64.5 ± 2.4
05 32 47.70	-05 23 43.9	17	5.1 ± 0.4	63.1 ± 2.5
05 32 47.70	-05 23 53.9	20.3	5.2 ± 0.4	54 ± 2.2
05 32 47.70	-05 24 03.9	41.1	3 ± 0.5	41.4 ± 5.1
05 32 47.70	-05 24 13.9	80.1	1.6 ± 0.2	48.5 ± 3.3
05 32 47.70	-05 24 23.9	115.2	1.4 ± 0.1	58.5 ± 2.9
05 32 47.70	-05 24 33.9	105.6	1.9 ± 0.1	62.8 ± 1.7
05 32 47.70	-05 24 43.9	84.4	2.3 ± 0.2	58.5 ± 1.9
05 32 47.70	-05 24 53.9	63	2.1 ± 0.2	57.2 ± 2.1
05 32 47.70	-05 25 03.9	36.7	1.5 ± 0.3	49.2 ± 6
05 32 47.70	-05 25 13.9	20.5	1.4 ± 0.4	41.7 ± 8
05 32 47.70	-05 25 23.9	15.7	0.8 ± 0.3	27.3 ± 10.6
05 32 47.70	-05 25 33.9	13.9	1.1 ± 0.5	23.7 ± 13.2
05 32 47.70	-05 25 43.9	12.4	0.8 ± 0.4	19.3 ± 14
05 32 47.70	-05 26 13.9	10.9	0.4 ± 0.4	21.3 ± 26.1
05 32 47.03	-05 21 53.9	4.8	4.1 ± 1.4	9.3 ± 9.6
05 32 47.03	-05 22 03.9	6.5	3.5 ± 0.8	9.9 ± 6.8
05 32 47.03	-05 22 13.9	7.9	3.1 ± 0.5	11.6 ± 4.8
05 32 47.03	-05 22 23.9	12.1	1.9 ± 0.5	13 ± 7.2
05 32 47.03	-05 22 33.9	21.4	2.1 ± 0.3	39.1 ± 4.7
05 32 47.03	-05 22 43.9	37.8	2.8 ± 0.2	56.8 ± 2.1
05 32 47.03	-05 22 53.9	46.4	4.1 ± 0.2	62.4 ± 1.2
05 32 47.03	-05 23 03.9	47.1	4.7 ± 0.2	62.5 ± 1.1
05 32 47.03	-05 23 13.9	40.4	4.6 ± 0.3	62.1 ± 1.6
05 32 47.03	-05 23 23.9	30.8	4.7 ± 0.3	64.7 ± 1.6
05 32 47.03	-05 23 33.9	23.8	6.3 ± 0.2	63.6 ± 1
05 32 47.03	-05 23 43.9	22.6	6.8 ± 0.3	63.1 ± 1.1
05 32 47.03	-05 23 53.9	30.9	5.6 ± 0.2	60.6 ± 1.3
05 32 47.03	-05 24 03.9	68.1	2.1 ± 0.2	51.9 ± 2.6
05 32 47.03	-05 24 13.9	132.7	0.9 ± 0.2	51.3 ± 5.6
05 32 47.03	-05 24 23.9	169	0.6 ± 0.1	66.2 ± 6.1
05 32 47.03	-05 24 33.9	130.6	1 ± 0.2	62.3 ± 5.7
05 32 47.03	-05 24 43.9	77.6	1.3 ± 0.1	55.1 ± 2.6
05 32 47.03	-05 24 53.9	49.7	1.5 ± 0.2	51.4 ± 3.6
05 32 47.03	-05 25 03.9	30.2	1.2 ± 0.3	41.7 ± 6.2
05 32 47.03	-05 25 13.9	17.3	1.5 ± 0.4	18.1 ± 6.9
05 32 47.03	-05 25 23.9	13.3	1.6 ± 0.4	21.9 ± 6.9
05 32 47.03	-05 25 33.9	11.3	1.7 ± 0.4	18.5 ± 6.6
05 32 47.03	-05 25 43.9	9.8	1.3 ± 0.7	7.5 ± 15.7
05 32 47.03	-05 25 53.9	8	1.6 ± 0.7	179 ± 12.1
05 32 47.03	-05 26 03.9	6.9	2.3 ± 0.9	164.5 ± 10.7
05 32 47.03	-05 26 13.9	6.6	2.4 ± 0.9	156.1 ± 10.9

Table C.1: Polarization data of the Orion OMC-1 map (continued).

α	δ	I [Jy]	p [%]	χ [°]
05 32 47.03	-05 26 23.9	5.8	2.6 ± 0.9	167 ± 10.4
05 32 47.03	-05 26 33.9	5	2.5 ± 1	12.6 ± 11.1
05 32 46.36	-05 21 43.9	4.2	1.6 ± 1	169.4 ± 17.3
05 32 46.36	-05 21 53.9	5.3	3.6 ± 0.8	177.8 ± 6.1
05 32 46.36	-05 22 03.9	7.4	3.5 ± 0.5	169.6 ± 4.1
05 32 46.36	-05 22 13.9	9.9	2.7 ± 0.6	170.2 ± 6.6
05 32 46.36	-05 22 23.9	16.9	1.7 ± 0.3	7.2 ± 4.3
05 32 46.36	-05 22 33.9	35.5	1.6 ± 0.3	47.8 ± 5.1
05 32 46.36	-05 22 43.9	57.8	2.6 ± 0.2	61.6 ± 2
05 32 46.36	-05 22 53.9	70.1	3.3 ± 0.2	65.5 ± 1.4
05 32 46.36	-05 23 03.9	65.2	3.8 ± 0.2	65.1 ± 1.2
05 32 46.36	-05 23 13.9	54.5	4.1 ± 0.2	61.8 ± 1.1
05 32 46.36	-05 23 23.9	40.7	4.4 ± 0.2	62.8 ± 1.4
05 32 46.36	-05 23 33.9	29.4	5.7 ± 0.2	62.8 ± 1.1
05 32 46.36	-05 23 43.9	28.5	6.8 ± 0.3	64.2 ± 1.2
05 32 46.36	-05 23 53.9	40.1	5.1 ± 0.2	64.7 ± 1
05 32 46.36	-05 24 03.9	71.6	2.2 ± 0.2	63.6 ± 2.5
05 32 46.36	-05 24 13.9	121.5	0.9 ± 0.2	73 ± 5.8
05 32 46.36	-05 24 23.9	139.1	0.7 ± 0.1	76.5 ± 5.2
05 32 46.36	-05 24 33.9	96	0.9 ± 0.1	65.2 ± 3.9
05 32 46.36	-05 24 43.9	53.3	1 ± 0.2	51.1 ± 6.7
05 32 46.36	-05 24 53.9	34	0.7 ± 0.3	30.7 ± 9.7
05 32 46.36	-05 25 03.9	23.5	1 ± 0.3	23.9 ± 8.1
05 32 46.36	-05 25 13.9	15.1	1.3 ± 0.5	30.9 ± 10.8
05 32 46.36	-05 25 23.9	11.1	1.6 ± 0.5	6.7 ± 8.7
05 32 46.36	-05 25 33.9	9.3	1.8 ± 0.3	8.8 ± 4.2
05 32 46.36	-05 25 53.9	6.5	3.7 ± 0.7	169.5 ± 5.5
05 32 46.36	-05 26 03.9	5.6	2.4 ± 1	177.3 ± 12.1
05 32 46.36	-05 26 13.9	5.1	2.5 ± 1.4	167.6 ± 15.7
05 32 45.70	-05 21 53.9	5	2.4 ± 1.5	141.9 ± 17.9
05 32 45.70	-05 22 03.9	7.1	3.2 ± 0.6	156.3 ± 5
05 32 45.70	-05 22 13.9	10.7	2.8 ± 0.4	153.1 ± 4.5
05 32 45.70	-05 22 23.9	19.3	0.9 ± 0.4	153.8 ± 11.6
05 32 45.70	-05 22 33.9	38.5	0.7 ± 0.2	60.2 ± 9
05 32 45.70	-05 22 43.9	61.3	1.9 ± 0.1	64.4 ± 2.1
05 32 45.70	-05 22 53.9	67.5	2.6 ± 0.2	67.6 ± 1.7
05 32 45.70	-05 23 03.9	55.7	3 ± 0.2	64 ± 2.2
05 32 45.70	-05 23 13.9	46.1	3.1 ± 0.2	60.4 ± 1.7
05 32 45.70	-05 23 23.9	35.5	4 ± 0.2	63.7 ± 1.6
05 32 45.70	-05 23 33.9	28.8	4.7 ± 0.2	65.2 ± 1.3
05 32 45.70	-05 23 43.9	29.1	5 ± 0.2	65.2 ± 1.4
05 32 45.70	-05 23 53.9	36.4	3.8 ± 0.3	64.3 ± 2

Table C.1: Polarization data of the Orion OMC-1 map (continued).

α	δ	I [Jy]	p [%]	χ [°]
05 32 45.70	-05 24 03.9	49.4	2.4 ± 0.2	67 ± 2.6
05 32 45.70	-05 24 13.9	65.1	1.3 ± 0.2	73.5 ± 3.9
05 32 45.70	-05 24 23.9	65.1	0.8 ± 0.2	69.9 ± 6.4
05 32 45.70	-05 24 33.9	50.6	0.7 ± 0.3	50.5 ± 10.1
05 32 45.70	-05 24 43.9	31.1	1 ± 0.4	20.9 ± 10.6
05 32 45.70	-05 24 53.9	22.9	1.6 ± 0.3	20.7 ± 5.9
05 32 45.70	-05 25 03.9	17	1.4 ± 0.3	23.2 ± 6.7
05 32 45.70	-05 25 13.9	12.5	1.8 ± 0.3	22.5 ± 5.4
05 32 45.70	-05 25 23.9	9.4	2.2 ± 0.7	6.3 ± 9.4
05 32 45.70	-05 25 33.9	8	1.5 ± 0.7	12.3 ± 13.9
05 32 45.70	-05 25 43.9	6.9	1.8 ± 0.7	10 ± 10.9
05 32 45.70	-05 25 53.9	6	4.6 ± 0.7	175.2 ± 4.7
05 32 45.70	-05 26 03.9	5	3.3 ± 1.3	174.5 ± 11
05 32 45.70	-05 26 13.9	4.3	5.3 ± 1.5	165.3 ± 7.8
05 32 45.03	-05 21 53.9	4.3	3 ± 1.4	131.6 ± 13.2
05 32 45.03	-05 22 03.9	6.4	2.6 ± 0.8	150.7 ± 9
05 32 45.03	-05 22 13.9	9.1	2.8 ± 0.5	152 ± 5.3
05 32 45.03	-05 22 23.9	16.8	1.4 ± 0.5	157.6 ± 9.9
05 32 45.03	-05 22 33.9	28.9	0.3 ± 0.2	142.6 ± 16.7
05 32 45.03	-05 22 43.9	41.7	1.3 ± 0.2	74.5 ± 3.6
05 32 45.03	-05 22 53.9	39	2.1 ± 0.2	69.2 ± 2.6
05 32 45.03	-05 23 03.9	33.5	1.9 ± 0.3	65.3 ± 4
05 32 45.03	-05 23 13.9	27.3	1.8 ± 0.3	64.2 ± 4.4
05 32 45.03	-05 23 23.9	24.2	2.3 ± 0.3	70.6 ± 3.6
05 32 45.03	-05 23 33.9	22.3	2.9 ± 0.3	63.7 ± 3.4
05 32 45.03	-05 23 43.9	22	2.9 ± 0.2	60.7 ± 2.3
05 32 45.03	-05 23 53.9	23.3	2.5 ± 0.3	63.3 ± 3.3
05 32 45.03	-05 24 03.9	26.2	1.7 ± 0.3	55.1 ± 5.7
05 32 45.03	-05 24 13.9	24.8	1.8 ± 0.4	57.9 ± 6.2
05 32 45.03	-05 24 23.9	24.9	1.4 ± 0.4	46.5 ± 8.1
05 32 45.03	-05 24 33.9	20.5	1.2 ± 0.3	44.1 ± 8.1
05 32 45.03	-05 24 43.9	17.2	1.5 ± 0.3	13.6 ± 6
05 32 45.03	-05 24 53.9	13.5	2.3 ± 0.3	16 ± 4.4
05 32 45.03	-05 25 03.9	11.6	1.5 ± 0.4	20.6 ± 8.2
05 32 45.03	-05 25 13.9	9.3	2.7 ± 0.6	10.4 ± 6.4
05 32 45.03	-05 25 23.9	7.6	2.6 ± 0.9	0.6 ± 9.6
05 32 45.03	-05 25 33.9	5.6	3 ± 0.6	174.7 ± 5.8
05 32 45.03	-05 25 43.9	4.9	3.7 ± 1.1	163.3 ± 8.4
05 32 45.03	-05 25 53.9	4.3	3.6 ± 1.3	6.3 ± 10.6
05 32 44.36	-05 22 03.9	5.2	4.7 ± 1.4	154.5 ± 8.3
05 32 44.36	-05 22 13.9	7.7	2.3 ± 0.7	154.6 ± 9
05 32 44.36	-05 22 23.9	10.7	2.4 ± 0.4	148.2 ± 4.7

Table C.1: Polarization data of the Orion OMC-1 map (continued).

α	δ	I [Jy]	p [%]	χ [°]
05 32 44.36	-05 22 33.9	17.2	1.3 ± 0.3	138.4 ± 6
05 32 44.36	-05 22 43.9	19.5	0.8 ± 0.4	100.1 ± 13.4
05 32 44.36	-05 22 53.9	19.4	1 ± 0.4	90.9 ± 10.6
05 32 44.36	-05 23 03.9	16.7	0.4 ± 0.3	103.2 ± 22.7
05 32 44.36	-05 23 33.9	15.5	1.4 ± 0.6	59.7 ± 11.5
05 32 44.36	-05 23 43.9	14.5	1.1 ± 0.4	53.8 ± 11
05 32 44.36	-05 23 53.9	13	1.9 ± 0.4	60.9 ± 5.8
05 32 44.36	-05 24 03.9	12	3 ± 0.4	50.6 ± 3.9
05 32 44.36	-05 24 13.9	11.3	2.6 ± 0.6	44.5 ± 6.1
05 32 44.36	-05 24 23.9	10.2	3 ± 0.6	34.8 ± 6
05 32 44.36	-05 24 33.9	9.4	2.4 ± 0.8	30.3 ± 10.2
05 32 44.36	-05 24 43.9	8.1	3 ± 0.7	19.2 ± 6.7
05 32 44.36	-05 24 53.9	8	3.8 ± 0.8	23.9 ± 6.1
05 32 44.36	-05 25 03.9	7.9	2.3 ± 0.8	13.2 ± 9.6
05 32 44.36	-05 25 23.9	5	4.2 ± 1.3	164.5 ± 8.8
05 32 44.36	-05 25 33.9	4	4.5 ± 1.1	4.8 ± 6.9
05 32 43.70	-05 22 03.9	4.6	4.9 ± 1.2	155.6 ± 6.7
05 32 43.70	-05 22 13.9	6	3 ± 0.8	153.5 ± 7.9
05 32 43.70	-05 22 23.9	7.8	3 ± 0.6	143.5 ± 5.3
05 32 43.70	-05 22 33.9	8.6	2.5 ± 0.6	146.5 ± 6.3
05 32 43.70	-05 22 43.9	9.8	1.4 ± 0.8	146.5 ± 16
05 32 43.70	-05 22 53.9	9.2	2.1 ± 0.7	118.2 ± 9.8
05 32 43.70	-05 23 03.9	10	1.3 ± 0.3	134.4 ± 7.5
05 32 43.70	-05 23 13.9	10.1	2.1 ± 0.5	126.5 ± 6.5
05 32 43.70	-05 23 23.9	10.5	1.6 ± 0.8	125.9 ± 14
05 32 43.70	-05 23 33.9	10.6	1.6 ± 0.6	108.7 ± 9.8
05 32 43.70	-05 23 43.9	10.1	1.1 ± 0.6	86.7 ± 15
05 32 43.70	-05 23 53.9	8.4	0.9 ± 0.6	66.8 ± 19.6
05 32 43.70	-05 24 03.9	6.8	3.2 ± 0.8	67.6 ± 7.4
05 32 43.70	-05 24 13.9	6.5	2.6 ± 1.1	54.3 ± 11.6
05 32 43.70	-05 24 23.9	6.5	2.3 ± 0.9	33.7 ± 11.9
05 32 43.70	-05 24 33.9	6.4	1.1 ± 0.7	177.7 ± 17.3
05 32 43.70	-05 24 43.9	5.8	1.4 ± 1	7.8 ± 19.2
05 32 43.70	-05 24 53.9	6.2	3.1 ± 0.7	173.9 ± 6.7
05 32 43.70	-05 25 03.9	6.5	3 ± 0.9	5.7 ± 8.4
05 32 43.70	-05 25 13.9	5.7	2.8 ± 0.9	31 ± 9.1
05 32 43.03	-05 22 13.9	4.3	2 ± 1	144 ± 14.7
05 32 43.03	-05 22 23.9	5.2	1.6 ± 0.9	117.1 ± 15.8
05 32 43.03	-05 22 43.9	5.4	3.8 ± 1	146 ± 7.3
05 32 43.03	-05 22 53.9	5.4	3.8 ± 1	118 ± 7.4
05 32 43.03	-05 23 03.9	6.5	3.4 ± 0.9	135.1 ± 7.5
05 32 43.03	-05 23 13.9	7.3	4.1 ± 0.9	127.9 ± 6

Table C.1: Polarization data of the Orion OMC-1 map (continued).

α	δ	I [Jy]	p [%]	χ [°]
05 32 43.03	-05 23 23.9	7.2	2.6 ± 0.8	132.4 ± 8.9
05 32 43.03	-05 23 33.9	7.1	2.3 ± 1.2	130.8 ± 14.7
05 32 43.03	-05 23 43.9	7.1	1.4 ± 0.8	124.4 ± 17.6
05 32 43.03	-05 24 03.9	4	3.4 ± 1.7	150.3 ± 14.3
05 32 43.03	-05 24 23.9	4.4	4.1 ± 1.2	173.7 ± 8.1
05 32 43.03	-05 24 43.9	5.4	2.7 ± 0.8	18.3 ± 8.7
05 32 43.03	-05 24 53.9	4.9	2 ± 0.9	153.2 ± 13.1
05 32 43.03	-05 25 03.9	4.4	4.1 ± 1.2	161.8 ± 8.3
05 32 42.36	-05 23 03.9	4.1	7.5 ± 1.2	145.1 ± 4.4
05 32 42.36	-05 23 13.9	4.8	4.1 ± 1.4	130.1 ± 9.5
05 32 42.36	-05 23 23.9	4.6	3.5 ± 1.2	138.5 ± 9.9
05 32 42.36	-05 23 33.9	4.6	3.2 ± 1.5	131 ± 13.9
05 32 42.36	-05 24 43.9	4.2	4 ± 1.2	16.7 ± 8.3

Table C.1: Polarization data of the Orion OMC-1 map (continued).

Acknowledgments

It is time to say thank you to the people that were involved in this work at different stages and at different levels. My first thought goes to the people that were working by my side in the bolometer group at MPIfR.

First of all, Ernst Kreysa: he is the man that made all this possible. He gave to me the great opportunity to work on this Ph.D. project and he followed its evolution step by step, guiding me through the many difficulties that we found along the way with suggestions and clever solutions. Thank you so much, Ernst. And thanks a lot to his wife Janet, she was so kind to help me with the language, in the desperate task to repair my broken English.

Many thanks to Walter Esch who never said "no" to my many help requests, to Peter Gemünd for the many suggestions about almost everything (from the filters transmission to the market where to buy good furniture), to Gundula Lundershausen for the help in the lab and in technical drawing and for her matchless Zwiebelkuchen, to Bernd Ufer who shared with me the secrets to produce wire-grids. And Peter van der Wal, Frank Schäfer, Albert Korn that were so friendly with me since the first days at the institute.

Thanks a lot to Karl Menten who supported my work in the Millimeter Group for more than three years, always trusting me and the evolution of my project.

Special thanks to Stefan Phillips and to the MPIfR Werkstatt: they were able to do a good job even when my drawings were impossible to understand.

The soundtrack, especially in the last months, was provided by Thomas Stanke and Ed Polehampton.

Moving to the US, I want to acknowledge with gratitude the astronomers and the FOT at the HHT. In particular, the director Tom Wilson, the secretary Susan Lake, the astronomers Harold Butner and Baltasar Vila Vilaro, the friends of the telescope

Doug Officer, Bob Stupak and Harry Fagg and William Peters for computer-related help.

And now my thoughts go to the "Italian Connection". Mille grazie to Andrea Raccanelli, who not only shared the office with me but also was supporting me during the bad times. Un grazie di cuore a Claudia Comito and Silvia Leurini who were so kind and so patient to tolerate my unbearable mood and, especially in the last few months during the preparation of this thesis, they gave me the strength to go on.

Giuseppe Cimò, in these three years has shared a lot of his time with me. We went to the HHT together but we went also to Köln for Karneval. I made a Doktorarbeit, in the meanwhile I found a good friend.

Last but not least, I want to say thank you to Lothar Reichertz. He was my best friend here in Bonn. Thank you Lothar, I would never have made it without you. And I am not just talking about the thesis.

Bibliography

Akeson, R. L., Carlstrom, J. E., Phillips, J. A., & Woody, D. P. 1996, ApJ, 456, L45

Attridge, J. M., Homan, D. C., Wardle, J. F. C., & Krichbaum, T. P. 2000, American Astronomical Society Meeting, 197, 0

Bally, J., Stark, A. A., Wilson, R. W., & Langer, W. D. 1987, ApJ, 312, L45

Barvainis, R., Clemens, D. P., & Leach, R. 1988, AJ, 95, 510

Beuther, H., Schilke, P., Gueth, F., McCaughrean, M., Andersen, M., Sridharan, T. K., & Menten, K. M. 2002a, A&A, 387, 931

Beuther, H., Schilke, P., Sridharan, T. K., Menten, K. M., Walmsley, C. M., & Wyrowski, F. 2002b, A&A, 383, 892

Broguiére, D., Neri, R., Sievers, A., & Wiesemeyer, H. 1995, NIC Bolometer Users Guide (IRAM internal report)

Burton, M. G., Minchin, N. R., Hough, J. H., Aspin, C., Axon, D. J., & Bailey, J. A. 1991, ApJ, 375, 611

Cawthorne, T. V., Wardle, J. F. C., Roberts, D. H., Gabuzda, D. C., & Brown, L. F. 1993, ApJ, 416, 496

Chini, R., Reipurth, B., Ward-Thompson, D., Bally, J., Nyman, L.-A., Sievers, A., & Billawala, Y. 1997, ApJ, 474, L135+

Chrysostomou, A., Hough, J. H., Burton, M. G., & Tamura, M. 1994, MNRAS, 268, 325

Cimò, G., Fuhrmann, L., Krichbaum, T. P., Beckert, T., Kraus, A., Witzel, A., & Zensus, J. A. 2002, ArXiv Astrophysics e-prints, 7038

Collett, E. 1993, Polarized light: fundamentals and applications (Marcel Dekker, Inc., New York)

Crutcher, R. M., & Kazes, I. 1983, A&A, 125, L23

Crutcher, R. M., Troland, T. H., Goodman, A. A., Heiles, C., Kazes, I., & Myers, P. C. 1993, ApJ, 407, 175

Crutcher, R. M., Troland, T. H., Lazareff, B., & Kazes, I. 1996, ApJ, 456, 217

Davidson, J. A., Schleuning, D., Dotson, J. L., Dowell, C. D., & Hildebrand, R. H. 1995, in ASP Conf. Ser. 73: From Gas to Stars to Dust, 225–234

Davis, L. J., & Greenstein, J. L. 1950, AJ, 55, 71

Emerson, D. T., Klein, U., & Haslam, C. G. T. 1979, A&A, 76, 92

Evans, A. 1994, The dusty universe (John Wiley & Sons/Praxis Publishing Ltd)

Fiebig, D., & Guesten, R. 1989, A&A, 214, 333

Flett, A. M., & Murray, A. G. 1991, MNRAS, 249, 4P

Glenn, J., Walker, C. K., & Jewell, P. R. 1997, ApJ, 479, 325

Glenn, J., Walker, C. K., & Young, E. T. 1996, Bulletin of the American Astronomical Society, 28, 912

Greaves, J. S., & Holland, W. S. 1999, MNRAS, 302, L45

Greaves, J. S., Holland, W. S., Jenness, T., Chrysostomou, A., Berry, D. S., Murray, A. G., Tamura, M., Robson, E. I., Ade, P. A. R., Nartallo, R., Stevens, J. A., Momose, M., Morino, J.-I., Moriarty-Schieven, G., Gannaway, F., & Haynes, C. V. 2003, MNRAS, 340, 353

Haller, E. E., Palaio, N. P., Rodder, M., Hansen, W. L., & Kreysa, E. 1982, Presented at the 4th Intern. Neutron Transmutation Doping Conf., Gaithersburg, Md., 1-3 June. 1982, 83, 28412

Haslam, C. G. T. 1974, A&AS, 15, 333

Hildebrand, R. H. 1983, QJRAS, 24, 267

Hildebrand, R. H., Dragovan, M., & Novak, G. 1984, ApJ, 284, L51

Holland, W., Duncan, W., & Griffin, M. 2002, in ASP Conf. Ser. 278: Single-Dish Radio Astronomy: Techniques and Applications, 463–491

Homan, D. C., Ojha, R., Wardle, J. F. C., Roberts, D. H., Aller, M. F., Aller, H. D., & Hughes, P. A. 2002, ApJ, 568, 99

Houde, M., Akeson, R. L., Carlstrom, J. E., Lamb, J. W., Schleuning, D. A., & Woody, D. P. 2001, PASP, 113, 622

Houde, M., Bastien, P., Dotson, J. L., Dowell, C. D., Hildebrand, R. H., Peng, R., Phillips, T. G., Vaillancourt, J. E., & Yoshida, H. 2002, ApJ, 569, 803

Huard, S. 1997, Polarization of light (John Wiley Sons, Chichester)

Inoue, M., Takahashi, T., Tabara, H., Kato, T., & Tsuboi, M. 1984, PASJ, 36, 633

Keene, J., Hildebrand, R. H., & Whitcomb, S. E. 1982, ApJ, 252, L11

Kreysa, E., Gemünd, H.-P., Raccanelli, A., Reichertz, L. A., & Siringo, G. 2002, in Experimental Cosmology at Millimetre Wavelengths: 2K1BC Workshop. AIP Conference Proceedings, Vol. 616. Breuil-Cervinia, Valle d'Aosta, Italy, 9-13 July, 2001. Edited by Marco De Petris and Massimo Gervasi., 262–269

Langenbeck, P. 1980, Sonderdruck aus Industrie Diamanten Rundschau IDR 2

Mack, K.-H., Klein, U., O'Dea, C. P., & Willis, A. G. 1997, A&AS, 123, 423

Martin, D. H., & Puplett, E. 1969, Infr. Phys., 10, 105

Matthews, B. C., & Wilson, C. D. 2000a, American Astronomical Society Meeting, 197, 0

—. 2000b, ApJ, 531, 868

Matthews, B. C., Wilson, C. D., & Fiege, J. D. 2001, ApJ, 562, 400

Meade, M. L. 1983, Lock-in amplifiers : principles and applications (P. Peregrinus on behalf of the Institution of Electrical Engineers)

Morsi, H. W., & Reich, W. 1986, A&A, 163, 313

Mouschovias, T. C. 1976, ApJ, 207, 141

Mouschovias, T. C., & Paleologou, E. V. 1980, ApJ, 237, 877

Mundy, L. G., Cornwell, T. J., Masson, C. R., Scoville, N. Z., Baath, L. B., & Johansson, L. E. B. 1988, ApJ, 325, 382

Naumann, H. 1967, Handbuch der Physik (ed. S.Flugge, Springer-Verlag, Berlin)

Novak, G., Gonatas, D. P., Hildebrand, R. H., & Platt, S. R. 1989, PASP, 101, 215

Novak, G., Predmore, C. R., & Goldsmith, P. F. 1990, ApJ, 355, 166

Parker, E. N. 1966, ApJ, 145, 811

Platt, S. R., Dotson, J. L., Dowell, C. D., Hildebrand, R. H., Schleuning, D., & Novak, G. 1995, in ASP Conf. Ser. 73: From Gas to Stars to Dust, 543–

Platt, S. R., Hildebrand, R. H., Pernic, R. J., Davidson, J. A., & Novak, G. 1991, PASP, 103, 1193

Pudritz, R. E., & Norman, C. A. 1983, ApJ, 274, 677

Rao, R., Crutcher, R. M., Plambeck, R. L., & Wright, M. C. H. 1998, ApJ, 502, L75+

Reichertz, L. A., Weferling, B., Esch, W., & Kreysa, E. 2001, A&A, 379, 735

Richards, P. L. 1994, Journal of Applied Physics, 76, 1

Schleuning, D. A. 1998, ApJ, 493, 811

Schleuning, D. A., Dowell, C. D., Hildebrand, R. H., Platt, S. R., & Novak, G. 1997, PASP, 109, 307

Shapiro, J. B., & Bloemhof, E. E. 1990, IJIMW, 11, 973

Shinnaga, H., Tsuboi, M., & Kasuga, T. 1999, PASJ, 51, 175

Simmons, J. F. L., & Stewart, B. G. 1985, A&A, 142, 100

Sridharan, T. K., Beuther, H., Schilke, P., Menten, K. M., & Wyrowski, F. 2002, ApJ, 566, 931

Stevens, J. A., Robson, E. I., & Holland, W. S. 1996, ApJ, 462, L23+

Taylor, G. B. 1998, ApJ, 506, 637

—. 2000, ApJ, 533, 95

Torre, J. P., & Chanin, G. 1985, Review Sci. Instr., 56, 318

Troland, T. H., & Heiles, C. 1982, ApJ, 252, 179

Tsuboi, M., Kawabata, T., Kasuga, T., Handa, T., & Kato, T. 1995, PASJ, 47, 829

Verschuur, G. L., & Kellermann, K. I. 1974, Galactic and extra-galactic radio astronomy (Springer-Verlag, New York)

Wagner, S. J., & Witzel, A. 1995, ARA&A, 33, 163

Wardle, J. F. C., & Kronberg, P. P. 1974, ApJ, 194, 249

Witzel, A., Heeschen, D. S., Schalinski, C., & Krichbaum, T. 1986, Mitteilungen der Astronomischen Gesellschaft, Vol. 65, p.239, 65, 239

Zylka, R. 1998, Pocket Cookbook for the MOPSI Software (MPIfR internal report)

List of Figures

1.1 Polarization vs. flux in M17 15

1.2 Schematic design of a thermal detector 19

1.3 Schematic design of a composite bolometer 20

1.4 HUMBA and MAMBO-1 arrays of bolometers 23

1.5 MAMBO-2 array of 117 bolometers 23

2.1 Comparative block diagram of polarization and total power measurement systems 30

2.2 Scheme of a reflection-type half-wave plate 37

2.3 Phase shift vs. wavelength for different values of the RHWP order . . . 38

2.4 Phase shift vs. incidence angle for $\lambda_0 = 0.87$ mm, $\alpha = 15°, 30°, 45°$ . . . 40

2.5 Transmission vs. wavelength for different rotation angles when PolKa is used with the HHT 19 channel array 41

2.6 Transmission vs. wavelength for different rotation angles when PolKa is used with the MAMBO-2 array 41

3.1 Schematic drawing of a wire-grid polarizer 46

3.2 Transmission curves of a wire-grid polarizer 48

3.3 One of the two sets of golden Tungsten wires 49

3.4 *Left*: The set of wires going to be stretched and cleaned. *Right*: The final product ready to be used 50

3.5 *Left*: The wire-grid machine as it was before the modifications. *Right*: The machine after the modifications 51

3.6 *Left*: Scheme of the frame used to collect the wire before the upgrade.*Right*: Section of the cylinder that replaced the rectangular frame. 51

3.7 The four steps of the winding process 53
3.8 *Left*: A detail of the gap between the two bars.*Right*: Side view at the edge of cylinder and bars 54
3.9 A set of wires removed from the machine 55
3.10 *Left*: The ultimate wire-grid. *Right*: A detailed microscopic view of the wires 56

4.1 The first prototype of RHWP 59
4.2 Experimental setup for the lab tests done in December 2000 60
4.3 Results of the lab tests of the first RHWP prototype 61
4.4 Load curves of the two bolometers of the two-channel polarimeter . . . 62
4.5 Geometrical relation between γ, γ' and α 62
4.6 The 146 mm RHWP 63
4.7 The 146 mm RHWP mounted on the air bearing in the lab 64
4.8 *Left*: Scheme of the position angle reference system. *Right*: A detail of the rotating part of the bearing 65
4.9 A signal modulated by the RHWP is plotted together with the signal from the reference system used to restore the information about the position angle of the RHWP 66
4.10 Setup used in the lab to test the 146 mm RHWP 66
4.11 Polarization modulation produced by the 146 mm RHWP 68
4.12 Projected angular velocity of the RHWP 69
4.13 Signals produced by the rotating RHWP plotted together with the signal produced by a chopper 71
4.14 The 246 mm RHWP 73

5.1 The Heinrich Hertz Telescope 77
5.2 The 19 channel bolometer array in the receiver cabin. 79
5.3 Layout of the 19 channel array. 79
5.4 Load curves of the 19 channel array. 80
5.5 The wobbler 81
5.6 Total power `On-Off` observing mode 83
5.7 Total power `On-the-Fly` observing mode 85

5.8 Polarization `On-the-Fly` observing mode 87
5.9 PolKABBA data acquisition example 92
5.10 Global scheme of the data acquisition 93
5.11 Atmospheric opacity at the HHT on May 2001. 94
5.12 PME measured at the telescope using a lab source. 95
5.13 Calibration of the position angle for the 19 channels. 96
5.14 Calibration of the measured position angle. Channel 1. 96
5.15 Atmospheric opacity at the HHT on January 2002. 97
5.16 PolKa at the HHT on January 2002. 98
5.17 PolKa at the HHT on January 2002. 98

6.1 Raw data acquired by PolKABBA during a `TPOO` scan 105
6.2 Typical signals of a `TPOO` scan 107
6.3 Calibration of the measured position angle. Channel 1. 114
6.4 Results of the `TPOO` on the planets 120
6.5 Bolometer beam map from a `On-the-Fly` map of Mars 121
6.6 Normalized bolometer response for the 19 channel of the HHT array . . 123
6.7 Spurious polarization measured observing planets. Polarization degree . 125
6.8 Spurious polarization measured observing planets. Polarization position angle 125
6.9 Calibration of the absolute position angle 126

7.1 Polarization detection on 3C279. Scan 1253 128
7.2 `POO` on 3C279: array configuration during scans 0451 and 0452 129
7.3 Linear polarization detection on point sources: 3C279, progressive averages 129
7.4 Linear polarization detection on point sources: 3C279, polarization degree 130
7.5 Detection of polarization variability in 3C279 131
7.6 Linear polarization detection on point sources: 1633+382, polarization degree 132
7.7 Linear polarization detection on point sources: 1633+382, position angle 132
7.8 Location of OMC-1 in the Orion constellation. Credits: *top, left*: © T. Credner, AlltheSky.com; *bottom, left*: Michael Weiland, Interessengemeinschaft Astronomie an der Universität Konstanz; *bottom, right*:unknown 134

7.9 Polarization `OtF` of Orion A OMC-1 136
7.10 Polarization map of Orion A OMC-1. The vectors are rotated by 90° . 137
7.11 Depolarization effect in Orion OMC-1 138
7.12 Total power map of Orion OMC-3 at 1.3 mm 139
7.13 Polarization map of OMC-3 140
7.14 The OMC-3 filament as seen by Matthews et al. (2001) 140
7.15 Molecular outflows in IRAS 05358+3543 141
7.16 Polarization map of IRAS 05358+3543 142

Giorgio Siringo

Curriculum Vitae et Studiorum

Personal data:
Family name: Siringo
Given names: Giorgio, Maria Antonio Giuseppe
Birth: Comiso, February the 1st, 1966
Citizenship: Italian
Marital status: not married
Military service: no obligations

Current address:

Max-Planck-Institut für Radioastronomie
Auf dem Hügel 69
53121 Bonn, Germany
phone: +49 (0) 228 525 270
email: gsiringo@mpifr-bonn.mpg.de

Studies:

2002 Participation to the school "Third IRAM Millimeter Interferometry Summer School", September 29th - October 6th, 2002, IRAM headquarters, Grenoble, France.

2002 Member of the International Max Planck Research School (IMPRS) for Radio and Infrared Astronomy, Rheinische Friedrich-Wilhelms-Universität of Bonn.

2001 Ph.D. fellowship at the Max-Planck-Institut für Radioastronomie, Bonn, Germany. Ph.D. student at the Rheinische Friedrich-Wilhelms-Universität of Bonn.

1999 Laurea in Fisica (degree in Physics), full marks (110/110), Rome, May 21st 1999. Title of the thesis: "Studio di un polarimetro per il lontano infrarosso" (study of a polarimeter for the far-infrared). Experimental Cosmology Group G31, Department of Physics, "La Sapienza" University, Rome, Italy.

1998 Participation to the school "3K Cosmology from Space", International School of Space Science, September 2nd - 12th, 1998, Scuola Superiore di Studi Guglielmo Reiss Romoli, L'Aquila, Italy.

1991 Qualification "Operatore su Computer" (computer operator) and qualification "Programmatore di sistemi di elaborazione in monoutenza" (programmer of single-user computer systems) released, after examination, by E.N.F.A.P. (Ente Nazionale Formazione e Addestramento Professionale), Siracusa, Italy.

1984 High school degree "Diploma di Maturità Scientifica", Liceo Scientifico "Luigi Einaudi", Siracusa, Italy, July 1984. Marks: 52/60.